Lowering the barriers to developing thermal renewable energy technologies

Ashok Athreya Kaniyal
BE.(Mech) Hons., BFin

Thesis submission for the degree of Doctor of Philosophy

School of Mechanical Engineering
Faculty of Engineering, Computer & Mathematical Sciences
The University of Adelaide, Australia

March 2016

CONTENTS

ABSTRACT

Impediments to investment in renewable energy resources arise in five areas, namely, infrastructure access, technological and resource uncertainty, competition from established fossil fuel alternatives, asset financing and public policy. Together these can lead to large capital cost penalties and poor resource productivity that reduce the viability of projects. Presented here are system-wide analyses of two novel pathways to generate new investment in concentrated solar thermal and in geothermal energy resources. The pathways are designed to reduce the minimum capital outlay required for the development of renewable energy resources, by identifying synergies with established energy and non-energy infrastructure and technologies.

The endothermic, thermochemical processing of fossil, waste and biomass using concentrated solar energy has been demonstrated, at experimental scales between 3-500 kW_{th}, to upgrade the calorific value of syngas relative to the feedstock by ~30%, depending on the reactor technology employed and the fuel that is processed. However, no process modeling analysis has previously been presented of the impacts of diurnal, seasonal and cloud-induced solar resource availability on the operational limits of commercially available Fischer-Tropsch (FT) liquids syngas processing infrastructure. Presented here, are process modeling analyses of the relative performance of two solar gasification reactor systems and the operational impacts of their integration with a coal-to-liquids polygeneration facility. The reactor designs assessed were the batch process, indirectly irradiated solar packed bed gasifier that operates with solar input alone and a hybridised configuration of the solar vortex reactor that is assumed to integrate combustion to account for solar resource transience and thus enable a continuous non-zero syngas throughput. To address the impacts of solar resource transience, the process

modeling analyses showed that the packed bed solar reactor requires syngas storage equivalent to >30 days of gas flow to maintain feasible operation of unit operations downstream of the gasifier. In comparison, the hybrid solar vortex reactor was shown to require only ~8 hours of syngas storage. A dynamic process modeling study of integrating a hybrid solar vortex coal gasifier with a FT liquids polygeneration system was shown to improve the overall energetic productivity by 24% and to reduce mine-to-tank CO_2 emissions by 28%. This is the first comprehensive system analysis of a solar hybridised coal-to-liquids process that has assessed all the impacts of solar resource transience on the unit operations that comprise a FT liquids polygeneration system.

Geothermal resources can face barriers to investment arising from their remoteness—in particular, distance from established electricity transmission lines—uncertainty in the cost of establishing well infrastructure and uncertainty in the scale of the recoverable resource. To address these challenges, presented here is a comprehensive system evaluation of the potential of high-value energy load data-centres to reduce the cost of developing geothermal resources. This potential arises from the data-centres' modularity, their stable load for both electricity and refrigeration, and because their energy demand can be scaled commensurate to geothermal resource availability. Moreover, they can be connected to market by fibre optic network infrastructure, which is at least two orders of magnitude less expensive than electricity transmission. System analyses of this concept showed that a hybrid energy system that integrates low-temperature geothermal resources to meet data-centres' refrigeration load, and natural gas to meet the electrical load, could generate expected returns of 25% and reduce the cost of developing geothermal resources by >30 times.

The systems modelled in this thesis have shown that, compared with stand-alone development, the hybridised development of renewable energy resources with fossil fuel energy technologies offers a lower cost pathway.

DECLARATION

I certify that this work contains no material which has been accepted for the award of any other degree or diploma in my name, in any university or other tertiary institution and, to the best of my knowledge and belief, contains no material previously published or written by another person, except where due reference has been made in the text. In addition, I certify that no part of this work will, in the future, be used in a submission in my name, for any other degree or diploma in any university or other tertiary institution without the prior approval of the University of Adelaide and where applicable, any partner institution responsible for the joint-award of this degree.

I give consent to this copy of my thesis when deposited in the University Library, being made available for loan and photocopying, subject to the provisions of the Copyright Act 1968.

The author acknowledges that copyright of published works contained within this thesis resides with the copyright holder(s) of those works.

I also give permission for the digital version of my thesis to be made available on the web, via the University's digital research repository, the Library Search and also through web search engines, unless permission has been granted by the University to restrict access for a period of time.

ACKNOWLEDGEMENTS

I thank my parents, my wife and my supervisors for their undivided support throughout my PhD candidature. I would like to thank my parents for having made the courageous decision to migrate to Australia over 20 years ago and thus affording me a unique opportunity to build a career in this country. Their support and guidance has and continues to be invaluable to my personal and professional growth. I would like to thank my wife for her support and encouragement throughout my candidature and always encouraging me to believe in my capability to succeed. Her personal and professional success continues to be an inspiration.

I would like to thank Dr Philip van Eyk for encouraging me to persevere, especially through the latter phases of my candidature. Our weekly meetings were invaluable in helping me air and identify solutions to a range of technical and professional challenges.

I thank Mehdi for his encouragement and friendship throughout my candidature and his specific assistance with improving my numerical programming skills. His support was especially important in ensuring the successful completion of Chapters 4 and 5 of my thesis.

Finally, I would like to thank, Prof. Gus Nathan and Prof. Jonathan Pincus, for believing in my abilities from the very early stages of my candidature and through my doctoral candidature helping me establish a personal ethos of continuous improvement. This ethos has been crucial to helping me believe in my abilities and understand that improving my communication skills is a lifelong practice.

I would also like to thank the School of Mechanical Engineering, the Ricoh Clean Energy Scholarship and the Energy Pipelines CRC program for the financial support that was critical to my doctoral work.

PREFACE

This thesis is submitted as a portfolio of publications according to the "Specifications for Thesis 2013" of the University of Adelaide. The journals in which the papers were published or submitted are two of the most highly ranked journals in the research field of energy systems analyses. Data on the impact factors of the journals are listed below:

Journal	**2013 Impact Factor**	**2013 Energy Engineering & Power Technology Ranking***
Applied Energy	5.261	2/420
Energy & Fuels	2.733	14/420

* Journal ranking in terms of 2013 Impact Factor in the field of Energy Engineering and Power Technology

The main body of work contained in this thesis is within the following four journal papers (listed chronologically):

1. **Kaniyal AA**, Nathan GJ, Pincus JJ. The potential role of data-centres in enabling investment in geothermal energy. Applied Energy. 2012: 98, 458-66. *(1 citation)*
2. **Kaniyal AA**, van Eyk PJ, Nathan GJ, Ashman PJ, Pincus JJ. Polygeneration of liquid fuels and electricity by the atmospheric pressure hybrid gasification of coal. Energy & Fuels. 2013: 27(6), 3538-55.
3. **Kaniyal AA**, van Eyk PJ, Nathan GJ. Dynamic modeling of the coproduction of liquid fuels and electricity from a hybrid solar gasifier with various fuel blends. Energy & Fuels. 2013: 27(6), 3556-69.

4. **Kaniyal AA**, Jafarian M, van Eyk PJ, Nathan GJ. Solar gasification of coal in a batch process packed bed reactor – a 1D heat transfer, devolatilisation and gasification model. Manuscript Format

5. **Kaniyal AA**, van Eyk PJ, Nathan GJ. Storage capacity assessment of liquid fuels production by solar gasification in a packed bed reactor with a dynamic process model. Applied Energy. (Resubmitted following request for revisions – Feb 2016).

Some additional aspects of this work have been submitted for review and are expected to lead to the following journal articles.

1. Saw WL, **Kaniyal AA**, van Eyk PJ, Nathan GJ, Ashman PJ. Solar hybridised coal-to-liquids via gasification in Australia: techno-economic assessment. Energy Procedia. 2015: 69, 1819-27.

Where the mind is without fear and the head is held high

Where knowledge is free

Where the world has not been broken up into fragments

By narrow domestic walls Where words come out from the depth of truth

Where tireless striving stretches its arms towards perfection

Where the clear stream of reason has not lost its way

Into the dreary desert sand of dead habit

Where the mind is led forward by thee

Into ever-widening thought and action

Into that heaven of freedom, my Father, let my country awake

Rabindranath Tagore

English translation of Chitto Jetha Bhayshunyo

Gitanjali (1912)

1

INTRODUCTION AND LITERATURE REVIEW

1.0 Impediments to investment in renewable energy resources

The key impediments to investment in renewable energy projects can be categorised into the four families of asset financing, infrastructure access, technical risks and competition from established fossil fuel alternatives [1-4]. The sub-headings below describe the individual risk factors that make up these families of project risk.

1.1 Asset finance

There are two key elements to the asset-financing barrier, first because renewable energy investments require large upfront capital expenditure to install the technology required to recover energy over the life of the asset and second because renewables face revenue uncertainty related to technological readiness and resource intermittency. Indeed, while renewable energy technologies do not have the large operational expenditure associated with fuel costs over the life of the asset, these future operating costs are discounted by the time value of money unlike current capital expenditure. Thus the viability of this large initial expenditure requires revenue certainty, which is hindered by the uncertain productivity of renewable resources, owing to technological uncertainty or climate variability [5-11]. This viability challenge is typically addressed by energy systems integrating renewables securing public subsidies, loan guarantees or long-term (25-30 year) purchasing agreements with public businesses or private power generators [2]. In the short term, the successful engagement of public and private sector institutions is critical to successful project implementation and viable long-term operation. In this respect, a project that demands a smaller capital outlay and thus has lower revenue demands is more likely to secure such an agreement than larger projects with capital outlays exceeding >$1 billion, such as some projects in Australia have demanded [2]. Inevitably, large capital requirements create significant portfolio risks for public and private financing institutions, which inevitably demand high costs of capital and in turn reduces project viability [2].

1.2 Infrastructure access

The most productive renewable energy resources are often in remote, sparsely populated regions [5, 12, 13]. As a result, access to electricity, water, road transport and oil and gas utility networks is typically limited in these regions. This is evident for example through remote regions of central and northern Australia and the mid-western United States (relative to the eastern US) where solar resources are abundant but access to network utilities is limited [14]. This poses considerable challenges to the cost of construction, operating expenditure and the cost of delivering the recovered resource to energy commodity markets [5, 6, 11, 13, 15]. Indeed, the absence of adequate infrastructure often creates the need for considerable added capital expenditure, which in-turn has a negative impact on the likelihood of project receiving private debt financing as identified above [2].

1.4 Technical reliability and resource intermittency

Renewable energy systems face technical challenges based on two broad factors, first, the intrinsic risks associated with the technology development cycle and, second, fundamental resource limitations related to transience of the renewable energy resource [3-11]. The level of technology readiness is related to the risk of a particular technology failing and thus not being operationally reliable or a technology not operating at optimal efficiency, thus affecting capital productivity and consumer confidence in the capacity for renewable energy technologies to provide reliable supply [16]. Transience in renewable energy resources has led to considerable efforts being directed towards the development of energy storage technologies [17, 18]. However, there remain considerable technical challenges associated with the development of those storage technologies with large enough capacity to accommodate long periods of low renewable energy availability. Furthermore, the growing need for high cost energy storage [6, 11], places an additional capital expense penalty on the development of renewable energy systems.

1.5 Competition from fossil fuel alternatives

Fossil fuel energy systems based on coal, natural gas and mineral crude oil do not face the same risks to investment as do renewable energy projects in financing, technical risk, resource transience or infrastructure access barriers [14]. The incremental development of fossil fuel energy technologies over the last 100 years has led to their high technical reliability, which in-turn has led to the establishment of network infrastructure that enables the efficient delivery of energy resources to market. In addition, conventional fossil fuel energy systems take advantage of low-cost energy storage systems to enable feasible operation. These include the use of pipelines to store gaseous and liquid fuels and in the use of stockpiles and un-mined reserves to store solid fuels [14].

1.6 Options to address the barriers

In the publicly available literature little information is currently available to quantify the potential benefit of the proposed approach in identifying specific new pathways by which to generate investment in renewable energy technologies. The impediments to investment in renewable energy systems outlined above can be addressed by:

a) reducing the size of renewable energy projects and thus the minimum capital outlay required for a commercially viable investment, to reduce lender's risk and improve the likelihood of successful project financing;
b) identifying new opportunities to capitalise on synergies with established energy and/or non-energy infrastructure to avoid additional investment in new non-productive network infrastructure;
c) identifying new opportunities to capitalise on complementarities with established fossil fuel energy technologies to improve the capital productivity issues associated with technical reliability and intermittency of renewable resources;
d) identifying new opportunities for renewable energy resources to improve the productivity of established fossil fuel energy systems and thereby reduce the specific capital cost of investment in a given unit of capacity.

2.0 Investment in geothermal energy

2.1 Geothermal resource categories

There are two broad categories of geothermal resource, namely volcanically sourced hydrothermal systems, and enhanced geothermal resources (EGS) of which hot sedimentary aquifer resources are a sub-set [19]. This section outlines the energy generating potential of these resource categories and the main challenges to, and limitations of, each.

2.1.1 Hydrothermal resources

Hydrothermal resources offer a resource potential of between 2400 – 9600 EJ. However their development has only been viable in a limited number of locations worldwide. While, the installed electricity generating capacity from hydrothermal resources worldwide has increased from 1.3 GW_e to 10 GW_e over the last 40 years [19], approximately 20 geothermal generating sites producing at least 100 MW_e account for >90% of all hydrothermal electricity generating capacity [19, 20]. In comparison with EGS resources, convective hydrothermal systems are easier to exploit because temperatures of ~200°C are available at depths in the range 1.5 to 3 km instead of > 4 km. Resource availability at shallower depths also means that these reservoirs have natural permeability that is 3 to 4 orders of magnitude higher than that of EGS reservoirs [21]. The combination of high thermal gradient and natural reservoir permeability allow for large steam and water recovery rates [20]. However these reservoirs are most productive for the first 10-15 years after the commencement of energy extraction. This initial period is followed by a natural decline in the rate of resource extraction, which typically must be compensated for by the drilling of additional wells [20]. The combination of fast resource depletion rates, the relatively low worldwide energy potential and limited accessibility leads to hydrothermal resources not being expected to offer significant electricity generating potential over the next 50 years [21]. In comparison, EGS resources are not expected to have the same rate of energy depletion because their resource potential is much higher. However their technical feasibility is yet to be proven in the field. There is a thus a need to identify new investment pathways to lower the barriers to developing the technical feasibility of recovering EGS resources.

2.1.2 Enhanced geothermal systems and hot sedimentary aquifers

Enhanced geothermal systems (EGS) have the potential to provide 100 GW_e of electricity generating capacity [21]. The development of EGS is based on recovering thermal energy from hot dry crystalline granite rocks where heat is generated by the radioactive decay of potassium, uranium and thorium [21]. The steps involved in establishing an EGS reservoir are, drilling an injection and production well to a access hot rock geothermal reservoirs at temperatures >200°C, hydraulically fracturing the rock to generate a network of fissures through which the geo-fluid (e.g. water) can flow, intercepting these fractures and extracting the geo-fluid through a production well before re-injecting the geo-fluid to form a closed loop after energy extraction for direct use or electricity generation [21]. In high-grade EGS resource regions, the thermal gradient of crystalline rock structures can exceed 50°C/km, whereas the thermal gradient of the insulating sedimentary continental crust is typically 25-30°C/km [20]. However, identifying the regions where high-grade EGS resources, T_{res}>200°C, are found is uncertain given the wide lateral variability in geological stratigraphy from one region to the next. Figure 1 qualitatively illustrates the impact of regional stratigraphy on the temperature distribution with depth for two geological regions. The isotherms drawn in this figure show that a region of lower thermal conductivity (and gradient) in sedimentary layers above depths of 4 km in region 2, relative to the granite basement rock, can trap heat within the upper part of the radiogenic granite basement. In comparison, the stratigraphy of region 1, leads to no insulation of the radiogenic granite layer from the continental crust, thus reducing the overall thermal gradient with depth as illustrated by the isotherms in Figure 1. The presence of this insulating layer is deduced to decrease the minimum well depth required to access EGS reservoir temperatures > 200°C [20] and, is explained by large lateral variations in thermal conductivity that are expected to vary by factors of as much as 100% from one location to another at depths of 2 to 4 km [21]. This means that the wells in region 1 would likely have to be drilled deeper than in region 2 to recover EGS resources at the same T_{res}. However, both the magnitude of thermal conductivity variations with depth and their impact on the identification of regions where T_{res}>200°C can be recovered at depths < 3-4 km has not be scientifically validated by observations. Importantly, reducing this uncertainty will enable the accurate siting of geothermal wells

to recover high temperature resources at relatively shallow depths. This requires the development of more EGS wells across regions where modeling studies have shown high-grade resources could be found [21]. However, no specific proposal outlining a financially sustainable pathway to developing sufficient EGS reservoirs, to collect statistically meaningful data across a wide network, has been presented to date.

Both the natural permeability of geothermal reservoir and the depth to which geothermal wells have to be drilled have a significant impact on the cost of developing these resources (see Section 2.2.1). The natural permeability of geothermal reservoirs is negatively correlated with reservoir depth. For example from the continental surface (depth < 2.5 km) to a depth of 5 km, the permeable area in a reservoir decreases from 10^{-11} m^2 to between 10^{-16} and 10^{-18} m^2 [21]. To accurately evaluate resource recovery potential, there is a need to resolve this large range of uncertainty in the natural permeability of radiogenic granite reservoirs. There is generally more uncertainty in reservoir permeability than there is in thermal conductivity. Here, the natural permeability of hot sedimentary aquifers (HSA), where natural hot water flows at temperatures of ~ 150°C are found at depths of 1.5 – 3 km, is typically three orders of magnitude greater than that of hot rock EGS resources (see Figure 1) [20, 21]. The successful development of HSA resources could offer a pathway to incrementally reduce the uncertainty in recovering deeper EGS resources [21]. The particular characteristics of HSA resources means that these systems are likely to offer much higher fluid flow rates than granite basement rock EGS resources, albeit at the expense of lower geo-fluid temperatures (i.e. < 150°C) [20]. The development of HSA resources offers a pathway to establish a network of energy producing wells in a geothermal resource region and by generating capital equity from energy producing geothermal assets, deeper and more uncertain granite basement rock EGS resources can incrementally be developed. However, no specific commercial pathway to developing lower-temperature hot sedimentary aquifer geothermal resources as a pathway to developing deeper EGS resources has been presented to date.

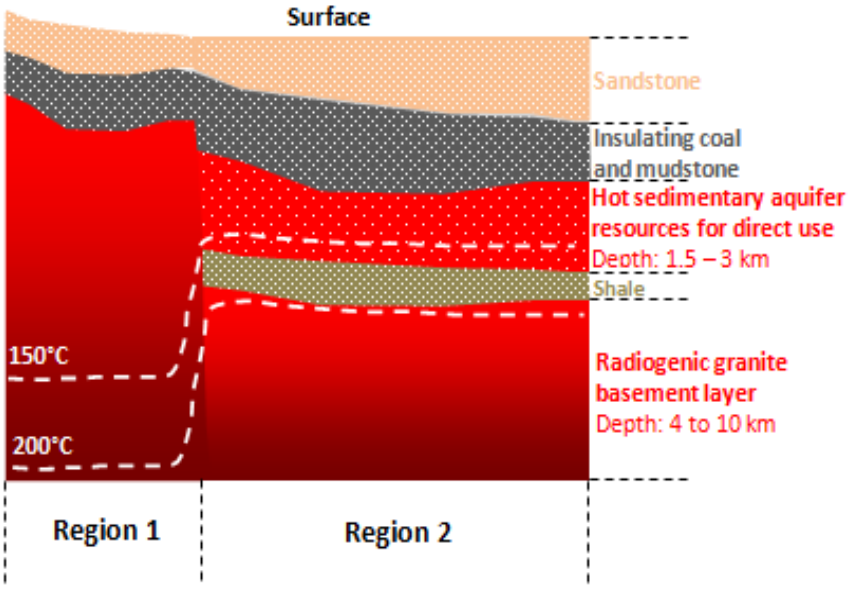

Figure 1: Cross-sectional view of geological layers and insulation of hot sedimentary aquifer and radiogenic granite – EGS geothermal mass distributions (not represented to scale) (adapted from [20]).

2.2 Recovering energy from hot rock resources

2.2.1 Uncertainty in drilling and reservoir stimulation costs

Drilling and stimulating an EGS reservoir constitutes more than 60% of total capital expenditure and are the most uncertain cost component of a geothermal resource development [21]. Figure 2 presents a relationship between the cost of drilling with well-depth for investments in wells to recover hydrothermal, EGS and oil and gas resources [21]. This figure shows that the historical cost of drilling a 3 km deep geothermal well can vary by as much as US$6 M (2004) or 2.5 times at a depth of 3 km. In comparison, the historical cost of oil and gas wells follows a linear function, with variance no greater than 20-30%, relative to the mean cost, for well depths < 6 km. While fewer than 10 geothermal wells of depth ~6 km have ever been drilled, less than 100 geothermal wells of depth <2.8 km are drilled annually, whereas thousands of oil and gas wells are drilled annually [21]. This leads to the significantly greater observed uncertainty in the cost of geothermal wells than oil and gas wells [21]. Although sophisticated drilling cost models offer predictions that account for a range of well-design parameters, very little data is available for model validation. This scarcity in cost data for geothermal wells leads to difficulties in developing statistically meaningful relationships. Future

reductions in the cost of developing geothermal wells is also influenced by advances in the oil and gas industry to recover resources from increasingly difficult geologies [21], which are also difficult to predict. Together, these large uncertainties in resource recovery potential mean that securing project financing to develop geothermal wells is a big challenge [21]. There is thus a need to identify alternative pathways to the development of productive EGS reservoirs that lower the risk. To address these challenges, there is a need to identify an opportunity to develop geothermal resources at a scale equivalent to the output of a single well doublet, enable a high level of resource utilisation such that the revenue generated from one well can create sufficient project equity to develop additional wells. No specific proposal that could enable these commercial outcomes has been presented in the literature to date.

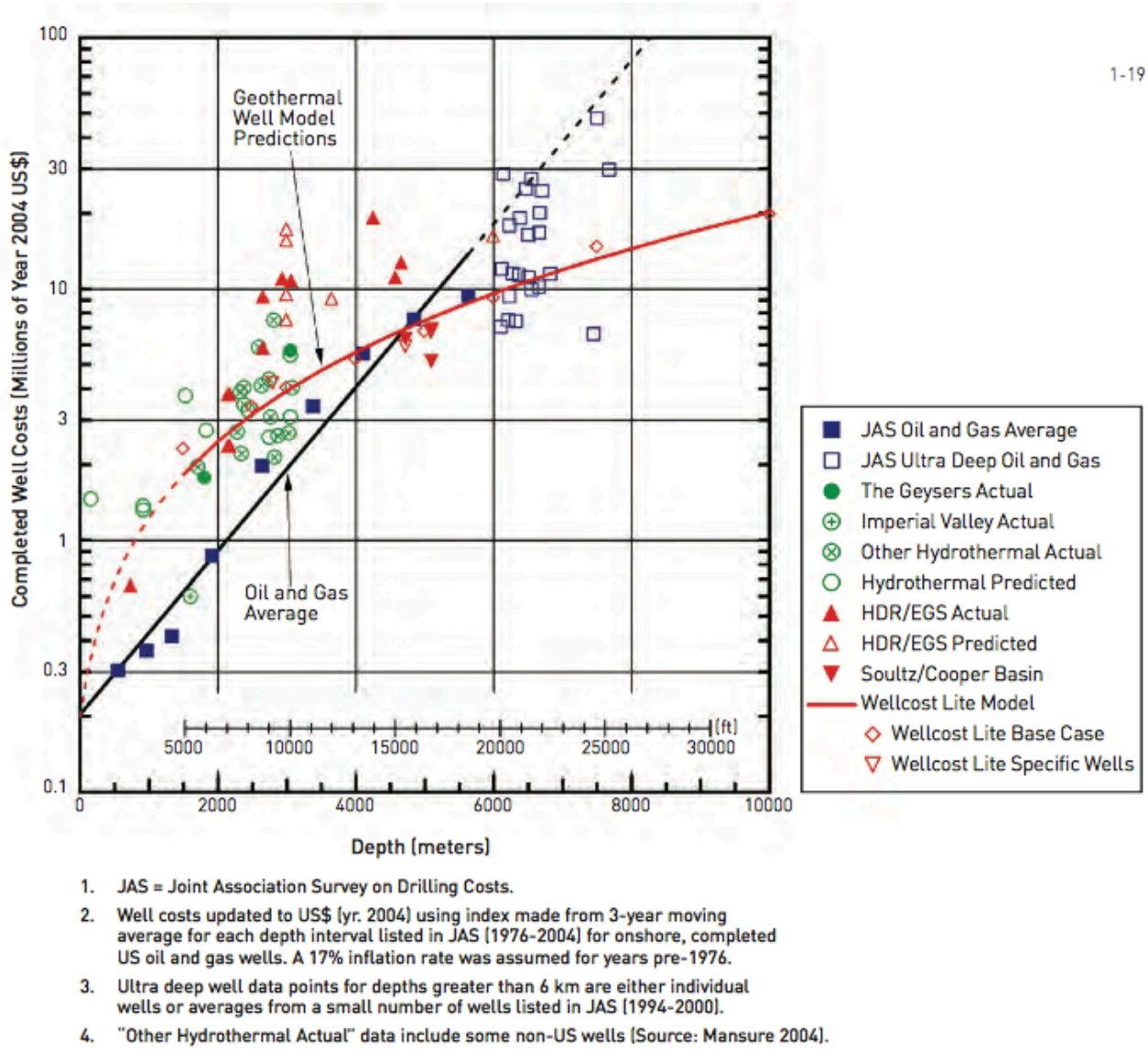

Figure 2: Relationships between the cost (US$ 2004) of completed wells and well depth for EGS resources (red), hydrothermal wells (green) and oil and gas wells (blue) (reproduced from [21]).

2.2.2 Energy conversion technologies

Depending on the geothermal reservoir temperature, one of three power generation cycle options are currently commercially available, the organic Rankine cycle (ORC), a single flash cycle or a double flash cycle. From these options, for low-temperature geo-fluids < 200°C, the ORC yields the highest thermal efficiency for power cycles. Figure 3 shows the relationship between the geofluid temperature and the specific cost of a power generation plant ($/kW$_e$ (net)) on the primary axis and the specific power output (kW$_e$) per unit geo-fluid flow extracted (kg/s) on the secondary axis for a 1 MW$_e$ organic Rankine cycle plant [21]. This figure shows that the cost of establishing a 1 MW$_e$ power generation

plant infrastructure is 1.5 times greater for a geo-fluid temperature ≤ 100°C, than for a geo-fluid temperature ≥175°C. Similarly, the specific power output per unit geo-fluid flow is at least 3.7 times larger for a geo-fluid temperature ≥175°C than it is for a temperature ≤100°C. For a geo-fluid temperature of 100°C, the thermal efficiency of an ORC is ~7%, and doubles to 14% for a geo-fluid temperature of 165°C [21]. Table 1 compares the cycle power outputs and specific costs for geo-fluid temperatures ≥ 200°C. This shows that for geo-fluid temperatures of 200°C, the organic Rankine cycle has the lowest cost per unit plant output and the highest specific power output per unit geo-fluid extraction rate of these cycles [21]. For geo-fluid temperatures ≥ 225°C and geo-fluid flow rates of 1000 kg/s, the single and double flash cycles have a specific plant cost ≤$1500/kW$_{e\ (net)}$. However, because the maximum sustainable mass flow rate from EGS reservoirs to date has been between 20 and 22 kg/s [21], these cycles are not expected to offer a lower cost alternative to the ORC. Hence, in the near-term the ORC is likely to offer the lowest cost route to power generation from enhanced geothermal systems and enable the most efficient conversion of a unit of geo-fluid flow to electricity. However, no analysis has been presented of a specific pathway to generating investment in EGS resources for electricity generation using an organic Rankine cycle process.

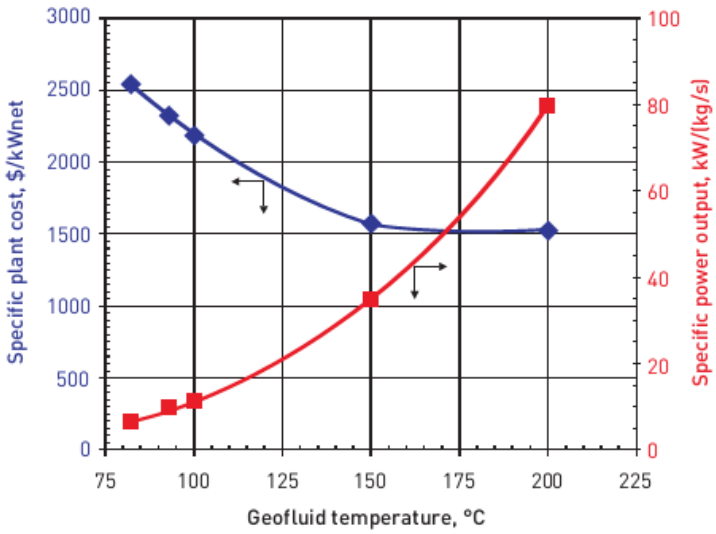

Figure 3: Influence of the geofluid temperature on the specific cost (US$/kW$_e$(net)) of developing a 1 MW$_e$ binary organic Rankine cycle energy conversion system and the specific power output per unit of geofluid flow (reproduced from [21]).

Table 1: Comparison of specific plant cost and cycle power output for the organic Rankine power cycle, single and double flash power cycles for geo-fluid temperatures ≥ 200°C [21].

Power generation cycle (1 MW_e)	**Specific plant cost ($/$kW_{e\ (net)}$)**	**Specific power output (kW_e/kg/s geo-fluid)**
Organic Rankine cycle ($T_{geo\text{-}fluid}$ = 200°C)	$1500	80
Single Flash cycle ($T_{geo\text{-}fluid}$ = 200°C)	$1880	53.9
Double Flash cycle ($T_{geo\text{-}fluid}$ = 250°C)	$1880	123.5

Supercritical Rankine cycles

Supercritical Rankine cycles present a new opportunity to increase the efficiency of generating electricity from geothermal resources from approximately 15 to 30% for geofluid temperatures recovered at temperatures >374°C and pressure >22 MPa. These systems take advantage of the non-linear relationship between the specific enthalpy and the temperature and pressure of pure water, taken as the geothermal fluid (geofluid). (Another supercritical Rankine cycle that uses CO_2 as the working fluid is also currently under development [22].) In this context, EGS reservoirs offer the potential to generate 10 MW_e with geo-fluid flow rates of 15 kg/s [21]. As a point of comparison, a geofluid at these conditions has five times the power generating potential of current hydrothermal systems recovering liquid water at 250°C [21]. While, significant technical challenges have to be overcome to improve the effectiveness of heat exchange devices and the mechanical efficiency and robustness of pumps and turbines, much of this development is taking place in the context of clean coal technologies [23]. Hence, the energy conversion technologies that are likely to be integrated with geothermal resources are likely to be those that have already been commercially proven and implemented.

2.3 Induced seismicity

Induced seismicity is minor earth tremors being triggered by the use of hydraulic fracturing techniques to increase the permeability of EGS and HSA reservoirs. The most prominent case of induced seismicity was at the site of the first commercial EGS project – the Deep Heat Mining project less than 5 km from the city of Basel, Switzerland. In this case, close proximity to a regional population of 700,000, a history of earthquakes and poor risk assessment procedures by the Geopower Basel consortium and regulatory stakeholders, led to the project eventually being put on hold following a magnitude-3.4 seismic event induced by the EGS development. Although the physical damage caused by this tremor to structures was superficial [24], public unpreparedness for the possibility of earthquakes caused significant damage to the perceived safety of this geothermal project [16]. Apart from the seismicity induced by the injection and production wells on a field-wide scale, much uncertainty remains with respect to the difference in seismic patterns induced by EGS operations relative to those from other industrial operations [24]. It is worth noting that induced seismicity is not limited to human activities to recover geothermal resources, the mining and oil and gas industry has dealt with this issue for a long time [24]. However, to ensure broad public acceptance of the development of geothermal resources, in the near term project sites are likely to be pushed towards areas that are well outside of major urban centres. Since sparsely populated areas are more likely to have limited connectivity to electricity transmission networks there is a need to identify alternative pathways to generating investment in geothermal resources that is not reliant on these networks or access to a proximate urban demand centre. No specific proposal that offers such an opportunity for geothermal resources has been presented in the publicly available literature to date.

2.4 Delivering energy to market

Access to oil and gas or electricity transmission networks is a critical driver of investment in geothermal resource capacity. Figure 4 highlights regions with high-grade EGS resources (T_{res}>200°C) potential overlaid on a map of the US electricity transmission networks [25]. High-grade EGS

resource regions are defined as locations where hot rock reservoirs with temperature >200°C can be found at depths of 3 to 5 km. Figure 4 shows that, while high-grade geothermal resources can be developed near established electricity transmission networks in the US and Europe [13], in Australia, geothermal resources are, at their nearest, 200 km from established electricity transmission networks. Supplying electricity over large distance typically requires a high voltage transmission line, which in turn requires generating capacity >100 MW_e. This is currently not feasible, given significant uncertainty in the cost of developing EGS reservoirs and predicting their energy recovery potential [21]. Hence, there is a need to identify alternative pathways to reliably deliver energy from unproven geothermal resources to consumers. Established oil and gas pipeline networks offer one possible opportunity to address this challenge. Figure 5 highlights regions with high-grade EGS resource potential on a map of the US and Australian oil and gas pipeline networks. This figure shows that high-grade geothermal resources in both Australia and the US could take advantage of this network of energy pipelines to deliver geothermal resources to market. Dickinson et al. recently reported the potential for 50 MW_e of EGS driven electricity generating capacity to electrolyse water to H_2 and thereby synthetically produce methane via the CO_2 consuming Sabatier process. This methane could then be transported through established natural gas pipeline networks connecting the Cooper Basin in SA to commercial gas markets in eastern and southern Australia [13]. However, at 50 MW_e, the minimum scale of electricity generating capacity required for this proposal is unlikely to be commercial in the near-term. Given the current state of geothermal technology, incremental well development at a scale < 10 MW_{th} is likely to offer a more attractive resource development pathway [21]. In this respect, geothermal resources can supplement complementary high-value energy demand that is currently not met by established electricity or gas transmission networks. No specific proposal as to how the geothermal industry could capitalise on synergies with established energy network infrastructure has been presented to date.

The development of geothermal power generation systems currently face significant cost challenges, in addition to the cost of developing the reservoir. While a geo-fluid flow rate of 20 kg/s at temperature 200°C, can sustainably enable an ORC to deliver 1 MW_e for a specific plant capital cost

of \$1500/kW_e [21], a micro-gas turbine of a similar size has a cost <\$600/kW_e [26]. There is thus a need to identify alternative applications where the hybridisation of geothermal resources with fossil fuel energy systems can improve productivity. Here, the direct use of geothermal energy within complementary renewable and fossil fuel power generation processes offers the potential to share above-ground infrastructure and reduce the capital expense of developing geothermal resources [21]. For example Bruhn described an application where a low-enthalpy geothermal resource improved the productivity of feedwater heating in a conventional power station and achieved a CO_2 avoidance cost similar to that achieved by wind power. However, this system is only feasible in a limited number of locations [27]. Tempesti et al. also described a novel micro-combined heat and power energy system integrating low temperature geothermal heat with an ORC that is supplemented by solar parabolic trough collectors to meet the load of a high-density apartment complex [28]. While these systems have been found to be feasible in a limited number of locations, no analysis has been presented of a system where the viability of geothermal resources can be delivered by co-locating an energy consumer with the resource and connected to a market using established infrastructure. No specific proposal that offers geothermal resources greater geographical flexibility in achieving connection to economic markets, than the proposals identified, using non-energy network infrastructure has been presented to date.

2.4.1 ICT infrastructure – Data-centres, telephone exchanges and supercomputers

Data-centres, telephone exchanges and supercomputers have the characteristics of modularity and a stable load for electricity and refrigeration. This makes them well suited to be co-located with a geothermal resource and their load characteristics can enable the viable development of co-generation systems. A geothermal – ORC cogeneration system can achieve a thermal efficiency of 16%, which is up to twice that of an ORC generating electricity alone, assuming an inlet temperature of 100°C. Data-centres and similar infrastructure are currently reliant on fossil fuel based trigeneration systems or retail electricity supplied through the grid to meet their large energy demands [29]. This presents a novel opportunity for geothermal resources to displace data-centres' energy load and thus the retail

price of electricity, which is on average five times larger than the wholesale price of electricity [13, 30]. Furthermore, the steady nature of data centres' energy demand is likely to enable 25% greater resource utilisation for a geothermal resource than a residential load [31]. This means that data-centres will yield a larger revenue stream than an equivalent residential load assuming the temporal price distribution of energy is fixed. Additionally, data centres can also flexibly expand their server capacity to match the energy generating capacity of a geothermal well [32]. Thus, they can accommodate the inherent uncertainty in the energy generating capacity of a geothermal well over the range 1 – 5 MW_e [30]. These energy load and scale characteristics make data-centres well suited for the energy output of geothermal systems. However, no systematic assessment of the potential opportunities offered by data-centres' modularity and the increasing ubiquity of fibre-optic networks, to generate new investment in geothermal resources constrained by access to existing energy markets, has been presented in the literature to date.

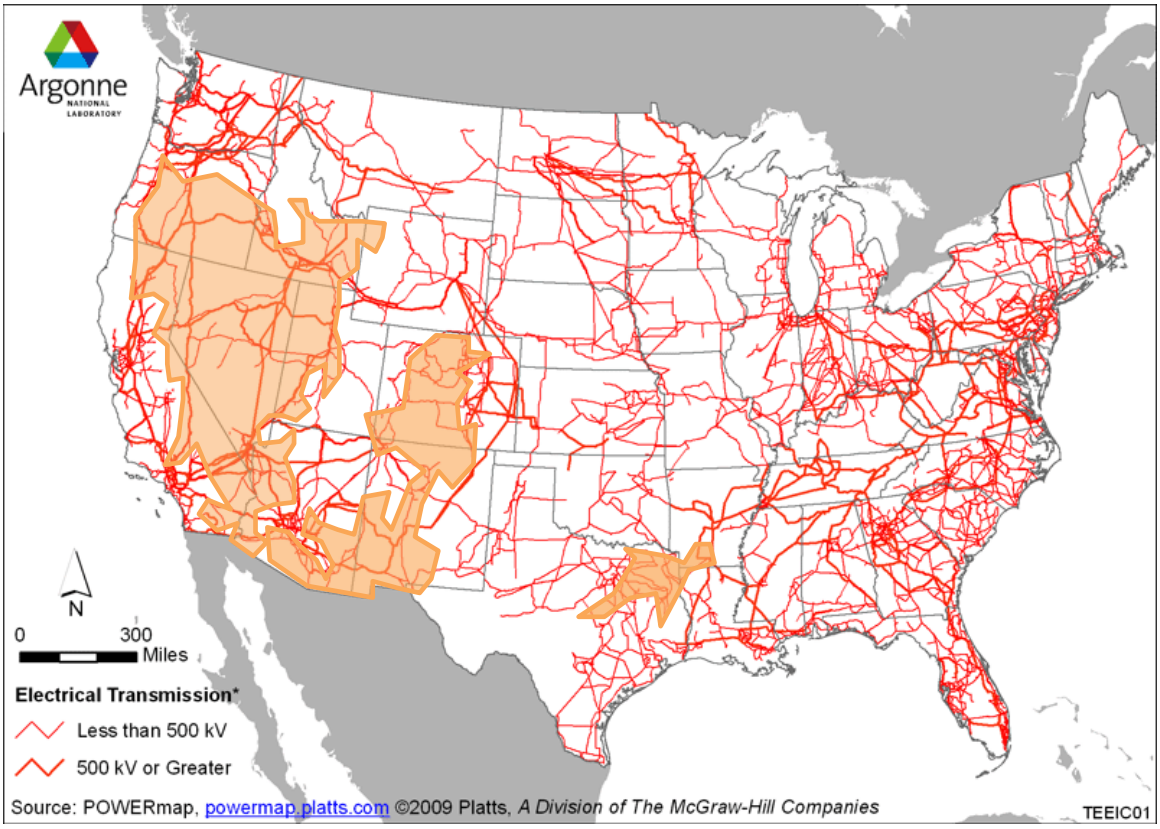

Figure 4: Regions of high grade geothermal resources (T>200°C at depth of 6.5 km for the US) overlaid on map of established US electricity networks [25].

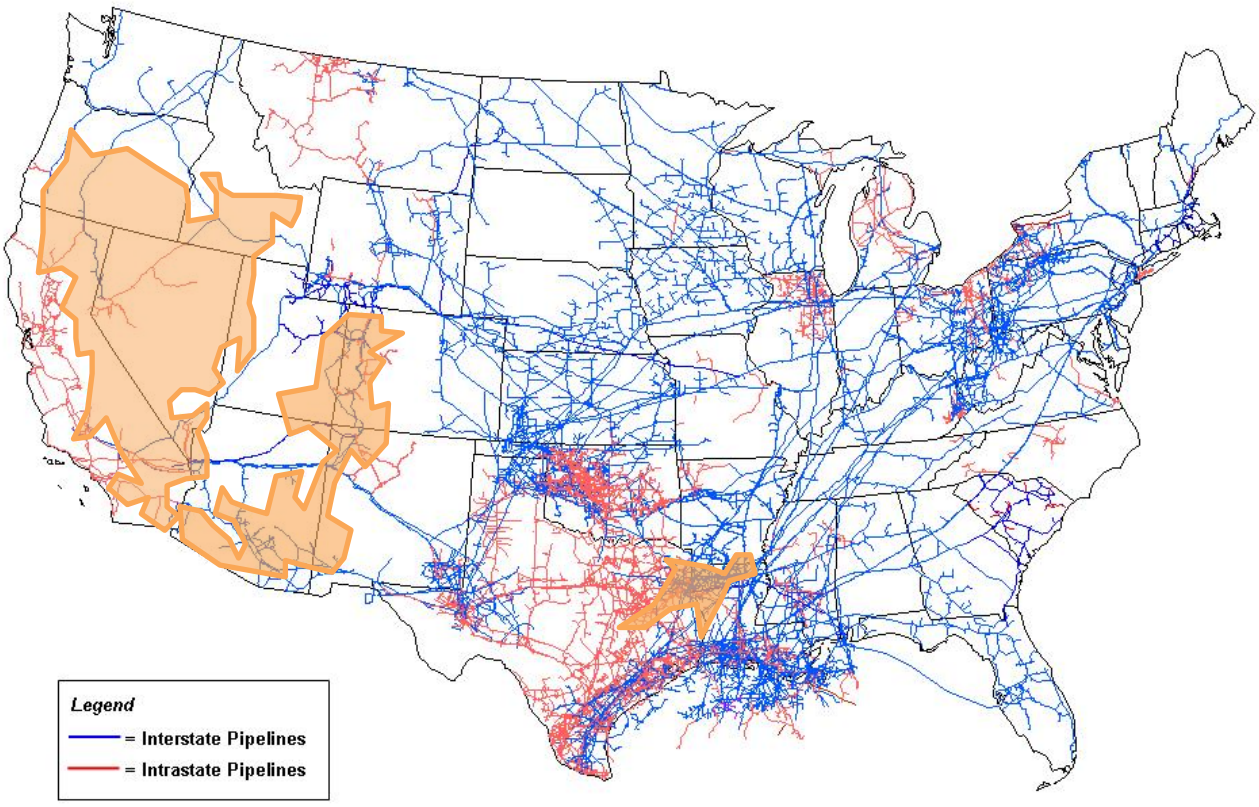

Source: Energy Information Administration, Office of Oil & Gas, Natural Gas Division, Gas Transportation Information System

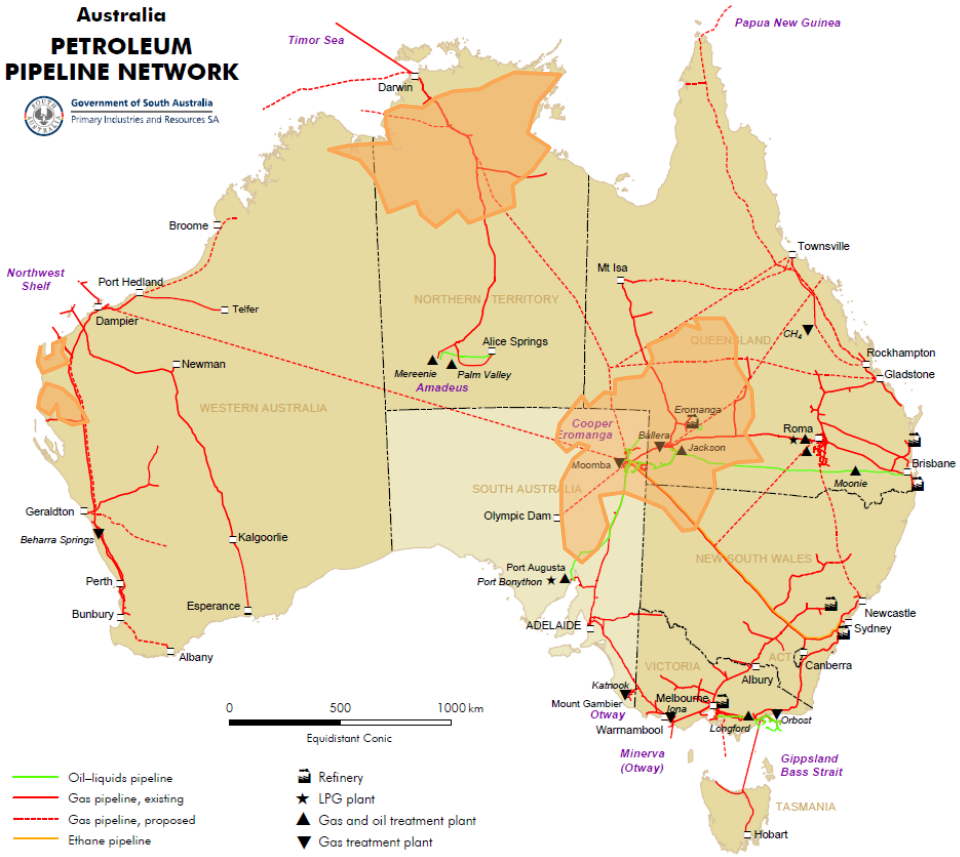

Figure 5: Regions of high grade geothermal resources (T>200°C at depth of 6.5 km for the US and >5 km for Australia) overlaid with established oil and gas pipeline networks for the US [15] and Australia [33].

3.0 Synthesis of transportation fuels from solar energy and carbonaceous fuels

3.1 Energy consumed by production of transportation fuels

All forms of transportation fuel, worldwide, cumulatively account for 96 EJ (x 10^{18} J) of energy consumption and 23% of energy-related greenhouse gas emissions. Similarly, refined fuels produced from mineral crude oil accounts for 89.3% of transport fuel demand, with alternative fuels like alcohols (e.g. ethanol, methanol), biodiesel, coal and gas to liquids processes, natural gas and LPG accounting for 7.7%, and biofuels accounting for the remaining 3% of demand [34]. The potential for low cost liquid fuels produced by the Fischer-Tropsch (FT) process has received renewed interest in China over the last 10 years, given the cheap and abundant availability of coal [35-43]. In addition, the energy efficiency of delivering refined mineral crude oil from the well-to-tank is 80-90% depending on the oil quality and source [44]. In comparison, the well-to-tank energy efficiency of Fischer-Tropsch derived liquid fuels from natural gas (gas-to-liquids – GTL) is 60%, while that for coal it is ~45% [39, 44], which is approximately half that of refining and extracting mineral crude oil from the ground. While biomass blends with coal has been widely proposed as a pathway to reducing the CO_2 emissions impact of producing FT liquids from coal, this has significant economic impacts on plant viability (see Section 3.2.2 below) [41, 42]. In comparison, the deployment of CCS technology is inherently parasitic to plant efficiency. There is therefore a need to identify alternative pathways to simultaneously improve the energy productivity of the coal-to-liquids process while also reducing CO_2 emissions [39]. The use of concentrated solar thermal energy in the high temperature syngas production process has been experimentally shown to offer this potential. However, no comprehensive assessment of a pathway to employing solar energy to improve the productivity of the coal-to-liquids process and enable continuous operation over a full solar year has been presented.

3.2 Synthetic crude oil production by the Fischer-Tropsch process

Syngas production by the autothermal gasification of coal is a highly endothermic, high temperature (>1400 K) process that takes place in an O_2 rich environment with or without the presence of steam [45]. Figure 6 presents a schematic flow diagram of the indirect coal liquefaction process. Gasification is the most energy-intensive step in the production of liquid fuels by the FT process and the process heat necessary to drive the endothermic reactions is typically provided by the combustion of ~30% of the fuel input in O_2. Oxygen is typically used instead of air in autothermal gasifiers integrated with the FT process, because the latter dilutes the syngas stream with N_2 and presents a large capital cost penalty from sizing plant components downstream from the gasifier [37, 41]. All commercial autothermal gasifiers also operate at high-pressures between 20 and 80 bar to reduce the cost of gasification reactors as it enables a larger syngas throughput per unit reactor volume, facilitates the removal of acid gases, reduces the size and thus capital costs of off-gas processes and the parasitic operational expense of compressing syngas for unit operations downstream from the gasifier [46, 47]. While several gasification reactor designs have been proposed and developed over the last 100 years, the two reactor configurations that account for >95% of all gasified coal are the fixed bed Lurgi and the entrained flow reactors [37, 41]. The sub-sections below provide a brief description of the operational characteristics of these gasifiers, which is followed by a discussion of their relative merits in processing coals of varying quality and coal-biomass fuel blends.

3.2.1 Autothermal coal gasifiers

Fixed bed Lurgi gasifier

The fixed-bed Lurgi gasifier is the dominant commercial gasification technology, with its most important application being the production of Fischer-Tropsch liquid transportation fuels from coal [47-49]. In this process, coal that is sized to a diameter of 5 - 50 mm is fed from a lock hopper at the top of the reactor and moves down under gravity, countercurrent to the rising, hot combustion gas stream [47, 49]. Oxygen is injected through the base of the reactor to oxidise coal and generate hot combustion gases. Excess steam is also injected to the fuel bed from below the grate to maintain the

combustion zone temperature below the ash fusion temperature. Indeed, only a small portion of the steam reacts with the coal, making CO_2 char gasification the dominant syngas production mechanism [47, 49]. The heat transfer mechanism employed within these reactors lead to a large temperature gradient through the bed. For example the temperature near to the base of the reactor is typically 1400 K, whereas it is typically 800 K at the top of the reactor, where coal is undergoing devolatilisation and drying and where there is very little O_2. Depending on the moisture content of the coal, the gas temperature at the exit from the gasifier is 600-800 K [47, 49]. The dry or molten ash that remains after the coal is gasified is continually removed from the grate through another lock-hopper at the base of the reactor.

Entrained flow gasifiers

Entrained flow (EF) gasifiers typically operate at temperatures in excess of 1400°C and pressures between 20 and 80 bar. While fuel residence time in EF gasifiers is no more than a few seconds, small fuel particles (<100 μm), uniform reactor temperatures and a high degree of contact between solid-liquid-gas reactive surfaces, facilitate fuel conversion rates >99% [43, 46]. An important feature of these reactors is their slagging behaviour, where high temperatures facilitate the formation of molten ash, which flows down the reactor walls and finally leaves the gasifier as liquid ash or slag. The slagging nature of these reactors reduces the adverse impacts from molten ash fouling the heat exchange equipment [43, 46]. The two most widely developed EF coal gasifiers are the coal water slurry feed GEE reactor and the dry coal feed Shell type reactor. While the GEE gasifier is best suited to gasifying high-rank anthracite and sub-bituminous coals, the Shell gasifier has been successfully used to gasify a range of coals from high-rank anthracite to brown coals. Furthermore, the excess water in the GEE slurry feed leads to its O_2 requirement being 3% higher per kg of coal than the dry-feed Shell gasifier, which requires 0.88 kg O_2 per kg coal [41, 43]. This increased O_2 demand is translated to the same increase in the parasitic electrical load of the air separation unit, which makes up 12.5% of the total plant parasitic load [41].

Discussion

The primary difference between the fixed-bed Lurgi gasification process and entrained flow systems is that, in the former configuration the physical flow of solids is independent of the flow of gases. The main advantages of the Lurgi system over the EF gasifier are the need for minimal coal pre-treatment and a simple reactor design that has far fewer moving parts. At the same time, Lurgi gasifiers are unable to process the fines, which are < 5 mm [47, 49]. The primary disadvantage of this reactor configuration relative to the EF gasifier is associated with the fouling impacts of tars (heavy hydrocarbons) that comprise up to 10% of the product gas, on equipment downstream from the gasifier [50]. Tars formed in the low-temperature upper, coal devolatilisation regions of the gasifier are neither cracked nor oxidised in this O_2 limited section [47]. In comparison, EF gasifiers produce negligible amounts of tars because of more uniform temperatures in these reactors. This leads to tars being oxidised or cracked to form smaller hydrocarbons [51]. The co-gasification of biomass in fixed bed gasifiers exacerbates tar forming fractions [52], which means that EF gasifiers are better suited to biomass gasification than fixed bed systems [53]. Furthermore, because the Shell EF gasifier has been proven to gasify brown coals, and given the broad similarities between biomass and brown coals in terms of their H/C and O/C fuel ratios, this EF reactor will offer greater flexibility in processing a range of feedstock while maintaining a high rate of feedstock conversion [53]. There has been only one comprehensive process modeling system analysis of a FT liquids system employing a dry-feed Shell EF gasifier with coal and coal-biomass fuel blends [41, 42]. However, no process modeling system analysis comparing the performance of the Shell based autothermal coal-to-liquids process and a solar gasification integrated coal-to-liquids process has been presented in the literature to date.

3.2.2 Upgrading syngas to Fischer-Tropsch fuels

After syngas is produced by the gasification of coal, it has to be cleaned of impurities, and upgraded to a H_2/CO ratio of 1.5 - 2.26, before it is directed to the Fischer Tropsch reactor. Figure 6 presents a process flow diagram of the coal-to-liquids polygeneration system. The coal-to-liquids process is comprised of a number of parasitic plant components that consume heat and electricity, including the

heat load of the gasifier, which cumulatively account for the loss of ~42% of the equivalent heating value of the coal input through the process. The single largest source of parasitic electricity consumption is from the air separation unit, which is used to produce cryogenically extracted O_2 (and pure nitrogen as a fuel carrier gas), and the O_2 and N_2 compression processes [41, 43]. These two plant operations consume approximately 0.18 kWh of electricity per kg coal gasified. This amounts to approximately 10% of the total heating value of the feedstock input to the coal-to-liquids process. Here, the use of concentrated solar thermal energy to displace the O_2 required by the gasifier, offers a pathway to reducing the electrical load of the air separation unit and thus an improvement in the productivity of converting coal to Fischer-Tropsch liquids. However, no comprehensive process modeling analysis that quantifies the energetic value of integrating a transient solar resource on the operational productivity of an adapted, autothermal coal-to-liquids process has been presented.

Before syngas is cleaned of impurities, it has to be cooled from ~1400°C, as it exits the EF gasifier, to 230°C. There are three options to achieve this, a total direct quench, a radiant-convective boiler or a combination of these systems. In the direct quench option, hot syngas leaves the reactor base to a quench-section, where it is saturated with water and rapidly cooled to ~230°C [43, 46]. In the syngas cooler mode a radiant-convective heat exchanger is used to generate low, intermediate and high-pressure steam, which is used to generate electricity and meet the process requirements of the gasifier, water-gas-shift reactor and coal drying plants [43, 46]. A recent comparative analysis of the cost implications of incorporating a syngas cooler instead of a direct quench system, showed that the latter yields a modest 2 to 4% point increase in efficiency at the expense of a 9 to 16% increase in the cost of energy for a system based on the GEE slurry-feed gasifier [38]. However, for a Shell EF gasifier, the excess steam that is generated serves a useful purpose in drying the coal and biomass fuel before it is fed into the gasifier [51, 53]. After syngas is cleaned of impurities, it is upgraded from a H_2/CO molar ratio of 0.7 – 1.1, as it exits the autothermal gasifier, to between 1.5 – 2.26 [37, 41] according to reaction 1 – the water gas shift (WGS) process.

$$H_2O + CO \leftrightarrow H_2 + CO_2 \qquad \Delta H_{298\,K} = -41\ kJ/mol \qquad (1)$$

The WGS process leads to further losses in the thermal efficiency of the coal-to-liquids process as a result of the energy expended to recover and compress the CO_2 by-product (for geological storage) and to a lesser extent from the heat lost by the mildly exothermic (forward) reaction [35]. The cumulative CO_2 emissions impact of all the parasitic processes that the autothermal coal-to-liquids process is comprised, is evident in liquid transportation fuels from coal producing six times more CO_2 emissions than the extraction and production of refined fuels from the cleanest form of mineral crude oil, which (excluding combustion emissions at the point of end-use) leads to ~20 kg CO_2-e/GJ [41, 42]. Here, the solar gasification of coal offers the potential to reduce the CO_2 emissions associated with the entire process, including the WGS reaction, given it upgrades the calorific value of the syngas relative to the feedstock by as much as 26%. However, no comprehensive assessment of the process wide CO_2 emissions performance of a solar coal-to-liquids system over a full year of continuous operation has been presented.

A process modeling study of a system co-producing FT liquid fuels and electricity recently presented the potential to combine syngas streams from natural gas steam reforming and that produced by coal gasification [35]. The value of this process arises from syngas production with a H_2/CO ratio of ~ 3 from the steam reforming of methane, which when blended with an appropriate amount of syngas derived from coal gasification, can yield the desired H_2/CO ratio of 2 for the FT reactor without the need for WGS upgrade [35]. This study showed the potential to improve thermal efficiency by 7.5 percentage points if natural gas contributed 30% of the heating value of the fuel input to the process, relative to a baseline based on syngas produced from coal alone [35]. It also showed that this concept could enable a reduction in the CO_2 emissions sequestration rate of up to 70% relative to the baseline, to achieve zero net mine-to-wheel emissions per GJ output (FT liquids and electricity) [35]. This dual fuel FT liquids and electricity polygeneration system was also shown to achieve a net present value 40% larger than the baseline system [35]. Hence, the concept was shown to enable a significant net positive impact on the plant's economic viability, thermal efficiency and CO_2 emissions. However, no process modeling study has evaluated the feasibility, energetic or CO_2 emissions performance over a

full year of continuous operation, of integrating a solar reforming system within a solar gasifier as part of a polygeneration system producing FT liquid fuels.

The co-gasification of biomass -coal fuel blends offers another pathway to reducing the CO_2 emissions intensity of liquid fuels production by the Fischer-Tropsch process [37, 41, 42, 54-57]. However, to reduce the mine-to-tank CO_2 emissions of the coal-to-liquids process to below that of mineral crude oil, a biomass fuel blend equivalent to >50% of the thermal input is required and only if CCS is also integrated with the process. Without CCS, a biomass blend fraction ≥70% (cal) is required [37], because biomass has a calorific value that is on average ~75% that of a sub-bituminous coal like Illinois #6 [41, 42]. Indeed, a recent techno-economic assessment of a biomass-to-liquids system reported a price for eucalyptus pellets that is 2.8 times the price of coal per GJ. Relative to the current Brent benchmark price of crude oil ~US$18/GJ, the cost of FT liquids is US$26/GJ if biomass fuel is used as the feedstock, compared with US$11 – 12/GJ if coal alone is used as a feedstock [41, 42]. Hence, displacing coal with biomass has a large parasitic impact on the economic performance of producing synthetic FT crude oil. There is thus a need to identify alternative pathways to reducing the fraction of biomass that has to be co-gasified with coal to reduce CO_2 emissions below that of commercially available refined mineral crude oil. Here, solar gasification technology offers the potential to improve the productivity of converting biomass to liquid fuels. However, no complete process modeling assessment of a FT liquids system that integrates a solar co-gasification system over a full year of operation has been presented to date.

3.2.3 Scale of a solar coal-to-liquids plant

The scale of a solar coal-to-liquids plant is constrained by two factors, the maximum viable scale of the heliostat collection capacity and the minimum viable scale of the gas cleaning, upgrade and FT liquids unit operations downstream from the solar reactor. The size of a heliostat field is limited to a radius of 1 km from the central tower, because large atmospheric attenuation limit the efficiency of solar collection at distances greater than this radius. In energy terms, this corresponds to ~50 MW_{th} limit to the peak annual solar thermal energy input to a solar reactor operating at temperatures

>1100°C [58]. In comparison, the calorific throughput of coal in autothermal EF gasifiers, as proposed in the literature, is on the order of 1 to 2 GW_{th} [35, 37-42]. However, these plant have construction lead times of five years and capital requirements > $1 billion [35, 37-42]. This presents significant portfolio risks to financiers, which has led to many projects failing to receive investment approval e.g. Shell gas-to-liquids plant in the US Gulf. Here, the recent emergence of micro channel Fischer-Tropsch reactors offers the potential to reduce the viable scale of FT liquids systems to coal throughput from 1 GW_{th} to 162 MW_{th} and an output of 1500 barrels per day [59, 60]. Using these technologies, a FT liquids polygeneration system could viably be developed for a capital outlay of $200 M and be operational within ~2 years. Reducing the minimum viable scale of a solar integrated FT liquids plant is likely to improve their commercial viability, given it reduces the capital requirement for the development and lenders' portfolio risks [2]. However, these systems rely on continuous operation throughout the year, because the Fischer-Tropsch reactor takes up to four days to reach steady-state productivity once syngas flow is shut down [60]. Importantly, no previous analysis of a solar coal-to-liquids system has determined the conditions under which continuous operation over a full solar year can be achieved.

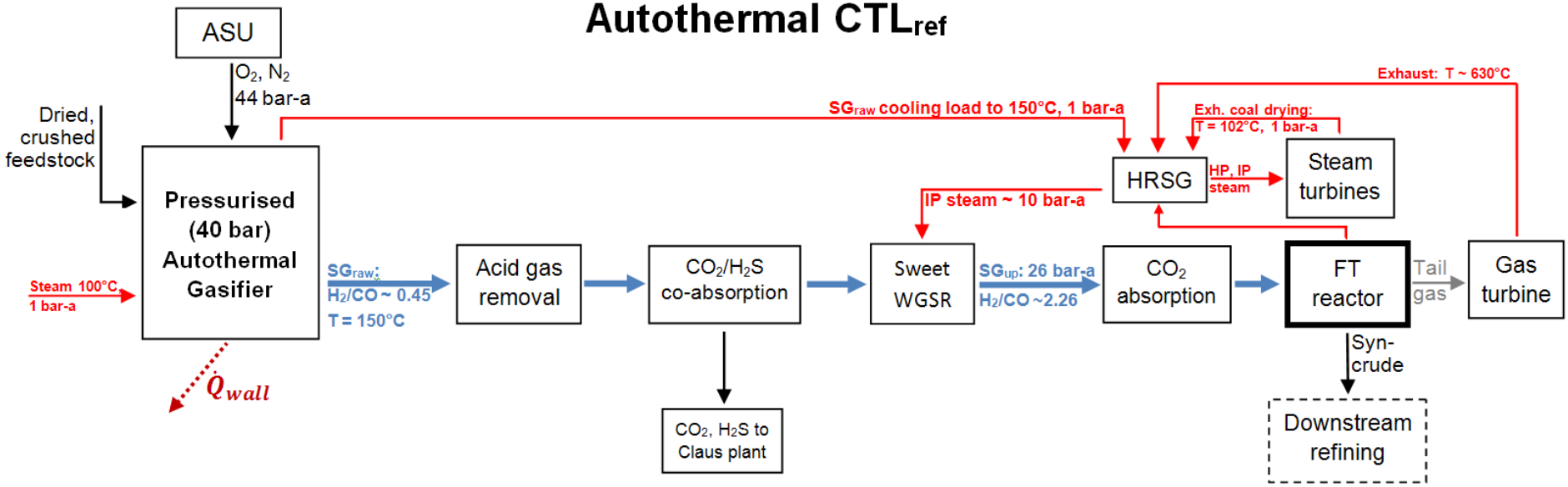

Figure 6: Simplified, annotated process scheme for a coal-to-liquids system that is based on a pressurised autothermal Shell gasification system with Illinois#6 coal as the feedstock.

3.3 Solar production of FT liquid fuels

The solar gasification and reforming processes offer the potential to convert a greater portion of the fuel input to syngas and then to a FT liquid fuels end-product by displacing the carbonaceous fuel that is otherwise burnt in O_2 to provide process heat [6, 61-73]. This enables the chemical storage of solar energy in the syngas product and a calorific upgrade of up to 26% relative to the calorific value of coal [66, 74]. While the stand-alone operational feasibility of these reactors has been demonstrated at a range of scales from 5 to 500 kW_{th}, no comprehensive analysis of the downstream impacts on an FT liquids production facility from syngas production that fluctuates in response to solar transience over a full solar year from the solar vortex or an indirectly irradiated packed bed solar gasifier has been presented [35, 36, 39-41, 43, 75-77]. Furthermore, no process modeling has evaluated the feasibility of integrating either a solar coal gasifier, the solar co-gasification of coal-biomass fuel blends, a solar gasifier that integrates natural gas solar co-reforming, with an adapted autothermal coal-to-liquids system such that no plant component except the solar reactor requires further development to enable continuous operation over a full solar year.

3.3.1 Reactor systems for the solar gasification and reforming of carbonaceous feedstock

Solar reactor designs can be broadly classified in terms of whether the fuel input to the reactor is directly or indirectly irradiated and whether the fuel feed is continuous or in batches. While reactor configurations like the solar vortex and fluidised bed reactors enable direct transfer of concentrated solar energy to the reaction zone, their primary limitation is the challenge of preventing particle deposition on the transparent window through which solar energy enters the reactor cavity. This has meant that windowed reactors have to date only been demonstrated to a prototype scale of 5 kW_{th}. In comparison, the packed bed and tubular reactor configurations, where the window is not directly exposed to fuel particles, have been demonstrated to scales of 150 kW_{th} and 500 kW_{th} respectively. These reactor configurations have been shown to be more operationally robust and been demonstrated to gasify a range of fuels from natural gas, coal, biomass, sewage sludge and scrap tyres [62, 63, 65, 74]. No study that comprehensively evaluates the long-term performance of integrating solar reactor

systems with a FT liquids production system, over a full solar year, using hourly or daily solar data has been presented to date [76, 78-83]. Indeed, no process modeling analysis has specifically compared the unique implications associated with the integration of specific reactor types with downstream FT liquids production infrastructure. Hence, an analysis is needed to determine the downstream system integration issues that would arise from the transient syngas output from a solar reactor on unit operations downstream from the gasifier (see Figure 6).

Directly irradiated solar vortex reactor

The directly irradiated solar vortex reactor configuration, shown in Figure 8, comprises an insulated cylindrical cavity and a quartz glass window up-beam of a smaller aperture that enables the introduction of concentrated solar energy into the high temperature cavity reaction zone [68, 84-87]. The reactants are injected into the cavity through a tangential nozzle to create a helical, vortex flow stream towards the rear of the cavity [68, 84-87]. The introduction of concentrated solar energy into the reactor rapidly leads to the particle reactants reaching temperatures ~1600°C, thus driving the highly endothermic reactions to completion [68, 84-87]. The experimental feasibility of the solar vortex reactor has been demonstrated for the steam gasification of petroleum coke at a scale of 5 kW_{th} [68, 84-87]. Like the autothermal entrained flow gasifier, this enables the fast and complete conversion of reactants to syngas, with particle residence of 1-2 seconds. Unlike the EF gasifier however, the directly irradiated vortex reactor enables and indirectly irradiated solar gasification systems, the reactor can only operate at, or near to, atmospheric pressure. This is because high reactor temperatures and pressures compromise the structural integrity of the quartz window. Conventional EF gasifiers operate above atmospheric pressure because it allows the reactor to capitalise on favourable volume to surface area ratios, thus decreasing the material cost of reactor construction. Given the solar vortex reactor can only operate at atmospheric pressure, a coal-to-liquids process incorporating this reactor requires off-gas compression systems to deliver syngas at the required pressure to cleaning processes and the FT reactor. However, no process modeling analysis of the

energetic or greenhouse gas emissions impact of integrating the atmospheric pressure solar vortex coal gasification reactor with a FT liquids polygeneration system has been presented previously.

Indirectly irradiated packed bed reactor

The indirectly irradiated packed bed reactor system, illustrated in Figure 7, is a geometrically simple and robust reactor configuration that has been shown to yield promising results for the gasification of a range of carbonaceous fuel and waste feedstock [62]. A recent experimental study of a scaled-up 150 kW_{th} reactor showed that over a single solar day the reactor enabled a fuel conversion rate of 56% and the syngas produced by the reactor had a calorific value 26% larger than the input feedstock [74]. Solar energy enters the reactor through a window at the top of the reactor and heats a SiC-coated emitter plate. The hot emitter plate then re-radiates the solar energy to heat the fuel batch, which is loaded into the reactor volume at the start of each solar day. However, the large thermal inertia associated with the cold reactor insulation and fuel mass, means that the reactor takes up to three hours to reach steady-state conditions. Furthermore, while the top of the fuel bed can reach temperatures of up to 1400 K at steady-state, the maximum temperature at the base is as low as 500 K [62, 74]. This large thermal gradient, primarily a result of coal and ash being poor conductors of heat, leads to heterogeneous fuel decomposition and gasification reactions taking place concurrently at different rates through the fuel bed [50, 88]. Ash accumulation at the top of the fuel bed further limits heat transfer through the bed over the solar day, because it blocks radiation from reaching the top of the fuel bed [72]. Although, Piatkowski recently presented an experimentally validated 1-D heat transfer and gasification model of the gasification of beech charcoal in the packed bed reactor, no rigorous model of this reactor has been presented for the gasification of coal (see Section 3.3.2 below for detailed discussion). Furthermore, all analyses of reactor performance have been limited to performance over a single solar day [62]. To present a comprehensive evaluation of the issues associated with integrating this reactor with a FT liquids polygeneration system, an accurate model for the gasification of coal is needed, as is a methodology to assess the dynamic performance of this

system over time-scales ranging from a single solar day to a full year. No such system-wide analysis has been presented to date.

Solar methane reforming reactors

The solar thermal reforming of methane has been shown to upgrade the calorific value of the syngas product (H_2 + CO) by ~28% relative to that of the feedstock. The endothermic methane reforming reaction is a catalytic process that takes place at a temperature >700 K [89, 90]. There are two reaction pathways for the reforming of methane, which are the steam and dry reforming processes described by reactions 2 and 3.

$CH_4 + H_2O \rightarrow CO + 3H_2$ $\Delta H_{298\,K} = 250$ kJ/mol (2)

$CH_4 + CO_2 \rightarrow 2CO + 2H_2$ $\Delta H_{298\,K} = 247$ kJ/mol (3)

While the steam reforming reaction enables the production of syngas with $H_2/CO \sim 3$, that is favourable for the FT process when combined with syngas produced by coal gasification, the dry reforming process offers the potential to reduce the water demand of producing syngas. This is important because regions with high solar availability are generally arid, with scarce water availability. Furthermore, solar dry reformed syngas offers a potential sink for CO_2 emissions captured by other industrial processes and sub-economic natural gas resources that are diluted with CO_2 [91-93]. There is thus a need to determine the specific rate of water consumption per unit of syngas produced for a system producing FT liquid fuels using coal and natural gas feedstock. No assessment has presented a comparative process modeling analysis of the impact of integrating either the solar steam or dry reforming processes with the solar gasification of coal to reduce the water demand of producing syngas.

Both methane reforming processes have been experimentally demonstrated in tubular reformer reactors and in a volumetric receiver-reactor at scales of up to 480 and 300 kW_{th} respectively [89, 94]. The heat transfer in a tubular reactor proceeds via radiation to the outside of the walls, the catalyst bed inside the tube is then heated by conduction. A 480 kW_{th} scale U-shaped tubular reformer reactor

was developed and tested at the Weizmann Institute of Science in Israel. This experiment showed that the reactor configuration could achieve methane conversion of up to 94% with a CO_2:CH_4 molar ratio of 1, chemical storage efficiency of 33-44%, pressure inside the tube of up to 20 bar using a Ni-rare earth supported catalyst at a temperature of ~1050 K [89, 95-97]. Another reactor configuration that has been proposed for the dry reforming of methane is the volumetric receiver, which has also been proven up to a scale of 300 kW_{th}. While this system was shown to enable methane conversion of 88% and the chemical storage of 32-66% of the incident solar energy as syngas, the reactor can only operate at low pressures (1.2 – 3 bar) because of the poor structural integrity of the quartz window [91-93]. It is worth noting that the production of syngas at elevated pressures is advantageous, because the FT reactor, syngas cleaning, and upgrade processes downstream from the reformer operate at pressures >20 bar. Hence, the tubular reformer reactor is preferred over the volumetric receiver configuration [98, 99]. The integration of this pressurised tubular reforming system with an atmospheric pressure gasifier thus offers the potential to reduce the energetic and greenhouse gas emissions of the solar coal-to-liquids process. However, no energetic and CO_2 emissions performance analysis has been presented previously of a solar co-gasification/tubular dry reforming system that is integrated with a FT liquids polygeneration system.

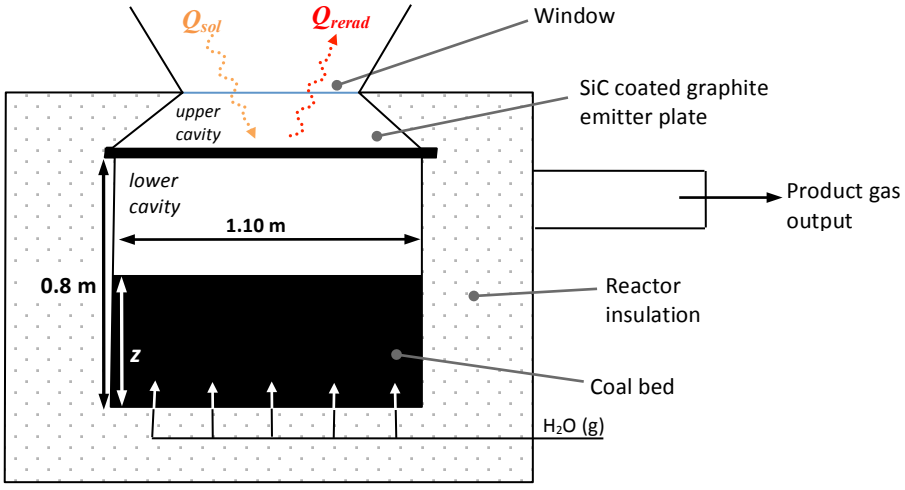

Figure 7: Cross-section of a directly irradiated, packed bed batch-mode CST gasification reactor (based on 150 kW_{th} scale experimental reactor configuration of [74]).

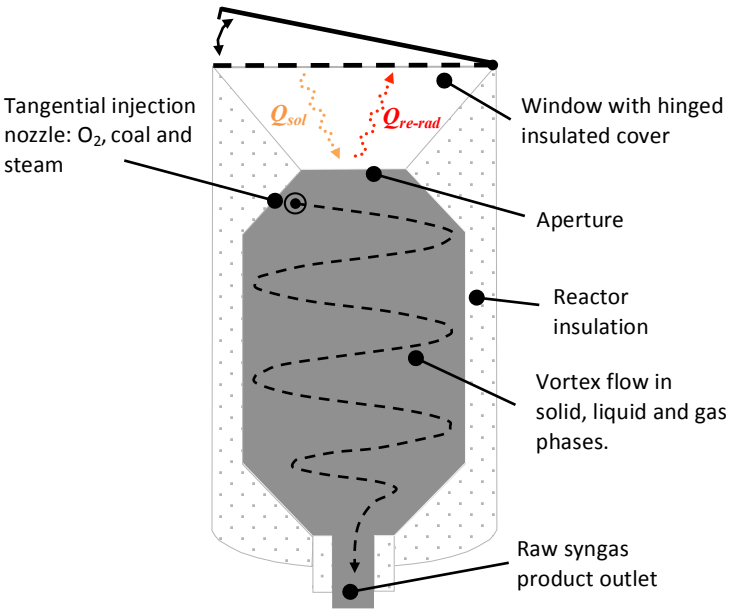

Figure 8: Cross-section of a directly irradiated, volumetric cavity solar vortex gasification reactor.

3.3.2 Modeling carbonaceous fuel gasification and reforming processes

The gasification of solid carbonaceous fuels can be described by the three processes of fuel drying, devolatilisation (pyrolysis) and char gasification. The devolatilisation and char gasification steps can be simplified to reaction 4, shown below. In this equation the individual terms x, y, u and v are taken from the ultimate analysis of the carbonaceous feedstock. However, the rate of this reaction and the individual processes that govern the devolatilisation and gasification reactions are far more complex [47, 50, 62, 88]. Devolatilisation typically occurs in the temperature range from 450-1000 K and involves the thermal decomposition of carbonaceous fuels to release volatiles and hydrogen rich gaseous compounds, leaving solid carbon or char [100]. At temperatures greater than 1100 K, highly endothermic char gasification reactions take place to produce CO and H_2. The solid phase char gasification reactions are described by reactions 5, 6 and 7 [101, 102]. The final composition of syngas that exits from the gasifier is determined in large part by the reversible, temperature controlled forward water gas-shift (reaction 1) and methane-reforming reactions (reactions 2 and 3). The gasification process also generates long-chain hydrocarbons known as tars. In the high temperature gasification environment these tars can be cracked to smaller hydrocarbons like methane, which are then reformed to CO and H_2 according to reactions 2 and 3.

$$CH_xO_yS_uN_v + (1-y)H_2O \rightarrow [y + (1-2x)u]H_2 + CO + uH_2S + vN_2 \quad (4).$$

$$C\ (s) + H_2O \rightarrow CO + H_2 \qquad \Delta H_{298\ K} = 172\ kJ/mol \quad (5).$$

$$C\ (s) + CO_2 \rightarrow 2CO \qquad \Delta H_{298\ K} = 230\ kJ/mol \quad (6).$$

$$C\ (s) + 2H_2 \rightarrow CH_4 \qquad \Delta H_{298\ K} = 75\ kJ/mol \quad (7).$$

Pseudo-dynamic Gibbs minimisation models for solar gasification and natural gas reforming

The Gibbs minimisation approach has been applied extensively to model autothermal entrained flow (and fixed bed) gasifiers and methane reforming reactors [35, 36, 39-41, 43, 75-77]. This approach provides a realistic representation of syngas composition, given the high reactor temperatures achieved in these reactors, the short residence time, fast feedstock conversion rates and the constant fuel and reagent (O_2, steam, CO_2) throughput. The parameterization of a Gibbs model is based on the ultimate analyses of coal, biomass or natural gas carbonaceous fuel feedstock [35, 36, 39-41, 43, 75-77]. While several process models of solar gasification and natural gas reforming reactors based on a Gibbs free energy minimisation approach have been presented, these models do not account for the impacts of solar resource transience on syngas production rates and compositions [67, 68, 85, 87]. Here, the dynamic impacts of solar resource transience on the solar gasifier could be represented by a piece-wise steady state model. The validity of a piece-wise-steady-state model is dependent upon the time-scale of the variations in solar flux relative to the thermal response of the reactor. This means that such a model could account for fluctuations in solar flux that is one to two orders of magnitude longer, i.e. minutes, than the residence time of the solar vortex reactor, which is approximately one second. In practice some gradients are likely to be greater than these, for example under conditions when clouds move past rapidly. This means that the model will not account for possible reduced performance due to very rapid fluctuations. Nevertheless, it is likely to offer a reasonable assessment of the impact of solar resource transience on fluctuating syngas output from a gasifier up to a time-step of one hour [76, 78-83, 103, 104]. However, no piece-wise-steady-state or pseudo-dynamic process modeling

analysis of a solar gasification or reforming reactor that is based on the Gibbs minimisation approach has been presented previously.

Dynamic Arrhenius kinetics models for fixed bed gasification reactors

Arrhenius kinetics relationships have been used extensively to develop dynamic models of coal devolatilisation and gasification for solar and autothermal fixed bed gasifiers with large thermal gradients, variable fuel composition and residences of the order of several hours [47, 88, 105]. Unlike a modeling approach based on Gibbs free energy minimisation alone, kinetics relationships offer a more robust methodology to quantify overall reaction rates in terms of fuel temperature and the changing proximate and atomic composition of the fuel over its period of residence in the reactor [47, 50, 88]. A reaction kinetics approach to gasification modeling was recently described by Piatkowski to predict syngas compositions for the gasification of beech charcoal in the indirectly irradiated solar packed bed coal gasifier [62]. This chemistry model was coupled with a detailed 1D heat transfer model that was used to predict wall temperatures and the temperature gradient through the fuel bed. Interestingly, the solar packed bed gasifier model used many of the same approaches described in the literature for fixed bed coal gasification systems [47], where the flow of solids is independent of the flow of gases [74]. However, the model used to describe devolatilisation and gasification chemistry was reduced to the overall gasification reaction described by equation 4 and Arrhenius kinetics derived from a thermogravimetric analysis. While this model predicted dynamic syngas production rates that achieved excellent agreement with experimentally observed results for the gasification of beech charcoal, predictions of syngas evolution over a full solar day were less accurate for more complex fuels like coal, which have significant volatile matter fractions [62]. A similar approach by Kruesi et al., to modelling the steam gasification of sugarcane bagasse in a solar-driven fixed bed-reactor showed good agreement between the modeled results and the final experimentally observed average temperatures and average gas compositions [78]. However, their assessment did not provide a comparative analysis of the dynamic syngas production rate against the observed dynamically variant gas evolution rates. There is thus a need to develop a more comprehensive chemistry model to

represent the complex devolatilisation and gasification behaviour of complex volatile bearing fuels like coal. Importantly, no calibrated dynamic model of the solar packed bed reactor has been presented for the gasification of coal. Indeed, no process modeling assessment of integrating this reactor with a FT liquids polygeneration system, over any mutli-day period has been presented previously.

3.4 Process modeling integrating dynamic variance in solar input

A comprehensive process modeling analysis is crucial to an accurate evaluation of the energetic and greenhouse gas emissions performance of upgrading syngas produced from a solar gasification or reforming reactor to a higher value energy commodity like FT liquid fuels. Sudiro and Bertucco recently presented a process modeling analysis of a solar integrated coal gasification reactor based on a steady-state gasification model based on the Gibbs minimisation approach [76]. While this model accounted for diurnal transience in the solar resource, it did not account for seasonal or cloud-induced resource transience, because it assumed the availability of solar insolation 12 hours per day continuously throughout the year. Accounting for these impacts of solar transience is critical to an accurate quantification of the capacity factor of downstream syngas upgrade processes and a realistic estimation of energetic, greenhouse gas emissions and economic performance of the entire system. Indeed, the NETL baseline studies of autothermal coal gasification reactors that are integrated with a combined cycle (IGCC) power system showed that an increase in gasifier capacity factor from 60 to 90% decreases the cost of energy by 30% [43]. However, no process modeling analysis of a solar integrated FT liquids polygeneration system has presented a complete assessment of the diurnal, seasonal and cloud-induced impacts of solar transience on system operation and performance over a full year of operation [76, 78-83].

3.4.1 Syngas storage

The incorporation of an intermediate gas storage system when solar energy is not available offers the potential to improve the capacity factor of a solar energy process [75, 106]. Here, alternative forms of energy storage such as that offered by molten salt systems is unlikely to be suitable because they are

limited to temperatures of 600°C [107], whereas the high temperature endothermic gasification process operates at temperatures >1100°C [66]. Hence, there is a need for alternative energy storage options that can improve the economic viability of solar gasification system that is integrated with a FT liquids production process. Pressurised gas storage devices like tanks and variable pressure pipelines have, for decades, been used by a number of power generation, oil refining and petrochemical industries to store a range of energy fluids including, natural gas, H_2 and CO [106, 108]. While petrochemical production facilities operate at steady state to maintain high capacity factors, other facilities like peaking open cycle gas turbines operate intermittently in response to short-term (<15 min) fluctuations in wholesale spot electricity prices. Apt and Newcomer recently presented a dynamic process model of an IGCC system assessing the potential for the pressurised storage of syngas to improve the viability of the power generation facility. This work showed that eight hours of storage capacity could improve the viability of the IGCC system by 10% [75, 106]. Given this potential, there is a need to evaluate the minimum gas storage capacity that would yield continuous operation of a solar integrated coal-to-liquids system over a full solar year. However, no dynamic process modeling assessment of the storage requirements of a solar vortex or packed bed gasifier has been presented to date.

The hybridisation of the solar gasifier with an autothermal process, which can flexibly be turned-up or down in response to solar resource transience, offers the potential to ensure a continuous non-zero syngas output over a full solar year. A number of recent publications have noted the complementarities between fossil fuel combustion systems and concentrated solar reactors in the context of power generation processes [82, 83, 109]. Nathan et al. recently presented a techno-economic analysis of a novel hybrid receiver-combustor (HRC) that circulated molten salt within a solar receiver and integrated combustion within the same reactor volume [82]. This system eliminated the need for a separate boiler and reduced the total heat-exchange area required to reduce the expected capital cost of the power generation infrastructure by 51% ($M/GWh/year) and the overall levelised cost of electricity by 24% relative to a conventional solar thermal power generating system that does

not incorporate the HRC [82]. Thus, a hybrid solar gasification system that incorporates both concentrated solar thermal energy input and autothermal coal combustion reduces the susceptibility of the coal-to-liquids process to solar resource transience [110]. A key limitation of the techno-economic analyses of the solar HRC power generation system was associated with an inadequate representation of solar resource transience over a full year. Their analysis assumed a single, annual average solar insolation figure to represent the process' solar share and capacity factor [82]. Importantly, no dynamic process modeling study quantifying the magnitude of gas storage required for a system integrating a hybrid solar gasification process, with a FT liquids polygeneration system has been presented to date.

4.0 Thesis aims

4.1.1 Chapter 2

Polygeneration of liquid fuels and electricity by the atmospheric pressure hybrid solar gasification of coal.

The overall aims of Chapter 2 are:

- *to identify the required adaptations to the conventional coal-to-liquids process that can enable the integration of an atmospheric pressure solar vortex entrained flow gasifier and maintain continuous operation over a full solar year;*
- *to determine the energetic and greenhouse gas emissions performance of the solar coal-to-liquids system integrating an atmospheric pressure hybrid solar vortex coal gasification reactor, relative to a baseline CTL system integrating an autothermal pressurised Shell type entrained flow gasifier using Illinois #6 coal.*

4.1.2 Chapter 3

Dynamic modeling of the co-production of liquid fuels and electricity from a hybrid solar gasifier with various fuel blends.

The overall aims of Chapter 3 are:

- *to quantify the energetic and greenhouse gas emissions performance of the hybrid, atmospheric pressure, solar gasification of coal-biomass fuel blends and of integrating a solar steam or dry natural gas reformer within a hybrid solar gasifier for the production of Fischer Tropsch liquid fuels;*

- *to quantify the influence of the above process improvement strategies on capital utilisation of the hybrid solar gasifier and heliostat field relative to the benchmark solar coal-to-liquids process outlined in Chapter 2.*

Chapters 2 and 3 address the gap in understanding identified in Section 3 regarding the need to reduce

- the susceptibility of a coal-to-liquids process integrating a hybrid atmospheric pressure solar vortex gasifier to that integrates autothermal reactions, to long periods of poor solar insolation and
- the mine-to-tank emissions from a solar coal-to-liquids process to below that of conventional mineral crude oil.

The aims of both chapters are met by employing, for the first time, a pseudo-dynamic (piece-wise steady state) process model of a solar coal-to-liquids system that accounts for the diurnal, seasonal and cloud-induced characteristics of solar resource transience over a full year of operation using an hourly solar insolation time-series.

4.1.3 Chapter 4

A one-dimensional heat transfer, devolatilisation and gasification model of a solar packed bed coal gasifier

The overall aims of Chapter 4 are:

- *to develop a dynamic one-dimensional heat transfer, devolatilisation and gasification reaction kinetics model of indirectly irradiated solar packed bed reactor for the gasification of coal;*
- *to assess the performance of this model relative to experimental observations with respect to reactor and fuel bed temperatures, the dynamic evolution of syngas species over a full solar day and the sensitivity of coal conversion productivity to the initial fuel batch mass and fuel composition;*

This chapter addresses the gap presented in Section 3.3.2 by developing a rigorous model that employs rigorous devolatilisation and gasification chemistry reaction kinetics within a 1-D heat transfer model.

4.1.4 Chapter 5

Storage capacity assessment of liquid fuels production by solar gasification in a packed bed reactor using a dynamic process model

The overall aims of this chapter are:

- *to quantify the minimum quantum of energy storage required to integrate a stand-alone, batch process solar packed bed gasifier with a FT liquids polygeneration system and enable continuous operation over a full solar year;*
- *to assess the impact on the relationship between syngas storage and operational capacity factor of a FT reactor over a full solar year under:*
    - *two fuel loading strategies for the batch process, solar packed bed gasification reactor*
    - *three heliostat field area scenarios and the*
    - *solar reaion.*

This chapter addresses the gaps in understanding identified in Section 3, related to the technical feasibility of a solar coal-to-liquids process integrating a packed bed gasification reactor that is reliant on solar energy alone and is thus susceptible to extended periods of poor solar insolation over a full year of operation. Addressed therefore is the impact of these fluctuations on unit operations downstream from the storage system and gasifier over a range of scenarios, assuming constant syngas throughput to downstream plant.

4.1.5 Chapter 6

Potential value of data-centres in enabling investment in stranded geothermal resources.

The overall aims of this chapter are:

- *to determine a technically feasible pathway to generate commercially acceptable returns on investment in stranded geothermal resources using synergies with established energy and non-energy network infrastructure;*
- *to capitalise on data-centres' modularity and stable energy load for refrigeration and electricity to ensure high capital productivity, for a range of energy delivery pathways incorporating geothermal resources;*
- *to propose a pathway that incrementally reduces both the technical and project financing impediments to investment in geothermal energy resources.*

5.0 References

[1] Painuly J. Barriers to renewable energy penetration; a framework for analysis. Renew Energy. 2001;24:73-89.

[2] Martin N, Rice J. Developing renewable energy supply in Queensland, Australia: A study of the barriers, targets, policies and actions. Renew Energy. 2012;44:119-27.

[3] Rao K, Kishore V. A review of technology diffusion models with special reference to renewable energy technologies. Renew Sustain Energy Rev. 2010;14:1070-8.

[4] Balachandra P, Nathan H, Reddy B. Commercialisation of sustainable energy technologies. Renew Energy. 2010;35:1842-51.

[5] Gurgenci H. Challenges for electrical power generation from EGS. World Geoth Congress. Bali, Indonesia: International Geothermal Association; 2010. p. 5.

[6] Schaber C, Mazza P, Hammerschlag R. Utility-scale storage of renewable energy. Electricity Journal. 2004;17:21-9.

[7] Scheer H. The solar economy: renewable energy for a sustainable global future. Sterling, VA, USA: Earthscan; 2004.

[8] Steinfeld A. Solar thermochemical production of hydrogen - a review. Solar Energy. 2005;78:603-15.

[9] Steinfeld A, Meier A. Solar fuels and materials. Encyclopedia of Energy. 2004;5:623-37.

[10] Steinfeld A, Palumbo R. Solar thermochemical process technology. In: Meyers R, editor. Encyclopedia of Physical Science & Technology: Academic Press; 2001. p. 237-56.

[11] Sayeef S, Heslop S, Cornforth D, Moore T, Percy S, Ward J, et al. Solar intermittency: Australia's clean energy challenge. Newcastle, NSW, Australia: ASI; 2012.

[12] Atrens A, Gurgenci H, Rudolph V. Thermosiphon for competitive geothermal power generation. Energy & Fuels. 2009;23:553-7.

[13] Dickinson R, Battye D, Linton V, Nathan G. Alternative carriers for remote renewable energy sources using existing CNG infrastructure. Int J Hydrogen Energy. 2010;35:1321-9.

[14] ABARES. Australian Energy Resource Assessment. In: ABARES, editor. Canberra: Australian Government; 2010.

[15] EIA. U.S. Natural Gas Pipeline Network. Washington DC: U.S. Department of Energy; 2009. p. Map.

[16] Giardini D. Geothermal quake risks must be faced. Nature. 2009;462:848-9.

[17] Sharma A, Tyagi V, Chen C, Buddhi D. Review on thermal energy storage with phase change materials and applications. Renew Sustain Energy Rev. 2009;13:318-45.

[18] Hadjipaschalis I, Poullikkas A, Efthimiou V. Overview of current and future energy storage technologies for electric power applications. Renew Sustain Energy Rev. 2009;13:1513-22.

[19] Gallup D. Production engineering in geothermal technology: A review. Geothermics. 2009;38.

[20] Huddlestone-Holmes C, Hayward J. The potential of geothermal energy. In: Garnaut R, editor. Carnaut Climate Change Review. Canberra 2011.

[21] MIT. The future of geothermal energy - impact of enhanced geothermal systems (EGS) on the United States in the 21st century. In: Tester J, editor. Idaho: US Dept. of Energy; 2007.

[22] Atrens A, Gurgenci H, Rudolph V. CO2 thermosiphon for competitive geothermal power generation. Energy and Fuels. 2009;23:553-7.

[23] Li F, Fan L-S. Clean coal conversion processes-progresses and challenges. Energy Environ Sci. 2008;1:248-67.

[24] Majer E, Baria R, Stark M, Oates S, Bommer J, Smith B, et al. Induced seismicity associated with Enhanced Geothermal Systems. Geothermics. 2007;36:185-222.

[25] NPR. Visualising the U.S. electric grid. Power Hungry: Reinventing the US Electric Grid: National Public Radio; 2009.

[26] Pilavachi P. Mini and micro-gas turbines for combined heat and power. Appl Therm Engng. 2002;22:2003-14.

[27] Bruhn M. Hybrid geothermal–fossil electricity generation from low enthalpy geothermal resources: geothermal feedwater preheating in conventional power plants. Energy. 2002;27:329-46.

[28] Tempesti D, Manfrida G, Fiaschi D. Thermodynamic analysis of two micro CHP systems operating with geothermal and solar energy. Applied Energy. 2012;97:609-17.

[29] Verge J. Google: We've Bought 1 Gigawatt of Renewable Energy. Data Center Knowledge. West Chester, OH: DCK; 2014.

[30] James G, Horn M, Lilley W. Alternative energy solutions for data centre consolidation. Energy Transformed Flagship CSIRO; 2009.

[31] Sailor D, Lu L. A top–down methodology for developing diurnal and seasonal anthropogenic heating profiles for urban areas. Atmospheric Environment. 2004;38:2737-48.

[32] Shaw H. IBM launches Portable Modular Data Centre in Australia. IBM. Brisbane2010.

[33] PIRSA. Australia Petroleum Pipeline Network. Adelaide: Government of South Australia Primary Industries and Resources SA; 2012. p. Map.

[34] IEA. IEA-Advanced Motor Fuels Annual Report. Paris, France: IEA-AMF/Energy Technology Network; 2010.

[35] Adams II T, Barton P. Combining coal gasification and natural gas reforming for efficient polygeneration. Fuel Process Technol. 2011;92:639-55.

[36] Chiesa P, Consonni S, Kreutz T, Williams R. Co-production of hydrogen, electricity and CO2 from coal with commercially ready technology. Part A:Performance and emissions. Int J Hyd Energy. 2005;30:747-67.

[37] Kreutz T, Larson E, Liu G, Williams R. Fischer-Tropsch fuels from coal and biomass. 25th Ann Intl Pittsburgh Coal Conference. Pittsburgh, Pennsylvania, USA 2008.

[38] Kreutz T, Williams R, Consonni S, Chiesa P. Co-production of hydrogen, electricity and CO2 from coal with commercially ready technology. Part B: Economic analysis. Int J Hyd Energy. 2005;30.

[39] Larson E, Fiorese G, Liu G, Williams R, Kreutz T, Consonni S. Co-production of decarbonized synfuels and electricity from coal + biomass with CO2 capture and storage: an Illinois case study. Energy Environ Sci. 2010;3:28-42.

[40] Liu G, Larson E, Williams R, Kreutz T, Guo X. Making Fischer-Tropsch fuels and electricity from coal and biomass: performance and cost analysis. Energy Fuels. 2011;25:415-37.

[41] Meerman J, Ramirez A, Turkenburg W, Faaij A. Performance of simulated flexible integrated gasification polygeneration facilities. Part A: A technical-energetic assessment. Renew Sustain Energy Rev. 2011;15:2563-87.

[42] Meerman J, Ramirez A, Turkenburg W, Faaij A. Performance of simulated flexible integrated gasification polygeneration facilities, Part B: Economic evaluation. Renew Sustain Energy Rev. 2012;16:6083-102.

[43] Woods M, Capicotto P, Haslbeck J, Kuehn N, Matuszewski M, Pinkerton L, et al. Volume 1: Bituminous coal and natural gas to electricity final report, DoE/NETL -2007/1281. Cost and performance baseline for fossil energy plants US DoE; 2007.

[44] ANL. Well-to-Tank Energy Use and Greenhouse Gas Emissions of Transportation Fuels – North American Analysis. Chicago: Argonne National Laboratory; 2001.

[45] NETL. Bituminous coal and natural gas to electricity Revision 2. In: Black J, editor. Cost and Performance Baseline for Fossil Energy Plants US Department of Energy; 2010.

[46] Higman C, van der Burgt M. Gasification. Second edition ed: Elsevier; 2008.

[47] Hobbs M, Radulovic P, Smoot L. Combustion and gasification of coals in fixed-beds. Prog Energy Comb Sci. 1993;19:505-86.

[48] Tullo A. Exploiting China's coal. Chem Eng News: ACS; 2010. p. 10.

[49] Turna O. Sasol-Lurgi Fixed bed dry bottom gasification for fuels and chemicals. 2nd Intl Freiberg Conf on IGCC & XtL Technologies. Freiberg, Germany: Sasol-Lurgi Technology Company; 2007.

[50] Hobbs M, Radulovic P, Smoot L. Prediction of effluent compositions for fixed-bed coal gasifiers Fuel. 1992;71:1177-94.

[51] van der Drift A, Boerrigter H, Coda B, Cieplik M, Hemmes K. Entrained flow gasification of biomass - Ash behaviour, feeding issues, and system analyses. Eindhoven, The Netherlands: ECN; 2004.

[52] Brage C, Yu Q, Chen G, Sjostrom K. Tar evolution profiles obtained from gasification of biomass and coal. Biomass Bioenergy. 2000;18:87-91.

[53] Prins M, Ptasinski K, Janssen F. More efficient biomass gasification via torrefaction. Energy. 2006;31:3458-70.

[54] Chen Y, Adams II T, Barton P. Optimral design and operation of static energy polygeneration systems. Industrial and Engineering Chemistry Research. 2011;50:5099-113.

[55] Hamelinck C, Faaij A, Uil H, Boerrigter H. Production of FT transportation fuels from biomss; technical options, process analysis, and optimisation and development potential;. Utrecht, The Netherlands: Universiteit Utrecht; 2003.

[56] Van Vliet O, Faaij A, Turkenburg W. Fischer-Tropsch diesel production in a well-to-wheel perspective: A carbon, energy flow and cost analysis. Energy Conversion & Management. 2009;50:855-76.

[57] IEA. Synthetic gasoline and diesel oil produced by Fischer-Tropsch Technology: A possibility for the future? In: IEA, editor. IEA/AMF Annex XXXI. Göteborg, Sweden2007.

[58] Saw W, Kaniyal A, van Eyk P, Nathan G, Ashman P. Solar hybridized coal-to-liquids via gasification in Australia: techno-economic assessment. Energy Procedia. 2015;(In press).

[59] Hargreaves N. The Microchannel Advantage: Enabling the Pioneering Projects Pemex – World Bank GGFR Gas Utilization and Flare Reduction Workshop. Veracruz, Mexico2012.

[60] Deshmukh S, Tonkovich A, Jarosch K, Schrader L, Fitzgerald S, Kilanowski D, et al. Scale-up of microchannel reactors for Fischer-Tropsch synthesis. Ind Eng Chem Res. 2010;49:10883-8.

[61] Kodama T, Kondoh T, Tamagawa T, Funatoh A, Shimizu K-I, Kitayama Y. Fluidized bed coal gasification with CO2 under direct irradiation with concentrated visible light. Energy Fuels 2002;16:1264-70.

[62] Piatkowski N. Solar driven steam gasification of carbonaceous feedstocks feedstock characterization to pilot facility testing. Zurich: ETH Zurich 2011.

[63] Piatkowski N, Steinfeld A. Solar-driven coal gasification in a thermally irradiated packed-bed reactor. Energy Fuels. 2008;22:2043-52.

[64] Piatkowski N, Steinfeld A. Solar gasification of carbonaceous waste feedstocks in a packed-bed reactor - Dynamic modeling and experimental validation. AIChE Journal. 2011;57:3522-33.

[65] Piatkowski N, Wieckert C, Steinfeld A. Experimental investigation of a packed-bed solar reactor for the steam gasification of carbonaceous feedstocks. Fuel Process Technol. 2009;90:360-6.

[66] Piatkowski N, Wieckert C, Weimer A, Steinfeld A. Solar-driven gasification of carbonaceous feedstock - a review. Energy Environ Sci. 2011;4:73-82.

[67] Z'Graggen A, Haueter P, Maag G, Romero M, Steinfeld A. Hydrogen production by steam-gasification of carbonaceous materials using concentrated solar power - IV. Reactor experimentation with vacuum residue. Int J Hyd Energy. 2008;33:679-84.

[68] Z'Graggen A, Haueter P, Maag G, Vidal A, Romero M, Steinfeld A. Hydrogen production by steam-gasification of petroleum coke using concentrated solar power - III. Reactor experimentation with slurry feeding. Int J Hyd Energy. 2007;32:992-6.

[69] Z'Graggen A, Haueter P, Maag G, Romero M, Steinfeld A. Hydrogen production by steam gasification of carbonaceous materials using concentrated solar energy - IV. Reactor experimentation with vacuum residue. International Journal of Hydrogen Energy. 2008;33:679-84.

[70] Z'Graggen A, Haueter P, Maag G, Vidal A, Romero M, Steinfeld A. Hydrogen production by steam-gasification of petroleum coke using concentrated solar power - III. Reactor experimentation with slurry feeding. International Journal of Hydrogen Energy. 2007;32:992-6.

[71] Fletcher E. Solar thermal processing: a review. Journal of Solar Energy Engineering. 2001;123:63-75.

[72] Kodama T. High temperature solar chemistry for converting solar heat to chemical fuels. Progress in Energy and Combustion Science. 2003;29:567-97.

[73] Steinfeld A. Solar thermochemical production of hydrogen - a review. Solar Energy. 2005;78:603-15.

[74] Wieckert C, Obrist A, von Zedtwitz P, Maag G, Steinfeld A. Syngas production by thermochemical gasification of carbonaceous waste materials in a 150 kWth packed-bed solar reactor. Energy & Fuels. 2013;27:4770-6.

[75] Apt J, Newcomer A, Lave L, Douglas S, Dunn L. An engineering-economic analysis of syngas storage. In: Reed M, editor.: NETL; 2008.

[76] Sudiro M, Bertucco A. Synthetic fuels by a limited CO2 emission process which uses both fossil and solar energy. Energy Fuels. 2007;21:3668-75.

[77] Yu G, Xu Y, Hao X, Li Y, Liu G. Process analysis for polygeneration of Fischer–Tropsch liquids and power with CO2 capture based on coal gasification. Fuel. 2010;89:1070-6.

[78] Kruesi M, Jovanovic Z, dos Santos E, Yoon H, Steinfeld A. Solar-driven steam-based gasification of sugarcane bagasse in a combined drop-tube and fixed-bed reactor - Thermodynamic, kinetic, and experimental analyses. Biomass Bioenergy. 2013;52:173-83.

[79] Kim J, Johnson T, Miller J, Stechel E, Maravelias C. Fuel production from CO2 using solar thermal energy: System level analysis. Energy Environ Sci. 2012;5:8417-29.

[80] Kim J, Henao C, Johnson T, Dedrick D, Miller J, Stechel E, et al. Methanol production from CO2 using solar thermal energy: process development and techno-economic analyses. Energy Environ Sci. 2011;4:3122-32.

[81] Meier A, Gremaud N, Steinfeld A. Economic evaluation of the industrial solar production of lime. Energy Convers Mgmt. 2005;46:905-26.

[82] Nathan G, Battye D, Ashman P. Economic evaluation of a novel fuel-saver hybrid combining a solar receiver with a combustor for a solar power tower. Applied Energy. 2014;113:1235-43.

[83] Jafarian S, Arjomandi M, Nathan G. A hybrid solar and chemical looping combustion system for solar thermal energy storage. App Energy. 2013;103:671-8.

[84] Z'Graggen A, Haueter P, Maag G, Romero M, Steinfeld A. Hydrogen production by steam-gasification of carbonaceous materials using concentrated solar power - IV. Reactor experimentation with vacuum residue. Int J Hyd Energy. 2008;33:679-84.

[85] Z'Graggen A, Haueter P, Trommer D, Romero M, de Jesus J, Steinfeld A. Hydrogen production by steam-gasification of petroleum coke using concentrated solar power—II Reactor design, testing, and modeling. Int J Hyd Energy. 2006;31:797-811.

[86] Z'Graggen A, Steinfeld A. Heat and mass transfer analysis of a suspension of reacting particles subjected to concentrated solar radiation – Application to the steam-gasification of carbonaceous materials. Int J Heat Mass Trans. 2009;52:385-95.

[87] Z'Graggen A, Steinfeld A. Hydrogen production by steam-gasification of carbonaceous materials using concentrated solar energy - V. Reactor modeling, optimization and scale-up. Int J Hyd Energy 2008;33:5484-92.

[88] Hobbs M, Radulovic P, Smoot L. Modeling fixed-bed coal gasifiers. AIChE Journal. 1992;38:681-702.

[89] Kodama T. High-temperature solar chemistry for converting solar heat to chemical fuels. Progress in Energy and Combustion Science 2003;29:567-97.

[90] Kodama T, Ohtake H, Shimizu K-I, Kitayama Y. Nickel catalyst driven by direct light irradiation for solar CO2 reforming of methane. Energy Fuels. 2002;16:1016-23.

[91] Buck R, Abele M, Bauer H, Seitz A, Tamme R. Development of a volumetric receiver-reactor for solar methane reforming. ASME J Sol Energy Eng. 1994;116:73-8.

[92] Abele M, Bauer H, Buck R, Tamme R, Worner A. Design and test results of a receiver-reactor for solar methane reforming. ASME J Sol Energy Eng. 1996;118:339-46.

[93] Worner A, Tamme R. CO2 reforming of metahne in a solar driven volumetric receiver-reactor. Catal Today. 1998;46:165-74.

[94] Rodat S, Abanades S, Coulie J, Flamant G. Kinetic modelling of methane decomposition in a tubular solar reactor. Chem Eng J. 2009;146:120-7.

[95] Gronchi P, Fumagalli D, Del Rosso R, Centola P. Carbon deposition in methane reforming with carbon dioxide dry reforming. J Therm Anal. 1996;47:227-34.

[96] Choudhary V, Uphade B, Mamman A. Large enhancement in methane-to-syngas conversion activity of supported Ni catalysts due to precoating of catalyst supports with MgO, CaO or rare-earth oxide. Catal Lett. 1995;32:387-90.

[97] Levitan R, Rosin H, Levy M. Chemical reactions in a solar furnace-direct heating of the reactor in a tubular receiver. Solar Energy. 1989;42:267-72.

[98] Edwards J, Do K, Maitra A, Schuck S, Fok W, Stein W. The use of solar-based CO2/CH4 reforming for reducing greenhouse gas emissions during the generation of electricity and process heat Energy Convers Mgmt. 1996;37:1339-44.

[99] Berman A, Karn R, Epstein M. A new catalyst system for high-temperature solar reforming of methane. Energy & Fuels. 2006;20:455-62.

[100] Piatowski N, Wieckert C, Weimer A, Steinfeld A. Solar-driven gasification of carbonaceous feedstock - a review. Energy Environ Sci. 2011;4:73-82.

[101] Gregg D, Aiman W, Otsuki H, Thorsness C. Solar coal gasification Solar Energy 1980;34:313-21.

[102] Govind R, Shah J. Modeling and simulation of an entrained flow coal gasifier AIChE Journal. 1984;30:79-92.

[103] Kordabadi H, Jahamiri A. A pseudo-dynamic optimization of a dual-stage methanol synthesis reactor in the face of catalyst deactivation. Chem Eng Proc. 2007;46:1299-309.

[104] Berreni M, Wang M. Modelling and dynamic optimizaation of thermal cracking of propane for ethylene manufacturing. Computers Chem Eng. 2011;35:2876-85.

[105] Laurendeau N. Heterogeneous kinetics of coal char gasification and combustion. Prog Energy Comb Sci. 1978;4:221-70.

[106] Newcomer A, Apt J. Storing syngas lowers the carbon price for profitable coal gasification. Environ Sci Technol. 2007;41:7974-79.

[107] Medrano M, Gil A, Martorell I, Potau X, Cabeza L. State of the art on high-temperature thermal energy storage for power generation. Part 2—Case studies. Renew Sustain Energy Rev. 2010;14:56-72.

[108] Dickinson R. Part 1: Potential corrosion impacts of using hydrogen as an energy carrier in existing CNG pipelines. In: Ashman P, editor. RP3-03 Corrosion by New Energy Fluids. Adelaide, Australia: Energy Pipelines CRC; 2010.

[109] Kolb G. Economic evaluation of solar-only and hybrid power owers using molten-salt technology. Sol Energy. 1998;62:51-61.

[110] NREL. National solar radiation database 1991-2005 update. Renewable resource data center: US DoE EERE; 2009.

Page Intentionally Left Blank

2

POLYGENERATION OF LIQUID FUELS AND ELECTRICITY BY THE ATMOSPHERIC PRESSURE HYBRID SOLAR GASIFICATION OF COAL

Ashok A Kaniyal [a,c], Philip J van Eyk [a,b], Graham J Nathan [a,c], Peter J Ashman [a,b], Jonathan J Pincus [a,d]

a Centre for Energy Technology, The University of Adelaide South Australia 5005
b School of Chemical Engineering, The University of Adelaide South Australia 5005
c School of Mechanical Engineering, The University of Adelaide South Australia 5005
d School of Economics, The University of Adelaide, South Australia 5005

Energy & Fuels 2013 (27) 3538-55

energy&fuels

Article

pubs.acs.org/EF

Polygeneration of Liquid Fuels and Electricity by the Atmospheric Pressure Hybrid Solar Gasification of Coal

Ashok A. Kaniyal,*[,†] Philip J. van Eyk,[†,‡] Graham J. Nathan,[†] Peter J. Ashman,[†,‡] and Jonathan J. Pincus[†,§]

[†]Centre for Energy Technology, The University of Adelaide, South Australia 5005

[‡]School of Chemical Engineering, The University of Adelaide, South Australia 5005

[§]School of Economics, The University of Adelaide, South Australia, Australia 5005

ABSTRACT: An analysis of system operation and performance has been undertaken, for the first time, of a solar-hybrid coal-to-liquids polygeneration facility incorporating solar resource variability. The energetic and environmental performance of a coal-to-liquids process that is integrated with a solar hybridized, oxygen blown, atmospheric pressure gasifier (CTL_{sol}) is compared with that of a reference, nonsolar, autothermal, pressurized gasification integrated, CTL_{ref} configuration. To allow the plant to respond to solar resource transience, pressurized storage of upgraded syngas and oxygen is incorporated into the proposed CTL_{sol} system. The CTL_{sol} process is simulated using a dynamic model that assumes pseudosteady state operation at each time-step, for a 12-month, hourly averaged solar insolation time-series. Both the CTL_{sol} and CTL_{ref} systems were modeled using AspenPlus and Aspen HYSYS (v 7.1) software. The analysis of the CTL_{sol} system's performance showed an annually averaged improvement of 21% to the total energetic output and a reduction of 30% in the mine-to-tank greenhouse gas emissions relative to the CTL_{ref} system assuming equilibrium gasification conditions of 1400 °C and 1 bar-a. The integration of a pressurized syngas storage facility was shown to enable the CTL_{sol} system to allow the variation in throughput of each unit of process equipment to be maintained within normal operational ranges despite the fluctuations in the transient solar input to the solar-hybrid coal gasification process.

1. INTRODUCTION

The production of Fischer−Tropsch liquid (FTL) fuels via the entrained flow gasification of coal has received much interest in the literature recently due to the long-term need for reliable sources of transport fuels.[1−9] However, a barrier to the implementation of systems producing FTL fuels from coal is that its mine-to-tank (MTT) greenhouse gas (GHG) emissions are more than twice that of diesel produced from tar sands[10] and more than three times that of diesel produced from conventional mineral crude.[11] One potential approach to lower the CO_2-e emissions of the coal-to-liquids (CTL) process is to employ concentrated solar thermal power to meet the endothermic demand of the high temperature coal gasification reactions. Solar gasification has been shown to enable the chemical storage of solar energy and boost by up to 30% the calorific value of the raw syngas output (SG_{raw}) from the gasifier relative to the input feedstock,[12−17] thus also reducing the carbon emissions from the CTL process. This approach is thus differentiated from other technologies designed to lower the CTL processes' CO_2-e emissions, namely carbon capture and storage and biomass cogasification, which have a net parasitic impact on system productivity.[4,5,18] However, the transient nature of the solar resource and the continuous operation of the conventional CTL process lead to a process integration challenge. One approach by which this challenge could be addressed is by the solar hybridized of FTL from coal gasification and natural gas co-reforming, which was recently proposed by Sudiro and Bertucco.[19] However, to date no comprehensive assessment of the performance and operation of a solar hybridized−CTL_{sol} process has been presented, especially in a way that accounts for the dynamic, seasonal, diurnal, and cloud-related variability of the solar resource. Hence, the overall objective of the present investigation is to meet this need.

Solar gasification reactors have been under investigation since the 1980s. Early studies examined packed-bed solar reactors based on the operation of the gravity fed Lurgi reactor.[12,20] Packed bed reactors are generally simple and robust, can accommodate feedstocks of different sizes and forms, and do not require excess steam flows. This makes them inexpensive relative to entrained flow reactors. However, these advantages typically do not overcome the limitations in heat and mass transfer associated with the bed, which inhibits the reaction rate and syngas throughput.[12,21] Additionally, ash buildup at the surface decreases the absorptivity of the irradiated bed, leading to slagging and sintering. This is especially so with high ash feedstocks, which is the case for many coals. Fluidized-bed reactors resolve some of the heat and mass transfer limitations of the packed bed configurations.[12] However, the narrow reaction zone, loss of sensible heat through the exit gas, and the need for excess (over stoichiometric) steam or inert gas to achieve fluidization reduces the net energetic performance of this reactor configuration relative to an entrained flow gasifier.[12,22−26] A third alternative is the indirectly irradiated entrained flow reactor,[27] in which heat is transferred to the reactants flowing within a cavity, typically a tube made of silicon carbide.[27,28] However, the inefficiency of indirect heat transfer limits the performance of this configuration. Recently, an innovative design that couples entrained flow gasification with direct solar irradiation was

Received: February 1, 2013
Revised: May 19, 2013
Published: May 20, 2013

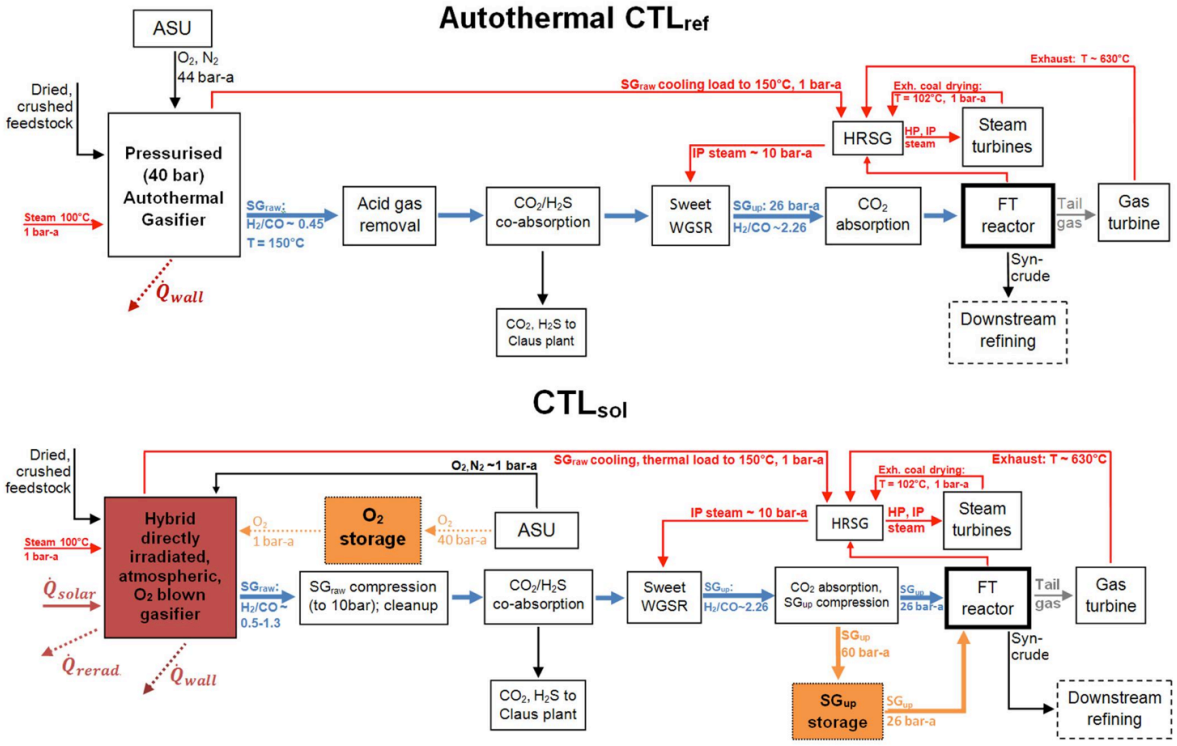

Figure 1. Simplified, annotated process schemes for the reference, pressurized autothermal Shell gasification integrated CTL polygeneration system (top) and the directly irradiated solar O_2 blown hybrid atmospheric pressure gasification, syngas, and O_2 storage integrated CTL_{sol} polygeneration system (bottom).

proposed and experimentally demonstrated.[16,17,29,30] The technical viability of the atmospheric pressure, windowed solar vortex reactor to gasify petroleum coke (petcoke) has been demonstrated on a small scale,[16,29,31] and a 300 kW pilot scale reactor has also been tested successfully.[17] However, while this reactor appears to be well suited to being adapted to operate as a hybrid device, its potential benefit has yet to be evaluated. In such a hybrid device, the endothermic demand of the gasification process could be met by solar energy when it is available and/or by oxygenated coal combustion when sufficient solar thermal power is unavailable—e.g. during periods of high cloud cover or at night. Importantly, unlike a conventional, entrained flow gasifier, the solar hybrid vortex reactor has not yet been demonstrated at pressures above atmospheric levels, given the constraint of the quartz window.[32,33] Furthermore, no system-level operational, energetic, or environmental performance analysis has been presented that integrates a directly irradiated solar, oxygen blown hybrid, entrained flow coal gasification reactor with a FT liquid polygeneration system. Hence, more specifically, the present investigation aims to quantify the benefits of integrating an atmospheric pressure solar-hybrid vortex reactor as part of a CTL_{sol} process.

A number of studies of solar integrated fossil fuel reactor systems have been presented over the past 20 years for electricity and/or hydrogen production,[20,34−38] but much less attention has been paid to solar hybridized CTL plants. Sudiro and Bertucco's recent investigation of FT liquids production by solar hybridized coal gasification and natural gas co-reforming in a directly irradiated, pressurized reactor[19] is significant in this regard. However, that approach is limited by the need for a windowed reactor that is not structurally compromised by high temperatures or elevated pressures.[16,17,39] Thus, it is desirable to pursue alternative configurations that avoid the need for pressurization. In addition, none of the publicly available studies of solar hybridized polygeneration systems[19,40−43] have adequately accounted for the effects of the variable nature of the solar resource, which is important because polygeneration systems operate most efficiently under constant load, steady-state conditions. Previous assessments have, at best, only examined the impacts of diurnal solar transience on system operation and performance.[19,40−43] No assessment has accounted for the stochastic and seasonal transience of solar insolation on the performance of a CTL_{sol} polygeneration system. Hence, the present investigation aims to develop a modeling approach that comprehensively accounts for the seasonal, diurnal, and stochastic variability of the solar resource in the evaluation of the performance of the CTL_{sol} polygeneration system.

Pressurized gas storage is a potentially feasible option to accommodate the impact of variable input from a transient solar resource on the various unit operations of a CTL_{sol} polygeneration system. Pressurised syngas storage, which has previously been shown to improve the viability of a conventional IGCC facility,[2,44] could also reduce the size and frequency of fluctuations in solar-boosted syngas flow to the Fischer−Tropsch reactor (FTR). However, its effectiveness in reducing the impact of these variations is yet to be adequately evaluated. Similarly, a pressurized O_2 storage system could also contribute to the management of the variable solar resource, while enabling operation of the CTL_{sol} facility with an air separation unit with a

reduced production capacity relative to the nonsolar, autothermal CTL system. This has the advantage of reducing the polygeneration system's total parasitic load as well as its contribution to the CTL facility's total capital cost. The ASU typically contributes ~15% to the total capital cost of the autothermal CTL facility.[1,9] However, an assessment of the performance of a CTL_{sol} system with pressurized syngas and O_2 storage requires a transient model and an analysis over a representative year-long solar insolation data series. Hence, the present investigation also aims to meet this need.

The overall objective of this investigation is to present a conceptual design that could feasibly integrate concentrated solar radiation into a coal-to-liquids plant in an atmospheric pressure vortex reactor, while accommodating the variability in the solar resource by the pressurized storage of syngas and oxygen. To achieve this, the first aim is to develop a pseudo-steady-state dynamic model that calculates the transient performance with a time series of solar insolation and to verify steady-state operation for the nonsolar autothermal CTL_{ref} polygeneration system. The second aim is to identify with the model a feasible operating regime for the CTL_{sol} system, and to estimate its energetic and environmental performance relative to the nonsolar CTL_{ref}. Finally, the third aim is to examine the sensitivity of system performance to gasification temperature and heliostat collector area.

2. METHODOLOGY

The energetic and environmental performance of the solar hybridized gasification integrated coal-to-liquids (CTL_{sol}) polygeneration system was assessed relative to a "reference" system based on a conventional, autothermal, pressurized (40 bar) "Shell" type gasifier, hereafter term the CTL_{ref}.[5] Both, the CTL_{ref} and CTL_{sol} plants were sized for a nominal coal feed rate of 1 kg/s (0.89 kg/s dry, ash free basis).

Figure 1 presents simplified, annotated schemes of both the CTL_{ref} (top) and the CTL_{sol} systems (bottom). Both systems are assumed to be configured to maximize the production of Fischer–Tropsch liquid fuels (FTL). This avoids the need to divert the upgraded syngas (SG_{up} with $H_2/CO \sim 2.26$) that is produced in the sweet water gas-shift reactor (SWGSR) to the gas turbine for electricity generation. The present autothermal CTL_{ref} system is consistent with, and verified against (see Table 5), the baseline scheme reported by Meerman et al.[5] Both the CTL_{sol} and CTL_{ref} systems assume all captured CO_2 emissions from the facility to be vented (i.e., no carbon sequestration). All unit operations were modeled using Aspen Plus v7.1 software, except for the gasifier, which was modeled using Aspen HYSYS v7.1 software.

2.1. The Concept: Hybrid Atmospheric, Directly Irradiated, O_2 Blown Solar Reactor. *2.1.1. Hybrid Solar-Autothermal Gasifier.* The CTL_{sol} system was assumed to be configured based on the experimentally demonstrated solar vortex gasification reactor.[16,17,29,39] In those studies, petroleum coke was injected into the cavity of the solar vortex reactor through a tangential nozzle to generate a turbulent, helical, vortex flow pattern for transport and heat transfer.[14] The reactor configurations studied were shown to achieve near-complete conversion of petroleum coke to syngas for a feed-rate of 0.005 kg/s. Figure 2 presents the solar hybrid reactor, adapted from previous work by Z'Graggen and Steinfeld[17] with a ZrO_2 insulated cylindrical cavity and an aperture sealed by a larger, quartz glass window for sealing the vessel while transmitting radiation.

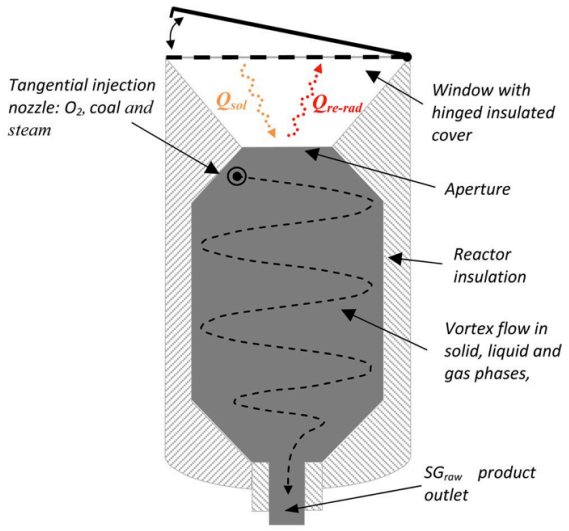

Figure 2. Cross-section of a directly irradiated hybrid volumetric concentrated solar thermal receiver-reactor (adapted from[14]) with a hinged, insulated window cover to seal the reactor when $\eta_{abs} = 0$ (e.g., at night and periods of high cloud cover).

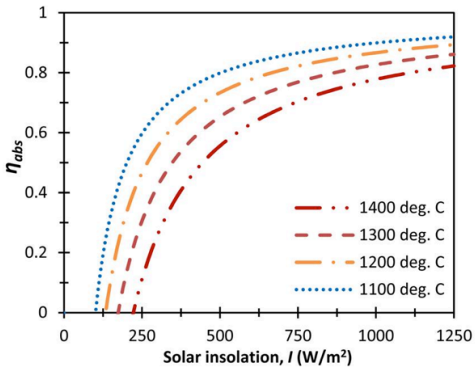

Figure 3. Dependence of solar absorption efficiency (η_{abs}) on the direct normalized solar radiation intensity for T_g = 1100–1400 °C and for $\tilde{C}$ = 2000 suns.[15]

The present assessment assumes that the solar vortex reactor[17] can be feasibly scaled up, to a nominal, constant coal flow rate of 1 kg/s. It is also assumed that a hinged, insulated window cover is used to prevent radiation losses when the solar insolation falls below the threshold where the energy reradiated out of the reactor exceeds the solar power absorbed (i.e., $\eta_{abs} = 0$), e.g. at night or during periods of high cloud cover (see Figure 3); the window can withstand the thermal shocks of oxygenated coal combustion; a constant T_g can be maintained for the four scenarios of 1100, 1200, 1300, and 1400 °C; and the solar flux is sufficient to completely satisfy the gasifier's total endothermic demand for 100% conversion of the carbon in the dry coal fed into the gasifier at 1 kg/s to raw syngas (SG_{raw}).

The assumption of 100% carbon conversion was made based both on the experimentally reported values from the solar vortex reactor by Z'Graggen et al.[16,17,29,45] and on the process model analysis by Meerman et al.[5] Meerman et al. (whose data and methodology was used to verify our model) assumed a carbon

conversion of 99.7%. This assumption was made based on their discussion with Shell Global Solutions for a reactor temperature of 1500 °C, while the present assessment covered the range of 1100−1400 °C. Nevertheless, the extent of conversion depends both on the temperature and residence time, so that near complete conversion was confirmed for the 5 kW small scale swirling reactor at ∼1400 °C and 1 bar-a by Z'Graggen and Steinfeld,[17] who used a less reactive fuel of petroleum coke than is assumed here. Furthermore, the swirling flow in the vortex reactor greatly increases the residence time over an entrained flow gasifier of equivalent length. Hence, while the assumption of 100% carbon conversion represents a best case scenario, it is reasonable to assume that the reactor could be made sufficiently large, or incorporate sufficient swirl, to approach this value for the range of conditions assessed here.

The radiation losses through the hybrid solar reactor aperture, shown in Figure 2, were calculated using the solar absorption efficiency, η_{abs}, given by eq 1 below. The rate of radiation losses through the quartz window was calculated at each time-step in the year-long solar insolation (I) time-series for the gasification temperature (T_g) range 1100−1400 °C, while assuming a mean solar flux concentration ratio ($\tilde{C}$) of 2000 suns.[35] The quartz window is assumed to be cleaned with an inert gas to minimize losses due to dust particles. In calculating η_{abs}, the hybrid reactor was assumed to have an optimal aperture size that maximizes the capture of radiation from the heliostat field and minimizes radiation losses from the aperture.[15] Figure 3 presents the relationship between η_{abs} and solar insolation (I) in the range 0−1250 W/m^2 for four gasification reactor temperatures. Given the assumption of an hourly averaged solar insolation time-series data set, the rate of solar absorption is assumed to vary on an hourly basis.

Optical losses through the quartz window from any dust particles remaining on the clean glass or compound parabolic concentrator are taken into account by including an additional loss of 5%[46] to the optical efficiency term from the work of Meier et al.[35] The proposed hybrid gasification system was assumed to be configured in a beam down optical arrangement. The overall optical efficiency (η_{opt}) of all mirrors and reflectors, including the compound parabolic concentrator, was assumed to be 50%.[35,46]

$$\eta_{abs} = 1 - \left(\frac{\sigma T_g^4}{I\tilde{C}}\right) \quad (1)$$

The net solar power input to the reactor ($\dot{Q}_{sol,net}$) was estimated using eq 2, where $\dot{Q}_{wall}$ is the assumed rate of heat lost through the gasifier walls and slag and is given by eq 3. The rate of heat loss was assumed based on the Shell gasifier, which has losses of the on the order of 3% of the heating value of the input feedstock.[47] Using the year-long solar insolation time-series, an equivalent data set was calculated for $\dot{Q}_{sol,net}$ for a given A_{coll} and T_g scenario.

Equation 4 presents the ratio of $\dot{Q}_{sol,net}$ to the thermal power required by the hybrid gasifier (HG) to drive the gasification of 1 kg/s of coal to completion at T_g ($\dot{Q}_{HG}^{T_g-R}$). When $\Phi > 1$, the potential solar thermal power output from the heliostat field is spilled at the rate $\dot{Q}_{sol,net} - \dot{Q}_{HG}^{T_g-R}$ MW$_{th}$. Some spillage occurs above a critical size of heliostat field because the flow rate of coal is fixed. In practical terms, this means that the heliostat collectors are turned to a suboptimal angle to limit the collection capacity. Figure 4 presents as a function of Φ (see eq 4), the net solar thermal power input to the reactor ($\dot{Q}_{sol,net}$ in MW$_{th}$).

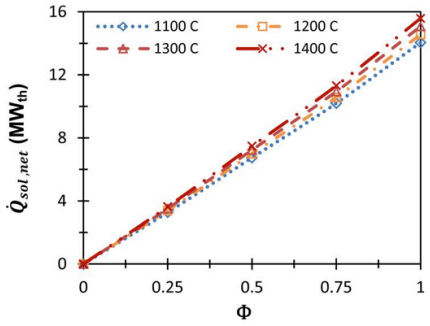

Figure 4. Relationship between the net solar thermal power input ($\dot{Q}_{sol,net}$) to the hybrid gasification reactor and the portion of the endothermic demand of the gasifier fed with 1 kg/s of dry coal met by the net solar thermal power input (Φ, see eq 4).

Table 1. Relationship between the Heliostat Field Collector Area (A_{coll}) and $\Phi_{peak}^{A_{coll}} - 1$

A_{coll} (× 10^3 m^2)	63	51	44	38
$\Phi_{peak}^{A_{coll}} - 1$	1.39	0.91	0.68	0.44

The primary advantage of sizing the heliostat field such that some spillage of the solar radiation occurs is in enabling full utilization of the gasifier. Full utilization is desirable because the solar hybrid gasifier is expected to account for a large proportion of the total capital expenditure of the CTL$_{sol}$ system based on knowledge of the nonsolar, autothermal entrained flow gasifier.[1,4,7,9,48,49] At the same time, the heliostat collection field is also capital intensive, contributing ∼50% to the capital cost of concentrated solar power systems.[50] An assessment of the trade-off in the utilization of both the hybrid solar gasifier and heliostat field is presented in a recently published paper by Kaniyal et al.[51]

The energetic and environmental performance of the CTL$_{sol}$ system was assessed for four A_{coll} scenarios given in Table 1. The heliostat collection capacity is represented in normalized terms using the peak value calculated for the year-long, hourly averaged $\dot{Q}_{sol,net}$ time series. The normalized representation of A_{coll} is hereafter termed $\Phi_{peak}^{A_{coll}} - 1$, which is defined by eq 5. Hence, $\Phi_{peak}^{A_{coll}} - 1$ is the fraction by which the peak, annual, hourly averaged thermal power output of a heliostat field of area A_{coll} exceeds the endothermic demand of the hybrid reactor to completely gasify 1 kg/s of coal at T_g. Table 1 summarizes the normalized equivalent of each A_{coll} scenario.

$$\dot{Q}_{sol,net} = \eta_{abs}\eta_{opt}A_{coll}I - \dot{Q}_{wall} \quad (2)$$

$$\dot{Q}_{wall} = \dot{m}_{coal}.0.03.Q_{coal(HHV)} \quad (3)$$

$$\Phi = \frac{\dot{Q}_{sol,net}}{\dot{Q}_{HG}^{T_g-R}} \quad (4)$$

$$\Phi_{peak}^{A_{coll}} = \frac{(\dot{Q}_{sol,net}^{A_{coll}})_{ann(peak)}}{\dot{Q}_{HG}^{T_g-R}} \quad (5)$$

2.1.2. Solar Resource Analysis. The hourly averaged solar insolation time-series chosen was for the summer-to-summer period: June 1st, 2004 to May 31st, 2005. The insolation data set corresponds to the Farmington site, in northern New Mexico (USAF #723658),[52,53] whose latitude is 37 °N. Using this data set, a normalized probability density profile of the number of

dx.doi.org/10.1021/ef400198v | *Energy Fuels* 2013, 27, 3538−3555

continuous hours with zero net solar power input to the reactor ($t_{\Phi=0}$) was evaluated. Figure 5 illustrates the normalized probability density of $t_{\Phi=0}$ for two cases: the summer-to-summer 2004/05, 12 month study period and a long-term comparator for the period: Jun 2004 to Dec 2009. Importantly, Figure 5 shows that the study period curve closely follows the long-term distribution. This provides some confidence in the representativeness of the solar time-series used in the present analysis. Figure 5 also shows that the probability of prolonged periods of zero solar insolation, i.e. $t_{\Phi=0} \geq 72$ h is low, but not negligible, corresponding to about <0.0001, which is slightly less than once a year. Similarly, although the events when $t_{\Phi=0} \geq 16$ h number less than 10 times a year, their potential impacts on a fuel to liquids process are large. Hence, it is important to account for these events in the design of any solar integrated system to ensure continuous and steady plant operation and to avoid unscheduled plant shut-downs.

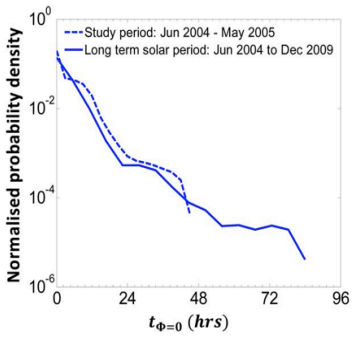

Figure 5. Logarithmic scale normalized probability density distribution of the number of continuous hours with zero net solar input ($\Phi = 0$) to the hybrid solar reactor for the 2004/05 summer-to-summer study period and a long-term comparator at the chosen location of Farmington, New Mexico.[52,53]

For a solar-only plant, accommodating the transience in the solar resource results in an inevitable trade-off between the increased capital cost with increased storage infrastructure and the economic penalties of unscheduled plant shut-downs. Hybridization significantly reduces these operational and capital cost penalties in enabling a continuous syngas output from the gasifier using the autothermal process when no solar radiation is available. Nevertheless, storage is also required for the hybrid case, since both the flow-rate and composition of the product gases vary with the transient solar resource, while the F−T reactor has very narrow operating ranges. This also results in a trade-off in storage capacity. The present investigation thus examines the use of pressurized syngas storage to mitigate the impacts of solar transience on the unit operations downstream from the hybrid gasification reactor.

2.2. Process Models. Two process models were developed, the first for the autothermal, nonsolar CTL_{ref} process and the second for the CTL_{sol} polygeneration process. The veracity of the reference model was assessed by comparing the simulation results with those reported by Meerman et al.,[5] who studied the performance of a Fischer−Tropsch liquids polygeneration system for a "Shell" type entrained flow gasifier, using Illinois #6 coal. The parametrization data reported by Meerman et al.,[5] was used to achieve as close an agreement as possible with the reported results. A description and the parametrization of the autothermal CTL_{ref} and CTL_{sol} process models is summarized in subsection 2.2.2. Section 2.2.1 describes the pseudodynamic simulation of the steady-state CTL_{sol} process model and the assumptions underlying the simulation of the upgraded syngas pressurized storage system.

2.2.1. CTL_{sol}−Pseudodynamic Model. The dynamic operation of the CTL_{sol} system was modeled using MATLAB code that assumed steady-state operation in each time-step of the CTL_{sol} system using Aspen Plus and Aspen HYSYS (v7.1). The MATLAB code used unique linear or log−linear relationships to describe the parasitic load, energetic output, and/or CO_2 emissions of each unit operation of the CTL_{sol} polygeneration system. A regression analysis was carried out with respect to the clean, upgraded syngas (SG_{up}) hourly production rate, using these process models. Linear and/or log−linear relationships were determined between SG_{up} and the following unit operations: the air separation unit, O_2 compression air separation unit, O_2 compression, and storage plant—to evaluate its parasitic load; hybrid gasifier, cleaning plant, and water gas shift reactor—to evaluate its parasitic load and the CO_2 emissions of the unit operations; syngas compression and storage plant—to evaluate its parasitic load; Fischer−Tropsch reactor—to evaluate the heating value of the FTL output, end-use CO_2 emissions and the parasitic loads; power island—to evaluate its electrical output and CO_2 emissions.

The dynamic variation in SG_{up} production and the CTL_{sol} system's unit operations were approximated using a series of steady-state results obtained with a model developed in Aspen Plus and Aspen HYSYS. The pseudodynamic representation of the CTL_{sol} system in MATLAB was based on a linear interpolation of the simulation results of five solar conditions, namely $\Phi = \{0, 25, 50, 75, 100\}$%. Using the simulation results of the steady-state CTL_{sol} process model and the calculated $\dot{Q}_{sol,net}$ time-series, the hourly rate of SG_{up} production was evaluated by linear interpolation. A unique SG_{up} time-series was evaluated for each set of A_{coll} and T_g scenarios—leading to a total of 16 scenarios in all.

Part load performance was taken into account in the unit operation models of the Brayton cycle, the steam Rankine cycle, and the SG_{raw} compression and storage plants. For the Brayton cycle and syngas compression plant, the isentropic efficiency was varied according to a quadratic function (see eq 6).[5] For the steam Rankine cycle, part load performance was calculated by correcting the Aspen Plus simulation results using the efficiency correction factors published by Bahadori and Vuthaluru.[54] The air separation unit (ASU) was assumed to operate at constant load, given the incorporation of an O_2 storage system. The gas cleanup, H_2S/CO_2 absorption, and water gas-shift reactor (WGSR) and Fischer−Tropsch reactor plants were all assumed to be operable with variable input feed rates. It was also assumed that the variable input feed rates to these plants did not have a significant negative impact on the overall electrical and thermal performance of the CTL_{sol} facility.[5]

2.2.2. Syngas Storage Model. The Fischer−Tropsch reactor (FTR) and power island were assumed to have the same turn-down because the tail gas fuel flow to the gas turbine and the exothermic heat flow from the FTR to the Rankine cycle are both dependent on FTR productivity. The plants downstream from the SG_{up} storage plant, the FTR, and power island, were both assumed to be operable at three load factors, full load, 98.5% load, and minimum load. The full load condition was assumed to be equal to the throughput of SG_{up} for production at $\Phi = 50$%. The full load SG_{up} throughput was calculated for each size of storage tank. A larger SG_{up} storage capacity enables a smaller value for the full load SG_{up} throughput. The minimum load SG_{up}

throughput was assumed to be equal to the minimum SG_{up} production rate from the WGSR, which in turn corresponds to operation of the hybrid solar gasifier with $\Phi = 0$. These conditions enable the maintenance of production conditions that are within the range of turn-down of the FTR and lead to no shutdown of the facility for the entire solar year under analysis. The condition of minimum SG_{up} throughput to the FTR was assumed to be triggered when the stored level of SG_{up} falls below one hour of SG_{up} production at a rate equal to CTL_{sol} operation with the hybrid gasifier under autothermal conditions. This backstop condition was assumed to ensure that the level of SG_{up} in the storage tank never fell below zero for the entire simulation period. The stored level of SG_{up} increased whenever the SG_{up} output from the WGSR was larger than the throughput to the FTR. The SG_{up} throughput to the FTR was assumed to be increased to the 98.5% load from the minimum load condition, when the stored SG_{up} level rose above 2% of the tank capacity. The full load condition was assumed to be triggered when the stored SG_{up} level rose above 25% of the tank capacity.

The three storage tank capacities scenarios were 4, 8, and 16 h of SG_{up} production at an hourly rate corresponding to operation of the CTL_{sol} plant under autothermal conditions, i.e. with T_g = 1100 °C, 1 bar-a, and $\Phi = 0$. The estimated size, in cubic meters, of the 60 bar-a SG_{up} storage tank is shown in Table 2 for 4, 8, and 16 h of storage.

Table 2. Relationship between the Hours of SG_{up} Storage and the Estimated Size of the Tank (m^3) at a Pressure of 60 bar-a

SG_{up} storage (h)	tank size (60 bar-a in m^3)
4	579
8	1157
16	2314

The CTL_{sol} system was found not to be particularly sensitive to the SG_{up} storage tank capacity. Increasing the storage tank capacity from 4 to 8 h of SG_{up} production decreased the ratio of full to minimum load SG_{up} throughput by 2%. A further increase in storage tank capacity to 16 h of SG_{up} production led to only a 1% decrease in the ratio of full load to minimum load SG_{up} throughput to the FTR. Section 3.2.3 outlines the impact of increasing SG_{up} storage capacity on the utilization of the compression and storage system and on the hourly averaged variance in the SG_{up} flow to the FTR.

The results of the pseudodynamic simulation of all major components of the CTL_{sol} polygeneration system including the SG_{up} and O_2 storage models are presented later in Figure 7, for both a six-day "summer" period representing consistent solar insolation and a six-day data series in "winter," representing an extended period of intermittent, poor solar insolation.

2.2.3. CTL_{ref} and CTL_{sol} Process Model Unit Operations. The following subsection outlines the methodology and parametrization of the Aspen Plus and Aspen HYSYS (v 7.1) process models used to simulate the processes' steady state operation. For brevity, detailed descriptions of each unit operation are not provided, given the availability of extensive descriptions in the peer-reviewed literature.[5]

Design Coal and Gasifier HYSYS Model Parametrization. The properties of the "Illinois 6" design coal are presented in Table 3.[5] The main challenge with this study was to represent coal, being a complex material, in a form that is sufficiently simple to be utilized in the Aspen HYSYS model. Specifically, the challenge was to represent the coal volatile matter in HYSYS. To achieve this, three sets of coal properties were used: the gross calorific value, to reliably model the heat balance within the reactor; the ultimate analysis of the coal, to ensure the mass conservation of the various elemental compounds; and the proximate analysis.

Table 3. Proximate and Ultimate Analyses of "Illinois 6" Design Coal[7]

proximate analysis (wt %)	as received
moisture	11.12
ash	9.7
volatile matter	34.99
fixed carbon	44.19
total	100
sulfur	2.51
LHV (MJ/kg)	26.15
HHV (MJ/kg)	27.11
ultimate analysis (wt %)	dry
carbon	71.72
hydrogen	5.06
oxygen	7.75
nitrogen	1.41
chlorine	0.33
sulfur	2.82
ash	10.91
LHV (MJ/kg)	29.40
HHV (MJ/kg)	30.51
modeled composition (wt %)	dry, ash free
CO	15.2
H_2	0
CO_2	0
CH_4	21.8
H_2O	0
N_2	1.58
C	57.7
Ar	0
O_2	0
H_2S	3.36
HCl	0.38

The "Illinois 6" coal was modeled by assuming that fixed carbon is solid carbon and that the volatile matter is comprised of the compounds CH_4, CO, N_2, H_2S, and HCl, with compositions shown in Table 3. The modeled quantity of solid carbon is 57.7% (wt), which is within 5% of the d.a.f. carbon fraction from the ultimate analysis of 55% (wt). The modeled composition shown in Table 3 gives the closest fit to the actual composition while achieving a mass balance of individual elements and an overall heating value that equals that calculated from the ultimate analysis. The relative quantities of each of the other gaseous compounds were determined using the ultimate analysis. Other gases including H_2O, H_2, and CO_2 were also considered but led to a less accurate match to the gross calorific value.

Gasifier. The hybrid solar gasifier was modeled using Aspen HYSYS v7.1 simulation software. The reactor was modeled as a Gibbs reactor, which minimizes Gibbs free energy to determine the equilibrium composition at the outlet from the gasifier. Thermodynamic properties of the chemical species were obtained using the Peng−Robinson model. Inputs to the reactor were the model coal (as discussed above), nitrogen used for the carrier gas for the coal feed, steam used as a gasifying agent, and oxygen that is needed when $\Phi < 1$. The quantities of the various gas inputs were determined based on the following:

dx.doi.org/10.1021/ef400198v | *Energy Fuels* 2013, 27, 3538−3555

Table 4. Model Input Parameters for the Autothermal CTL_{ref} and the Solar Hybridized Gasification Integrated CTL_{sol} Polygeneration Systems[3]

parameter	units	CTL_{ref}	CTL_{sol}				
coal mass flow rate ($\dot{m}_{coal}$) (dry)	kg/s	1.0	1.0				
N_2 carrier gas for dry coal	kg/s	0.125	0.125				
gasification temperature (T_g)	°C	1500	1100				
gasification pressure (P_g)	bar-a	42	1.0				
Φ: $\dot{Q}_{sol,net}/\dot{Q}_{HG}^{T_g-R}$	%	0	100	75	50	25	0
thermal power input required[a] ($\dot{Q}_{HG}^{T_g-R}$)	MW_{th}	0	0	3.39	6.78	10.2	13.6
oxidant flow rate (94.3% mol O_2)	kg/s	0.92	0.85	0.64	0.43	0.21	0.0
steam flow rate	kg/s	0.1	0.1	0.32	0.55	0.77	1.0

[a]To achieve conversion of 100% of carbon content in coal to raw syngas.

- Steam: For the periods when $\Phi = 0$, the steam flow rate was 10% of the coal flow rate.[7] For periods when $\Phi > 0$, the steam flow rate was determined by ensuring that less than 0.1% methane was present at the outlet from the gasifier.
- Oxygen: The oxygen flow rate was varied in response to the net solar thermal power input to the hybrid reactor to maintain a given reactor temperature.
- Nitrogen: Based on the NETL baseline studies,[7] the nitrogen flow rate was assumed to be 12.5% of the coal flow rate.

Examples of the parameters utilized in the gasifier model are given in Table 4. Additionally, as noted above, the heat loss from the gasifier was assumed to be 3% of the coal heating value.[47]

Fuel Sizing. The crusher was modeled to produce particles with a maximum diameter of 150 μm and based on a conservative Hardgrove grindability index of 40. A specific electrical consumption of 15 kWh_e/ton coal was assumed.[55]

Fuel drying. The coal was assumed to be dried to <2 wt % using the atmospheric pressure steam exhaust from the steam turbines.[5] A small portion of the nitrogen waste stream from the air separation unit was assumed to be diverted to the materials handling model to carry the dry coal into the gasifier (see Table 3).

Air Separation Unit (ASU): Production. The cryogenic air separation unit (ASU) was modeled to deliver oxygen to the solar integrated hybrid gasifier at a purity of 94.3 mol %. For the autothermal CTL_{ref} process model, the oxygen was compressed through four intercooled (40 °C) stages to 48 bar-a at an isentropic efficiency of 75%. For the hybrid plant, oxygen was assumed to be delivered to the gasifier at 1 bar-a. For both the CTL_{sol} and autothermal CTL_{ref} systems, the ASU was assumed to operate continuously at full load. A conservative specific energy consumption rate of 0.20 kWh/kg O_2 was predicted using the Aspen Plus model.[5]

Oxygen Storage (for CTL_{sol} Process Model). Oxygen was assumed to be compressed and stored at 60 bar-a, whenever the hourly supply of O_2 from the ASU exceeded the hybrid solar gasifier's hourly demand. The fill and discharge cycles of the O_2 storage system were modeled by calculating the dependence of the gasifier's demand for O_2 on the net solar thermal power input to the reactor (see Table 4).

The minimum feasible hourly ASU production rate required to meet the hybrid gasifier's demand throughout the year was determined using a MATLAB code. The minimum ASU production capacity was determined while ensuring that the stored level of O_2 in the tank was always above zero for the entire solar insolation time-series under evaluation. For the purposes of the annualized assessment of plant performance, a storage capacity of 5000 kmol (~3300 m^3) was assumed. The intercooled O_2 compression plant was assumed to operate with an isentropic efficiency of 75%.[5]

Syngas Compression (for CTLsol Process Model). The four-staged intercooled (to 25 °C) compression of syngas was configured to take place in two steps. The first step occurs before the cleaning plant where the cooled SG_{raw} stream was compressed to 10 bar-a before being fed into the H_2S and CO_2 coabsorber.[56] The second step of compression to 20 bar-a occurs after the syngas is upgraded to $H_2/CO \sim 2.26$ (mol/mol) and after the CO_2 produced by the WGS process is removed. The isentropic efficiency of the compression stages was varied according to eq 6, where x is the ratio of mass flow of syngas for the part load condition to that at full load.[5]

$$\eta_{isen} = 0.65 + 0.3577x - 0.1757x^2 \quad (6)$$

COS Hydrolysis. The hydrolysis of carbonyl-sulfide (COS) produced in the gasification process takes place according to reaction 7. This hydrolysis process was modeled to occur before the H_2S and CO_2 gas cleaning block and the sweet water gas shift process.

$$COS + H_2O \rightarrow H_2S + CO_2 \quad (7)$$

H_2S and CO_2 Co-absorption. The cleaning process model was based on the Selexol H_2S and CO_2 "co-capture" process described by Chiesa et al.[56] This process is employed in natural gas fields to clean syngas for pipeline transport. The reactor was modeled using the Peng–Robinson (PR) physical property method separately to the gas cleaning block in Aspen Plus at 10 bar-a. The absorption process was simulated to capture >99% of the CO_2 formed through the gasification process and the WGSR. Fluctuations in the concentration of H_2S and CO_2 were accounted for by varying the Selexol solvent flow rate.

The present investigation does not examine the compression and sequestration of the products H_2S and CO_2. However, CO_2 compression is taken into account for the verification of the reference model developed for this study, to ensure consistency with the analysis by Meerman et al.[5]

Claus Plant. The oxidation of the H_2S recovered in the absorber was modeled using the *RStoic* block in Aspen Plus in the presence of O_2 bled from the ASU. The reactions that led to the dissociation of H_2S to sulfur and SO_2 were modeled in a stoichiometric reactor according to reactions 8 and 9. The Claus plant was assumed to have a zero net steam demand.[1] The steam produced by H_2S combustion was balanced by the steam required to keep the sulfur molten.[56]

$$2H_2S + O_2 \leftrightarrow 2H_2O + 2S \quad (8)$$

$$2H_2S + 3O_2 \leftrightarrow 2H_2O + 2SO_2 \quad (9)$$

Water Gas Shift Reactor (WGSR). The sweet water-gas shift reactors (SWGSR) were configured after the cleaning plant in the Aspen Plus model. The SWGSR was modeled using the

RStoic block in Aspen Plus and the Peng−Robinson physical property methods. The reactor was operated at a pressure of 10 bar-a and temperature of 260 °C,[5] by passing the entire cleaned stream of SG through the reactor and controlling the rate of steam input to achieve a H_2/CO molar ratio of ∼2.26 in the upgraded product gas (SG_{up}).[5] The SWGS process was assumed to be unaffected by variations in SG_{raw} in-flow.[5]

Fischer−Tropsch Reactor. The Fischer−Tropsch reactor (FTR) was modeled assuming the use of a cobalt catalyst. A CO conversion rate of 90% was assumed by ensuring excess H_2 in the SG_{up} in-flow.[5] The assumed H_2/CO ratio of 2.26 exceeds the minimum ratio of 2 required for a Co catalyst.[5] The reactions in the FTR were modeled to take place at 24 bar-a and 240 °C[48] to produce paraffinic hydrocarbons (C_nH_{2n+2}) according to reaction 10. In Aspen Plus, the conversion of SG_{up} to paraffin waxes for the carbon number range from $n = 1$ to 36 was modeled using the *RStoic* block using the Peng−Robinson physical property methods. The distribution of hydrocarbon products was estimated using the Anderson−Schulz−Flory function given by eq 11.[57] In eq 11, x_n is the product mixture mole fraction of straight chain hydrocarbon of length n, and α is the distribution parameter assumed to be 0.95.[5]

$$n\mathrm{CO} + (2n + 1)\mathrm{H_2} \rightarrow \mathrm{C}_n\mathrm{H}_{2n+2} + n\mathrm{H_2O} \tag{10}$$

$$x_n = (1 - \alpha)\alpha^{n-1} \tag{11}$$

The products of the FT-synthesis process were assumed to be light gases (C_{1-4}), naphthalenes (C_{5-11}), diesel (C_{12-20}), light wax (C_{21-30}), and heavy wax (C_{31+}). The separation of light gases and unreacted syngas was modeled to occur in a distillation column. These light gases were assumed to be sent to the gas turbine for electricity generation. The product upgrade processes were not explicitly modeled, but the refined products and their proportions were assumed to be gasoline (52%) and diesel (48%). Importantly, the FT synthesis process was also assumed to have good part-load behavior down to 40% of the full load SG_{up} throughput.[5]

The exothermic heat flow from the FT process to the HRSG was modeled to generate steam at 550 °C and 42 bar-a for the intermediate pressure (IP) steam turbine and 368 °C and 12.5 bar-a for the low pressure (LP) steam turbine. Following Bahadori and Vuthaluru,[54] part load efficiency correction factors were used to correct for variations in the exothermic output of the FTR.

Electricity Generation and Heat Recovery. The raw syngas heat recovery and electricity generation section of the plant were designed to meet the polygeneration system's parasitic demand for both electricity and steam. Both the CTL_{sol} and autothermal CTL_{ref} process models were configured to completely satisfy the facility's parasitic electrical and thermal requirements, while maximizing the production of FT liquids.

Brayton Cycle. The unconverted tail gas stream from the FT plant was assumed to be mixed with air and fed through the gas turbine at 24 bar-a. The air was assumed to be compressed in an intercooled compressor to 110% of the turbine inlet pressure and mixed with the tail gas stream to reduce the inlet temperature to ∼1295 °C. The exhaust (∼630 °C) was assumed to be sent to the HRSG to generate IP steam for the WGS process.[5] Part load performance of the gas turbine was taken into account by calculating the isentropic efficiency given by eq 6, where x is the ratio of flue gas for the part load condition to the mass flow corresponding to the full load scenario.[5]

Heat Recovery Steam Generator (HRSG) and Steam Rankine Cycle. The HRSG plant was used to model the recovery of heat from the raw syngas (SG_{raw}) exiting the gasifier, the gas turbine exhaust, and the heat generated by the exothermic FTR. A portion of the steam produced in the HRSG was directed to satisfy the demands of the gasifier and WGSR plant. The hot SG_{raw} was assumed to be cooled to 150 °C in the HRSG before being directed to the gas cleaning plant. Steam generated at 550 °C and 125 bar-a was passed through the high pressure turbine. Steam generated via a reheat cycle at 550 °C and 42 bar-a was passed through the intermediate pressure (IP) turbine, and the remaining steam was passed through the low pressure (LP) turbine at 368 °C and 12.5 bar-a.[5] The atmospheric pressure steam exhausted from the low pressure turbine was assumed to be used in the coal drying plant. An isentropic efficiency of 85% was assumed for the HP turbine, 93% for the IP turbine and 89% for the LP turbine.[5]

The network of heat exchangers designed to cool SG_{raw} was assumed to incorporate a reheat cycle between the HP and the IP turbines. The water flow to the HP and IP feed-pumps were varied for the five scenarios of solar heat input to maintain steam flow to the three turbines under the design temperature and pressure conditions. The feed-pumps were assumed to have an isentropic efficiency of 92.5% and a mechanical efficiency of 97%.[5] Following Bahadori and Vuthaluru, part load efficiency correction factors were used to correct for variations in steam generated by cooling the variable flow of SG_{raw}.[54]

2.2.4. Plant Utilization Analysis. The annual averaged utilization (8760 h) of the installed SG_{up} pressurized storage and compression system, FTR, gas turbine Brayton cycle (GT), and the steam cycle were calculated using eq 12. This presents the hourly averaged utilization of these unit operations as the ratio of the stored SG_{up} to the storage tank capacity, or of the plant's output (x_h) for a given hour of operation to the unit operation's maximum potential output (x_{cap}). The annually averaged utilization of these unit operations was calculated by taking the mean of the $\overline{U}_h$ time-series.

$$\overline{U_h} = \left(\frac{x_h}{x_{cap}}\right) \tag{12}$$

Equation 13 presents the annual, maximum turn-down of the FTR, GT, and steam cycle as the minimum ratio of plant output for any two contiguous hours of plant operation for the entire study year.

$$\mathrm{TD}_{max} = \min\left(\frac{x_h}{x_{h+1}}\right)_{8760h} \tag{13}$$

Using eq 14, the utilization of the installed heliostat collection capacity was calculated for each hour of the year, by estimating the amount of solar thermal power consumed by the hybrid solar gasifier. In eq 14, $\dot{Q}_{HG}^{T_g-R}$ is the thermal power required by the hybrid solar gasifier, operating at T_g, to completely gasify the coal fed into the reactor at 1 kg/s. The annually averaged utilization of the heliostat field was calculated by taking the mean of the $\overline{U}_{A_{coll},h}$ time-series.

$$\overline{U}_{A_{coll},h} = \begin{cases} 1 & \text{if } \Phi \leq 1 \\ \left(\dfrac{(\dot{m}_C \cdot \dot{Q}_{HG}^{T_g-R})_h}{\dot{Q}_{sol,net,h}}\right) & \text{if } \Phi > 1 \end{cases} \tag{14}$$

2.3. Mine-to-Tank (MTT) CO_2-e Emissions. The greenhouse gas emissions calculated for all scenarios account for all the

dx.doi.org/10.1021/ef400198v | *Energy Fuels* 2013, 27, 3538−3555

emissions associated with the predicted energy output except for the CO_2 emissions associated with fuel combustion at the point of end use and those associated with the construction of the polygeneration facility. However, the latter contribution is small over the life of the facility. The emission sources accounted for herein are those from mining the coal resource, producing FT liquid fuels by the coal-to-liquids polygeneration process, refining the synthetic fuel[11] to diesel, and all miscellaneous transportation emissions.[11]

2.4. Summary of Performance Analyses. The output parameters used to represent the energetic performance of the CTL_{sol} system were normalized with respect to the equivalent CTL_{ref} parameters. For the parameters unique to the presented CTL_{sol} polygeneration system, the following normalization methodology was adopted: (1) solar insolation and net heat rate were normalized as the ratio Φ (see eq 4), and (2) O_2 and SG_{up} tank levels were normalized with respect to hourly production rates of the reference model ASU and WGSR, respectively.

3. RESULTS

3.1. Model Verification. Table 5 compares the results of the autothermal (nonsolar) CTL_{ref} model developed for the present investigation with those reported by Meerman et al.[5] This comparison shows that all plant outputs, with the exception of the net electrical output parameter, were calculated to be within 5% of the reference values.[5] Additionally, the proportions of carbon stored in the FTL product and emitted (or stored) between the two models are exactly the same. This analysis thus validates the veracity of the autothermal CTL_{ref} model and so provides confidence that the predictions for the CTL_{sol} model are reasonable. The discrepancy between the net electrical output predicted with the CTL_{ref} model and that of Meerman[5] is attributed to differences in the assumed composition of the fuel. (As described above, the properties of coal are too complex to fully model in Aspen HYSYS, so that a much simpler composition must be assumed). An exact comparison of the two models is not possible because Meerman et al. do not report the specific composition that they assumed in their model.[5]

Table 5. Comparison of the Output from the Model for the CTL_{ref} Model with That of Meerman et al.[5] for the Same Operating Conditions at a Gasification Temperature of 1500 °C

		CTL_{ref}	Meerman et al.
O_2 (wt 100%)/coal (kg/kg)		0.90	0.88
CGE		80%	82%
H_2/CO (mol/mol)		0.45	0.47
specific energy output (HHV)	W_{net}/Q_{coal}	0.07	0.10
	Q_{FTL}/Q_{coal}	0.50	0.49
	$\eta_{th,(l)}$	0.57	0.60
carbon output as proportion of input	in FTL product (%)	37	37
	emitted or stored (%)	63*	63

3.2. CTL_{sol} System—Operation and Performance. *3.2.1. Hybrid Solar Gasifier.* Figure 6 presents the dependence of the SG_{raw} molar flow rate and the H_2/CO molar ratio on Φ, the portion of the gasifier's endothermic demand met by the net solar thermal power input to the reactor for T_g = 1100 °C. The SG_{raw} molar flow rate is shown to increase by a factor of 1.5 and the

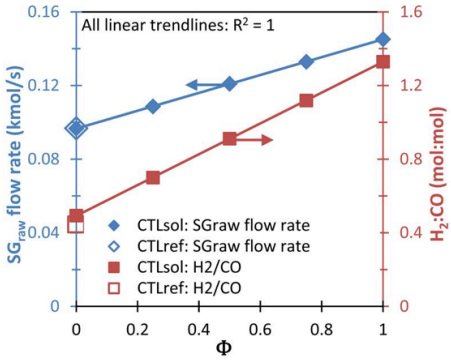

Figure 6. Dependence of the SG_{raw} molar flow rate and H_2/CO molar ratio on the solar fraction, the portion of the gasifier's endothermic demand met by the net solar thermal power input to the reactor (Φ). Assumptions: T_g = 1100 °C, P_g = 1 bar-a.

H_2/CO ratio by a factor of 2.7, as Φ is increased from 0 to 1. For Φ = 1, a syngas calorific upgrade factor of ~1.3 was calculated. Experimental studies of the solar gasification of petcoke in a vortex reactor report an upgrade factor of 1.19,[17] which is within 10% of the figure calculated with the present model. The upgrade factor calculated here is also within 10% of the values reported for other experimental analyses of the gasification of sewage sludge, albeit for different configurations. An upgrade factor of 1.16 was measured in a packed bed solar reactor,[58] while a value of 1.35 was predicted by an analytical model of the same reactor and fuel concept.[58] Although not directly comparable, this level of agreement provides further confidence in the veracity of the present results.

For Φ = 0, the SG_{raw} H_2/CO ratio is 7% higher for T_g = 1100 °C than for 1400 °C, and 10% higher than that predicted for the CTL_{ref} system with T_g = 1500 °C.[5] The anticorrelation between the H_2/CO ratio and T_g is a result of the exothermic water gas shift reaction favoring the production of H_2 at lower temperatures and CO at higher temperatures. In comparison, the CTL_{ref} scenario has a lower H_2/CO ratio because a greater portion of the coal's carbon content is consumed to deliver the process heat required to maintain the higher reactor temperatures.

3.2.2. Plant Operational Performance. The off-gas plant performance is presented for two six-day (144 h) solar insolation time-series representative of summer and winter conditions for the case A_{coll} = 63 000 m^2 and T_g = 1100 °C.

Time Resolved Plant Operation. Figure 7 presents the pseudo-dynamic response of the CTL_{sol} polygeneration system for two six-day hourly averaged time-series, calculated with a steady-state approximation. The results are presented for a representative period from a simulation of the CTL_{sol} system for a full solar year. These results are presented for a system that incorporates a pressurized O_2 storage system to reduce the production capacity of the ASU to 67% of the size of the CTL_{ref} system.

The first panel in each Figure 7A and B presents the diurnal variation in Φ for the winter and summer time-series, respectively. The second panel presents the CTL_{sol} system's hourly averaged, CTL_{ref} normalized, SG_{up} production rate $((\dot{S}G_{up})_{CTL_{sol}}/(\dot{S}G_{up})_{CTL_{ref}})$, the heating value of the FTL output $((\dot{Q}_{FTL})_{CTL_{sol}}/(\dot{Q}_{FTL})_{CTL_{ref}})$ − HHV basis) and its net electrical output $(\dot{W}_{net})_{CTL_{sol}}/(\dot{W}_{net})_{CTL_{ref}}$. The third panel of Figure 7 shows the time-history of the contemporaneous levels of stored ("stg") O_2 and SG_{up}, normalized to the CTL_{ref} system's rate of O_2 and SG_{up} production.

dx.doi.org/10.1021/ef400198v | Energy Fuels 2013, 27, 3538−3555

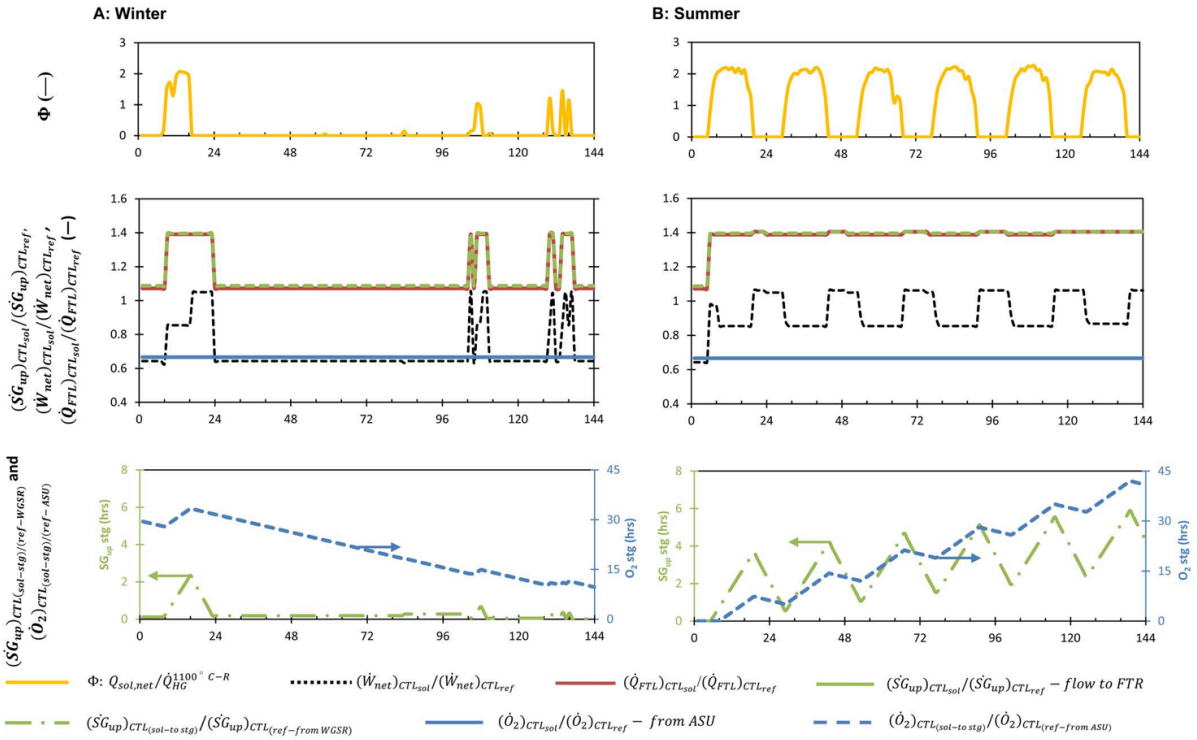

Figure 7. Time-series profile (1) of net solar thermal power input to the hybrid solar gasifier as a ratio of the power required to gasify 1 kg/s of coal at 1100 °C, (2) for the CTL_{sol} scenario: the CTL_{ref} normalized flow of upgraded syngas (SG_{up}) to the FTR; the net electrical output $(\dot{W}_{net})_{CTL_{sol}}/(\dot{W}_{net})_{CTL_{ref}}$ and the normalized HHV of the FTLs output $(\dot{Q}_{FTL})_{CTL_{sol}}/(\dot{Q}_{FTL})_{CTL_{ref}}$, and (3) of stored O_2 and SG_{up} levels normalized by the corresponding hourly rate of O_2 and SG_{up} production from ASU_{CTLref} and $WGSR_{CTLref}$. Assumptions: A_{coll} = 63 000 m^2, SG_{up} storage tank capacity equal to 8 h of SG_{up} production (see section 2.2.2 and Table 2 for details).

Figure 7B shows that the solar input through the six-day summer time-series enables a 40% increase in the steady rate of FT liquid production, relative to the CTL_{ref} system. The steady flow of SG_{up} to the FTR is shown to be maintained throughout this summer period by the storage of part of the surplus SG_{up} produced during the day and its discharge at night (see bottom panel of Figure 7B). Even during the winter time series, the availability of stored oxygen, with the tank ~30% full at the start of the time series, the FTL production rate is 9% larger than the reference system despite no solar energy being available. This result is explained by the average ratio of SG_{raw} H_2/CO being ~10% larger for the solar hybrid gasifier than for the autothermal gasifier integrated with the CTL_{ref} system (see Figure 6 above and discussion). Overall, the average calculated difference in FTL productivity was 31% larger over the summer period than the winter. Importantly, this difference in FTL productivity between the summer and winter time-series is within the bounds of good part-load performance for the FTR (up to 40% of full load[5]).

The second panel of Figure 7B shows that $(\dot{W}_{net})_{CTL_{sol}}/(\dot{W}_{net})_{CTL_{ref}}$ varies approximately in anti phase to the solar insolation. That is, $(\dot{W}_{net})_{CTL_{sol}}/(\dot{W}_{net})_{CTL_{ref}}$ increases from ~0.83 during the day to 1.02 at night. This diurnal fall in $(\dot{W}_{net})_{CTL_{sol}}/(\dot{W}_{net})_{CTL_{ref}}$ is a result of the larger syngas compression load corresponding to its solar-boosted production (see Figure 6). Figure 7A for the winter time-series shows that $(\dot{W}_{net})_{CTL_{sol}}/(\dot{W}_{net})_{CTL_{ref}}$ falls to 0.63 when solar energy is not available at all but increases from 0.85 to 1.02 in the last solar hour of the first day. The 32% difference in the six-day time-series averaged $(\dot{W}_{net})_{CTL_{sol}}/(\dot{W}_{net})_{CTL_{ref}}$ figure between the summer and winter time-series is a result of the smaller tail gas flow from the FTR to the Brayton cycle, and the lower thermal power contribution to the steam Rankine cycle from both the exothermic FTR and from cooling the solar-boosted SG_{raw} output of the hybrid solar gasifier.

Parasitic Load. Figure 8 presents the dependence of the CTL_{sol} system's CTL_{ref} normalized parasitic load $((\dot{W}_{para})_{CTL_{sol}}/(\dot{W}_{para})_{CTL_{ref}})$ on Φ. This shows that $(\dot{W}_{para})_{CTL_{sol}}/(\dot{W}_{para})_{CTL_{ref}}$ is increased by 44%, as Φ is increased from zero to unity. This increase in parasitic load is largely attributable to the compression load resulting from the solar-boosted production of syngas (see Figure 6). On its secondary axis, Figure 8 shows the dependence on Φ, of the ratio of parasitic loads for the ASU system with $(ASU_{w/stg})$ and without storage $(ASU_{w/ostg})$. The $ASU_{w/ostg}$ has a production capacity equal to the hybrid gasifier's demand for operation with Φ = 0. Specifically, Figure 8 shows that the advantage of reducing the ASU's O_2 production capacity is offset completely by the work expended to compress and store the O_2 that is not used by the hybrid gasifier, when Φ = 0.75. For Φ = 1, the parasitic load of the ASU w/stg is 10% larger than the system without storage. The net annually averaged impact on $(\dot{W}_{net})_{CTL_{sol}}$ of incorporating O_2 storage with the ASU is presented in Figure 10.

On an annually averaged basis, the syngas compression load accounts for between 52 and 54% of $(\dot{W}_{para})_{CTL_{sol}}$, for T_g = 1100 and 1400 °C, respectively. In comparison, the combined annually averaged load of the ASU and O_2 storage system was calculated

dx.doi.org/10.1021/ef400198v | *Energy Fuels* 2013, 27, 3538−3555

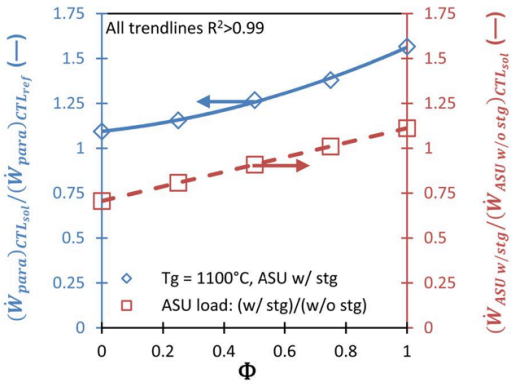

Figure 8. Dependence on the proportion of the gasifier's endothermic demand met by solar thermal power (Φ) of the CTL_{sol} system's parasitic load normalized to the CTL_{ref} system's parasitic load $-(\dot{W}_{para})_{CTL_{sol}}/(\dot{W}_{para})_{CTL_{ref}}$ on the primary axis, and on the secondary axis the ratio of the CTL_{sol} system's total ASU load for a configuration with O_2 storage ($\dot{W}_{ASUw/stg}$) and an ASU without storage ($\dot{W}_{ASUw/ostg}$). Assumptions: T_g = 1100 °C, P_g = 1 bar-a, A_{coll} = 63 000 m^2.

to account for ~26% of $(\dot{W}_{para})_{CTL_{sol}}$. The large proportional contribution of syngas compression, which is not required for the CTL_{ref} process leads to $(\dot{W}_{para})_{CTL_{sol}}$ being ~22% larger than $(\dot{W}_{para})_{CTL_{ref}}$ on an annually averaged basis. This corresponds to Φ = 0.4 in Figure 8. Here, it is worth noting that both the CTL_{sol} and CTL_{ref} systems are configured to maximize the facility's FTL output.

Fischer–Tropsch Liquids (FTL) and Electrical Plant Outputs. Figure 9 presents the CTL_{ref}-normalized output of the CTL_{sol} system gas turbine, $(\dot{W}_{GT})_{CTL_{sol}}/(\dot{W}_{GT})_{CTL_{ref}}$, and of the steam turbine: $(\dot{W}_{ST})_{CTL_{sol}}/(\dot{W}_{ST})_{CTL_{ref}}$. It also presents the CTL_{ref}-normalized FTL output on a HHV basis: $(\dot{Q}_{FTL})_{CTL_{sol}}/(\dot{Q}_{FTL})_{CTL_{ref}}$. This figure shows that $(\dot{Q}_{FTL})_{CTL_{sol}}/(\dot{Q}_{FTL})_{CTL_{ref}}$ and $(\dot{W}_{GT})_{CTL_{sol}}/(\dot{W}_{GT})_{CTL_{ref}}$ both decrease by approximately 5% for an increase in T_g from 1100 to 1400 °C. This result is explained by the SG_{raw} H_2/CO ratio being 7% larger for T_g = 1100 °C than 1400 °C. In comparison, with these findings, $(\dot{W}_{ST})_{CTL_{sol}}/(\dot{W}_{ST})_{CTL_{ref}}$ has a strongly positive relationship with T_g. This result can be explained by the dominance of the thermal output from cooling the gasifier's SG_{raw} output over the smaller beneficial exothermic contribution to the HRSG from the FTR, since the latter's productivity decreases with increased T_g. Significantly, the strong solar insolation all through the "summer" time-series leads to the six day average $(\dot{W}_{ST})_{CTL_{sol}}/(\dot{W}_{ST})_{CTL_{ref}}$ being ~28% larger than the winter time-series figure. In comparison, the summer time-series, six-day average $(\dot{W}_{GT})_{CTL_{sol}}/(\dot{W}_{GT})_{CTL_{ref}}$ and $(\dot{Q}_{FTL})_{CTL_{sol}}/(\dot{Q}_{FTL})_{CTL_{ref}}$ are ~24% larger than that calculated for the winter time-series. Interestingly, Figure 9 shows the annually averaged $(\dot{Q}_{FTL})_{CTL_{sol}}/(\dot{Q}_{FTL})_{CTL_{ref}}$ to be 14% larger than the six-day average output through the winter time-series but only 7% lower than the average output through the summer time-series.

Figure 10 presents the dependence of the CTL_{sol} system's CTL_{ref}-normalized net electrical output, $(\dot{W}_{net})_{CTL_{sol}}/(\dot{W}_{net})_{CTL_{ref}}$ on T_g. This shows that the large parasitic SG compression load leads to $(\dot{W}_{net})_{CTL_{sol}}/(\dot{W}_{net})_{CTL_{ref}}$ being less than unity for all data points presented. Interestingly, the annually averaged $(\dot{W}_{net})_{CTL_{sol}}/(\dot{W}_{net})_{CTL_{ref}}$ curve is 23% larger than the average output through the winter time-series, but only 7% smaller than the average output through the summer time-series. Figure 10 also shows that integrating the CTL_{sol} system's ASU with O_2 storage improves $(\dot{W}_{net})_{CTL_{sol}}/(\dot{W}_{net})_{CTL_{ref}}$ by ~6% over the CTL_{sol} configuration without O_2 storage, across the T_g range studied. This result brings about an important trade-off between the capital cost penalty of an oxygen compression and storage plant relative to the capital and operating cost advantages of reducing the ASU production capacity and improving the CTL_{sol} system's net electrical output. However, it is important to note that the O_2 storage system is likely to play an important role in maintaining autothermal reactions in the gasifier in response to those large fluctuations in solar insolation on the time-scale of seconds to minutes. This is discussed in section 3.2.3 below. Identifying the optimum configuration of the CTL_{sol} system's

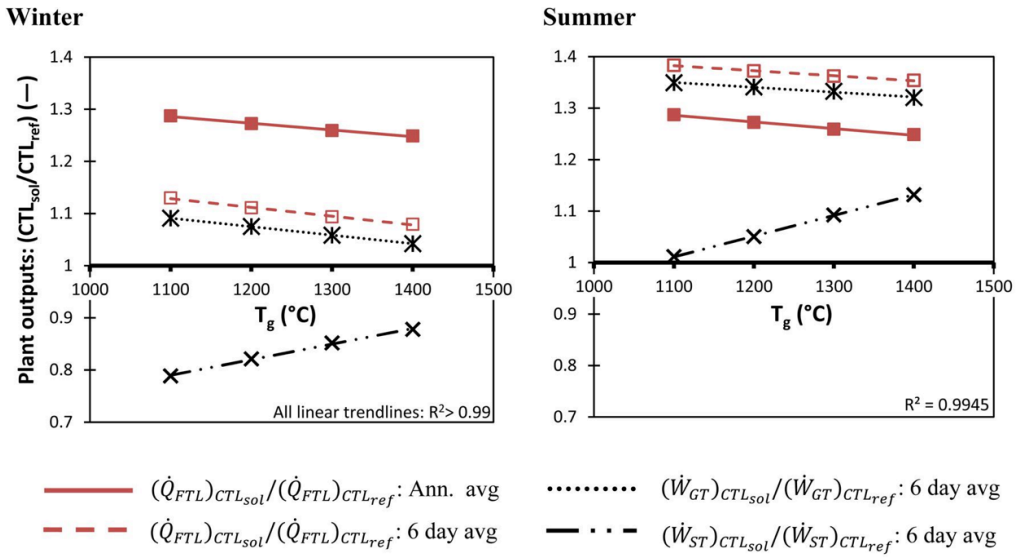

Figure 9. Dependence of the CTL_{sol} system's CTL_{ref}-normalized, gas turbine, steam turbine, and Fischer–Tropsch liquid output on gasification temperature. Assumptions: A_{coll} = 63 000 m^2, SG_{up} tank capacity equal to 8 h of SG_{up} production (see section 2.2.2 and Table 2 for details).

dx.doi.org/10.1021/ef400198v | Energy Fuels 2013, 27, 3538–3555

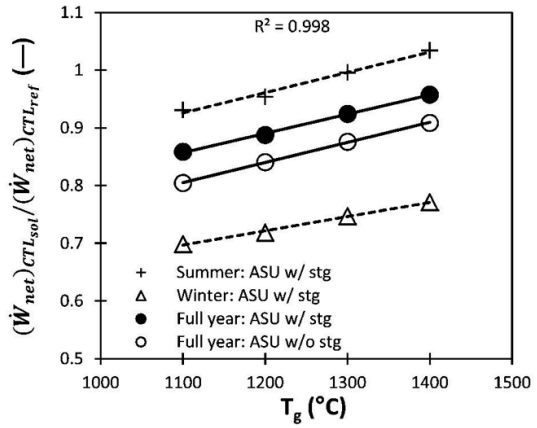

Figure 10. Dependence on gasification temperature of the CTL_{sol} system's CTL_{ref}-normalized net electrical output for scenarios incorporating an ASU with (w/) and without (w/o) O_2 storage (stg). Assumptions: A_{coll} = 63 000 m^2, SG_{up} tank capacity equal to 8 h of SG_{up} production (see section 2.2.2 and Table 2 for details).

ASU thus requires careful economic assessment on a case-by-case basis.

3.2.3. Plant Utilization Analysis. Heliostat Field. Figure 11 presents the normalized probability density distribution of the installed heliostat capacity's hourly averaged utilization ($\bar{U}_{A_{coll},h}$) for four A_{coll} scenarios. These probabilities were calculated only for the cases when the solar input to the reactor exceeds the minimum threshold to make a contribution, i.e. when the shutter is open, $\eta_{abs} > 0$, to avoid the large nocturnal peak that would otherwise dominate the figure. This figure illustrates that the highest peak in the distribution corresponds to full utilization of the installed heliostat collection capacity, i.e., $\bar{U}_{A_{coll},h} = 1$. These periods of full utilization occur when $0 < \Phi \leq 1$ and can thus be attributed largely to solar hours in winter and at dusk/dawn, when insolation is inherently low (see Figure 7). However, the area under this part of the curve is low. Figure 11 also shows a lower but more significant peak in the distribution when the hourly averaged heliostat capacity utilization is between 46% for A_{coll} = 38 000 m^2 and 78% for A_{coll} = 63 000 m^2. This peak corresponds to periods of high solar insolation, when the solar energy that is available outstrips the hybrid gasifier's endothermic demand. Further, as the hybrid gasifier is assumed to be operated with a constant coal feed rate to the gasifier, the prominence of this dominant peak grows exponentially with increasing A_{coll}. For A_{coll} = 38 000 m^2, the annually averaged heliostat utilization is approximately 92%, while for A_{coll} = 63 000 m^2, the annually averaged utilization is only 67%.

O_2 Storage System. The hourly averaged variation in solar resource assessed here is sufficient to estimate the output and greenhouse gas emissions from the process but insufficient to address issues of operation and control. In practice, a control system should be able to provide rapid changes in the O_2 flow to the gasifier in response to significant changes in insolation on the time scale of seconds to minutes to maintain autothermal reactions and a constant reactor temperature. The proposed system offers the potential to achieve this through the storage of O_2 at 60 bar-a. Figure 12 shows that the stored level of O_2 is greater than 20% of capacity (~50 h of storage) for the majority of the hours in the year. In addition, for 99.9% of the hours of the year, the tank has a stored level of O_2 equal to at least 1% (~0.5 h

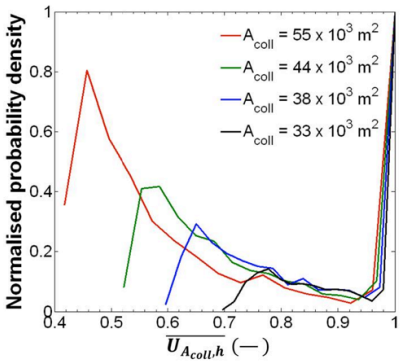

Figure 11. Normalized probability density distribution of the installed heliostat capacity's hourly averaged utilization ($\bar{U}_{A_{coll},h}$) for four heliostat collector area scenarios (A_{coll}). Assumptions: T_g = 1100 °C and P_g = 1 bar-a.

of storage) of its capacity. Furthermore, because the operation of the ASU at 1.4 bar-a allows 0.4 bar over the pressure of the hybrid reactor, it is anticipated to enable a continuous supply to be maintained at other times. Hence the response time of the system will be limited by the control system rather than by the pressure of the storage.

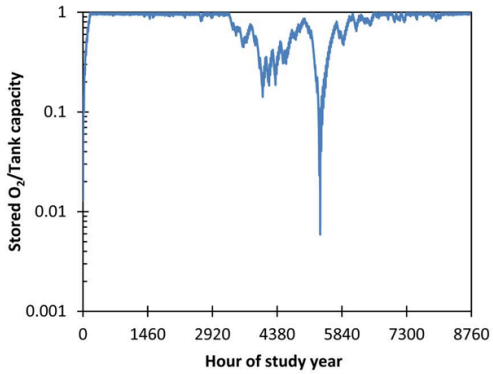

Figure 12. Hourly averaged stored oxygen level as a proportion of tank capacity (tick marks every two months).

SG_{up} Storage System. Figure 13 presents on a logarithmic scale the normalized probability distribution of the hourly averaged utilization of the SG_{up} storage tank ($\bar{U}_{SG_{up}stg,h}$) for three scenarios of tank capacity equal to 4, 8, and 16 h of SG_{up} production (see section 2.2.2 and Table 2 for details). It can be seen that the utilization of the SG_{up} storage tank is generally low, decreasing from only 26% for 4 h of storage down to some 13% for 16 h of storage. Specifically, the proportion of hours for which the tank was calculated to be less than 20% full was 51% for the 4 h storage scenario, 67% for the 8 h storage scenario, and 85% for the 16 h storage scenario.

Figure 14 presents the annually averaged utilization of the SG_{up} storage tank (primary axis) and variance in the normalized SG_{up} flow to the FTR (secondary axis) as a function of the number of hours of SG_{up} storage. The figure shows $\bar{U}_{SG_{up}stg,ann}$ to decrease from 25% for the 4 h of storage scenario to 12% for the 16 h of storage scenario by a power law relationship.

dx.doi.org/10.1021/ef400198v | *Energy Fuels* 2013, 27, 3538−3555

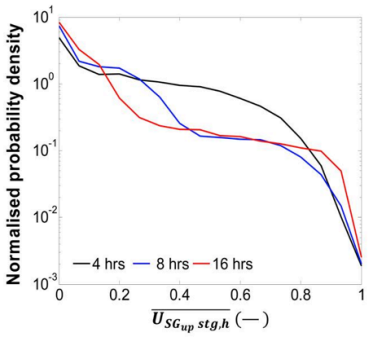

Figure 13. Normalized probability density distribution of the calculated hourly averaged utilization of the SG_{up} storage tank ($\overline{U}_{SG_{up}stg,h}$), for the entire study year for three tank capacity scenarios. Tank capacities are equal to 4, 8, and 16 h of SG_{up} production (see section 2.2.2 and Table 2 for details). Assuming A_{coll} = 63 000 m^2.

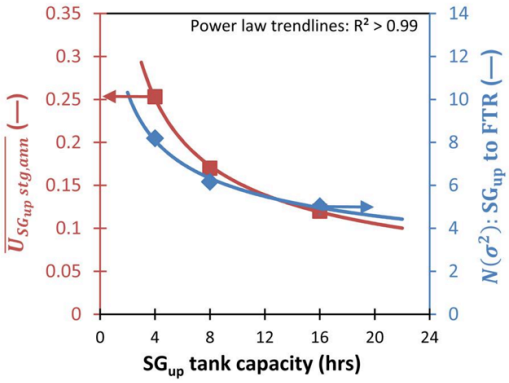

Figure 14. Dependence on SG_{up} storage tank capacity of the annually averaged utilization of the SG_{up} storage tank on the primary axis and on the secondary axis the variance in the SG_{up} flow to the Fischer–Tropsch reactor (from the tank and the WGSR) normalized to the minimum SG_{up} flow rate to the FTR. Assumed tank capacities for CTL_{sol} system are equal to 4, 8, and 16 h of SG_{up} production (see section 2.2.2 and Table 2 for details).

The secondary axis of the figure shows that the variance in the SG_{up} in-flow to the FTR decreases by 40% with an increase in storage from 4 to 16 h of storage, as expected. This result is also consistent with the lower utilization described above.

Larger variance in the SG_{up} flow to the FTR and the long-term cyclical loading of the FTR may have a detrimental impact on product quality and thereby increase the costs of plant maintenance. This observation is guided by the likelihood of a reactor that can feasibly operate at unsteady load being inevitably more complex than a reactor that operates with a steady load.[59] Hence, the present analysis has identified a potentially important economic trade-off between the capital cost impacts of increased storage capacity and the potential operational and thus capital utilization impacts of ensuring reliable operation of the FTR on the viability of the CTL_{sol} system.

Table 6 presents a comparative analysis of the impact of SG_{up} storage on the annually averaged utilization of the CTL_{sol} system's FTR, gas turbine plant (GT), and steam cycle unit operations, $\overline{U}_{ann}$ (see eq 12). Also shown is the annual, minimum turn-down for these unit operations (TD_{min}), calculated as a ratio of the plant output for any two contiguous hours of operation

Table 6. Presents for the CTL_{sol} System, Fischer–Tropsch Reactor, Gas Turbine and Steam Cycle, the Annually Averaged Plant Utilization ($\overline{U}_{ann}$) and the Annual, Minimum Plant Turndown (TD_{min})[a]

	with SG_{up} storage		without SG_{up} storage	
unit operation	$\overline{U}_{ann}$	TD_{min}	$\overline{U}_{ann}$	TD_{min}
Fischer–Tropsch reactor	92%	0.77	78%	0.66
Gas turbine	92%	0.76		
Steam Rankine cycle	84%	0.68		

[a]Assumptions: A_{coll} = 63 × 10^3 m^2, CTL_{sol} system SG_{up} tank capacity equal to 8 h of SG_{up} production (see section 2.2.2 and Table 2 for details).

(see eq 13). These results show that integration of a SG_{up} storage system increases the $\overline{U}_{ann}$ of the FTR and GT system by 18% and their TD_{min} by 17%. For the steam cycle, the integration of a SG_{up} storage system increases its $\overline{U}_{ann}$ by 8% and the TD_{min} by 4%. The calculated increases in the steam cycle's $\overline{U}_{ann}$ and TD_{min} are lower than that estimated for the FTR and GT unit operations because the steam cycle's output is linked to thermal flow of cooling the hybrid gasifier's SG_{raw} output, which is not stored (see Figure 1). Conversely, the steam cycle, for the system which incorporates SG_{up} storage, has a larger U_{ann} and TD_{min} than for the configuration without SG_{up} storage. This is because its electrical output is also coupled to the exothermic output of the FTR and thus the SG_{up} storage system.

Importantly, the TD_{min}'s of the unit operations shown in Table 6 are within the bounds of technically feasible operation for these plant components.[5,54,60] This implies that all unit operations of the CTL_{sol} system, except the solar hybrid gasifier, could be procured and constructed using plants that are commercially available and thus have proven operational reliability.[5] Both the CTL_{sol} and CTL_{ref} systems are assumed to have the same periods of scheduled and unscheduled shutdowns. These details are presented in Table 6, which also reports the reduction in the utilization of the listed CTL_{sol} plant components relative to the 100% assumed utilization of the equivalent CTL_{ref} components.

3.2.4. Annually Averaged Plant Performance. Fischer–Tropsch Liquids and Net Electrical Output. Figure 15 presents the percentage change in the specific thermal FTL output of the CTL_{sol} system (HHV) – $(\dot{Q}_{FTL}/\dot{Q}_{coal})_{CTL_{sol}}$ relative to the CTL_{ref} system and the percentage change in the specific total energetic

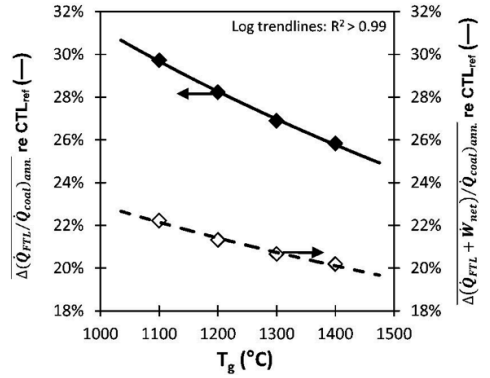

Figure 15. Dependence on gasification temperature of the percentage increase in the CTL_{sol} system's annually averaged FTL output (primary axis) and total energetic output (secondary axis) (HHV) relative to the autothermal CTL_{ref} system. Assumptions: P_g = 1 bar-a, A_{coll} = 63 × 10^3 m^2, CTL_{sol} system SG_{up} tank capacity equal to 8 h of SG_{up} production (see section 2.2.2 and Table 2 for details).

dx.doi.org/10.1021/ef400198v | *Energy Fuels* 2013, 27, 3538–3555

output $((\dot{W}_{FTL} + \dot{Q}_{FTL})/\dot{Q}_{coal})_{CTL_{sol}}$ as a function of T_g. For T_g = 1400 °C, the CTL_{sol} system's FTL productivity was estimated to increase by 26% from $(\dot{Q}_{FTL}/\dot{Q}_{coal})_{CTL_{sol}}$ = 0.49, while the total energetic productivity is improved by approximately 20% from $((\dot{W}_{net} + \dot{Q}_{FTL})/\dot{Q}_{coal})_{CTL_{ref}}$ = 0.57. This difference in the relative improvement in the FTL and total energetic output can be partly explained by a decrease of 4% in $(\dot{W}_{net}/\dot{Q}_{coal})_{CTL_{sol}}$ relative to the CTL_{ref} system for T_g = 1400 °C (see Figure 10). Figure 15 also shows that the percentage change in $(\dot{Q}_{FTL}/\dot{Q}_{coal})_{CTL_{sol}}$ relative to the CTL_{ref} system increases from 26% to 30% with a decrease in T_g from 1400 to 1100 °C. In comparison, the percentage improvement in $((\dot{W}_{net} + \dot{Q}_{FTL})/\dot{Q}_{coal})_{CTL_{ref}}$ is only 2% over the same range of T_g. Interestingly, the two curves shown in Figure 15 are not parallel, this is because the solar system's net electrical productivity increases with T_g (see Figure 9) while the FTL productivity decreases. The parasitic impact of the CTL_{sol} system's large SG_{raw} compression load on the system's total energetic output is mitigated by the configuration being optimized to maximize the production of FTL. This operational regime for the CTL_{sol} system leads to the electrical output accounting for only ~15% of the system's total energetic output.

Figure 16 is similar to Figure 15 except that it presents the dependence of the above parameters on the normalized heliostat collection capacity $(\Phi_{peak}^{A_{coll}} - 1)$—see eq 5. Figure 16 shows that the CTL_{sol} system's total energetic output increases by 22% for $(\Phi_{peak}^{63000m^2} - 1)$ = 1.4 and T_g = 1100 °C, relative to the autothermal CTL_{ref} system. Importantly, the specific FTL heating value and total energetic productivity of the CTL_{sol} system are shown to be insensitive to the heliostat collection capacity. This insensitivity is explained by the assumed operation of the hybrid gasifier with a coal feed rate that is invariant with the amount of solar thermal power available. It should be noted that the CTL_{sol} system's energetic performance can be improved by flexibly increasing the coal feed rate to the hybrid gasifier, when sufficient solar thermal power is available, i.e. $\Phi > 1$.[51] This would enable the CTL_{sol} system to improve the process' solar share and also the annually averaged utilization of the heliostat collection capacity.

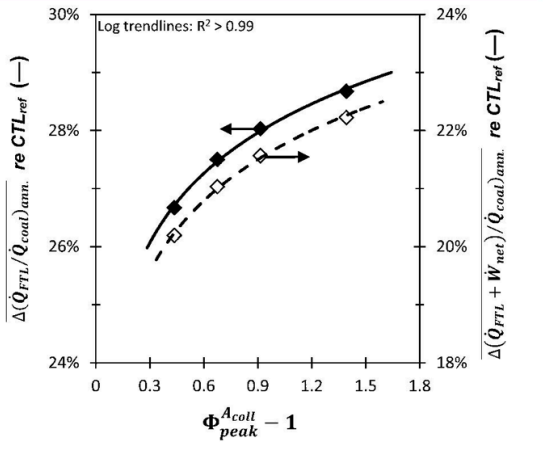

Figure 16. Dependence on the normalized heliostat collection area of the percentage change in the CTL_{sol} system's annually averaged FTL productivity (primary axis) and total energetic output (secondary axis) (HHV) relative to the autothermal CTL_{ref} system. Assumptions: T_g = 1100 °C, P_g = 1 bar-a, A_{coll} = 63 000 m^2, CTL_{sol} system SG_{up} tank capacity equal to 8 h of SG_{up} production (see section 2.2.2 and Table 2 for details).

Greenhouse Gas Emissions. Figure 17 presents the dependence of the CTL_{sol} system's mine-to-tank (MTT) CO_2-e emissions on T_g while Figure 18 shows its dependence on $\Phi_{peak}^{A_{coll}} - 1$. Both figures reveal a logarithmic dependence of ($R^2 > 0.99$) the absolute (primary axis) and the percentage change in MTT emissions relative to the autothermal CTL_{ref} system. Figure 17 shows that solar hybridization enables a 30% decrease in CO_2-e emissions on a mine-to-tank basis for T_g = 1400 °C to ~76 kg CO_2-e/GJ $(Q_{FTL} + W_{net})$ relative to the autothermal CTL_{ref} system. Over the range of T_g reported here, the percentage change in emissions is shown to vary by ~2%, which in absolute terms is approximately ~4 kg CO_2-e/GJ $(Q_{FTL} + W_{net})$. Figure 18 shows that the CTL_{sol} system's emissions performance increases only slightly as the heliostat collection capacity is increased from 38 000 to 63 000 m^2. This result is explained by the assumed operation of the hybrid gasifier with a constant coal flow rate, which is invariant with the amount of solar thermal power available.

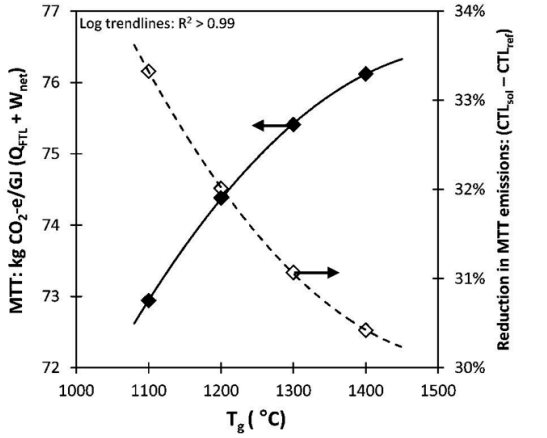

Figure 17. Dependence on gasification temperature of the CTL_{sol} system's annually averaged mine-to-tank (MTT) CO_2-e emissions (primary axis) and the percentage decrease in emissions relative to the CTL_{ref} system (secondary axis). Assumptions: A_{coll} = 63 000 m^2, SG_{up} tank capacity equal to 8 h of SG_{up} production (see section 2.2.2 and Table 2 for details).

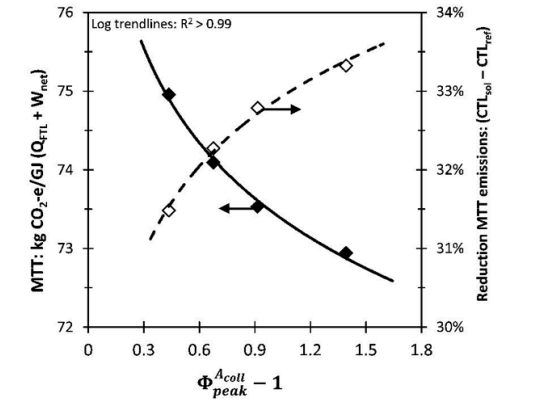

Figure 18. Dependence on the normalized size of the heliostat array of the CTL_{sol} system's annually averaged mine-to-tank (MTT) CO_2-e emissions (primary axis) and the percentage decrease in emissions relative to the CTL_{ref} system (secondary axis). Assumptions: A_{coll} = 63 000 m^2, SG_{up} tank capacity equal to 8 h of SG_{up} production under autothermal conditions (see section 2.2.2 and Table 2 for details).

dx.doi.org/10.1021/ef400198v | *Energy Fuels* 2013, 27, 3538–3555

The CTL_{sol} system's tank-to-wheel (TTW) emissions were estimated to be 63 kg CO_2-e/GJ ($Q_{FTL} + W_{net}$) (HHV basis). This value was found not to vary appreciably across the scenarios studied. To decrease the CTL_{sol} system's MTT emissions performance to below the well-to-tank emissions of all mineral crude currently in production (8 kg CO_2-e/GJ diesel),[11] it is necessary to sequester approximately 58 kg CO_2-e/GJ ($Q_{FTL} + W_{net}$). This is approximately 33% less than the 91 kg CO_2-e/GJ ($Q_{FTL} + W_{net}$) that would need to be sequestered to achieve the same outcome for the autothermal CTL_{ref} system. Further reductions in mine-to-wheel CO_2-e emissions can be achieved by blending the coal with biomass and/or by incorporating natural gas. These options are explored further by Kaniyal et al. in a recently published paper.[51]

Table 7 presents the carbon balance for the autothermal CTL_{ref} system relative to the CTL_{sol} systems for two T_g scenarios. These data show that the solar hybrid gasification process enables a 23−26% increase in the fraction of the coal's carbon content that is converted usefully into fuel relative to the conventional, autothermal entrained flow gasification process. Consistently, the solar hybridized gasification process also decreases by the same amount the carbon that is parasitically consumed to deliver process heat. These results are thus consistent with other findings in this paper that the CTL_{sol} system lowers carbon emissions of producing liquid fuels by the chemical storage of solar energy in the end product. This is in contrast with the strategy of increasing electricity generation relative to the production of the higher value FT liquids production, which has been proposed by previous studies to reduce the CTL polygeneration system's net mine-to-wheel emissions.[1,4,5,18]

Table 7. The Distribution of Carbon from the Original Fuel That Is in the Product or Is Parasitically Consumed in the Process for the CTL_{sol} System and the Autothermal CTL_{ref} System[a]

	CTL_{sol}		CTL_{ref}
gasification temperature (T_g)	1100 °C	1400 °C	1500 °C
carbon in FTL product	47%	46%	38%
carbon consumed in process	53%	54%	62%

[a]Assumptions: CTL_{sol} scenarios based on A_{coll} = 63 000 m^2, 8 h of SG_{up} production (see section 2.2.2 and Table 2 for details).

4. CONCLUSIONS

The incorporation of concentrated solar thermal radiation into the autothermal coal gasification process is found to significantly improve the energetic and GHG emissions performance of the process. It is found that solar resource transience can be accommodated effectively into plant operation by the novel introduction of the pressurized storage of both O_2 and the upgraded (clean) syngas. This conclusion is derived from a pseudodynamic model incorporating a year long, hourly averaged solar insolation time-series for the solar resource of Farmington, New Mexico (37 °N).

The proposed CTL_{sol} system was estimated to improve, on an annually averaged basis, the energetic productivity of the autothermal CTL_{ref} system by 21%, assuming equilibrium gasification conditions of 1400 °C and 1 bar-a. This enabled an estimated 30% reduction in the CTL_{ref} system's mine-to-tank (MTT) CO_2-e emissions under the same conditions. This reduction in MTT CO_2-e emissions was found to increase by ∼3 percentage points if the equilibrium gasification temperature was decreased from 1400 to 1100 °C. However, further work is required to verify whether, and for which fuels, a gasification temperature of 1100 °C can be achieved without suboptimal carbon conversion rates. This is an important consideration assuming the solar hybrid gasifier has a similar cost profile to the nonsolar, autothermal entrained flow gasifier, which forms the single largest cost component of a CTL polygeneration system.

To match the well-to-tank emissions of 18 kg CO_2-e/GJ for conventional mineral crude, the CTL_{sol} process MTT emissions would need to be reduced by an additional 57 kg CO_2-e/GJ ($Q_{FTL} + W_{net}$) (e.g., by biomass cogasification, carbon capture, and storage). In comparison, the CTL_{ref} process MTT emissions would need to be reduced by a further 91 kg CO_2-e/GJ ($Q_{FTL} + W_{net}$) to achieve the same outcome. Importantly, the solar integrated system was shown to enable the storage of 21% more carbon (as CO_2) in the FTL products than the CTL_{ref} system. These benefits are possible because the solar hybridized gasification process decreases by 17% the parasitic consumption of carbon through the autothermal reactions, thereby making available more of the coal's carbon content for liquids production.

The pressurized storage of O_2 was shown to enable the CTL_{sol} system to feasibly reduce the required capacity of the ASU and thereby increase the annually averaged net electrical output of the process by approximately 6%, to 96% of the autothermal CTL_{ref} system's output, for gasification temperatures of 1400 °C. Here, it is worth noting that the CTL_{sol} system's annually averaged parasitic load is 22% larger than that of the CTL_{ref} and that ∼53% of this parasitic load is attributed to compressing the syngas from the atmospheric pressure of the gasifier. Nonetheless, the influence of syngas compression on the CTL_{sol} system's total energetic output is limited when maximizing FTL production, leading to it comprising ∼85% of the total net energetic output.

The pressurized storage of upgraded syngas was shown to improve the annually averaged capital utilization of the Fischer−Tropsch reactor and gas turbine unit operations by 18% over the configuration without storage and improve by 8% the annually averaged utilization of the HRSG and steam Rankine cycle. The storage of the upgraded syngas was also shown to allow the variation in throughput of each unit of process equipment to be maintained within normal operational ranges[5,54,60] despite the diurnal and stochastic fluctuations in solar insolation. This means that no units of the polygeneration process plant require further development, except for the hybrid solar gasification reactor, which has presently only been demonstrated on a small scale and only for stand-alone solar operation.[16,17,39]

As expected, increasing the heliostat field collection area from 38 000 to 63 000 m^2 was shown to decrease the mine-to-tank CO_2-e emissions logarithmically. However, the environmental benefit of increasing A_{coll} above 38 000 m^2 was found to be small, at least for the case of a constant feed rate of coal. The large capital outlay associated with the heliostat array[19,35] highlights the need for economic optimization on a case-by-case basis.

Finally, it is important to note that there are many options to enable further reductions in the CTL_{sol} process mine-to-tank CO_2-e emissions over those identified herein. These include variation of the reactor pressure, flexibility to vary the fuel flow rate in response to transience in solar insolation, the incorporation of natural gas reforming, and the blending of coal with biomass.[51]

■ AUTHOR INFORMATION

Corresponding Author

*Phone: +61403691321. E-mail: ashok.kaniyal@adelaide.edu.au.

Notes

The authors declare no competing financial interest.

■ ACKNOWLEDGMENTS

A.A.K. would like to thank Ricoh for providing the Clean Energy Scholarship. P.J.v.E. would like to acknowledge the support of the Australian Solar Institute (ASI) for providing a postdoctoral fellowship. The Australian Government, through the ASI, is supporting Australian research and development in solar photovoltaic and solar thermal technologies to help solar power become cost competitive with other energy sources. G.J.N. wishes to thank the Australian Research Council (ARC) for the Discovery Outstanding Researcher Award used to support this work. The authors gratefully acknowledge the financial and other support received for this research from the Energy Pipelines Cooperative Research Centre (EPCRC) which was established under the Australian Government's Cooperative Research Centre's program.

■ NOMENCLATURE

A_{coll} = heliostat collection area (m^2)
ASU w/o stg = air separation unit without an oxygen storage system
ASU w/stg = air separation unit with a pressurized oxygen storage system
$\tilde{C}$ = solar mean flux concentration ratio
CTL = coal-to-liquids polygeneration system
CGE = cold gas efficiency (%)
CO_2-e = CO_2 equivalent emissions
d.a.f. = dry, ash-free basis
FT = Fischer–Tropsch synthesis process
FTL = Fischer–Tropsch liquid fuels
FTR = Fischer–Tropsch reactor
GHG = greenhouse gas emissions
HP = high pressure (steam)
HRSG = heat recovery steam generation
I = direct normal solar insolation (W/m^2)
$\dot{W}$ = electrical work load or output (kW)
IP = intermediate pressure (steam)
HHV = lower heating value (kJ/kg)
LP = low pressure (steam)
mol % = molar fraction
NSRDB = National Solar Radiation Database (U.S. DOE NREL)
O_2 = 94.3 mol % O_2 (unless stated otherwise)
$\dot{Q}$ = thermal heat flow rate
SG = syngas
MTT = mine-to-tank GHG emissions
t = time in hours
TD = turn-down of a component of the CTL plant for operation between two contiguous hours
T_g = gasification reactor temperature (°C)
wt % = weight percent
S = pressurized gas storage system, compressor, and tank
(S)WGS(R) = (sweet) water gas shift (reactor)
U = capital utilization

Greek Letters

η = efficiency
Φ = ratio of the net solar thermal power output from the heliostat array ($\dot{Q}_{sol,net}$) to the total endothermic demand of completely gasifying 1 kg/s of dry coal at T_g ($\dot{Q}^{T_g-R}_{HG,(NGR)}$; see eq 4)
$N(\sigma^2)$ = normalized variance (statistical)
$\Phi^{A_{coll}}_{peak} - 1$ = fraction by which the annual peak net solar thermal power output of the heliostat array exceeds the gasifier's total endothermic demand
σ = Stefan–Boltzmann constant ($J/m^2\ s\ K^4$)

Superscripts

T_g–R = temperature at which gasification reactions occur

Subscripts

abs = solar energy absorption efficiency
ann = parameter based on year-long time-series
avg = average
cap = capacity
FTL = Fischer–Tropsch liquids
GT = gas turbine (Brayton) cycle
HG = hybrid solar gasifier
isen = isentropic efficiency of compressors/turbines
min = minimum
net = net (of parasitic losses) electrical output or flow of thermal power from the heliostat field to the solar hybrid reactor (net of optical and reradiation losses)
peak = maximum value in the year-long time series
opt = optical (e.g., re efficiency of the heliostat array)
raw = syngas output direct from the gasifier
ref = autothermal, reference CTL polygeneration system
stg = stored levels of O_2 and SG_{up} (subscript)
sol = solar
ST = steam
total = endothermic load of the complete gasification of dry coal fed at 1 kg/s
SG_{up} = upgraded syngas
up = upgraded syngas output from the sweet WGSR (H_2/CO = 2.26)
wall = heat losses through the walls of the entrained flow gasifier
Φ = see Greek letters

■ REFERENCES

(1) Adams, T., II; Barton, P. Combining coal gasification and natural gas reforming for efficient polygeneration. *Fuel Process. Technol.* **2011**, *92*, 639–55.
(2) Apt, J.; Newcomer, A.; Lave, L.; Douglas, S.; Dunn, L. *An Engineering-Economic Analysis of Syngas Storage*; NETL: Pittsburgh, PA, 2008.
(3) Bell, D.; Towler, B. *Coal Gasification and Its Applications*. Elsevier: Oxford, U. K., 2011.
(4) Kreutz, T.; Larson, E.; Liu, G.; Williams, R. Fischer–Tropsch Fuels from Coal and Biomass, 25th Ann. Intl Pittsburgh Coal Conference, Pittsburgh, Pennsylvania, PA, 2008.
(5) Meerman, J.; Ramirez, A.; Turkenburg, W.; Faaij, A. Performance of simulated flexible integrated gasification polygeneration facilities. Part A: A technical-energetic assessment. *Renew. Sustain. Energy Rev.* **2011**, *15*, 2563–87.
(6) van Vliet, O.; Faaij, A.; Turkenburg, W. Fischer–Tropsch diesel production in a well-to-wheel perspective: A carbon, energy flow and cost analysis. *Energy Convers. Manage.* **2009**, *50*, 855–76.
(7) Woods, M.; Capicotto, P.; Haslbeck, J.; Kuehn, N.; Matuszewski, M.; Pinkerton, L.; Rutkowski, M.; Schoff, R. *Bituminous coal and natural gas to electricity final report, DoE/NETL –2007/1281*; U. S. DOE: Washington, DC, 2007; Vol. *1*.
(8) Chen, Y.; Adams, T., II; Barton, P. Optimal design and operation of flexible energy polygeneration systems. *Ind. Eng. Chem. Res.* **2011**, *50* (8), 4553–66.
(9) Larson, E.; Fiorese, G.; Liu, G.; Williams, R.; Kreutz, T.; Consonni, S. Co-production of decarbonized synfuels and electricity from coal + biomass with CO2 capture and storage: an Illinois case study. *Energy Environ. Sci.* **2010**, *3*, 28–42.

(10) Lattanzio, R. *Canadian Oil Sands: Life-Cycle Assessments of Greenhouse Gas Emissions*; Congressional Research Service: Washington D.C., 2012; p 31.
(11) Gerdes, K. *An evaluation of the extraction, transport and refining of imported crude oils and the impact on life cycle greenhouse gas emissions*; NETL: Pittsburgh, PA, 2009; p 42.
(12) Kodama, T. High-temperature solar chemistry for converting solar heat to chemical fuels. *Prog. Energy Combust. Sci.* **2003**, *29* (6), 567−97.
(13) Piatkowski, N.; Steinfeld, A. Solar-driven coal gasification in a thermally irradiated packed-bed reactor. *Energy Fuels* **2008**, *22* (3), 2043−2052.
(14) Piatkowski, N.; Wieckert, C.; Weimer, A.; Steinfeld, A. Solar-driven gasification of carbonaceous feedstock - a review. *Energy Environ. Sci.* **2011**, *4*, 73−82.
(15) Steinfeld, A.; Palumbo, R. Solar thermochemical process technology. In *Encyclopedia of Physical Science & Technology*; Meyers, R., Ed.; Academic Press: New York, 2001; Vol. *15*, pp 237−56.
(16) Z'Graggen, A.; Haueter, P.; Maag, G.; Vidal, A.; Romero, M.; Steinfeld, A. Hydrogen production by steam-gasification of petroleum coke using concentrated solar power - III. Reactor experimentation with slurry feeding. *Int. J. Hydrogen Energy* **2007**, *32*, 992−6.
(17) Z'Graggen, A.; Steinfeld, A. Hydrogen production by steam-gasification of carbonaceous materials using concentrated solar energy - V. Reactor modeling, optimization and scale-up. *Int. J. Hydrogen Energy* **2008**, *33* (20), 5484−5492.
(18) Liu, G.; Larson, E.; Williams, R.; Kreutz, T.; Guo, X. Making Fischer−Tropsch fuels and electricity from coal and biomass: performance and cost analysis. *Energy Fuels* **2011**, *25*, 415−37.
(19) Sudiro, M.; Bertucco, A. Synthetic fuels by a limited CO2 emission process which uses both fossil and solar energy. *Energy Fuels* **2007**, *21*, 3668−75.
(20) Baykara, S.; Bilgen, E. Synthesis gas and H2 production from solar gasification of Albertan coal. *Energy Convers. Manage.* **1985**, *25* (4), 391−398.
(21) Osinga, T.; Olalde, G.; Steinfeld, A. Solar carbothermal reduction of ZnO: shrinking packed-bed reactor modeling and experimental validation. *Ind. Eng. Chem. Res.* **2004**, *43*, 7981−8.
(22) Ingle, G.; Levy, M.; Gordon, J. Gasification of oil shales by solar energy. *Sol. Energy Mater.* **1991**, *24*, 478−89.
(23) Kodama, T.; Kondoh, T.; Tamagawa, T.; Funatoh, A.; Shimizu, K.-I.; Kitayama, Y. Fluidized bed coal gasification with CO2 under direct irradiation with concentrated visible light. *Energy Fuels* **2002**, *16*, 1264−70.
(24) Müller, R.; von Zedtwitz, P.; Wokaun, A.; Steinfeld, A. Kinetic investigation on steam gasification of charcoal under direct high-flux irradiation. *Chem. Eng. Sci.* **2003**, *58*, 5111−9.
(25) Murray, J.; Fletcher, E. Reaction of steam with cellulose in a fluidized bed using concentrated sunlight. *Energy* **1994**, *19*, 1083−98.
(26) van Heek, K. H. General aspects and engineering principles for technical application of coal gasification. In *Carbon and Coal Gasification*; Figueiredo, J. L., Ed.; NATO ASI Series, Springer: New York, 1986; pp 383−411.
(27) Melchior, T.; Perkins, P.; Lichty, A.; Weimer, A.; Steinfeld, A. Solar-driven biochar gasification in a particle-flow reactor. *Chem. Eng. Proc.* **2009**, *48*, 1279−87.
(28) Service, R. Biomass fuel starts to see the light. *Science* **2009**, *326* (5959), 1474.
(29) Z'Graggen, A.; Haueter, P.; Trommer, D.; Romero, M.; de Jesus, J.; Steinfeld, A. Hydrogen production by steam-gasification of petroleum coke using concentrated solar power—II Reactor design, testing, and modeling. *Int. J. Hydrogen Energy* **2006**, *31*, 797−811.
(30) Z'Graggen, A.; Steinfeld, A. A two-phase reactor model for the steam-gasification of carbonaceous materials under concentrated thermal radiation. *Chem. Eng. Proc.* **2008**, *47*, 655−62.
(31) Z'Graggen, A.; Steinfeld, A. Heat and mass transfer analysis of a suspension of reacting particles subjected to concentrated solar radiation − Application to the steam-gasification of carbonaceous materials. *Int. J. Heat Mass Transfer* **2009**, *52*, 385−95.
(32) Kogan, A.; Kogan, M. The tornado flow configuration - an effective method for screening of a solar reactor window. *J. Solar Energy Eng.* **2002**, 206−14.
(33) Steinfeld, A. Solar thermochemical production of hydrogen - a review. *Solar Energy* **2005**, *78* (5), 603−15.
(34) Hirsch, D.; Epstein, M.; Steinfeld, A. The solar thermal decarbonisation of natural gas. *Int. J. Hydrogen Energy* **2001**, *26*, 1023−33.
(35) Meier, A.; Gremaud, N.; Steinfeld, A. Economic evaluation of the industrial solar production of lime. *Energy Convers. Manage.* **2005**, *46*, 905−26.
(36) Möller, S.; Kaucic, D.; Sattler, C. Hydrogen production by solar reforming of natural gas: a comparison study of two possible process configurations. *J. Solar Energy Eng.* **2006**, *128* (1), 16−23.
(37) Spath, P.; Amos, W. Using a concentrating solar reactor to produce hydrogen and carbon black via thermal decomposition of natural gas: feasibility and economics. *J. Solar Energy Eng.* **2003**, *125*, 159−64.
(38) Romero, M.; Steinfeld, A. Concentrating solar thermal power and thermochemical fuels. *Energy Environ. Sci.* **2012**, *5*, 9234−45.
(39) Z'Graggen, A.; Haueter, P.; Maag, G.; Romero, M.; Steinfeld, A. Hydrogen production by steam-gasification of carbonaceous materials using concentrated solar power - IV. Reactor experimentation with vacuum residue. *Int. J. Hydrogen Energy* **2008**, *33*, 679−84.
(40) Kribus, A.; Zaibel, R.; Carey, D.; Segal, A.; Karni, J. A solar-driven combined cycle power plant. *Sol. Energy* **1998**, *62* (2), 121−9.
(41) Nathan, G.; Battye, D.; Ashman, P. Economic evaluation of a novel fuel-saver hybrid combining a solar receiver with a combustor for a solar power tower. *Appl. Energy* **2012**, Submitted.
(42) Ordorica-Garcia, G.; Delgado, A.; Garcia, A. Novel integration options of concentrating solar thermal technology with fossil-fuelled and CO2 capture processes. *Energy Procedia* **2011**, *4*, 809−16.
(43) Sheu, E.; Mitsos, A.; Eter, A.; Mokheimer, E.; Habib, M.; Al-Qutub, A. A review of hybrid solar-fossil fuel power generation systems and performance metrics. *J. Solar Energy Eng.* **2012**, 134.
(44) Newcomer, A.; Apt, J. Storing syngas lowers the carbon price for profitable coal gasification. *Environ. Sci. Technol.* **2007**, *41*, 7974−79.
(45) Z'Graggen, A.; Haueter, P.; Maag, G.; Romero, M.; Steinfeld, A. Hydrogen production by steam-gasification of carbonaceous materials using concentrated solar power - IV. Reactor experimentation with vacuum residue. *Int. J. Hydrogen Energy* **2008**, *33*, 679−84.
(46) Segal, A.; Epstein, M.; Yogev, A. Hybrid concentrated photovolatic and thermal power conversion at different spectral bands. *Sol. Energy* **2004**, *76*, 591−601.
(47) Higman, C.; van der Burgt, M. *Gasification*, 2nd ed.; Elsevier: Oxford, U. K., 2008.
(48) Kreutz, T.; Williams, R.; Consonni, S.; Chiesa, P. Co-production of hydrogen, electricity and CO2 from coal with commercially ready technology. Part B: Economic analysis. *Int. J. Hydrogen Energy* **2005**, *30*, 769−84.
(49) Meerman, J.; Ramirez, A.; Turkenburg, W.; Faaij, A. Performance of simulated flexible integrated gasification polygeneration facilities, Part B: Economic evaluation. *Renew. Sustain. Energy Rev.* **2012**, *16* (8), 6083−102.
(50) Kolb, G.; Jones, S.; Donnelly, M.; Gorman, D.; Thomas, R.; Davenport, R.; Lumia, R. *Heliostat Cost Reduction Study*; Sandia National Laboratories: Alburquerque, NM, 2007; p 158.
(51) Kaniyal, A.; van Eyk, P.; Nathan, G. Dynamic modelling of the co-production of liquid fuels and electricity from various fuel blends via a hybrid solar gasifier. *Energy Fuels* **2013**, in press.
(52) NREL National Solar Radiation Database 1991−2005 update.
(53) *NREL National Solar Radiation Database 1991−2005 Update: User's Manual*; US DoE: Golden, CO, 2007.
(54) Bahadori, A.; Vuthaluru, H. Estimation of performance of steam turbines using a simple predictive tool. *Appl. Therm. Eng.* **2010**, *30*, 1832−8.
(55) Scott, D. *Coal Pulverisers - Performance and Safety.*; IEA Coal Research: London, 1995.

(56) Chiesa, P.; Consonni, S.; Kreutz, T.; Williams, R. Co-production of hydrogen, electricity and CO2 from coal with commercially ready technology. Part A:Performance and emissions. *Int. J. Hydrogen Energy* **2005**, *30*, 747−67.
(57) Steynberg, A.; Dry, M. *Fischer−Tropsch Technology*. Elsevier BV: Amsterdam, The Netherlands, 2004.
(58) Piatkowski, N.; Steinfeld, A. Solar gasification of carbonaceous waste feedstocks in a packed-bed reactor - Dynamic modeling and experimental validation. *AIChE J.* **2011**, *57* (12), 3522−33.
(59) Agar, D. Multifunctional reactors: old preconceptions and new dimensions. *Chem. Eng. Sci.* **1999**, *54*, 1299−1305.
(60) Marbe, Å.; Harvey, S.; Berntsson, T. Biofuel gasification combined heat and power—new implementation opportunities resulting from combined supply of process steam and district heating. *Energy* **2004**, *29* (8), 1117−37.

Page Intentionally Left Blank

Statement of Authorship

Title of Paper	Polygeneration of liquid fuels and electricity by the atmospheric pressure hybrid solar gasification of coal
Publication Status	Published
Publication Details	Kaniyal AA, van Eyk PJ, Nathan GJ, Pincus JJ, Ashman PJ. 2013. Polygeneration of liquid fuels and electricity by the atmospheric pressure hybrid solar gasification of coal. Energy & Fuels 27:3538-55.

Principal Author

Name of Principal Author (Candidate)	Ashok A Kaniyal		
Contribution to the Paper	Developed energy system process model and developed the structure based on which paper was written and modelling scenarios were presented. Carried out all drafting and paper revisions following editorial advice from primary and co-supervisors.		
Overall percentage (%)	55%		
Certification:	This paper reports on original research I conducted during the period of my Higher Degree by Research candidature and is not subject to any obligations or contractual agreements with a third party that would constrain its inclusion in this thesis. I am the primary author of this paper.		
Signature		Date	

Co-Author Contributions

By signing the Statement of Authorship, each author certifies that:

i. the candidate's stated contribution to the publication is accurate (as detailed above);

ii. permission is granted for the candidate in include the publication in the thesis; and

iii. the sum of all co-author contributions is equal to 100% less the candidate's stated contribution.

Name of Co-Author	Philip J van Eyk		
Contribution to the Paper	Provided early and ongoing guidance on conceptual design of modelling activities. Provided editorial assistance.		
Signature		Date	15/2/2016

Name of Co-Author	Graham J Nathan		
Contribution to the Paper	Provided early and ongoing guidance on conceptual design of modelling activities. Provided editorial assistance.		
Signature		Date	4 Feb, 2016

Name of Co-Author	Peter J Ashman		
Contribution to the Paper	Provided early guidance on conceptual design of modelling activities. Provided editorial assistance at final stages of manuscript development.		
Signature		Date	20/2/16

Name of Co-Author	Jonathan J Pincus		
Contribution to the Paper	Provided early guidance on conceptual design of modelling activities. Provided editorial assistance at final stages of manuscript development.		
Signature		Date	

Please cut and paste additional co-author panels here as required.

3

DYNAMIC MODELING OF THE COPRODUCTION OF LIQUID FUELS AND ELECTRICITY FROM A HYBRID SOLAR GASIFIER WITH VARIOUS FUEL BLENDS

Ashok A Kaniyal [a,c], Philip J van Eyk [a,b], Graham J Nathan [a,c]

a Centre for Energy Technology, The University of Adelaide South Australia 5005
b School of Chemical Engineering, The University of Adelaide South Australia 5005
c School of Mechanical Engineering, The University of Adelaide South Australia 5005

Energy & Fuels 2013 (27) 3556-69

energy&fuels

Article

pubs.acs.org/EF

Dynamic Modeling of the Coproduction of Liquid Fuels and Electricity from a Hybrid Solar Gasifier with Various Fuel Blends

Ashok A. Kaniyal,*[,†,‡] Philip J. van Eyk,[†,§] and Graham J. Nathan[†,‡]

[†]Centre for Energy Technology, [‡]School of Mechanical Engineering, and [§]School of Chemical Engineering, The University of Adelaide, Adelaide SA 5005, Australia

ABSTRACT: A sensitivity analysis is presented of the energetic and environmental performance of a hybridized solar gasification, coal-to-liquids (CTL_{sol}) polygeneration system using a pseudo-steady-state model outlined in a recently submitted paper. The hybrid CTL_{sol} system was assumed to be integrated with pressurized (upgraded) syngas and O_2 storage to reduce the impact of solar resource transience on the unit operations downstream of the hybrid gasifier. Reported is the sensitivity of the CTL_{sol} system's energetic and environmental performance to variations in gasification reactor pressure, to turn-down in the fuel feed rate to the hybrid gasifier, to the integration of an indirectly irradiated hybrid natural gas dry or steam reforming system, and to the proportion of biomass cogasified with the coal. The energetic performance of the CTL_{sol} system was shown to be only weakly sensitive to the solar hybrid gasifier pressure. The incorporation of a natural gas steam reformer within the hybrid solar coal gasifier was shown to reduce by an additional 15% the process' mine-to-tank CO_2-e emissions relative to the configuration without the co-reformer. However, the addition of the co-reformer to the solar hybrid gasifier also reduced the solar share of the system output to 17% from 20%. The use of a dry reforming process was found to enable similar energetic and environmental performance characteristics to the steam reforming process. Mine-to-tank greenhouse gas emissions parity with diesel production from mineral sands can be achieved with a 30% biomass cogasification fraction, by weight, in a solar hybrid cogasifier, while 45 wt % biomass is required for the nonsolar equivalent. This coal-biomass solar cogasification system also achieved a 22% improvement in energetic productivity relative to the nonsolar reference system. Mine-to-tank CO_2-e emissions of 0 was found to be achievable with a biomass cogasification fraction of 60 wt %, while the nonsolar equivalent was found to require a biomass fraction of 70 wt % to enable the same outcome. Reducing the amount of biomass to achieve a given environmental target is important given that biomass is typically three to four times more expensive than coal.

1. INTRODUCTION

Synthetic liquid fuels produced by the gasification of carbonaceous fuels coupled with Fischer−Tropsch synthesis (FT) is expected to play a significant role in meeting the energy needs of the transportation sector over the next 50 years.[1] However, a barrier to the implementation of coal to Fischer−Tropsch liquid systems is that the mine-to-tank greenhouse gas (GHG) emissions are almost 2.5 times larger than those of producing diesel from tar sands and more than 6 times those of producing diesel from conventional mineral crude.[2−5] This environmental challenge offers an opportunity to identify options to reduce the CO_2-e emissions associated with producing liquid fuels by the FT process. Hence, the present assessment seeks to determine the emission reduction potential of a range of renewable energy integrated coal-to-liquid (CTL) systems.

An innovative approach to lowering the net GHG emissions of the CTL process is the introduction of concentrated solar thermal power to the endothermic, oxygen-blown, autothermal coal gasification process. The value of solar hybridization has previously received extensive treatment in the context of power generation processes.[6−9] However, the work of Kaniyal et al.[10] was the first comprehensive process analysis of a solar hybrid coal-to-liquids, CTL_{sol} polygeneration system. The pseudo-steady-state system level analysis of the CTL_{sol} system showed the potential to increase by 21% the net energy output per unit feedstock input for a full solar year and reduce by 30% the mine-to-tank greenhouse gas emissions, relative to the verified autothermal CTL_{ref} system.[10] As in other examples of solar hybrid power generation systems, the CTL_{sol} polygeneration system showed the potential to eliminate the influence of solar intermittency on unscheduled plant shut downs and, with a modest amount of syngas storage,[7−9,11] on load fluctuations in the unit operations downstream of the solar hybrid gasifier.[10] Nevertheless, the GHG emissions of the CTL_{sol} system were found to be 1.6 times larger than those associated with producing diesel from tar sands and 4 times those of producing diesel from conventional mineral crude. Thus, there is a need to identify additional approaches to further reduce CO_2-e emissions. Options to achieve this include alternative reactor operating conditions, integration of solar natural gas co-reforming processes,[12] and the cogasification of coal with biomass. Hence, the present investigation aims to assess the energetic GHG emissions and capital utilization performance impacts of each of these three options.

A significant opportunity to improve the economic and GHG emissions performance of a CTL polygeneration system was recently identified by integrating the autothermal entrained flow gasifier with a conventional tubular, pressurized steam methane reforming (SMR) reactor.[13] Blending the output from the autothermal coal gasification process, which has a low ratio of $H_2/CO \sim 0.4$, with the syngas produced by the SMR

Received: February 5, 2013
Revised: April 30, 2013
Published: May 3, 2013

process, which has a high ratio of $H_2/CO \sim 3.0$, reduces the total CO_2 emissions intensity of the water−gas shift (WGS) upgrade reactions. This is because the FT synthesis process requires syngas with $H_2/CO \sim 2.26$.[3,10] Furthermore, the expected cost of integrating a tubular reformer within an entrained flow gasification system is expected to be low.[13] For the conventional gasification case, the integration of a tubular reformer was shown to increase the capital cost by <1%, offering the potential to significantly improve the viability of CTL polygeneration.[13] It should be noted, that while the total cost of this polygeneration configuration changes very little due to balance-of-plant savings, Adams and Barton[13] assume that it costs 25% more to use a radiant cooler in a gasifier with steam reforming than to use a traditional steam-only radiant syngas cooler. Furthermore, in the context of an atmospheric pressure, windowed, solar hybrid gasifier, the integration of a tubular co-reforming process offers a feasible approach to generate pressurized syngas without comprising the structural integrity of the quartz window, as would occur with the use of elevated pressures[14] and/or temperatures.[15−17] This approach could reduce the technical challenges associated with the need for a pressurized, windowed, directly irradiated, gasification, co-reforming reactor, as was recently proposed in Sudiro's study of a FT liquid polygeneration system.[12] However, to date, no assessment has been reported of the energetic and GHG emission performance of a FT liquid polygeneration system integrated with a co-reforming reactor. Hence, an additional aim of the present investigation is to meet this need.

A disadvantage of both the solar-hybridized coal gasification and the steam methane reforming process (SMR) is its large combined steam demand.[18] This is an important issue, not only because of the parasitic impact of producing steam for internal use in a polygeneration system but also because access to water is typically poor in the arid regions where the solar resource is greatest. The dry reforming of natural gas with CO_2 is one option by which the water consumption intensity of the solar-intensive portion of the CTL_{sol} polygeneration system could be reduced.[19] Such a process could also offer important synergies with CO_2 geo-sequestration pipeline networks, which are anticipated to be introduced in the medium-term.[20] Furthermore, the solar dry reforming process could also improve the viability of natural gas reserves that are currently made uneconomic by high dissolved CO_2 concentrations.[21] Hence, a further aim of the present investigation is to compare the net energetic, GHG emissions and steam consumption performance of integrating an indirectly irradiated dry co-reformer with that of a steam co-reformer within a solar hybrid coal gasification system.

The flexibility to vary the fuel feed rate to the solar hybrid gasifier in response to the amount of solar thermal power that is available has the potential to significantly improve the energetic and GHG emissions performance of the CTL_{sol} system relative to operation based on an invariant fuel feed rate.[10] One approach to increase the flexibility of the plant to respond to variations in the input of concentrated solar radiation is to allow the fuel feed rate to be boosted intermittently above the nominal design value (1 kg/s for the case investigated by Kaniyal et al.[10]). Gasifier operation with a constant fuel flow rate leads to the suboptimal use of the installed heliostat collection capacity and therefore the "spillage" of solar radiation whenever the optimal potential thermal power output of the heliostats exceeds the endothermic demand of gasifying coal at the nominal design rate of fuel flow.[10] However, the solar-boosted production of syngas has the disadvantage of increasing the polygeneration system's large, parasitic syngas compression load.[10] This is because the windowed solar-hybridized gasification process is unlikely to be feasible at elevated pressures.[22−24] One option to partially offset the solar-boosted syngas compression load is to turn-down the fuel flow rate to the hybrid gasifier below the nominal design flow rate at night, which has the added advantage of also reducing the gasifier's O_2 demand.[10] The hybrid solar gasifier and heliostat field could reasonably be expected to be the two most expensive components of a CTL_{sol} polygeneration system. This is assuming that the hybrid solar gasifier has a similar cost profile to the autothermal entrained flow gasification system[2,13,25−29] and because the heliostat field typically forms ∼50% of the cost of concentrated solar power systems.[30] Thus, the flexibility to boost and turn-down the fuel feed rate to the gasifier gives rise to an important capital productivity trade-off between the gasifier's excess thermal capacity and the installed heliostat collection capacity. No quantitative assessment of these trade-offs has been reported previously. Hence, the present investigation aims to quantify the trade-off between the performance, energy output per unit feedstock, GHG emissions, and the capital utilization of the installed excess hybrid gasifier and excess heliostat collection capacity.

Biomass cogasification is likely to be necessary to reduce the CO_2-e emissions of diesel produced by the autothermal CTL process to below that of production from conventional mineral crude or tar sands, in the absence of carbon capture and storage technology.[2,3,25,27] However, the autothermal coal-biomass-to-liquids (CTL_{bio}) process requires biomass cogasification fractions of at least 60% by weight to reduce its GHG emissions to below that of (non-tar sands/bitumen) mineral crude-derived diesel.[2,25,27] Such large cogasification fractions are likely to present significant technical challenges in both sourcing biomass at the required scale[31] and in gasifier design.[32−34] Additionally, because biomass has typically been 3−4 times more expensive than coal,[31,34−36] there are significant economic advantages in reducing the biomass fraction to achieve a given CO_2 emissions target. This could potentially be achieved by the solar-hybridized cogasification of coal-biomass since the CTL_{sol} process stores ∼23% more carbon in the FTL end product than the autothermal CTL_{ref} process.[10] However, the magnitude of these potential benefits is yet to be reported. Hence, the present investigation also aims to quantify the potential benefits of the hybridization of concentrated solar thermal radiation into the autothermal coal-biomass cogasification process for the production of FTL fuels.

The primary objective of the present assessment is to identify effective combinations of operating conditions, reactor configurations, and blend ratios of biomass with coal that achieve CO_2-e emissions parity with diesel derived from conventional mineral crude or tar sands or that achieve carbon-neutral production on a mine-to-tank basis. Specifically, the investigation aims to evaluate the operating conditions that optimize the utilization of both the hybrid gasification reactor and heliostat field. It also aims to examine the potential GHG emissions and energetic value of incorporating an indirectly irradiated, pressurized dry or steam natural gas reforming system within the solar hybrid gasifier, for the production of FTL fuels.

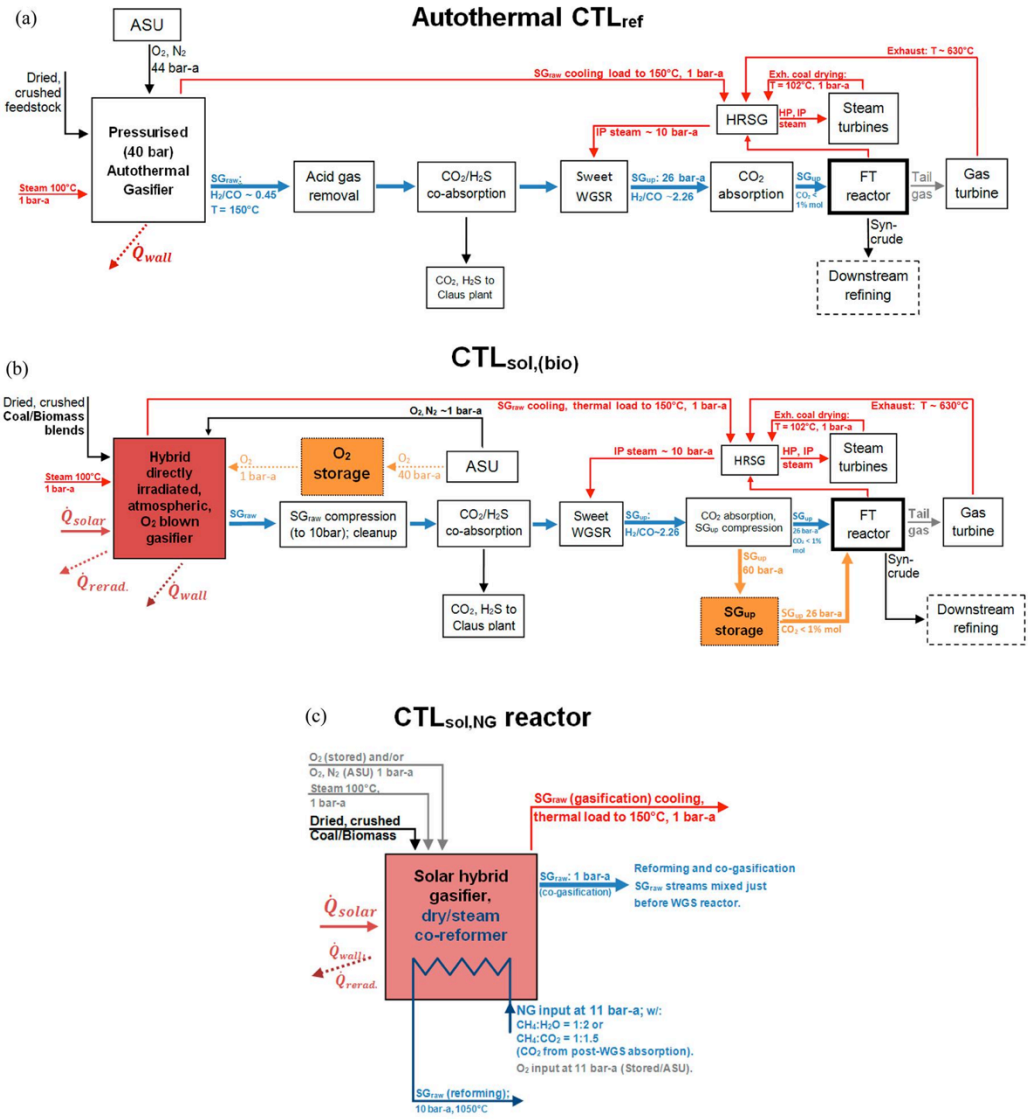

Figure 1. Simplified, annotated process schemes for the (a) reference, pressurized autothermal Shell gasification integrated CTL_{ref} polygeneration system (top); (b) CTL_{sol} polygeneration system integrated with a directly irradiated solar, O_2-blown hybrid atmospheric pressure gasifier, upgraded syngas, and O_2 storage system (middle); and (c) (c) schematic diagram of the solar hybrid gasifier/natural gas dry or steam co-reformer (bottom), which replaces the hybrid solar (co)gasifier shown in (b) and is integrated with the downstream process of the CTL_{sol} polygeneration system.

2. METHODOLOGY

The energetic and environmental performance of the solar-hybridized gasification, coal-to-liquids polygeneration system, hereafter termed CTL_{sol}, was assessed relative to a "reference" system based on a conventional, autothermal, pressurized (40 bar) "Shell"-type gasifier, hereafter termed CTL_{ref}.[3] The autothermal CTL_{ref} system developed by Kaniyal et al.[10] (see Figure 1a) is consistent with and verified against the baseline scheme investigated by Meerman et al.[3] The CTL_{sol} system was also developed and investigated by Kaniyal et al.[10] As in the authors' earlier work,[10] all scenarios investigated herein assume that all of the CO_2 produced by the facility is vented. Hence, further mitigation could be achieved were carbon sequestration to be incorporated. All unit operations, except the gasifier section, were modeled using Aspen Plus v7.1 software, while the hybrid cogasifier section of the CTL_{ref} and CTL_{sol} systems was modeled using Aspen HYSYS v7.1 software.

Figure 1 presents simplified, annotated schematic diagrams of three systems, including the baseline CTL_{sol} configuration investigated by Kaniyal et al.[10] The first additional system, shown in Figure 1b, is the $CTL_{sol,bio}$ polygeneration system used to model the solar hybrid cogasification of coal-biomass fuel blends. Figure 1c shows the second additional system, namely, the hybrid solar gasifier/co-reformer component of the $CTL_{sol,NG}$ system. This process uses a pressurized counter-current flow natural gas dry or steam co-reformer, which is integrated with the hybrid solar gasifier. A conceptual configuration of the proposed hybrid solar gasification/co-reforming reactor is shown in Figure 2, and the model is described in section 2.2.1.

Figure 2 presents the reactor configuration on which the performance calculations were based during operation with a solar input. This extends further the system proposed previously by Kaniyal et al.[10] by the addition of an indirect heat exchanger to allow the reforming of natural gas under pressure following Dahl et al.[14] Like the previous investigation, Figure 2 modifies the original solar-only

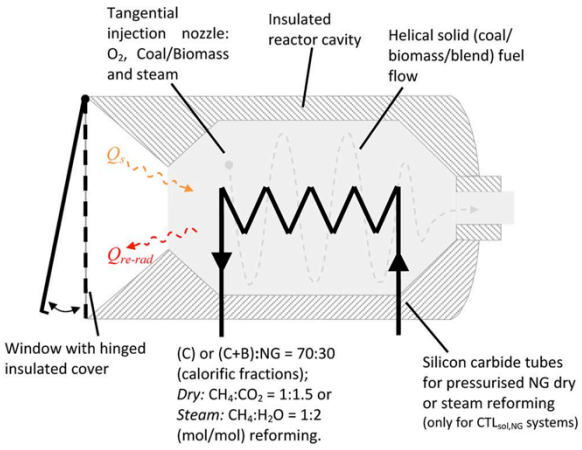

Figure 2. Configuration of the directly irradiated atmospheric pressure hybrid solar reactor used to estimate heat losses by radiation, $\dot{Q}_{rerad}$ during operation with solar thermal power input.[14] The hinged shutter is assumed to allow these losses to be avoided during autothermal gasification of coal (C) and biomass (B) blends.[10] Also shown is the configuration assumed to allow the hybrid, continuously operational co-reforming (with cogasification) of natural gas flowing counter-current to the gasification vortex stream, in pressurized, silicon carbide tubes with CO_2 as the reagent for the dry process or H_2O as the reagent for the steam reforming reactions. The indirectly irradiated, oxygen-blown natural gas reforming reactions are assumed to take place at 1050 °C and 11 bar-a.[14] The hybrid vortex gasifier and co-reforming reactor are assumed to be sized to achieve a sufficiently long residence time for 100% conversion of the coal and 99% of the input natural gas to syngas.

configuration of Z'Graggen et al.[24] by the addition of an external shutter to avoid radiant losses during periods of low solar insolation.[10]

The electricity generated by the CTL processes is designed to satisfy the parasitic demand of the various unit operations within the process. This maximizes the production of Fischer–Tropsch liquid fuels (FTL), minimizes the number of energy processing steps between the feedstock and final energy product, and avoids any diversion of the upgraded syngas to the gas turbine for electricity generation. The upgraded syngas, SG_{up}, is produced in the sweet water–gas shift reactor, SWGSR, to achieve a composition with H_2/CO (mol/mol) ~ 2.26[3] as is required for the Fischer–Tropsch reactor (FTR). Relative to the heating value of the coal input, the parasitic electrical output is ~15% for all scenarios. Avoiding exporting electricity is likely to be the best option at the small scale considered here because the additional investments in substation and electricity transmission infrastructure are likely to be considerable. However, there may be scenarios in which it could be desirable to configure a plant to also supply peaking power during periods of high electricity prices.

The sensitivity of the energetic and environmental performance of the CTL_{sol} polygeneration system proposed by Kaniyal et al.[10] is assessed for variation of the following parameters:

- the pressure of the gasifier reactor over the range of 1 to 4 bar-a
- the feed rate of fuel to the hybrid gasifier in response to the transient availability of solar radiation, for four heliostat collector area scenarios (A_{coll}); see Table 4
- the type of natural gas reforming (NGR): dry (CO_2) or steam methane reforming (SMR);
- the biomass (B) weight fraction relative to that of coal (C) in the fuel blend (m_B/m_{C+B}): {0, 10, 20, 30, 60, and 100%}.

2.1. Solar Resource Analysis. The study year selected for all simulations of the CTL_{sol} system is the summer-to-summer period: 1 Jun 2004 to 31 May 2005. The insolation data set corresponded to the Farmington site in northern New Mexico (USAF #723658) whose latitude is 37°N (USAF #723658).[37,38] The net solar thermal power input to the hybrid solar gasifier ($\dot{Q}_{sol,net}$) was estimated using eq 1. In eq 1, $\dot{Q}_{wall}$ is the assumed rate of heat lost through the gasifier walls and η_{opt} is the optical efficiency of all mirrors and reflectors, including the compound parabolic concentrator, which was assumed to be 50%.[10] The hourly averaged rate of reradiation losses through the quartz window was calculated using the solar absorption efficiency parameter, η_{abs}. This parameter was calculated using eq 2 for each gasification temperature (T_g), which spanned the range of 1100–1400 °C. For the year-long solar insolation time series, η_{abs} was calculated for each hour assuming a mean solar flux concentration ratio ($\tilde{C}$) of 2000 suns[39] and a reactor design with an optimal aperture size that maximises the capture of radiation from the heliostat field and minimises radiation losses from the aperture.[17] The hybrid solar gasifier was also assumed to lose heat through the reactor walls at a rate equal to $\dot{Q}_{wall}$, which is given by eq 3.[40] Figure 3 presents the relationship between η_{abs} and solar insolation (I)[17] for four gasification reactor temperatures.

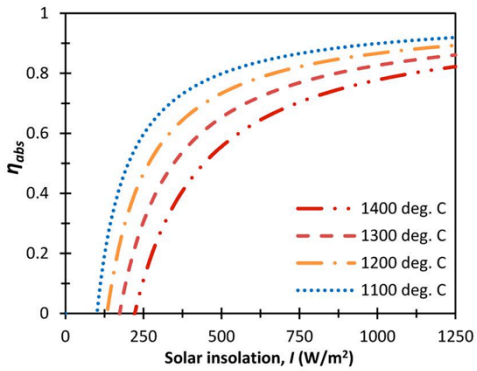

Figure 3. Dependence of solar absorption efficiency (η_{abs}) on the direct normalized solar radiation intensity for T_g: 1100–1400 °C and for $\tilde{C}$ = 2000 suns.[17]

Using the solar insolation time series data set, a time series for $\dot{Q}_{sol,net}$ was calculated for a given heliostat collection area (A_{coll}) and gasification temperature (T_g). The parameter $\dot{Q}_{sol,net}$ is normalized by $\dot{Q}_{HG\text{-}(NGR)}^{T_g\text{-}R}$, the power required by the hybrid gasifier and natural gas reformer (under the conditions shown in Table 2) to obtain the dimensionless parameter, Φ, shown in eq 4.

$$\dot{Q}_{sol,net} = \eta_{abs}\eta_{opt}A_{coll}I - \dot{Q}_{wall} \quad (1)$$

$$\eta_{abs} = 1 - \left(\frac{\sigma T_g^4}{I\tilde{C}}\right) \quad (2)$$

$$\dot{Q}_{wall} = \dot{m}_{coal} \times 0.03 \times Q_{coal(HHV)} \quad (3)$$

$$\Phi = \frac{\dot{Q}_{sol,net}}{\dot{Q}_{HG\text{-}(NGR)}^{T_g\text{-}R}} \quad (4)$$

2.2. Pseudodynamic Process Model. The simulation of the CTL_{sol} process model in the present investigation is based on the pseudodynamic model detailed previously.[10] Following that work, all scenarios assessed herein were optimized to maximize the production of Fischer–Tropsch liquids. The dynamic operation of the CTL_{sol} system was modeled using an in-house MATLAB code that employed a steady-state approximation for each time-step, based on simulations in Aspen Plus and Aspen HYSYS (v 7.1). The MATLAB code used unique linear or log–linear relationships to describe the parasitic load, energetic output, and CO_2 emissions of each unit operation of the CTL_{sol} polygeneration system for each scenario summarized in section

dx.doi.org/10.1021/ef400217n | Energy Fuels 2013, 27, 3556–3569

2.1. The part-load performance of each unit operation was accounted for by following the methodology outlined previously.[10] The unique components of all of the CTL_{sol} systems, in comparison with the CTL_{ref}, namely, the SG_{up} storage system and the O_2 storage system, are illustrated in the process model of Figure 1(b).

For all of the scenarios modeled herein, the capacity of the upgraded syngas (SG_{up}) storage tank was assumed to be equal to 8 h of SG_{up} output from the water−gas shift reactor at a rate corresponding to operation of the hybrid solar gasifier at 1100 °C, 1 bar-a, and $\Phi = 0$. The sensitivity of this assumption of energetic performance was assessed by Kaniyal et al.[10] for three cases of storage tank capacity, equal to 4, 8, and 16 h of SGup production, at the hourly rate specified in the previous sentence. This analysis showed that the main effect of increased storage capacity on the energetic and environmental performance of the CTL_{sol} system was on the statistical variance in SG_{up} throughput to the FTR, which was assumed to have good part-load performance down to 40% of its rated capacity.[3]

Oxygen produced in the air separation unit (ASU) was assumed to be stored in a pressurized tank at 60 bar-a. A fixed O_2 storage capacity of 5000 kmol (at 94.3% mol ∼ 3300 m^3) was assumed for all cases. This was based on the finding of Kaniyal et al.[10] that the hybrid system's energetic and greenhouse gas (GHG) performance is only weakly sensitive to the capacity of O_2 storage.

2.2.1. Hybrid Solar Autothermal Gasifier Sensitivity to Operating Conditions. Reactor Pressure. The solar hybrid coal gasification reactor was also modeled using the same methodology and the boundary conditions as Kaniyal et al.[10] The impact of increasing reactor pressure from 1 to 4 bar-a was assessed for gasifier reactor temperatures (T_g) of 1100 and 1400 °C. Although technical feasibility of the windowed, solar hybrid gasification reactor under pressurized conditions is not yet verified, the objective of the present analysis is to assess the magnitude of any potential benefits from pressurized operation.

Fuel Flow Flexibility. The present model allows the solid fuel flow rate to the hybrid gasifier to be varied in response to variations in the solar flux from a heliostat field of a given area (A_{coll}). This differs from the earlier work,[10] which assumed a constant coal (C) flow rate of 1 kg/s ($\dot{m}_C$) to the gasifier and varied the rate of O_2 and steam flow rate to the gasifier as a function of the solar thermal power input ($\dot{Q}_{sol,net}$). The earlier assumption of a fixed fuel flow rate to the gasifier places an upper limit on the amount of solar energy that can be absorbed of $\dot{Q}_{HG\text{-}(NGR)}^{T_g\text{-}R}$. This corresponds to the amount of solar thermal power required by the hybrid gasifier to completely gasify 1 kg/s of coal or a coal-biomass blend fed to the reactor, operating at temperature T_g. Hence, when $\dot{Q}_{sol,net} > \dot{Q}_{HG}^{T_g\text{-}R}$ for a heliostat field of a given capacity, solar thermal power is spilled at the rate $\dot{Q}_{sol,net} - \dot{Q}_{HG}^{T_g\text{-}R}$. Here, the spillage of solar energy can be reduced (or even avoided) if the gasifier is operated with the flexibility to increase the fuel flow rate above 1 kg/s, on a pro rata basis when $\dot{Q}_{sol,net} \geq \dot{Q}_{HG}^{T_g\text{-}R}$. This flexibility has two advantages. First, it enables the solar share of the syngas produced to be increased, thereby improving energetic productivity and GHG emissions, and second, it enables greater economic utilization of the installed heliostat collection capacity. In addition, it reduces $\dot{m}_{C+B}$ from a reference flow rate of 1 kg/s at night, offering the potential to improve plant productivity by reducing both the gasifier's O_2 demand and also the larger, solar-boosted SG compression load during the day when $\dot{m}_{C+B}$ is increased above 1 kg/s.

The size of the energetic and GHG emissions performance improvements possible is limited by the gasifier's turn-down and turn-up capacity. Here it is assumed that the maximum and minimum limits of turn-down are ±20% from the reference flow rate of $\dot{m}_{C+B} = 1$ kg/s. The four coal(+biomass) fuel flow rate flexibility scenarios are summarized in eq 5.

$$\dot{m}_{C+B(max,min)} = \dot{m}_{(1.2,0.8)}\ \text{kg/s};\quad \dot{m}_{(1.2,0.9)}\ \text{kg/s};\quad \dot{m}_{(1.1,0.8)}\ \text{kg/s or}\quad \dot{m}_{(1.1,0.9)}\ \text{kg/s} \tag{5}$$

Capital Utilization Analysis. The capital utilization analyses were limited to the hybrid solar entrained flow gasifier and heliostat collectors (see section 2.3), given their large expected proportional contribution to the total plant cost. This assumption is based on the solar hybrid gasifier having a similar cost profile to the nonsolar, autothermal entrained flow gasifier, which forms the single largest cost component of a CTL polygeneration system[2,13,25−29] and because the heliostat collectors typically contribute 50% of the capital outlay of CSP plants.[30] Here, it is important to note that a complete assessment of the economic viability of the CTL_{sol} polygeneration system has not been carried out as it is outside of the scope of the present assessment.

The annually averaged utilization of the hybrid gasifier was calculated using eq 6 based on its maximum fuel flow rate capacity. This equation defines the annually averaged utilization as the mean of the hourly averaged flow of the coal or coal-biomass (C+B) fuel blend to the hybrid gasifier as a ratio of the maximum fuel flow rate capacity.

$$\overline{U_{HG}} = \overline{\left(\frac{\dot{m}_{C+B,hr}}{\dot{m}_{C+B(max)}}\right)} \tag{6}$$

2.2.2. Integration of an Indirectly Irradiated Pressurized, Natural Gas (Dry/Steam) Reformer. Figure 1c presents a schematic diagram of $CTL_{sol,NG}$ polygeneration system, which was modeled with a 30:70 calorific ratio of natural gas (NG) to solid fuels (coal and biomass). As shown in Figure 1c, the raw syngas output from the steam or dry reforming process was assumed to be cooled in the HRSG and then combined with the (co)gasification raw syngas output stream after it is cleaned just before the sweet WGS reactor. The combined syngas stream was assumed to be upgraded in the WGS reactor to a H_2/CO ratio of 2.26 by varying the steam flow to the reactor depending on the H_2/CO ratio of the combined syngas input. The system was assessed for both coal alone and for a coal-biomass blend with $m_B/m_{C+B} = 0.3$ (see Figures 17 and 18). The assumed natural gas composition is given in Table 1, and the operating conditions are summarized in Table 2.

Table 1. Assumed Composition and Higher Heating Value of Natural Gas (NG)

component	mole fraction
CH_4	95.2%
C_2H_6	2.5%
C_4H_8	0.3%
N_2	1.3%
CO_2	0.7%
HHV (MJ/kg)	53.2

The calculation of the parameters in Table 2 is based on the assumptions outlined below. All scenarios modeled assume that the NG flow rate is fixed, while the solid fuel flow rate is varied in response to the amount of solar thermal power that is available, as summarized by eq 5. This assumption was made because the indirect reforming process has a lower heat transfer efficiency than the directly irradiated gasification process.

Figure 2 shows a configuration of the solar hybrid reactor, with an integrated tubular silicon carbide reformer. The tubular reforming reactor was assumed to operate at 11 bar-a, while the supply pressure of natural gas was assumed to be 30 bar-a.[13] The model assumes that the reactor can be developed to achieve equilibrium conversion of the natural gas under the heat duties and syngas outlet performance conditions summarized in Table 2, so neither depends on, nor accounts for, the details of the configuration shown in Figure 2. Nevertheless, the reformer is likely to be most effective in driving the endothermic reforming reactions to completion if the flow of natural gas and the reforming reagent in the pressurized tubes is countercurrent to the gasification vortex stream and to the incoming radiation. This configuration leads to the highest flux of solar energy being at the outlet end of the reformer. When 99% conversion of the fuel is assumed, the model also implicitly assumes that the combined assembly can be made large enough and/or incorporate sufficient swirl to achieve enough residence time for this to occur. Furthermore, it is worth noting that unlike the natural gas reformed integrated within the radiant cooler section of the entrained flow gasifier proposed by

dx.doi.org/10.1021/ef400217n | Energy Fuels 2013, 27, 3556−3569

Table 2. Model Input Parameters for the Solar-Hybridized, Indirectly Irradiated, Tubular, Pressurized, Natural Gas (NG) Dry and Steam Reforming Reactor Configurations

parameter		units	value				
operating pressure		bar-a	11				
operating temperature		°C	1050				
natural gas flow rate ($\dot{m}_{NG}$)		kg/s	0.20				
steam reforming	H_2O (340 °C, 11 bar-a)	kg/s	0.40				
dry reforming	CO_2 (98.3% mol)	kg/s	0.73				
ratio of net solar thermal power input to power required by natural gas reformer	Φ_{NGR}	%	0	25	50	75	100
steam reforming	thermal power load ($\dot{Q}_{sol,net\text{-}NGR}$)	MW_{th}	0	1.3	2.6	3.9	5.2
dry reforming			0	1.2	2.3	3.5	4.7
steam reforming	oxidant (O_2 at 94.3 mol %)	kg/s	0.32	0.24	0.16	0.08	0
dry reforming			0.29	0.22	0.14	0.07	0

Adams and Barton,[13] in the present solar reactor, the particles are assumed to flow in a vortex around the outside of the reactor, radiating heat to the natural gas reforming tubes. Hence, the present model implicitly assumes that any potential influences of slagging and fouling of the tubes can be remedied.

Reradiation losses from the hybrid gasifier−reformer system as a whole are accounted for separately by the methodology detailed by Kaniyal et al.[10] (also summarized in section 2.1). The integration of the hybrid, indirectly irradiated, oxygen-blown, tubular reformer was assumed not to impact on the vortex reactor's reradiation characteristics and thus its absorption efficiency.[10] While the complete system is yet to be demonstrated, sufficient information is available on the performance of all components as stand-alone items to enable the performance to be estimated with the assumption that the components are all independent.

Table 2 summarizes the modeling parameters that were used to simulate the solar hybrid co-reforming system. Following Melchior et al.,[41] it was assumed that approximately 15% of the heat delivered to the reforming tubes is lost by conduction through the walls of the tubular reactor. This loss to the surroundings is used to calculate the net thermal power required by the tubular reforming reactor ($\dot{Q}_{sol,net\text{-}NGR}$), given in Table 2, to convert >99% of the methane in the natural gas to raw syngas (see Figure 2). The O_2 flow rate to the tubular reformer was assumed to be varied in response to the solar thermal power input to the reactor, to maintain a constant raw syngas output temperature of 1050 °C. Specifically, the oxidant feed to the reforming reactor is varied between 0.32 and 0 kg/s for the steam co-reforming scenario and 0.29 and 0 kg/s for the dry co-reforming process (Table 2). This is consistent with the steam reforming reaction having a slightly lower reaction enthalpy than the dry reforming process, as is apparent from reactions 7 and 8. Both the dry and steam reforming reactions were modeled using the Gibbs minimization reactor in Aspen Plus.

The proposed hybrid solar gasification, co-reforming system is assumed to operate continuously with constant flow rates both of natural gas and either one of the two reforming reagents, CO_2 or H_2O. To minimize carbon deposition, the dry reforming reactor was modeled with a CH_4/CO_2 molar ratio of 1:1.5[20] and the steam reforming model with an input CH_4/H_2O molar ratio of 1:2.[18] The CO_2 demand of the natural gas dry reforming process was assumed to be met by the post-WGS capture of CO_2 (see Figure 1c). The consumption of CO_2 by the reforming process is accounted for in the process' lifecycle emissions analysis. The CO_2 that is not consumed by the reforming process, typically 55−70% of the plant's total CO_2 emissions, is assumed to be vented to the atmosphere. Further mitigation of CO_2 is thus possible either by reuse or sequestration of this stream.

$$CH_4 + CO_2 \rightarrow 2CO + 2H_2 \quad \Delta H^{\circ}_{298K} = +247\ \text{kJ/mol} \tag{7}$$

$$CH_4 + H_2O \rightarrow CO + 3H_2 \quad \Delta H^{\circ}_{298K} = +206\ \text{kJ/mol} \tag{8}$$

Table 3. Assumed Proximate and Ultimate Analysis of Cane Trash[42] and Illinois #6 Coal[3,10]

proximate analysis (%)	biomass (B)	Illinois #6 coal (C)
moisture (AR)	35	11.1
ash (dry)	12	10.9
HHV (dry) (MJ/kg)	19.5	30.5
volatile matter (d.a.f.)	83	44.2
fixed carbon (d.a.f.)	17	55.8
ultimate analysis (% d.a.f.)		
carbon	45	80.5
hydrogen	5.8	5.7
oxygen	44	8.7
nitrogen	0.6	1.6
sulfur	0.2	3.2

2.2.3. Hybrid Solar Cogasification of Coal-Biomass Blend. Table 3 presents the proximate and ultimate analyses of both the cane trash,[42] the design biomass feedstock, and the Illinois #6 coal.[3] These two fuels are assumed to be blended at biomass weight fractions (m_B/m_{C+B}) of 10, 20, 30, 60, and 100%. All coal-biomass cogasification scenarios investigated here are identified by the symbol $CTL_{sol,bio\text{-}X\%wt}$, where X = ($m_B/m_{C+B}$). The assessment of carbon emissions also assumed the biomass to be 100% renewable and thus ignored the extraneous emissions associated with fuel harvest and transport.

The solar hybrid cogasification model assumes that the fuel blend is dried to <2 wt % moisture by the atmospheric pressure exhaust from the low-pressure steam turbine prior to being fed into the gasifier. Following Kaniyal et al.,[10] the hybrid cogasification simulation assumes that the O_2 and steam flow rate to the cogasifier is varied to maintain a constant gasification temperature of 1100 °C and char conversion of 100%.[10] The coal-biomass hybrid solar cogasification model further assumes that the fuel flow rate can be varied in response to the amount of solar thermal power available through any given hour as described in section 2.2.2.

2.3. Mine-to-Tank (MTT) CO_2-e Emissions. The greenhouse gas emissions calculated for all scenarios account for all of the emissions associated with the predicted energy output bar of the CO_2-e emissions associated with fuel combustion at the point of end-use. The emission sources accounted for herein are those from mining the coal resource, producing FT liquid fuels by the fuel-to-liquid polygeneration process, and refining the synthetic fuel[4] to diesel and all miscellaneous transportation emissions.[4] The CO_2-e emissions calculated for the cogasification scenarios assume biomass to be carbon-neutral.[2,3,25,27] Furthermore, for these scenarios, the MTT CO_2-e emissions are credited for the molar proportion of biomass combusted at the point of end-use. In addition, the emissions associated with building the solar plant are not accounted for in the present analysis, given its small contribution over the life of the facility. It should also be noted that use of the CO_2 physical absorption system provides an industrially pure stream of CO_2 which, if sequestered,

dx.doi.org/10.1021/ef400217n | Energy Fuels 2013, 27, 3556−3569

would further reduce the net CO_2 emissions from the baseline CTL_{sol} process by approximately 50%.

2.4. Heliostat Field Size Area Sensitivity. The impact of the heliostat field area (A_{coll}) on the energetic productivity and CO_2-e emission performance of the hybrid solar polygeneration system is assessed for four A_{coll} scenarios over the range of 33×10^3 to 89×10^3 m^2. Following the work of Kaniyal et al.,[10] each A_{coll} scenario is normalized using eq 9 as $\Phi_{peak}^{A_{coll}}$. Here, $\Phi_{peak}^{A_{coll}}$ is the fraction by which the annual, peak hourly averaged thermal power output of a heliostat field of a given collection capacity, $(\dot{Q}_{sol,net}^{A_{coll}})_{ann(peak)}$, exceeds the endothermic demand of the hybrid solar gasification reactor and natural gas reformer, $\dot{Q}_{HG\text{-}(NGR)}^{T_g\text{-}R}$ (for the relevant scenarios). The A_{coll} scenarios and the corresponding normalized parameters are summarized for the CTL_{sol} plant configuration and the two $CTL_{sol,NG}$ configurations in Table 4.

$$\Phi_{peak}^{A_{coll}} = \frac{(\dot{Q}_{sol,net}^{A_{coll}})_{ann(peak)}}{\dot{Q}_{HG\text{-}(NGR)}^{T_g\text{-}R}} \quad (9)$$

Table 4. Relationship between the Heliostat Field Collector Area (A_{coll}) and $\Phi_{peak}^{A_{coll}} - 1$

scenario	CTL_{sol}[a]	$CTL_{sol,NG}$ (dry)[a]	$CTL_{sol,NG}$ (steam)[a]
coal fuel flexibility scenario and NG fuel flow (kg/s)	$\dot{m}_{C(min,max)}$ = (1.2,0.8)	$\dot{m}_{C(min,max),NG}$ = ((1.2,0.8),0.2)	
gasifier maximum thermal capacity (MW_{th} – HHV)	34	34	
co-reformer maximum thermal capacity (MW_{th} – HHV)	0	10	
A_{coll} ($\times 10^3$ m^2)		$\Phi_{peak}^{A_{coll}} - 1$	
89	not assessed	1.41	1.49
63	1.39	0.72	0.78
51	0.91	0.38	0.42
44	0.68	0.21	0.25
38	0.44	not assessed	not assessed

[a]For the CTL_{sol} scenario hybrid gasifier assumed to operate at 1100 °C and 1 bar-a; for $CTL_{sol,NG}$, see Table 3.

2.4.1. Capital Utilization Analysis. The second component of the capital utilization analysis is that of the heliostat collector field. This is assumed to be the other most significant capital expense on the basis that numerous assessments of concentrated solar electrical power systems have shown that the cost of the heliostat field contributes ~50% of the total capital expense.[30] Equation 10 is used to estimate the hourly averaged utilization of the installed heliostat collection capacity as the ratio of the amount of solar thermal power consumed by the hybrid solar gasifier and co-reforming system (if applicable) to the output of the heliostat array for that hour—calculated using eq 1. In eq 10, $\dot{Q}_{HG\text{-}(NGR)}^{T_g\text{-}R}$ is the combined endothermic load of the hybrid solar gasifier operating with a coal or a coal-biomass (C+B) blend, fuel flow rate of 1 kg/s, and (if applicable) the natural gas reformer whose operating conditions are outlined in Table 2. The annually averaged utilization of the heliostat field was calculated by taking the mean of the $U_{A_{coll},h}$ time series.

$$U_{A_{coll},h} = \begin{cases} 1; & \text{if } \dot{Q}_{sol,net,h} \le \dot{Q}_{HG\text{-}(NGR)}^{T_g\text{-}R} \\ \left(\dfrac{\left(\dot{m}_{C+B} \times \dot{Q}_{HG}^{T_g\text{-}R} \right)_h}{\dot{Q}_{sol,net,h}} \right); & \text{if } \dot{Q}_{sol,net,h} > \dot{Q}_{HG\text{-}(NGR)}^{T_g\text{-}R} \end{cases} \quad (10)$$

3. RESULTS

3.1. Hybrid Solar CTL System (CTL_{sol}). *3.1.1. Reactor Pressure.* Figures 4 and 5 present the dependence on the gasification reactor pressure of the CTL_{sol} system's specific net electrical (W_{net}/Q_{coal}) and FTL (Q_{FTL}/Q_{coal}) output. Figure 4 shows that W_{net}/Q_{coal} is increased by 21% (at 1100 °C) and 29% (at 1400 °C) for an increase in gasifier pressure from 1 to 4 bar-a. In contrast, Figure 5 shows the CTL_{sol} system's FTL productivity to be fairly insensitive to gasification pressure for both gasification temperatures presented. Indeed, the difference between the maximum and minimum Q_{FTL}/Q_{coal} or both curves was calculated to be less than 1% across the temperature range of 1100–1400 °C. Further, it is important to note that Q_{FTL}/Q_{coal} is 6–8 times larger than W_{net}/Q_{coal} for all reactor pressure and temperature scenarios. Hence, the overall energetic performance of the CTL_{sol} polygeneration system is largely insensitive to gasifier pressure. This is an important result given the significant technical challenges associated with the feasible operation of a windowed solar vortex reactor at elevated pressures and temperatures >1100 °C.[15−17]

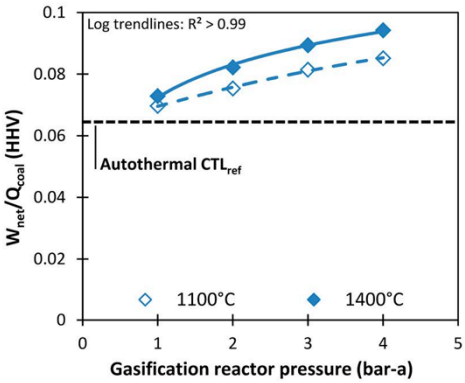

Figure 4. Dependence on the gasification pressure (bar-a) of the CTL_{sol} system's net electrical output normalized by the coal input on a higher heating value basis, for T_g = 1100 and 1400 °C. Assumptions: A_{coll} = 63 × 10^3 m^2, $\dot{m}_{(1.2,0.8)}$ kg/s coal flow flexibility operational scenario.

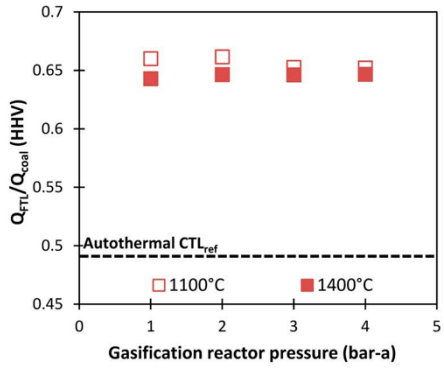

Figure 5. Dependence on the gasification pressure (bar-a) of the CTL_{sol} system's FTL production normalized by the coal input on a higher heating value basis, for T_g = 1100 and 1400 °C. Assumptions: A_{coll} = 63 × 10^3 m^2, $\dot{m}_{(1.2,0.8)}$ kg/s coal flow flexibility operational scenario.

dx.doi.org/10.1021/ef400217n | Energy Fuels 2013, 27, 3556–3569

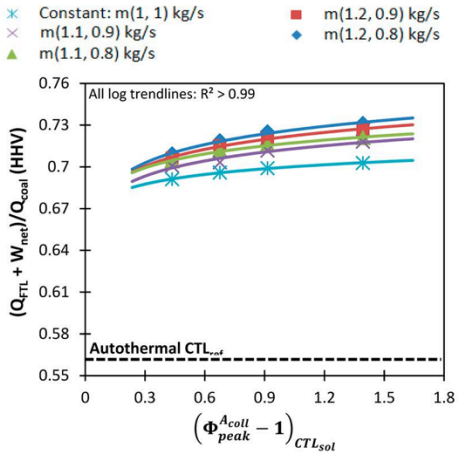

Figure 6. Dependence of the CTL_{sol} system's total energetic productivity on the normalized representation of the excess heliostat collection capacity, for four operational flexibility scenarios denoted in terms of the $\dot{m}_{(max,min)}$ kg/s limit on the fuel flow rate to the hybrid gasifier. Assumptions: T_g = 1100 °C and P_g = 1 bar-a.

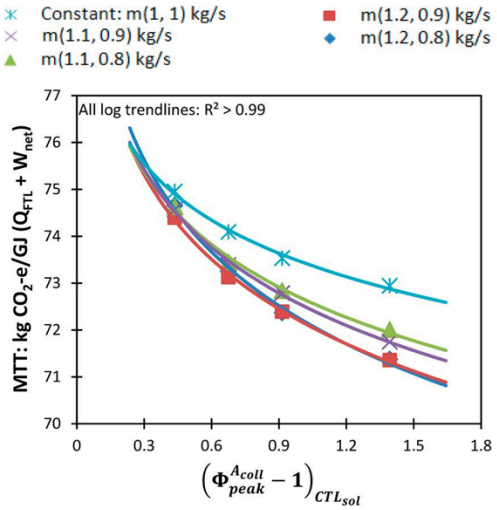

Figure 7. Dependence of the CTL_{sol} system's mine-to-tank (MTT) GHG emissions on the normalized representation of the excess heliostat collection capacity, for four operational flexibility scenarios denoted by the $\dot{m}_{(max,min)}$ kg/s limit on the fuel flow rate to the hybrid gasifier. Assumptions: T_g = 1100 °C and P_g = 1 bar-a.

3.1.2. Fuel Flow Flexibility. Figure 6 presents the dependence of the CTL_{sol} system's specific total energetic productivity $-(W_{net} + Q_{coal})/Q_{coal}$ on the normalized heliostat collection capacity, $\Phi^{A_{coll}}_{peak} - 1$, for five cases of fuel boost/turn-down, that is, $\dot{m}_{(max,min)}$). In all cases, the total productivity increases with heliostat collection area, as expected. However, the dependence on $\Phi^{A_{coll}}_{peak} - 1$ is relatively weak, so that increasing it by a factor of 3.2 increases the energetic productivity by ~2−3% relative to the autothermal CTL_{ref} system. Significantly, a greater benefit is achieved by introducing a flexible flow rate, with the $\dot{m}_{(1.2,0.8)}$ kg/s coal flow flexibility scenario estimated to improve the CTL_{sol} system's specific, total energetic productivity by 25−29% relative to the CTL_{ref} autothermal polygeneration system. This constitutes an improvement of 3−5 percentage points over the estimated improvement in energetic productivity for the constant flow rate CTL_{sol} operational scenario (for $0.44 < \Phi^{A_{coll}}_{peak} - 1 < 1.39$). The improvement in energetic output for the $\dot{m}_{(1.1,0.9)}$ kg/s operational flexibility scenario is 23−26% relative to the CTL_{ref} system over the range of A_{coll} scenarios studied. Given the heliostat field has a high capital cost, the capacity to control the fuel input to the hybrid gasifier could deliver a significant economic benefit.

Figure 7 presents the dependence of the CTL_{sol} system's mine-to-tank CO_2-e emissions on $\Phi^{A_{coll}}_{peak} - 1$ for the same set of scenarios as Figure 6. For this case, the dependence on A_{coll} is greater than that on turn-down over these ranges. Relative to the constant flow rate scenario, the $\dot{m}_{(1.2,0.8)}$ and $\dot{m}_{(1.2,0.9)}$ kg/s coal flow flexibility scenarios are predicted to enable a modest 2% reduction in emissions for $A_{coll} = 63 \times 10^3$ m^2. Consistent with Kaniyal et al.,[10] tank-to-wheel emissions were found to not vary appreciably from 63 kg CO_2-e/GJ ($Q_{FTL} + W_{net}$) for the set of operational scenarios examined here. It is thus apparent that the benefit of operational flexibility in the fuel feed rate to the hybrid gasifier is largely to improve the productivity of the CTL_{sol} system's energetic output rather than influence its GHG emissions performance. Also, as expected, there is a benefit to energetic productivity of turning up the fuel flow rate to the gasifier, and hence to having a hybrid gasifier with a larger thermal throughput capacity with excess heliostat collection capacity.

Capital Utilization Analysis. Figure 8 presents the normalized probability distribution of the hourly averaged utilization of the $U_{A_{coll}h}$ of the installed heliostat capacity for three coal flow rate flexibility scenarios. These probabilities were calculated only for the cases when the solar input to the reactor exceeds the reradiation losses, that is, when $\eta_{abs} > 0$, to avoid the large nocturnal peak that would otherwise dominate the distribution. It also combines the cases with different minimum mass flow rates into one curve since only the maximum limit on the range of fuel flow rate flexibility was found to influence the utilization of the heliostat field. This figure shows that the highest peak in the distribution corresponds to full utilization of the installed heliostat

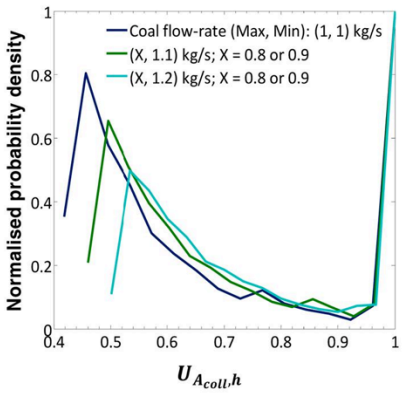

Figure 8. Normalized probability density distribution of the hourly averaged utilization of the installed heliostat collection capacity for three coal flow rate scenarios. These distributions are presented only for positive solar inputs to avoid the large nocturnal peak for clarity. Assumptions: $A_{coll} = 63 \times 10^3$ m^2, gasification at 1100 °C and 1 bar-a.

dx.doi.org/10.1021/ef400217n | *Energy Fuels* 2013, 27, 3556−3569

collection capacity (i.e., $U_{A_{coll},h} = 1$). These periods of full utilization occur when $\Phi \leq 1$ and can largely be attributed to solar hours in winter and at dusk/dawn when insolation is inherently low. However, the area under this part of the curve is low relative to the more significant peak in the distribution when $U_{A_{coll},h}$ is between 46 and 54%. This more significant peak corresponds to periods of seasonally high solar insolation when the maximum solar output of the heliostat field is approximately double the hybrid gasifier's endothermic demand. Here, operation of the hybrid gasifier with the flexibility to increase the coal flow rate to the hybrid gasifier to up to 1.2 kg/s from 1.0, when sufficient solar energy is available, reduces the magnitude of the dominant peak by 38% and thus the annually averaged utilization of the heliostat collection capacity from 67 to 76%. The flexibility to boost the fuel flow rate to the gasifier up to the intermediate value of 1.1 kg/s from 1.0 reduces by 20% the size of the dominant peak in the distribution and by 7% the annual average utilization of the heliostat field.

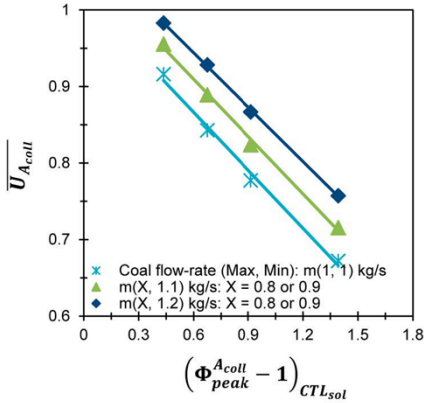

Figure 9. Dependence of the annually averaged utilization of the installed heliostat collection capacity on the normalized excess heliostat collection capacity for the CTL_{sol} polygeneration system and for three coal flow rate flexibility scenarios. The curves with different minimum limit on the coal flow rate are combined because this parameter was found not to effect the utilization of the heliostat field.

Figure 9 presents the dependence of the annually averaged utilization of the heliostat field ($\overline{U_{A_{coll}}}$) on the excess heliostat field area, $(\Phi_{peak}^{A_{coll}} - 1)_{CTL_{sol}}$. This shows that allowing a boost in the maximum coal flow rate to the gasifier of up to 1.2 kg/s, from 1 kg/s, increases $\overline{U_{A_{coll}}}$ by 6−13% for a given $\Phi_{peak}^{A_{coll}} - 1$ range. In comparison, an intermediate maximum coal flow rate of 1.1 kg/s leads to a 4−7% improvement in $\overline{U_{A_{coll}}}$ over the constant flow rate hybrid gasifier operational scenario.

Figure 10 also shows that the hybrid gasifier's annually averaged utilization, $\overline{U_{HG}}$ is fairly insensitive to $\Phi_{peak}^{A_{coll}} - 1$ but very sensitive to the fuel turn-down/boost operational scenario. Relative to the constant flow rate scenario, the $\overline{U_{HG}}$ is shown to fall by 12 percentage points for the $\dot{m}_{(1.1,0.9)}$ kg/s operational scenario and to fall by 24 percentage points for the $\dot{m}_{(1.2,0.8)}$ kg/s scenario. Interestingly, the $\dot{m}_{(1.2,0.9)}$ and $\dot{m}_{(1.1,0.9)}$ kg/s scenarios are estimated to both yield $\overline{U_{HG}} \sim 82\%$. Importantly, flexibly

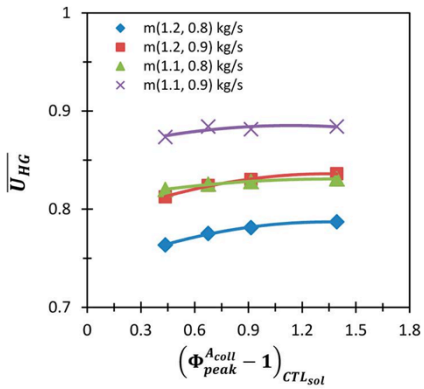

Figure 10. Dependence of the annually averaged utilization of the hybrid gasifier on the normalized excess heliostat collection capacity for the CTL_{sol} polygeneration system, for four coal flow operational flexibility scenarios.

boosting or turning down the flow rate has a larger influence on $\overline{U_{HG}}$ than does varying the heliostat collection area.

Taken together, Figures 9 and 10 highlight the inevitable trade-off between maximizing the economic utilization of the heliostat field and the hybrid solar gasifier. Maximizing the utilization of the heliostat field compromises the utilization of the hybrid gasifier, but this has the benefit of increasing the solar share of the process and thus the energetic and GHG emissions performance of the CTL_{sol} polygeneration system. Note that Figures 9 and 10 also assume that the dynamic variation in fuel flow to the reactor does not significantly influence either the scheduled or unscheduled plant maintenance. While yet to be confirmed, this assumption is considered to be reasonable because these turn-down/fuel-boost ratios are comparable with standard ratios of similar commercial gasification equipment.[43]

3.2. Hybrid Solar Coal Gasification Integrating Dry/Steam Natural Gas Reformer ($CTL_{sol,NG(dry/steam)}$). Figure 11 compares the effect of incorporating dry reforming or steam co-reforming of natural gas with the CTL_{sol} polygeneration system on the calculated mine-to-tank (MTT) CO_2-e emissions as a function of the normalized excess heliostat collection capacity $(\Phi_{peak}^{A_{coll}} - 1)_{CTL_{sol,(NG)}}$. It can be seen that both the $CTL_{sol,NG(dry)}$ and $CTL_{sol,NG(steam)}$ systems enable approximately the same reduction in emissions of ~15 ± 1.5 kg CO_2-e/GJ (Q_{FTL} + W_{net}) relative to the CTL_{sol} system. Relative to the autothermal CTL_{ref} system, this constitutes a 43−46% reduction in emissions, which corresponds to a further 12 percentage point reduction over that enabled by the CTL_{sol} system. Figure 11 also shows that there is little benefit to the GHG emissions from extending the excess heliostat collection capacity above 50%. Importantly, both $CTL_{sol,NG}$ systems examined produce ~32 kg CO_2-e/GJ (Q_{FTL} + W_{net}) more emissions than do the tar-sands-derived diesel, which is the most carbon intensive form of diesel currently in production.[5] That is, the use of solar energy alone, with 70−30% calorific fraction of coal to natural gas, in a hybrid gasification, co-reforming process, is not sufficient to achieve parity with conventional diesel production. Hence, additional approaches are required, such as blending with biomass.

Figure 12 presents the energetic performance of both the CTL_{sol} and $CTL_{sol,NG(dry)}$ and $CTL_{sol,NG(steam)}$ systems as a

dx.doi.org/10.1021/ef400217n | Energy Fuels 2013, 27, 3556−3569

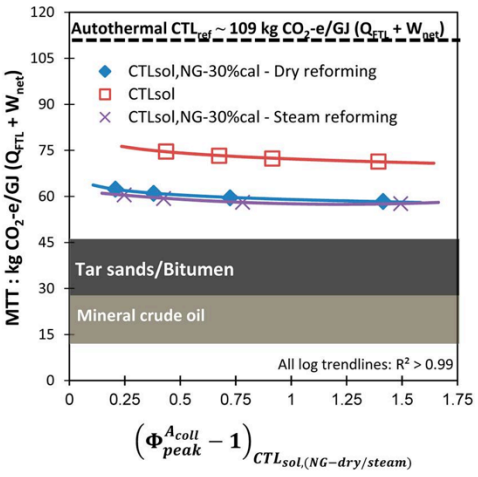

Figure 11. Dependence of mine-to-tank (MTT) CO_2-e emissions on the normalized heliostat collection area for the CTL_{sol} and $CTL_{sol,NG(dry)}$ and $CTL_{sol,NG(steam)}$ systems. Assumptions: coal gasification T_g = 1100 °C; $\dot{m}_{(1.2,0.8)}$ kg/s flexibility in coal flow; natural gas dry/steam internal reforming at 1050 °C, 11 bar-a, with no flexibility in NG flow in response to solar insolation.

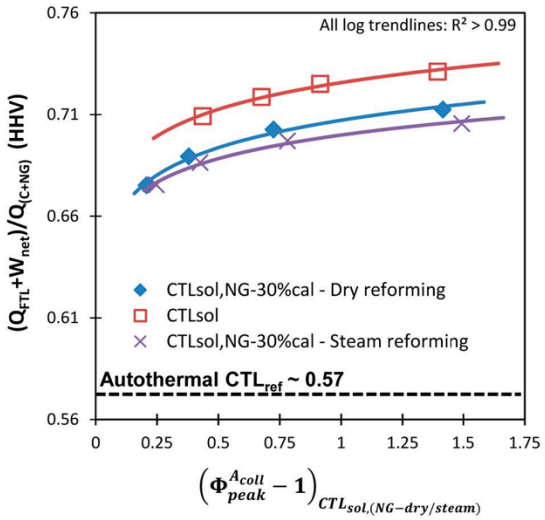

Figure 12. Dependence of total energetic productivity on the normalized heliostat collection area for the CTL_{sol} and $CTL_{sol,NG(dry)}$ and $CTL_{sol,NG(steam)}$ systems. Assumptions: coal gasification T_g = 1100 °C; $\dot{m}_{(1.2,0.8)}$ kg/s coal flow flexibility operational scenario; natural gas dry/steam internal reforming at 1050 °C, 11 bar-a, with no flexibility in NG flow in response to solar insolation.

function of $(\Phi_{peak}^{A_{coll}} - 1)_{CTL_{sol,(NG)}}$. This shows that the energetic productivity increases significantly with A_{coll} for all cases throughout the range. Interestingly, a small but significant reduction of 2 percentage points is estimated for the $CTL_{sol,NG(dry)}$ and $CTL_{sol,NG(steam)}$ systems, relative to the CTL_{sol} system for A_{coll} = 89 × 10^3 m^2 and a 5 percentage points reduction for A_{coll} = 44 × 10^3 m^2. Furthermore, the $CTL_{sol,NG(dry)}$ and $CTL_{sol,NG(steam)}$ systems enable, respectively, a 34 or 32% increase in the absolute energetic output relative to the CTL_{sol} configuration.

Figure 13 presents the relationship between the solar share of the CTL_{sol}, the $CTL_{sol,NG(dry)}$, and the $CTL_{sol,NG(steam)}$ systems'

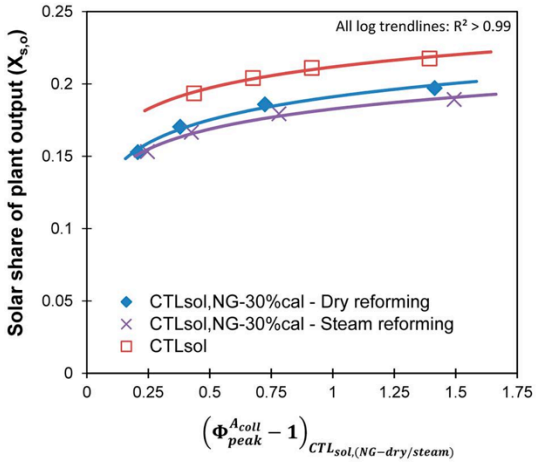

Figure 13. Dependence of the solar share of plant output ($X_{s,o}$) from Sheu et al.[6] on the normalized heliostat collection area for the CTL_{sol} and $CTL_{sol,NG(dry)}$ and $CTL_{sol,NG(steam)}$ systems. Assumptions: coal gasification T_g = 1100 °C; $\dot{m}_{(1.2,0.8)}$ kg/s coal flow flexibility operational scenario; natural gas dry/steam internal reforming at 1050 °C, 11 bar-a, with no flexibility in NG flow in response to solar insolation.

individual net energetic output as a function of $(\Phi_{peak}^{A_{coll}} - 1)_{CTL_{sol,(NG)}}$. It can be seen that the solar share of the output increases with the size of the normalized heliostat collection capacity for all scenarios, by approximately three percentage points from 19 to 22% for the CTL_{sol} system, 15 to 20% for the $CTL_{sol,NG(dry)}$, and 15 to 19% for the $CTL_{sol,NG(steam)}$ systems. This result shows that the integration of the natural gas co-reforming system decreases the solar share of the polygeneration system as the solar upgrade achieved by natural gas reforming is smaller than that achieved by coal gasification.

Nevertheless, given the low expected cost[13] of integrating a NG co-reforming system within an entrained flow autothermal gasifier, its integration within a hybrid solar gasifier could enable significant improvements to the economic productivity of the reactor assembly, heliostat collection field, and downstream unit operations. It should be clear, however, that this expectation of a low cost of integration is based on the balance-of-plant savings that are assumed to apply to the proposed solar integrated, $CTL_{sol,NG}$ polygeneration system as they do for the equivalent autothermal polygeneration system.[13] The $CTL_{sol,NG(dry)}$ system's annually averaged $\overline{U_{A_{coll}}}$ is estimated to be between 7 (A_{coll} = 44 × 10^3 m^2) and 13 (A_{coll} = 63 × 10^3 m^2) percentage points larger than the CTL_{sol}, assuming the $\dot{m}_{(1.1,0.9)}$ kg/s flexibility case (see Figure 11). This is an important result as the hybrid solar vortex gasifier[2,13,25−29] and heliostat field[30,39] are likely to be the most expensive components of a CTL_{sol} polygeneration facility.

Interestingly, while the addition of either dry or steam reforming to the solar-hybridized gasification process yields significant benefits that are broadly similar (Figure 12), there are some small differences. Unlike in Figure 11, where the emissions of the $CTL_{sol,NG(dry)}$ system converge to match those of the $CTL_{sol,NG(steam)}$ system as the excess collection capacity is increased, the energetic productivity of the two systems

dx.doi.org/10.1021/ef400217n | Energy Fuels 2013, 27, 3556−3569

diverges with increasing excess field capacity. This is a result of the $CTL_{sol,NG(dry)}$ system's larger total endothermic demand (see Table 2), which enables it to consume more of the solar energy that becomes available as the excess heliostat collection capacity is increased. However, the $CTL_{sol,NG(dry)}$ system's larger energetic productivity is balanced by the low H_2/CO ratio of the raw syngas output from the co-reformer, leading to its WGS upgrading process producing 3% more CO_2-e emissions than the $CTL_{sol,NG(steam)}$ WGS process. This leads to the two systems having approximately the same CO_2-e emissions profile in Figure 11.

3.3. Hybrid Solar Coal-Biomass to Liquids ($CTL_{sol,bio}$) System. Figure 14 presents the mine-to-tank (MTT) CO_2-e emissions from the $CTL_{sol,bio}$ system as a function of the biomass fuel weight fraction (m_B/m_{C+B}). Also shown is a comparison of the $CTL_{sol,bio}$ system's CO_2-e emissions performance with that of the nonsolar, autothermal CTL_{bio} polygeneration system. The calculated MTT CO_2-e emissions of the $CTL_{sol,bio}$ system were credited with the proportion of biomass, on a carbon mol fraction basis, combusted at the point of end-use. Figure 14 shows that the $CTL_{sol,bio}$ system achieves CO_2-e emissions parity with the upper limit of conventional diesel from tar sands for $m_B/m_{C+B} \sim 0.3$.[5] In comparison, emissions from the nonsolar CTL_{bio} system are calculated to match those of diesel derived from tar sands for $m_B/m_{C+B} \sim 0.45$.[5] For $m_B/m_{C+B} \sim 0.53$, the $CTL_{sol,bio}$ system's energetic output achieves lower GHG emissions than all forms of mineral crude currently in production.[4] Additionally, the $CTL_{sol,bio}$ system's MTT emissions are reduced to 0 for a biomass cogasification weight fraction of 60%, while the comparable autothermal CTL_{bio} system requires a biomass cogasification weight fraction of 70%. Furthermore, the CO_2-e emissions avoidance potential of the solar biomass-to-liquids, BTL_{sol} ($m_B/m_{C+B} = 1$) system is 13% higher on a MTT basis, than the nonsolar, autothermal CTL_{bio} polygeneration system, after accounting for the molar proportion of biomass-derived carbon burnt at the point of end-use. As expected, the percentage contribution of solar energy to the reduction in CO_2 emissions decreases with increasing m_B/m_{C+B} because the calorific content of coal is 1.36 times that of biomass on a mass basis. The potential for the solar-hybridized cogasification process to significantly reduce the amount of biomass required to meet a given CO_2-e emissions standard is important given biomass is typically three to four times more expensive than coal.

Figure 15 presents the total energetic productivity of the $CTL_{sol,bio}$ and the nonsolar, autothermal CTL_{bio} cases, as a function of the biomass fuel weight fraction (m_B/m_{C+B}). Here, the difference between the dotted and solid lines shows that the solar hybridization of the coal-biomass cogasification process increases by 27−33% the $CTL_{sol,bio}$ system's total specific energetic productivity over the range of biomass weight fractions from 0 to 100%. It is interesting to note that the BTL_{sol} system can yield 104% of the autothermal CTL_{ref} system's energetic productivity, whereas the autothermal, nonsolar BTL system yields only 72% of the autothermal CTL_{ref} system's energetic productivity. The improved energetic productivity of the solar-hybridized cogasification process is expected to significantly improve the viability of producing biofuels relative to the nonsolar autothermal process, especially because the cost of biomass is typically three to four times higher than that of coal.[34−36]

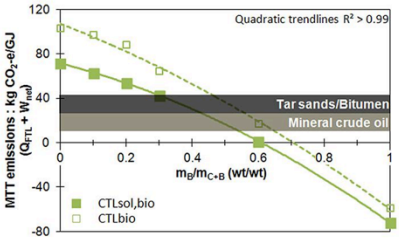

Figure 14. Dependence of the mine-to-tank (MTT) CO_2-e emissions of the $CTL_{sol,bio}$ system and the nonsolar, autothermal CTL_{bio} polygeneration system on the biomass blend fraction by weight (m_B/m_{C+B}). Assumptions: coal-biomass cogasification at T_g = 1100 °C; $\dot{m}_{(1.2,0.8)}$ kg/s flexibility in the blended fuel flow to gasifier; A_{coll} = 63 × 10^3 m^2.

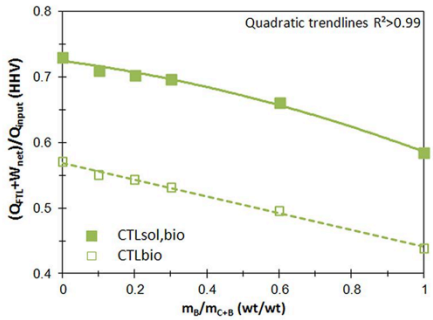

Figure 15. Dependence of the total specific energetic productivity of the $CTL_{sol,bio}$ system and the nonsolar, autothermal CTL_{bio} polygeneration facility on the biomass blend fraction by weight (m_B/m_{C+B}). Assumptions: coal-biomass cogasification at T_g = 1100 °C, P_g = 1 bar-a; $\dot{m}_{(1.2,0.8)}$ kg/s flexibility in the blended fuel flow to gasifier; A_{coll} = 63 × 10^3 m^2.

3.4. Steam Consumption. Figure 16 presents the annually averaged consumption of steam by the hybrid gasifier for the reference hybrid solar gasifier in comparison with three other cases. It can be seen that the CTL_{sol} system consumes ∼2% more steam than the CTL_{ref} system, while the $CTL_{sol,bio\text{-}60wt\%}$ process consumes 20% less. The $CTL_{sol,NG(dry)}$ system has the highest specific rate of steam consumption, which is an additional 7% per mole of SG_{up} than the CTL_{ref} system. In comparison with the dry reforming integrated process, the $CTL_{sol,NG(steam)}$ consumes 10% less steam than the CTL_{ref} system.

Interestingly, Figure 16 also shows that over 74% of the $CTL_{sol,NG(steam)}$ system's total steam consumption can be attributed to co-reformer section of the hybrid gasifier, whereas it is ∼31% for the $CTL_{sol,NG(dry)}$ configuration. The balance of the steam for both processes is consumed in the water−gas shift reactor, WGSR. The proportion of steam consumed by the solar-intensive hybrid gasification/co-reforming relative to the WGSR is an important issue as the most productive solar resources are often in arid regions where access to fresh water is difficult. One advantage of the $CTL_{sol,NG(dry)}$ process is that the gasifier section requires a proportionally low level of steam consumption relative to all other configurations (other than the 60 wt % biomass cogasification configuration). This advantage enables the option to separate the solar energy intensive gasification/dry co-reforming process' from the water-intensive downstream processes to a site where water availability is less constrained.

dx.doi.org/10.1021/ef400217n | Energy Fuels 2013, 27, 3556−3569

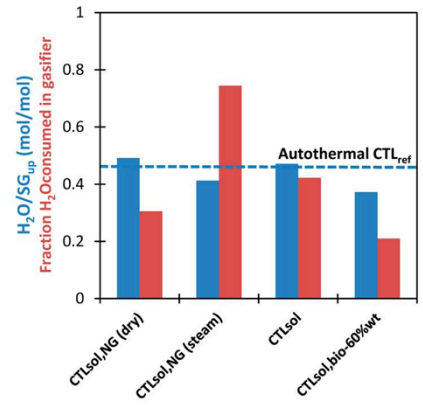

Figure 16. Annually averaged ratio of the total molar steam consumption to the production of upgraded syngas ($SG_{up}/H_2/CO \sim 2.26$) (blue); annually averaged fraction of steam consumed by the hybrid gasifier relative to the total (red) for four CTL_{sol} plant scenarios and the CTL_{ref} system.

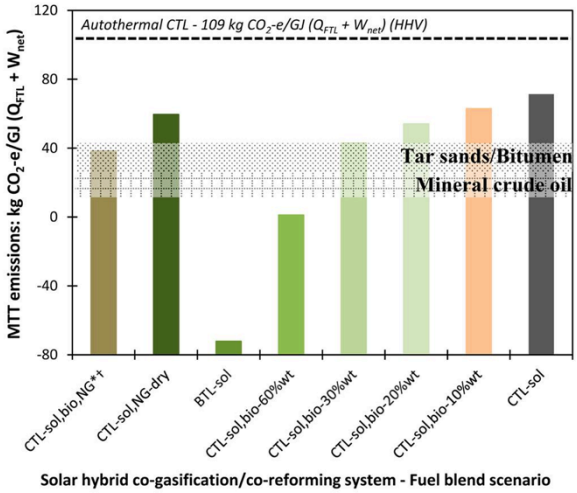

Figure 17. Summary of the mine-to-tank (MTT) CO_2-e emissions performance of the CTL_{sol} base system for all range of fuel blend scenarios ($*m_B/m_{C+B}$ = 30 wt %, $^{\dagger}Q_{NG}/Q_{total}$ = 30% cal). All scenarios are based on the $\dot{m}_{(1.2,0.8)}$ kg/s operational flexibility scenario in solid (biomass-coal blend) fuel flow, $A_{coll} = 63 \times 10^3$ m^2, T_g = 1100 °C, and P_g = 1 bar-a.

3.5. Overall Scenario Comparison. Figures 17 and 18 summarize the MTT CO_2-e emissions and total energetic productivity (HHV) for eight key scenarios of fuel blends and hybrid solar gasification reactor configurations. In particular, Figure 17 shows that the use of solar gasification with a 30% blend of biomass (the $CTL_{sol,bio\text{-}30wt\%}$ case) achieves CO_2-e emissions parity with that of conventional production of synthetic crude from tar sands, while the further incorporation of a natural gas dry co-reformer as part of the $CTL_{sol,bio\text{-}30\%wt,NG}$ system achieves an additional 10% reduction in MTT emissions. On a mine-to-tank basis, the $CTL_{sol,bio\text{-}60wt\%}$ system produces 0 CO_2-e emissions and the solar gasification with pure biomass enables a net avoidance of 72 kg CO_2-e/GJ (Q_{FTL} + W_{net}) on a MTT basis. It is important to note that these CO_2-e

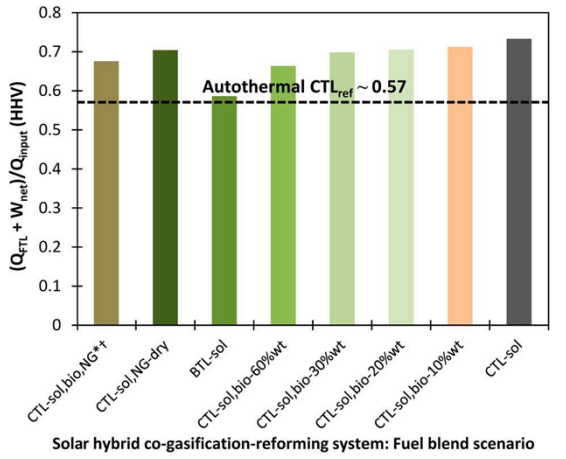

Figure 18. Summary of the total energetic productivity of the CTL_{sol} base system for a range of fuel blend scenarios ($*m_B/m_{C+B}$ = 30 wt %, $^{\dagger}Q_{NG}/Q_{total}$ = 30% cal). All scenarios are based on the $\dot{m}_{(1.2,0.8)}$ kg/s operational flexibility scenario in solid (biomass-coal blend) fuel flow, $A_{coll} = 63 \times 10^3$ m^2, T_g = 1100 °C, and P_g = 1 bar-a.

emissions results are credited with the molar proportion of biomass that is burnt at the point of end-use.

Figure 18 shows the $CTL_{sol,bio,NG}$ system to have 95% of the energetic productivity of the $CTL_{sol,bio\text{-}30wt\%}$, but this corresponds to a 37% improvement on an absolute energy output basis. This has important implications for the economic productivity of the hybrid cogasification reactor system. On the far right of the two distributions, the $CTL_{sol,NG}$ system has 94% of the carbon emissions of the $CTL_{sol,bio\text{-}10wt\%}$ configuration but energetic productivity that is only 2% lower.

It is worth noting that all of the results presented in Figures 17 and 18 are based on the $\dot{m}_{(1.2,0.8)}$ kg/s operational flexibility scenario in solid fuel flow to the gasifier. The sensitivity to variations in pressure and heliostat area is likely to be similar to the analysis presented in section 3.1.2 .

4. CONCLUSIONS

The incorporation of concentrated solar radiation into a coal-to-liquids, coal-natural-gas-to-liquids process or into a coal-biomass-to-liquids process offers significant potential advantages both to the energetic productivity of the polygeneration system and to lowering its mine-to-tank CO_2-e emissions intensity. In particular, solar hybridization decreases by up to 33% the weight fraction of biomass required to meet the CO_2-e emissions associated with diesel derived from tar sands and reduce by 17% the weight fraction required to eliminate CO_2-e emissions at production altogether relative to the autothermal cogasification-based, coal-biomass-to-liquids process. This may enable a significant economic advantage given that biomass has typically been 3−4 times more expensive than coal.[31,34−36]

The incorporation of an indirectly irradiated solar hybrid steam natural gas reformer within the hybrid gasifier ($CTL_{sol,NG}$) was shown to improve by 33% the system's absolute energetic output, reduce by 15% its GHG emissions, and improve by 15% the annually averaged utilization of a heliostat field with $A_{coll} = 63 \times 10^3$ m^2, relative to the CTL_{sol} system. Importantly, the dry co-reformer was found to halve the combined hybrid gasifier/co-reformer assembly's rate of water consumption relative to the steam co-reformer, while achieving

dx.doi.org/10.1021/ef400217n | Energy Fuels 2013, 27, 3556−3569

similar levels of improvement to the polygeneration system's energetic and environmental performance. Although, the low water consumption intensity of the hybrid gasifier/dry co-reformer is balanced by the higher consumption of water by the process' water-gas shift reactor relative to the system incorporating a steam co-reformer this is still an important result. Given the generally poor availability of fresh water in arid regions where the solar resource is most productive, the dry co-reforming process is a feasible path to reducing the steam consumption of the solar intensive section of the $CTL_{sol,NG}$ polygeneration process.

It is further found that both the energetic productivity and greenhouse gas mitigation could be improved by 4% and capital utilization of the heliostat array by up to 13% for $A_{coll} = 63 \times 10^3$ m^2 if the fuel feed rate to the hybrid gasifier could be varied flexibly by ±20% relative to the nominal design value of 1 kg/s in response to transient fluctuations in solar input. Interestingly, the present assessment also found that the overall energetic performance of the hybrid system is only weakly sensitive to gasifier operating pressure. This is because the FTL liquid heating value forms >85% of the net energy output. This is significant, as operation of a solar gasifier at atmospheric pressure increases the viability of using direct solar radiation heat transfer, notably by increasing the feasibility of a window or aperture through which the solar radiation can be introduced into the reactor.

■ AUTHOR INFORMATION

Corresponding Author

*E-mail: ashok.kaniyal@adelaide.edu.au. Phone: +61403691321.

Notes

The authors declare no competing financial interest.

■ ACKNOWLEDGMENTS

A.A.K. would like to thank the generous support of Ricoh for providing the Clean Energy Scholarship. P.J.vE. would like to acknowledge the support of the Australian Solar Institute (ASI) for providing a postdoctoral fellowship. The Australian Government, through the ASI, is supporting Australian research and development in solar photovoltaic and solar thermal technologies to help solar power become cost competitive with other energy sources. G.J.N. wishes to thank the Australian Research Council (ARC) for the Discovery Outstanding Researcher Award in the thermal applications of concentrated solar radiation. The authors gratefully acknowledge the financial and other support received for this research from the Energy Pipelines Cooperative Research Centre (EPCRC) which was established under the Australian Government's Cooperative Research Centre's program.

■ NOMENCLATURE

A_{coll} – heliostat field area (m^2)
AR – as received
BTL – biomass to liquids polygeneration system
cal – calorific fraction (%)
CCS – carbon capture and storage technology
CTL – coal to liquids polygeneration system
d.a.f. – dry, ash-free basis
FT – Fischer−Tropsch reactor
FTL – Fischer−Tropsch liquid fuels
GHG – greenhouse gas
$\dot{m}$ or m – fuel mass flow rate (kg/s) or fuel mass (kg)
mol – molar fraction
MTT – mine-to-tank CO_2-e emissions
NGR – natural gas reformer
$\dot{Q}$ or Q – thermal power or heat
$\bar{U}$ – average capital utilization
$\dot{W}$ or W – power or work output
wt – weight (%)
$\dot{m}_Y$ – flow rate of fuel "Y" in kg/s; where Y can be coal, natural gas, or a coal-biomass blend
HHV – higher heating value

Greek letters

Φ – ratio of the net solar thermal power output from the heliostat array($\dot{Q}_{sol,net}$) to the total endothermic demand of completely gasifying the fuel fed into the hybrid gasifier and co-reformer (if applicable) at an assumed reactor temperature ($\dot{Q}_{HG,(NRG)}^{T_g\text{-}R}$)
η – efficiency
$\Phi_{peak}^{A_{coll}} - 1$ – fraction by which the annual peak net solar thermal power output of the heliostat array exceeds the gasifier's total endothermic demand

Superscripts

ann. peak – peak hourly averaged value from a year-long time series
NGR – refers to thermal power required by the natural gas (dry/steam) reformer to completely convert $\dot{m}_{NG}$ kg/s of fuel to raw syngas
T_g-R – temperature at which gasification reactions occur

Subscripts

abs – solar energy absorption efficiency
ann – parameter based on year-long time series
B – biomass fuel
bio-Xwt% – cogasification of X wt% biomass with coal
C+B – coal + biomass fuel blend
C – coal fuel
dry – CO_2 natural gas reforming
FTL – Fischer−Tropsch liquids
HG – hybrid, entrained flow solar gasifier
isen – isentropic efficiency of compressors/turbines
(min,max) – the minimum and maximum values of an operating range
net – net (of parasitic losses) electrical output or flow of thermal power from the heliostat field to the solar hybrid reactor (net of optical and reradiation losses)
NG – natural gas fuel
opt – heliostat field optical efficiency
R – thermal power required to enable conversion of 99% of design coal at a fuel flow rate of 1 kg/s
raw – syngas output straight from the gasifier
ref – autothermal, reference CTL polygeneration system
sol – solar
steam – steam natural gas reforming
stg – refers to stored levels of O_2 and SG_{up}
total – calorific value of total fuel input to the solar hybrid cogasification, co-reforming reactor
up – upgraded syngas output from the sweet WGSR (H_2/CO = 2.26:1)

wall – heat losses through the walls of the entrained flow gasifier

REFERENCES

(1) Takeshita, T.; Yamaji, K. Important roles of Fischer−Tropsch synfuels in the global energy future. *Energy Policy* **2008**, *36*, 2773−2784.

(2) Liu, G.; Larson, E.; Williams, R.; Kreutz, T.; Guo, X. Making Fischer−Tropsch fuels and electricity from coal and biomass: performance and cost analysis. *Energy Fuels* **2011**, *25*, 415−437.

(3) Meerman, J.; Ramirez, A.; Turkenburg, W.; Faaij, A. Performance of simulated flexible integrated gasification polygeneration facilities. Part A: A technical-energetic assessment. *Renew. Sustain. Energy Rev.* **2011**, *15*, 2563−2587.

(4) Gerdes, K.; Skone, T. J. *An Evaluation of the Extraction, Transport and Refining of Imported Crude Oils and the Impact on Life Cycle Greenhouse Gas Emissions*; NETL: Pittsburgh, PA, 2009; p 42.

(5) Lattanzio, R. *Canadian Oil Sands: Life-Cycle Assessments of Greenhouse Gas Emissions*; Congressional Research Service: Washington DC, 2012; p 31.

(6) Sheu, E.; Mitsos, A.; Eter, A.; Mokheimer, E.; Habib, M.; Al-Qutub, A. A review of hybrid solar-fossil fuel power generation systems and performance metrics. *J. Solar Energy Eng.* **2012**, 134.

(7) Kribus, A.; Zaibel, R.; Carey, D.; Segal, A.; Karni, J. A solar-driven combined cycle power plant. *Sol. Energy* **1998**, *62*, 121−129.

(8) Ordorica-Garcia, G.; Delgado, A.; Garcia, A. Novel integration options of concentrating solar thermal technology with fossil-fuelled and CO_2 capture processes. *Energy Procedia* **2011**, *4*, 809−816.

(9) Nathan, G.; Battye, D.; Ashman, P. Economic evaluation of a novel fuel-saver hybrid combining a solar receiver with a combustor for a solar power tower. *Appl. Energy* **2012**, submitted for review.

(10) Kaniyal, A.; van Eyk, P.; Nathan, G.; Ashman, P.; Pincus, J. Polygeneration of liquid fuels and electricity by the atmospheric pressure hybrid solar gasification of coal. *Energy Fuels* **2013**, submitted for review.

(11) Turchi, C.; Ma, Z.; Erbes, M. Gas turbine/solar parabolic trough hybrid designs. In *ASME Turbo Expo 2011*, NREL: Vancouver, Canada, 2011.

(12) Sudiro, M.; Bertucco, A. Synthetic fuels by a limited CO_2 emission process which uses both fossil and solar energy. *Energy Fuels* **2007**, *21*, 3668−3675.

(13) Adams, T., II; Barton, P. Combining coal gasification and natural gas reforming for efficient polygeneration. *Fuel Process. Technol.* **2011**, *92*, 639−655.

(14) Dahl, J.; Weimer, A.; Lewandowski, A.; Bingham, C.; Bruetsch, F.; Steinfeld, A. Dry reforming of methane using a solar-thermal aerosol flow reactor. *Ind. Eng. Chem. Res.* **2004**, *43*, 5489−5495.

(15) Weimer, A. Solar thermal chemical processing challenges and commercial path forward. *Curr. Opin. Chem. Eng.* **2012**, *1*, 211−217.

(16) Trainham, J.; Newman, J.; Bonino, C.; Hoertz, P.; Akunuri, N. Whither solar fuels? *Curr. Opin. Chem. Eng.* **2012**, *1*, 204−210.

(17) Steinfeld, A.; Palumbo, R. Solar thermochemical process technology. In *Encyclopedia of Physical Science & Technology*; Meyers, R., Ed.; Academic Press: New York, 2001; Vol. *15*, pp 237−256.

(18) Opoku-Gyamfi, K.; Adesina, A. Forced composition cycling of a novel thermally self-sustaining fluidised-bed reactor for methane reforming. *Chem. Eng. Sci.* **1999**, *54*, 2575−2583.

(19) ABARES, Australian Energy Resource Assessment. In *ABARES*; Australian Government: Canberra, 2010.

(20) Sun, Y.; Ritchie, T.; Hla, S.; McEvoy, S.; Stein, W.; Edwards, J. Thermodynamic analysis of mixed and dry reforming of methane for solar thermal applications. *J. Nat. Gas Chem.* **2011**, *20*, 568−576.

(21) Price, L. Origins, characteristics, controls and economic viabilities of deep-basin gas resources. *Chem. Geol.* **1995**, *126*, 335−349.

(22) Z'Graggen, A.; Haueter, P.; Maag, G.; Romero, M.; Steinfeld, A. Hydrogen production by steam-gasification of carbonaceous materials using concentrated solar power - IV. Reactor experimentation with vacuum residue. *Int. J. Hydrogen Energy* **2008**, *33*, 679−684.

(23) Z'Graggen, A.; Haueter, P.; Maag, G.; Vidal, A.; Romero, M.; Steinfeld, A. Hydrogen production by steam-gasification of petroleum coke using concentrated solar power - III. Reactor experimentation with slurry feeding. *Int. J. Hydrogen Energy* **2007**, *32*, 992−996.

(24) Z'Graggen, A.; Steinfeld, A. Hydrogen production by steam-gasification of carbonaceous materials using concentrated solar energy - V. Reactor modeling, optimization and scale-up. *Int. J. Hydrogen Energy* **2008**, *33*, 5484−5492.

(25) Kreutz, T.; Larson, E.; Liu, G.; Williams, R. In *Fischer−Tropsch Fuels from Coal and Biomass*, 25th Ann. Intl Pittsburgh Coal Conference; Pittsburgh, Pennsylvania, 2008.

(26) Kreutz, T.; Williams, R.; Consonni, S.; Chiesa, P. Co-production of hydrogen, electricity and CO_2 from coal with commercially ready technology. Part B: Economic analysis. *Int. J. Hydrogen Energy* **2005**, *30*, 769−784.

(27) Larson, E.; Fiorese, G.; Liu, G.; Williams, R.; Kreutz, T.; Consonni, S. Co-production of decarbonized synfuels and electricity from coal + biomass with CO_2 capture and storage: An Illinois case study. *Energy Environ. Sci.* **2010**, *3*, 28−42.

(28) Meerman, J.; Ramirez, A.; Turkenburg, W.; Faaij, A. Performance of simulated flexible integrated gasification polygeneration facilities, Part B: Economic evaluation. *Renew. Sustain. Energy Rev.* **2012**, *16*, 6083−6102.

(29) Woods, M.; Capicotto, P.; Haslbeck, J.; Kuehn, N.; Matuszewski, M.; Pinkerton, L.; Rutkowski, M.; Schoff, R.; Vaysman, V. *Bituminous Coal and Natural Gas to Electricity Final Report*, DoE/NETL-2007/1281; US DoE, August 2007; Vol. *1*.

(30) Kolb, G.; Jones, S.; Donnelly, M.; Gorman, D.; Thomas, R.; Davenport, R.; Lumia, R. *Heliostat Cost Reduction Study*; Sandia National Laboratories: Alburquerque, NM, 2007; p 158.

(31) Berndes, G.; Hoogwijk, M.; van den Broek, R. The contribution of biomass in the future global energy supply: a review of 17 studies. *Biomass Bioenergy* **2003**, *25*, 1−28.

(32) Baxter, L. Biomass-coal co-combustion: opportunity for affordable renewable energy. *Fuel* **2005**, *84*, 1295−1302.

(33) Kirkels, A.; Verbong, G. Biomass gasification: Still promising? A 30-year global overview. *Renew. Sustain. Energy Rev.* **2011**, *15*, 471−481.

(34) Sami, M.; Annamalai, K.; Woolridge, M. Co-firing of coal and biomass fuel blends. *Prog. Energy Combust. Sci.* **2001**, *27*, 171−214.

(35) De, S.; Assadi, M. Impact of cofiring biomass with coal in power plants—A techno-economic assessment. *Biomass Bioenergy* **2009**, *33*, 283−293.

(36) Tijmensen, M.; Faaij, A.; Hamelinck, C.; van Hardeveld, M. Exploration of the possibilities for production of Fischer−Tropsch liquids and power via biomass gasification. *Biomass Bioenergy* **2002**, *23*, 129−152.

(37) NREL *National Solar Radiation Database Update: User'S Manual*, 1991−2005 update; US DoE; Golden, CO, 2007.

(38) NREL National solar radiation database 1991−2005 update.

(39) Meier, A.; Gremaud, N.; Steinfeld, A. Economic evaluation of the industrial solar production of lime. *Energy Convers. Manage.* **2005**, *46*, 905−926.

(40) Higman, C.; van der Burgt, M. *Gasification*, 2nd ed.; Elsevier: Oxford, UK, 2008.

(41) Melchior, T.; Perkins, P.; Lichty, A.; Weimer, A.; Steinfeld, A. Solar-driven biochar gasification in a particle-flow reactor. *Chem. Eng. Proc.* **2009**, *48*, 1279−1287.

(42) Moghtaderi, B.; Sheng, C.; Wall, T. An overview of the Australian biomass resources and utilization technologies. *BioResources* **2006**, *1*, 93−115.

(43) Marbe, Å.; Harvey, S.; Berntsson, T. Biofuel gasification combined heat and power—new implementation opportunities resulting from combined supply of process steam and district heating. *Energy* **2004**, *29*, 1117−1137.

Page Intentionally Left Blank

Statement of Authorship

Title of Paper	Dynamic Modeling of the Coproduction of Liquid Fuels and Electricity from a Hybrid Solar Gasifier with Various Fuel Blends
Publication Status	Published
Publication Details	Kaniyal AA, van Eyk, PJ, Nathan GJ 2013. Dynamic Modeling of the Coproduction of Liquid Fuels and Electricity from a Hybrid Solar Gasifier with Various Fuel Blends. Energy & Fuels 27:3556-69.

Principal Author

Name of Principal Author (Candidate)	Ashok A Kaniyal		
Contribution to the Paper	Developed energy system process model and developed the structure based on which paper was written and modelling scenarios were presented. Carried out all drafting and paper revisions following editorial advice from primary and co-supervisors.		
Overall percentage (%)	60%		
Certification:	This paper reports on original research I conducted during the period of my Higher Degree by Research candidature and is not subject to any obligations or contractual agreements with a third party that would constrain its inclusion in this thesis. I am the primary author of this paper.		
Signature		Date	

Co-Author Contributions

By signing the Statement of Authorship, each author certifies that:

i. the candidate's stated contribution to the publication is accurate (as detailed above);

ii. permission is granted for the candidate in include the publication in the thesis; and

iii. the sum of all co-author contributions is equal to 100% less the candidate's stated contribution.

Name of Co-Author	Philip J van Eyk		
Contribution to the Paper	Provided early and ongoing guidance on conceptual design of modelling activities. Provided editorial assistance.		
Signature		Date	15/2/2016

Name of Co-Author	Graham J Nathan		
Contribution to the Paper	Provided early and ongoing guidance on conceptual design of modelling activities. Provided editorial assistance.		
Signature		Date	04 February 2016

4

A ONE-DIMENSIONAL HEAT TRANSFER, DEVOLATILISATION, GASIFICATION MODEL OF A SOLAR PACKED BED COAL GASIFIER

Ashok A Kaniyal [a,c], Mehdi Jafarian [a,c], Philip J van Eyk [b,c], Graham J Nathan [a,c]

a School of Mechanical Engineering, The University of Adelaide South Australia 5005

b School of Chemical Engineering, The University of Adelaide South Australia 5005

c Centre for Energy Technology, The University of Adelaide South Australia 5005

Abstract

A one-dimensional dynamic, heat transfer and chemistry model incorporating complete devolatilisation and gasification reaction kinetics was developed to evaluate the performance of coal gasification using the indirectly irradiated packed bed solar reactor of Steinfeld and co-workers. This model was verified using the published experimental results for a 150 kW_{th} configuration of this reactor to gasify Indonesian low-rank coal. The model delivered reasonable qualitative and quantitative agreement with the published temperature profile data through the fuel bed, with the steady-state gasification temperature, the dynamic gas composition profiles and the final fuel conversion over a 10-hour full solar day. This dynamic model was used to evaluate the sensitivity of syngas composition, production and fuel conversion rates to changes in fuel composition and to the initial mass of the fuel batch at the start of a given solar day. The sum of H_2 and CO was predicted to comprise 55% of the syngas fraction for Indonesian low-rank coal, and ~65% of the mole fraction of the Pittsburgh No. 8 and Illinois #6 coals. This result was found to be within 10% of experimental measurements for the solar gasification of Indonesian low-rank coal. The model also reproduced an experimental finding that the fuel conversion is very sensitive to the size of the initial batch mass. This was because carbon conversion was found to be dependent both on the rate of coal devolatilisation, which is a function of the average bed temperature, and on the maximum steady state bed surface temperature, which drives the endothermic solid phase char gasification reactions. The size of the initial batch mass has a significant influence on the average bed temperature and the temperature differential between the top of the fuel bed and the base. This confirmed that there is an optimal batch size to maximise the mass of fuel converted over a given solar day.

Nomenclature

a – mean atomic weight (g/mol).	H° – reference enthalpy relative to T = 273.15 K.
A – area (m^2).	F – radiation shape factor.
af – ash free basis	$k_{b,j}$ – overall thermal conductivity of bed layer j (W/m-K).
AR – as received basis.	k_g – devolatilisation or gasification reactions kinetics coefficient (see Table 1 and Table 2).
bd – bed density including void fractions (kg/m^3).	m – mass of fuel in a given layer of the discretised bed.
$\tilde{C}$ - solar concentration ratio (suns)	Mw – molecular weight of gas, g.
c – concentration of gasification reagent g (mol/m^3)	N, n or $\dot{n}$ – moles or molar flow rate.
y_g^o – initial functional group concentration of volatile gas g (af weight fraction).	$\dot{q}, Q$ or $\dot{Q}$ – heat flux (kW/m^2), heat (J) or heat flow (kW).
c_p – specific heat capacity (J/kg-K).	R – Universal gas constant (J/mol-K – unless otherwise stated).
d – true density of daf material not including void fractions (kg/m^3).	R – reaction rate (mol/s)
dz – depth of bed layer j (metres).	T – temperature in Kelvins unless otherwise stated.
daf – dry, ash free.	t – time in seconds.
g_1 – Einstein specific heat function.	v_s – reaction stoichiometric coefficient

I – solar insolation	WGS – water-gas-shift reaction.
H – enthalpy.	y – mass fraction of element u or volatile g in fuel bed layer j.
$\Delta_f H^\circ$ – enthalpy of formation.	

Subscripts

0 – time period equal to zero	p – emitter plate
abs – absorption efficiency	r – reverse WGS reaction
b – fuel bed	s – particle surface area
c – carbon	sol – solar
C – char gasification – SG/DG or HG	SG – steam gasification of char
f – final time period	t – total
DG – dry gasification of char with CO_2	u – elemental component of fuel (C, H, O, N or S)
g – component of gas input or output stream (CO/ CO_2/ H_2/ CH_4/ H_2O/ H_2S or HCN)	w – reactor wall insulation (see Figure 1)
HG – hydrogen gasification of char	wdw - window
i – coal, ash or water fraction of fuel bed total mass	x – cross-sectional
j – reference to discretised bed layer (see Figure 2)	

Greek letters

η – efficiency	τ – window transmissivity.
ϵ - bed void volume (m^3)	σ – Stefan-Boltzmann constant
ε – numerical model temperature error function.	μ – atomic weight of element u

$\gamma -$ coefficient for element u to determine true density of coal	ζ – solid-to-gas heat transfer coefficient

1.0 Introduction

The production of synthetic crude oil by the gasification of coal and subsequent Fischer-Tropsch (FT) processing has received much interest in the literature over the last ten years [1-9]. Coal gasification is the most energy-intensive step of the FT liquids production process [4,10,11] The introduction of concentrated solar energy to the gasification process offers one path to improving fuel productivity and reducing the greenhouse gas emissions associated with producing synthetic crude oil from the FT process relative to that of mineral crude oil. Kaniyal et al. recently presented an analysis outlining the energy and greenhouse gas emissions performance of a coal-to-liquids process incorporating solar energy relative to one that does not. Solar energy was introduced into this process to meet a portion of the gasifier's endothermic demand, with the remainder being met by the oxygenated combustion of coal. Integrating a hybridised solar-autothermal coal gasification system with a FT liquids production train was predicted to improve operational productivity by 25% on an energy basis and reduce GHG emissions by 28% relative to the non-solar, conventional autothermal process [4,10,11]. This system analysis further outlined the feasibility of a modest, 5 hours of syngas storage enabling continuous operation over a full year for the solar coal-to-liquids system for the first time [4,10,11]. However, there has been no such system analysis for integrating a stand-alone solar coal gasification system, with a FT liquids production train. Such an analysis is important, given the stand-alone packed bed solar gasification reactor has been proven to the largest experimental scale of ~150 kW_{th} [12, 13]. In comparison, the hybrid solar continuous flow gasifier proposed by Kaniyal's earlier work is based on the solar vortex reactor, which has only been proven to a scale of 5 kW_{th}. There has been no model of a standalone solar packed bed coal gasifier that can be used to estimate a time-series of syngas production and composition over a full solar year. Such a model is crucial to evaluating the feasibility of maintaining continuous productivity of a FT liquids production train over a full

year. The overall objective of the present work is to develop a tractable model of the solar packed bed coal gasification reactor for its integration within a process modeling analysis.

The packed bed solar gasifier employs indirect heat transfer via solar energy that enters the reactor through a quartz window and irradiates a Si-C coated graphite emitter plate [12], to heat the packed fuel bed in the reactor cavity. The reactor is operated in batch mode, with one batch of reactants being processed each day and replenished overnight. This configuration achieves high reliability, robust performance with a wide range of fuels in addition to the feasibility to operate at elevated pressures [12, 13], relative to the solar vortex reactor. However, it also has disadvantages, including the need for at least 2-3 hours, that is required to heat the bed surface to a steady-state operating temperature of ~1300 K from a cold start. The long startup is caused by the reactor's large thermal inertia owing to the reactor insulation mass and that of the fuel bed itself. The slow heating rate necessitates an alternative approach to determine fuel conversion rates and gas compositions than has been reported in previous models for this gasifier [12]. Hence, while a model has been developed for low volatile fuels [13-17], no model that adequately represents the gasification of complex, volatile bearing fuels such as coal in the solar packed bed gasifier has been reported previously [13-17]. Hence, the objective of the present paper is to develop such a model, to examine its sensitivity to feedstock composition and employ it to assess the implications of integrating this reactor with a downstream FT liquids production process.

Importantly, the packed bed reactor has to date only been assessed for short-term operation. As the temperature of the bed rises, the fuel at the surface is dried and devolatilised. The residual, devolatilised char is then gasified in the presence of steam, provided both by injection through the base of the reactor and by the heating of the moisture-laden fuel lower in the bed [12, 13]. While temperatures ~1300 K are achieved at the bed surface, a large

temperature gradient through the bed is observed, because of the low conductivity of the coal, together with the high thermal inertia of the bed. The temperature differential between the top and bottom of the bed and the overall rate of fuel conversion also depend upon the mass of the initial batch [12, 13]. However, no model of coal devolatilisation and gasification in a packed bed solar reactor is available with which to assess the productivity impacts of varying the initial batch mass. Hence, this paper aims to develop such a one-dimensional heat transfer and chemistry model of a solar packed bed coal gasifier, calibrated with existing experimental data [12] to develop a simple, tractable relationship between fuel conversion rates and the initial batch mass.

The SOLSYN numerical model was developed by calibrating modeling results to experimental measurements for a 5 kW_{th} lab-scale prototype of the packed bed solar reactor [13]. The results from this model were found to give good qualitative and quantitative agreement with the experimental temperature profile and gas evolution rates for the gasification of beech charcoal and waste sludge [13-17]. Indeed, the kinetics relationships used to model the gasification of beech charcoal showed close agreement with experimental observations. However, the agreement of the predicted gas evolution rates was less accurate for sewage sludge, which is a more complex heterogeneous, high volatile matter fuel. This is because the modelling methodology combined the fuel devolatilisation and char gasification into a single overall pseudo-chemical reaction based on the ultimate analysis of the feedstock [15]. However, the rate of devolatilisation is dependent on heating rate, which varies through the bed [18-21]. Furthermore, solid and gas phase reactions occur at different rates through the bed [18-21]. A chemistry model for the gasification of coal, necessitates an alternative approach to account for the evolution of individual volatile gas species and the concurrent solid and gas phase reactions that occur through the different temperature regions within the reactor. This paper aims to address this need for a detailed chemistry model by combining

explicit reaction kinetics data to represent devolatilisation, char gasification and the water gas shift and steam reforming reactions with a simple 1-D heat transfer model of the packed bed reactor. Importantly, the current work does not seek to replicate the detailed 1D heat transfer model of Piatkowski developed earlier. This enables the development of a simplified heat transfer model that can tractably be used as part of a full year process modeling assessment. The paper thus aims to compare the modelled results to experimental measurements of the temperature distribution through the packed fuel bed and achieve reasonable agreement with the average syngas productivity and composition over a full solar day based on the gasification of Indonesian low-rank coal in the 150 kW_{th} packed bed reactor reported by Wieckert et al [12].

The gasification of coal comprises the three sequential steps of drying, devolatilisation and char gasification [21, 22]. Drying leads to the evaporation of moisture from the fuel as steam. Devolatilisation involves the thermal decomposition of the fuel, typically between the temperatures of 500 and 1200 K, to release volatile gases comprising CO, CO_2, H_2, CH_4, acid gases and tars [21, 22]. The residual char is gasified through reactions between the solid carbon and steam or CO_2 to produce CO and H_2. Accompanying these solid phase reactions are the reversible water-gas-shift (WGS) and steam methane reforming (SMR) reactions, which determine the final composition of gases leaving the reactor [18-21]. The production of volatile gases can be determined using a functional group kinetics model [23]. Hobbs et al. successfully applied this approach with a zero-dimensional heat transfer model and a two-zone partial equilibrium model of an autothermal packed bed coal gasifier for a range of American coals [22]. This model assumes that devolatilisation gases are unreactive in the gasification zone and that the final gas composition can be represented by a Gibbs equilibrium model [22]. Although an equilibrium assumption may be reasonable for a gasification model of an autothermal reactor where temperatures in the combustion zone exceed 1500°C, this

assumption is less appropriate for a solar packed bed reactor that operates at much lower maximum temperatures [12, 21, 22]. Furthermore, the large temperature distribution through the bed means that devolatilisation and gasification rates will vary significantly through the length of the packed bed, as will overall char conversion rates [18, 21]. These performance parameters are closely linked with the magnitude of the initial batch mass and fuel composition, as reported in the experimental studies by Piatkowski [13] and Wieckert et al. [12]. However, no previous model of the packed bed solar reactor has examined the impact of these factors for high-volatile content fuels like sub-bituminous and brown coals. Significantly, no previous model has been reported that adapts the methodology used for coal devolatilisation and gasification in an autothermal reactor to a solar, packed bed coal gasifier.

To evaluate the feasibility of integrating a stand-alone solar packed bed coal gasification reactor with a syngas upgrading facility (e.g. FT process), this paper is followed by a detailed process modeling study that quantifies the minimum syngas storage capacity that would be required to enable steady-state operation over a full solar year [27]. Such data are needed to reasonably represent the influence of seasonal, diurnal and cloud-induced variability in solar insolation on syngas production and composition. The modelling of a reactor through each time-step of a solar year requires the use of a simplified model of the gasification process if the model is to be computationally tractable. Hence there is a need for a model of the gasification process that is sufficiently accurate to represent the key influence of the operation on the rates of production and syngas composition, while also being sufficiently computationally inexpensive to allow dynamic process modeling of a number of full solar year time-series.

For the reasons described above, the aims of the present paper are to develop a simple one-dimensional heat transfer and chemistry model of coal devolatilisation and char gasification in

a packed bed coal gasifier, to assess the agreement of the numerically modelled results with experimental measurements of bed temperature profiles and syngas compositions, and to assess the sensitivity of the reactor model both to the initial mass of coal batches and to the coal composition over a full solar day of operation.

2.0 Methodology

Figure 1 presents a schematic diagram of the packed bed reactor modelled here, based on the experimental investigation of Wieckert et al. [12]. The present investigation models the gasification of Indonesian low-rank coal using the same solar radiation and steam input time-series (see Figure 7) as that reported in the experimental study by Wickert et al [12] with a 150 kW_{th} packed bed reactor.

The packed bed reactor has an upper cavity comprising a window, through which concentrated solar radiation is incident on a SiC-coated graphite, emitter plate. While the window leads to a small reflective loss of ~7% it prevents much larger convective and IR-radiative losses. The bulk of the incident radiation heats the emitter plate, which then re-radiates the heat to the fuel bed in the lower cavity. The dimensions of the reactor are 1.1 m x 1.1 m x 0.8 m [12].

The present model assumes one-dimensional flows of heat and mass because the main reagent and energy flows are vertical, in the z direction (z = 0 at the top of the fuel bed and maximum at the at the reactor base), as seen in Figures 1 and 2. The assumption of one-dimensionality was made here because the emitter plate temperature is sufficiently uniform for its radiation to the top of the fuel bed to also be uniform. The emitter plate is expected to have a uniform temperature distribution given the high thermal conductivity of the graphite and SiC materials of which it is comprised. This means that there the radial variation in temperature is likely to be small, with the exception of regions close to the wall which may have a lower temperature. The magnitude of these effects were assumed to be negligible given the present analysis aims to develop a model of the packed bed reactor such that it can be integrated within a process modelling study. Note that the assumption of one-dimensionality was also made in the SOLSYN packed bed reactor model development and validation study by Piatkowski and is a

common approach for packed bed reactors [13, 15]. The experimentally reported solar concentration ratios, radiation fluxes incident on the reactor window and countercurrent steam flow rate reported by Wieckert et al. [12] are used as model inputs. Section 2.1 provides a detailed description of the energy, devolatilisation chemistry and gasification chemistry sub-models.

2.1 Reactor model

2.1.1 Energy balance

Figure 2 presents the energy flows to and from the three zones of the emitter plate, the bed surface and the discretised layers of the fuel bed. These zones are, in turn described by three sets of equations. The energy balance for the emitter plate and fuel bed is given by equation 2. Sequentially, the terms of this equation describe the heat gain from solar irradiation of the emitter plate and loss by re-radiation to the atmosphere and the second term the re-radiation of the fuel bed surface by the emitter plate. The re-radiation of solar thermal energy from the plate and out of the solar cavity reactor with rising plate temperature was calculated using the absorption efficiency (η_{abs}) given by equation 1. This equation assumes that the emitter plate, which is made from SiC coated graphite, has a high thermal conductivity. The high thermal conductivity further implies that the emitter plate can be assumed to have a uniform temperature distribution through its thickness. Equation 2 also incorporates a shape factor term to describe radiation transfer between the emitter plate, the insulated wall of the reactor and the top of the fuel bed (F_{pwb}). This shape factor was changed as the height of the fuel bed decreased as an increasing amount of coal being gasified. The value for this shape factor was derived from experimental work on an 8 kW_{th} [13-17].

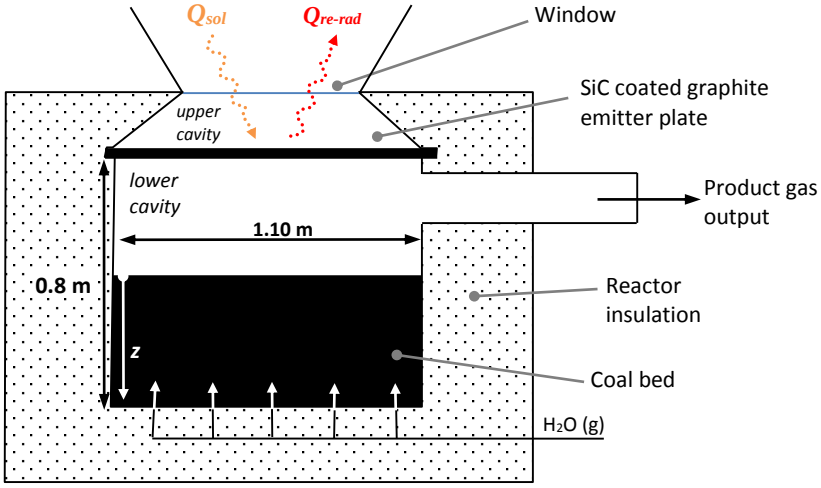

Figure 1: Schematic diagram of the packed bed reactor, based on the experimental configuration reported by Wieckert et al [12]; z = L at the base of the reactor and z = 0 at the top of the fuel bed.

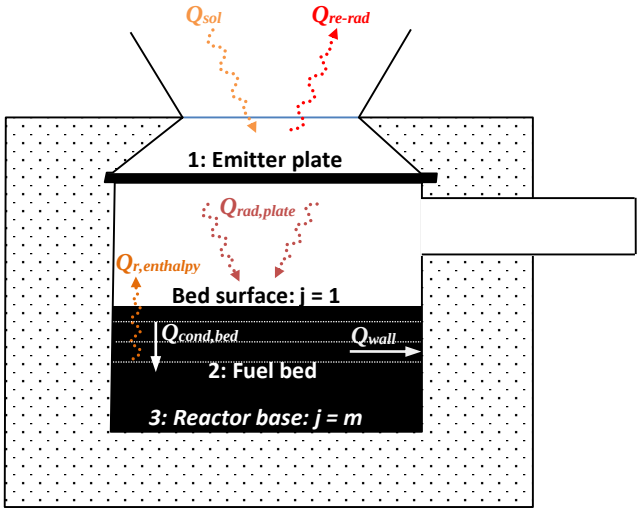

Figure 2: Simplified schematic diagram of the energy flows and fuel bed discretisation over layers j = 1 to m, in the one-dimensional model of the packed bed reactor. Labels 1 to 3 denote the three sets of equations used to describe the energy balance for the emitter plate – zone 1, bed surface – zone 2 and the discretised layers of the bed – zone 3 [12].

$$\eta_{abs} = 1 - \left(\frac{\sigma {T_p}^4}{I\tilde{C}}\right). \quad (1).$$

$$A_x \eta_{abs} \tau_{wdw} \dot{q}_{sol} + F_{pwb} A_x \sigma\left(T_{b,s}^4 - T_p^4\right) = 0 \quad (2).$$

Equation 3 presents the partial differential equation that was solved simultaneously with equation 2 to determine the temperature of the emitter plate and the temperature distribution through the fuel bed. Equation 4 presents the dynamic change in the mass balance for the fuel bed, where the mass left in the bed at time t is equal to the mass at time t-1 minus the mass of moisture released or unreacted (injected) steam that exits the bed and syngas produced. Equation 5 presents the enthalpy of the devolatilisation and gasification reactions that is the last term on the left hand side of the energy balance equation (3). Equation 6 presents the boundary condition for the infinitesimally thin bed surface and equation 7, which presents the boundary condition for the base of the reactor, which assumes that no heat is lost through the base.

$$-k\frac{\partial T^2}{\partial z^2} + \dot{Q}_{radiation} + \dot{Q}_w + \dot{Q}_{r,enthalpy} = mc_p \frac{\partial T}{\partial t} \quad (3).$$

$$\dot{Q}_{radiation} = A_x \eta_{abs} \tau_{wdw} \dot{q}_{sol} \quad (3a)$$

$$m_{b,t} = m_{b,t-1} - \dot{m}_{sg} + \dot{m}_{H_2O}|_{at\ time=t} \quad (4).$$

$$\dot{Q}_{r,enthalpy} = \sum_{g=1}^{5} \dot{n}_{g,in} \left(\Delta_f H^\circ + \left(H(T_{b,j}) - H^\circ\right)\right)_{g,in} - \sum_{out=1}^{5} \dot{n}_{g,out} \left(\Delta_f H^\circ + \left(H(T_{b,j}) - H^\circ\right)\right)_{g,out} \quad (5).$$

Boundary conditions

$$-k\frac{\partial T}{\partial z} = \dot{Q}_{radiation} + \dot{Q}_{evap} |\ z = 0\ \forall\ t \quad (6).$$

$$-k\frac{\partial T}{\partial z} = 0 \mid z = l\ at\ Reactor\ base\ \forall\ t \quad (7).$$

Equations 8, 9a and 9b describe the wall heat transfer model. In this equation $\dot{Q}_w$ represents the heat transfer between the wall and the bed, with $A_{b\text{-}w}$ being the contact area in layer 'j', $\dot{Q}_{w,cond.}$ the conduction through the wall, and the last term describes the unsteady state heat accumulation term. The physical parameters used to represent the wall thickness, mass, specific heat and thermal conductivity can be found in Piatkowski et al [13].

$$\dot{Q}_w + \dot{Q}_{w,cond.} = m_{w,j} cp_{w,j} \frac{dT_{w,j}}{dt};\ 1 \leq j \leq m \quad (8).$$

$$\dot{Q}_w = UA_{b-w,j}.(T_{b,j} - T_{w,j}) \quad (9a).$$

$$\dot{Q}_{w,cond} = \frac{k_{w,j}A_x}{dz_{b,j}} \left(T_{w,j+1} - T_{w,j}\right) \quad (9b).$$

Equations 10a and 10b were used to determine the height of each discretised layer of the bed and the actual bed density, including the pores. In equation 9b, $\rho_{coal} = 700$ kg/m^3; $\rho_{water} = 950$ kg/m^3 and $\rho_{ash} = 550$ kg/m^3. The physical properties of the discretised based change following each iteration of the model as do the thermal properties, namely the conductivity and specific heat capacity. These properties change until the model converges to an error less than 10^{-5} as summarised in Figure 3, which presents the numerical solution algorithm.

Physical relationships

$$dz_{b,j} = m_j / \left(bd_j A_x\right) \quad (10a)$$

$$bd_j = \left(\sum_{i=1}^{3} \frac{1}{\rho_i} \left(\frac{m_i}{m_j}\right)\right)^{-1} \quad i = coal, water\ or\ ash \quad (10b)$$

Equation 11a was used to determine the mass weighted average thermal conductivity of the fuel bed. Equations 11b – 11e describe the assumed thermal conductivity relationships for the

coal, water and ash components of the fuel bed [24]. The assumed true density (d) of the dry, ash free coal was estimated using equation 12c [24]. The assumed thermal conductivity relationships were adapted from the figures published in the literature to enable a quantitatively accurate representation of the heat transfer through the fuel bed.

Fuel bed thermal conductivity

$$k_{b,j} = \frac{1}{m_j}\sum_{i=1}^{3} m_{i,j}k_i(T_j)\,;\, i = coal, water\ or\ ash\ (\frac{W}{m.K}) \quad (11a).$$

$$k_{coal} = 2.\left(d_{b,j}/4511\right)^{3.5}T_{b,j}^{0.5} \quad (\frac{W}{m.K}) \quad (11b).$$

$$\left(\frac{1}{d}\right)_{b,j} = \sum_{u=1}^{5}\left(\gamma_u y_u/\mu_u\right)_{b,j}\,;\, u = C, H, O, N, S \quad (11c).$$

$$k_{water} = 0.6 \times 10^{-4} \quad (\frac{W}{m.K}) \quad (11d).$$

$$k_{ash} = 6 \quad (\frac{W}{m.K}) \quad (11e).$$

As above, equation 12a was used to determine the mass weighted average specific heat capacity of the fuel bed, with equations 12b – 12f being used to determine the heat capacity of the coal, water [25] and ash [26] components of the fuel bed layer, j.

Fuel bed specific heat capacity

$$c_{p,j} = \frac{1}{m_j}\sum m_{i,j}c_{p,i}(T_{b,j})\,;\, i = coal\ (c), water\ (w) and\ ash\ (a) \quad (12a).$$

$$c_{p,coal} = \left(\frac{R}{a}\right)\left[g_1\left(\frac{380}{T_{b,j}}\right) + 2g_1\left(\frac{1800}{T_{b,j}}\right)\right]\ (\frac{J}{kg.K}) \quad (12b).$$

$$\left(\frac{1}{a}\right)_{b,j} = \sum_{u=1}^{5}\left(y_u/\mu_u\right)_{b,j}\,;\ u = C, H, O, N, S \quad (12c).$$

$$g_1(z) = \frac{\exp(z)}{((\exp(z)-1)/z)^2} \quad (12d)$$

$$c_{p,ash} = 0.91 + 0.00246.T - 1.39 \times 10^{-6} T \left(\frac{J}{kg.K}\right) \text{T in °C} \quad (12e).$$

$$c_{p,water} = 4187 \left(\frac{J}{kg.K}\right) \quad (12f).$$

2.1.2 Coal drying and evaporation

A simple coal-drying model based on the enthalpy of evaporation was used to estimate the rate at which water is released as steam. This calculation is described by equation 13.

$$\Delta y_{H_2O,j} = \frac{\Delta T_j c_{p,j}}{(Mw_g.\Delta H_{vap})} y^o_{H_2O,j} \quad (13).$$

2.1.3 Coal devolatilisation

The composition of volatile gases that are generated by the coal devolatilisation process were estimated using a functional group (FG) model [22]. Experimental studies with the packed bed reactor demonstrate that tars are only formed during the initial reactor start-up phase, when the emitter plate is heated to its maximum temperature. Following this initial period, long-chain hydrocarbons are cracked to short-chain hydrocarbons and CH_4 as they are exposed to the hot emitter plate before exiting the reactor, see Figure 1 and 2. A specific tar model is thus not represented in the current assessment these compounds are cracked to CH_4, before the off-gas exits the reactor, when during steady-state operation. During the reactor start-up phase however an electric tar cracker is used to break-up long-chain hydrocarbons to methane.

Table 1 presents the initial moisture laden, ash free, volatile functional group weight fractions (y^o_g) for three coals, the Indonesian low-rank assessed by Wieckert et al. [12], the Illinois #6

and the Pittsburgh No. 8 coals [21-23]. Table 1 also presents a range of Arrhenius kinetic parameters for the volatile gases, H_2, CO, CO_2, CH_4, HCN and H_2S, selected based on whether the gases are tightly or loosely bound to the coal [21, 22]. The y_g^o values reported for the Illinois #6 and Pittsburgh No. 8 coals were adapted from those reported by Hobbs et al [22], to correct for the absence of oxygen in the solar reactor, and cross-referenced to the coal proximate and ultimate analyses. The same approach was followed to estimate the y_g^o concentrations for the Indonesian LR coal [12]. The assumed initial volatile functional group concentrations for the Wieckert et al. coal are corroborated by the model verification assessment in Section 3.1.

Equation 14 was used to calculate the mass concentration of a given volatile component, $y_{g,j}$ remaining in a given bed layer *j* at any point in time. The mass flow rate of volatiles from layer *j* was calculated as a function of the change in this concentration with the temperature of each layer of the discretised bed. The mole flow rate of volatile component, *g* released from layer *j*, at time *t*, was determined using equation 15.

$$y_{g,j}[T_j] = y_g^o . exp(-k_i) \quad (14).$$

$$\dot{n}_{g,j}|t > 1 = \Delta y_{g,j} . dM_{j\,(af)\,|\,t>1}/Mw_g \quad (15).$$

2.1.4 Coal gasification

Table 2 presents a summary of the stoichiometry, kinetics and rate equations for the three solid phase char gasification and two gas phase (water gas-shift and methane reforming) reactions that were used to calculate the final composition of gases that leave the fuel bed and exit the reactor. Char gasification reactions can be described through three resistances, namely

the surface reaction, molecular diffusion through the gaseous film and ash layer diffusion [21]. Surface reaction kinetics are assumed to be the rate determining step of char gasification. It is assumed that diffusion effects through both the gaseous film, the ash layer and the internal porous structure of the particles are negligible because of the slow fuel heating rate and low fuel bed temperatures for gasification [12]. This assumption was assessed by calculating the impact of the molecular diffusion kinetics resistance on the char gasification rate following the methodology outlined by Hobbs et al. [21]. It was determined that under these reaction conditions the rate of diffusion to the particle surface was fast enough to be considered instantaneous compared with the chemical reaction rate. Moreover, as noted by Laurendeau [28], diffusion kinetics are only noted to play a significant role when T>2000 K for char particles larger than 200 microns. This is applicable here because a new batch of as-received, coal is loaded into the reactor at the start of each solar day.

Table 1: Devolatilisation reaction kinetics and functional group volatile compositions for Indonesian low-rank coal, Illinois No. 6 and Pittsburgh No. 8 coals adapted from literature estimates for autothermal coal gasifiers. The initial functional group concentrations were estimated while matching the modelled coal ultimate and proximate analyses to the reported analyses of the three coals assessed [12, 22].

Volatile functional groups	**Kinetic parameters (g = CO, CO_2, CH_4, H_2, H_2S, HCN)**			**Ash free (af) mass basis of coal type**		
				Indonesian LR	**Illinois No. 6**	**Pittsburgh No. 8**
	k_g^o	E_g/R **(K)**	$\pm\sigma_g/R$ **(K)**	y_g^o	y_g^o	y_g^o
CO_2 (extra loose)	0.81 x 10^{13}	22500	1500	0.064	0.035	0
CO_2 (loose)	0.65 x 10^{17}	33850	1500	0.065	0.035	0.007
CO_2 (tight)	0.11 x 10^{16}	38315	2000	0	0	0.005
H_2O (moisture)	-	-	-	0.33	0.075	0.052
CO (ether loose)	0.14 x 10^{19}	40000	6000	0.068	0.09	0.0325
CO (ether tight)	0.15 x 10^{16}	40500	1500	0.07	0.09	0.0325
HCN (loose)	0.17 x 10^{14}	30000	1500	0.008	0.01	0.009
HCN (tight)	0.69 x 10^{13}	42500	4750	0	0.016	0.023
NH_3	0.12 x 10^{13}	27300	3000	0	0	0
CH_x (aliphatic)[A]	0.84 x 10^{15}	30000	1500	0	0.08	0.19
CH_4 (extra loose)	0.84 x 10^{15}	30000	1500	0	0.023	0
CH_4 (loose)	0.75 x 10^{14}	30000	2000	0.025	0.02	0
CH_4 (tight)	0.34 x 10^{12}	30000	2000	0.025	0.024	0.04
H (aromatic)[B]	0.10 x 10^{15}	40500	6000	0.02	0.01	0.005
CO (extra tight)	0.20 x 10^{14}	45500	1500	0	0	0.04
C (non-volatile)	0	NA	NA	0.3200	0.46	0.54

S (organic)[C]				0.0054		0.032		0.024	
Total $\sum y_i^o$				**1.000**		**1.000**		**1.000**	
Coal ultimate analysis (daf)				**Model[D]**	**Actual[D]**	**Model**	**Actual**	**Model**	**Actual**
Carbon				0.46	*0.46*	0.73	*0.71*	0.817	*0.846*
Hydrogen				0.07	*0.07*	0.054	*0.06*	0.069	*0.058*
Oxygen				0.47	*0.46*	0.17	*0.19*	0.072	*0.053*
Nitrogen				0.00	*0.00*	0.015	*0.01*	0.017	*0.017*
Sulfur				0.01	*0.01*	0.033	*0.03*	0.024	*0.024*
Coal proximate analysis (AR wt %)				**Model**	**Actual**	**Model**	**Actual**	**Model**	**Actual**
Moisture				0.33	*0.35*	0.083	*0.102*	0.056	*0.046*
Ash				0.042	*0.042*	0.091	*0.091*	0.077	*0.077*
Volatile matter				0.328	*0.321*	0.326	*0.352*	0.327	*0.374*
Fixed carbon				0.30	*0.287*	0.50	*0.46*	0.54	*0.503*

[A] Aliphatic CH_x released as CH_4; [B] Aromatic hydrogen released as H_2; [C] All sulfur released as H_2S with the same kinetic rates as HCN (loose); [D] Ash free basis;

Table 2: Solid-phase char gasification and gas phase methane reforming and equilibrium (eq - forward and reverse) water gas-shift bulk reaction kinetics.

Reaction (r)		**A (ms^{-1})**	**E_a/R (K)**	**Units**	**Rate equation (all units in mol/s)**	**Source**
Steam gasification (SG):	$C_{(s)} + H_2O_{(g)} \rightarrow CO + H_2$	$6.84.T_{b,j}$	15600	$m.s^{-1}$	$R_G = \frac{c_{g,j+1} A_s \nu_S}{\frac{1}{\zeta k_r}}$; $\{g: H_2O\ (SG), CO_2\ (DG)\ or\ H_2\ (HG)\}$	[21]
Dry gasification (DG):	$C_{(s)} + CO_2 \rightarrow CO + H_2$					
Hydrogen gasification (HG):	$C_{(s)} + 2H_2 \rightarrow CH_4$	$0.00684.T_{b,j}$				
Water gas-shift (WGS):	$CO + H_2 \rightleftharpoons CO_2 + H_2$	$k_{WGS} = 0.1 \times 10^8 . \exp(-1.256 \times 10^4 / T_{b,j})$		$m^3.kmol^{-1}.h^{-1}$	$R_{WGS-eq} = k_{WGS} \left\{ c_{CO} c_{H_2O} - \frac{1}{K_{eq}} c_{CO_2} c_{H_2} \right\}_{j+1} . \epsilon$	[18]
Steam methane reforming (SMR):	$CH_4 + H_2O \rightarrow CO + 3H_2$	$k_{SMR} = 312. \exp(-3 \times 10^4 / RT_{b,j})$ [A]		s^{-1}	$R_{SMR} = k_{CH_4} \{c_{CH_4, j+1}\} . \epsilon$	[19]
Notes: [A] R = 1.9872041 $cal.K^{-1}.mol^{-1}$						

2.2 Solution algorithm

Figure 3 presents a flow diagram of the solution algorithm for the packed bed reactor model. This algorithm comprises the following sub-models, which were solved simultaneously:

1. energy balance sub-model (see Section 2.1.1)
2. coal drying and devolatilisation sub-models (see Sections 2.1.2 and 2.1.3); and
3. char gasification sub-model (see Section 2.1.4) [18, 19, 21, 22].

The simultaneous solving of these sub-models is necessary because the energy balance and the composition of each discretized layer of the bed are inextricably linked through the temperature dependence of the devolatilisation and gasification reactions. Following each iteration, the proximate, ash, moisture and coal fractions of each layer of the bed are updated, together with the residual molar fractions of C, H, O, N and S to determine the new thermal conductivities, heat capacities and densities of each discretised layer in the bed. All sub-models were solved with the Gauss-Seidel numerical algorithm, until the temperatures of the bed, wall and plate satisfy the convergence criteria. The time-step used in the present analysis was one second, the convergence criteria is further specified in Figure 3. Grid-independence was achieved by assuming the number of layers at t = 0, to be 40. For an initial bed depth of 20 cm this would mean that each layer of the fuel bed would have an effective thickness of 0.5 cm. Increasing the number of layers above 40 led to very little change in model accuracy.

2.3 Performance parameters

Equations 16 was used to calculate the carbon conversion at every time step *t*. Equations 16 – 20 define the solar upgrade factor assuming LHV_C = 33 MJ/kg. Equation 21 describes the solar share of the packed bed gasification process.

$$X_{c,t} = 1 - \left(\frac{N_{c,0}}{N_{c,f}}\right)_t \quad (16).$$

$$U = \frac{Q_{syngas}}{Q_{C,conv.}} \quad (17).$$

$$Q_{syngas} = \sum_{i=1}^{3} \dot{n}_i LHV_i \; ; i = CO, H_2 \; and \; CH_4 \quad (18).$$

$$Q_{C,conv.} = X_c N_{c,t} LHV_c \quad (19).$$

$$X_{sol} = \frac{Q_{sol}}{Q_{sol} + Q_{C,conv.}} \quad (20).$$

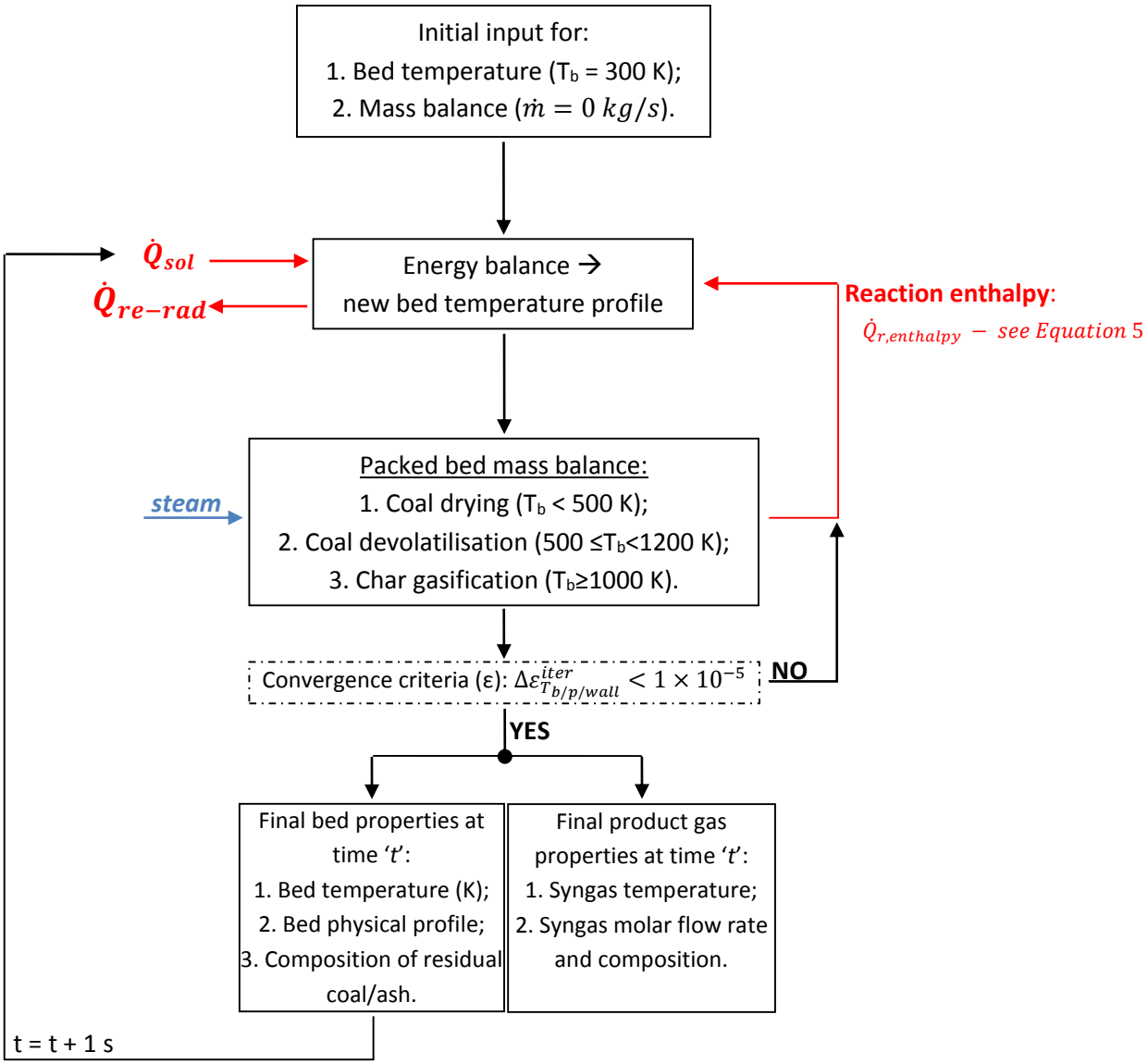

Figure 3: Solution algorithm for the Gauss-Seidel numerical algorithm of the one-dimensional solar packed bed reactor energy balance, devolatilisation and gasification sub-functions.

3.0 Results

3.1 Comparison of modelled and experimental data

Figures 4 and 5 compare the experimentally measured temperature and syngas molar flow rates with the numerically modelled values for the solar packed bed gasification of Indonesian low-rank coal. Figure 4 presents this comparison of the temperatures at the fuel bed surface (T_{bs}), and at heights of ~5 cm ($T_{5\ cm}$), 10 cm ($T_{10\ cm}$) and 15 cm ($T_{15\ cm}$) from the base of the reactor. Figure 5 presents the same comparison for the molar flow rates of CO, H_2, CO_2 and CH_4. Both figures demonstrate reasonable qualitative and quantitative agreement between the model and the reported experimental data.

Figure 4 shows that the model reproduces the rate of increase in the bed-surface temperature quite well, even though there is an offset in the time, so that the temperature rise is predicted to start approximately half an hour earlier than the measurement. The simplifying assumption made, by excluding the upper cavity from the heat transfer model, led to the over prediction of the emitter plate and thus fuel bed surface temperature at the start of the solar day, as the model does not account for radiative heat losses from the emitter plate to the cold surfaces of the reactor's upper cavity. This was because the heat that is trapped in the reactor's upper cavity by radiation between hot surfaces was not taken into account. Nevertheless, the simplification led to only an 8% under prediction in the steady state bed surface temperature. Consistent with these discrepancies in fuel bed temperature predictions, the release of CO begins earlier in the model than the experimental data and rises to a peak value that is 15% higher than the measurement, while the agreement with the H_2 release is good (Figure 5). The predicted evolution of CO_2 exhibits a double hump that is not found in the experimental data. This is attributable to the earlier increase in the predicted T_{bs} at the start of the day, which leads to the forward and reverse WGS reactions being in equilibrium and results in the

predicted decrease in the CO_2 molar flow rate between t = 1.5 – 3 hours and an inflection point in the H_2 molar flow rate at t = 1.5 hours (Figure 5). Following this initial period, the maximum CO molar flow rate is predicted to correspond to t ~ 3 hours, when the T_{bs} reaches a steady-state condition.

It is also apparent from Figure 4 that the model underestimates the rate of conduction through the bed somewhat, so that T_{5cm} is under-predicted, even though the temperature at 10 cm, T_{10cm}, is well predicted. This discrepancy is attributed to a simplified wall heat transfer model, which does not represent the contribution of the reactor's thermal mass to the fuel bed-heating rate. This also explains the faster than observed decrease in bed temperature towards the end of the day when Q_{sol} decreases to zero. Consistent with the earlier reduction in temperature for the model is an earlier drop in the release of CO and H_2 for the last hour of the day from t = 9 to 10 hours (Figure 5). Nevertheless, the overall devolatilisation rate is in reasonable agreement with the measured data, as shown by the steady flow of CH_4 throughout the day, which is within 10% of the measured values (Figure 5).

Table 3 presents a comparison of the predicted and measured char conversion rates (X_c), average gas compositions and syngas upgrade factor (U) for the Indonesian low-rank coal. This comparison shows that the bulk carbon conversion rate, average temperature and syngas upgrade factor are quantitatively accurate, notwithstanding the differences during the heating and cooling of reactor, noted above. Furthermore, the discrepancies in the relative mole fractions of CO, H_2 and CO_2 are influenced by the unknown extent to which the measured gases were cooled between the reactor and the sampling point, which, as noted above, will lead to higher values of the measured H_2/CO (mol/mol) ratios over the modelled values due to the role of the forward WGS reaction.

Hence, in summary the level of agreement between the model and the experimental data both qualitatively and quantitatively, is comparable with the overall experimental uncertainty of the data, when accounting for the extent to which the boundary conditions are defined.

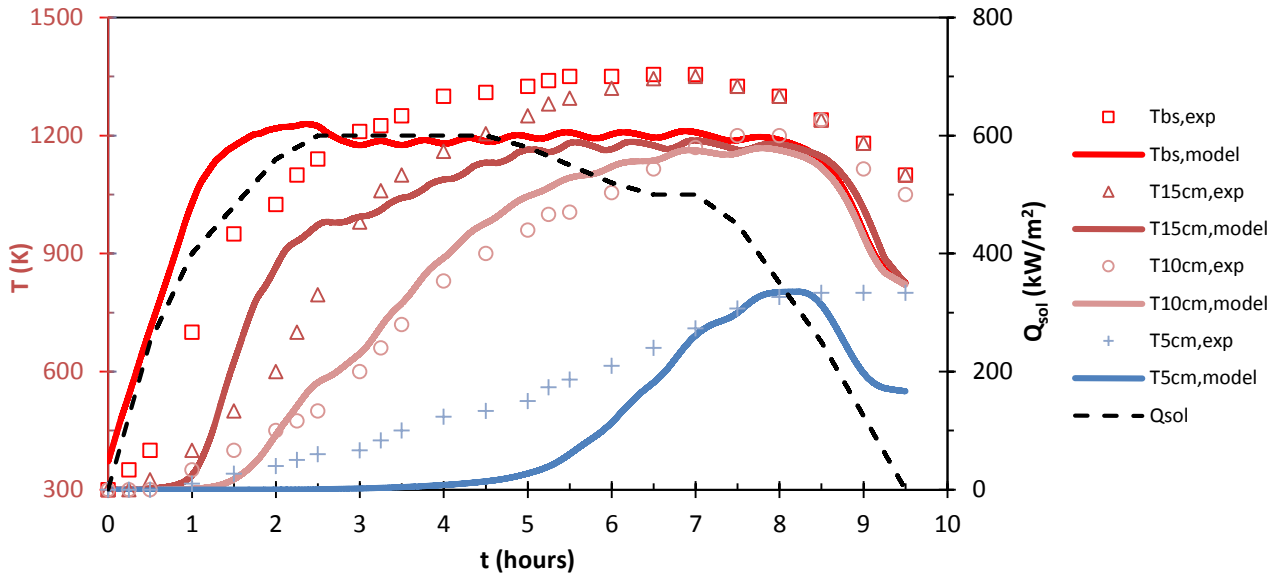

Figure 4: Comparison of experimentally measured and numerically modelled temperature for the bed surface (bs) and heights of 5, 10 and 15 cm from the reactor base, for a shrinking bed of Indonesian low-rank coal undergoing steam gasification, assuming an initial fuel batch mass, m_0 = 180 kg, z_L = 20 cm [12].

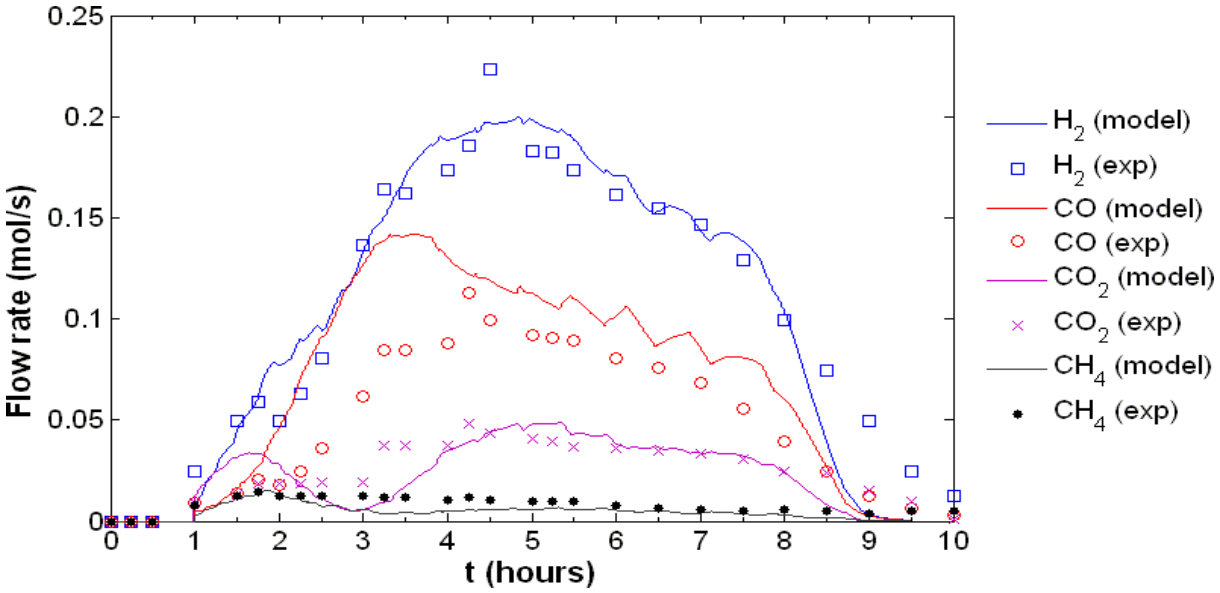

Figure 5: Comparison of experimentally measured and numerically modelled devolatilisation and gasification product flow rates for a shrinking bed of Indonesian low-rank coal undergoing steam gasification, based on an initial fuel batch mass, m_0 = 180 kg [12].

Table 3: Comparison of experimentally reported and numerically modelled average temperature parameters and average gas composition results for the gasification of Indonesian low-rank coal [12].

Parameter	Model	Experiment	Difference
X_c	52.2%	57%	-8.4%
Average maximum temperature (K)	1193	1301	-8.3%
H_2/CO (mol/mol)	1.53	2.27	-33%
CO/CO_2 (mol/mol)	2.99	2.0	50%
Syngas upgrade factor (U)	1.26	1.26	0%

3.2 Fuel sensitivity analyses

Figure 6 presents the numerically modelled temperature profiles for the steam gasification of Pittsburgh No. 8, Illinois #6 and Indonesian low-rank coals, at the fuel bed surface, and at three depths through the bed. Figure 7 presents the corresponding mole flow rates for the main gas species for the same conditions for all three coals. In comparison with the Indonesian LR coal, which has an ultimate carbon fraction of 46%, the Pittsburgh 8 and Illinois 6 coals have ultimate carbon fractions of 85% and 73% respectively. These high carbon weight fractions are calculated to exhibit a lower rate of heat transfer through the bed, which can be attributed to the combination of their lower moisture content and higher ash content, leading to a lower thermal conductivity. The lower heat dissipation leads to a higher initial peak temperature than is predicted for the Indonesian coal (1400 K cf 1200 K), and a higher steady-state surface temperature (1200 K cf 1150 K). Both high rank coals exhibit similar temperature profile (Figure 7a). Importantly, the predicted temperature distribution, together with the differences in the coal composition, has a significant influence on the calculated CH_4 mole fraction (which also represents tars in the model). That is, the high rank fuels exhibit a much higher initial release of CH_4 (and tars), together with a much lower initial release of both CO and H_2 than does the low-rank Indonesian coal. This can be explained as follows: the lower initial conductivity of the high rank coals is deduced to be responsible for the high initial bed temperature. However, the conductivity of the bed increases as the coal is gasified and the ash layer builds at the top of the bed.

For $t>2.5$ h, the rate of CH_4 (and tars) production peaks and decreases, giving way to a significant increase in the rate of gasification and an inflection in the CO and H_2 mole flow rate curves that correspond to the steam injection through the reactor base. This leads to the T_{15cm} plateauing during the period $2<t<4$ h as the heat in the layers above is removed predominantly by the endothermic gasification reactions. (Little heat is conducted through the

bed). As T_{15cm} rises again, when t>4 h, the heating rate of the rest of the bed increases also. This is represented by a steeper gradient in the T_{10cm} curve in both Figure 6a and 7a and the recovery of CH_4 production to a steady rate for the rest of the modelled period. It is contended that the conversion of the volatile CH_4 to CO and H_2 by steam reforming is limited by the low maximum temperature predicted for the solar packed bed reactor, in comparison with the directly irradiated vortex reactor. This also contrasts an autothermal reactor, where volatiles would be burnt off to facilitate faster gasification.

Figure 8 presents the dependence on time through the solar day of the fuel bed depth (dz_t) normalised by the initial fuel bed depth (dz_0), for the gasification of Indonesian low-rank coal, Pittsburgh No. 8 and Illinois #6 coals. This shows that, for all three coals, the bed shrinks approximately linearly with time. For the Illinois #6 and Pittsburgh No. 8 coals, there is only a relatively small change in the bed volume because the low moisture content of these coals. It should also be noted that the bed depth ceases to change significantly for t > 8 hours. This is caused by the reaction rate dropping to nearly zero as T_{bs} falls below 1000 K, not accounting for the ash that remains in the bed. Importantly, the figure also shows that the unconverted mass fraction of carbon at the end of the solar day is 30% for the Indonesian low-rank coal and over 60% for the higher carbon fraction Illinois #6 and Pittsburgh No. 8 coals, respectively. This is significant because the incomplete conversion of carbon is likely to represent a significant economic penalty.

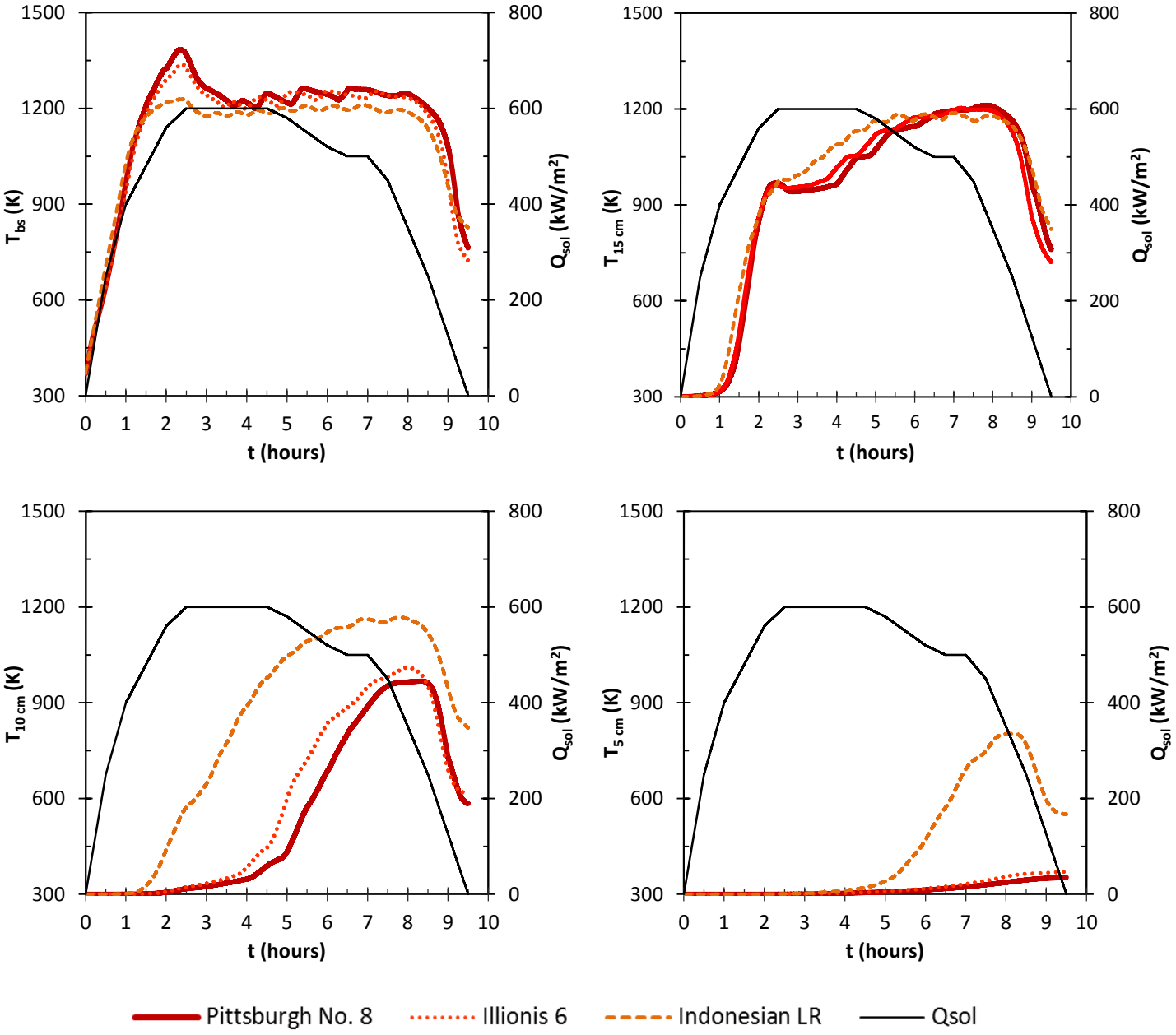

Figure 6: Evolution of 15 min rolling averaged temperature profiles for the bed surface (bs) and 5, 10 and 15 cm from the reactor base (clockwise from left) for the steam gasification of Pittsburgh No. 8, Illinois #6 and Indonesian low-rank coals, assuming an initial batch mass, m_0 = 180 kg and an initial fuel bed height, z_0 = 20 cm [21, 22].

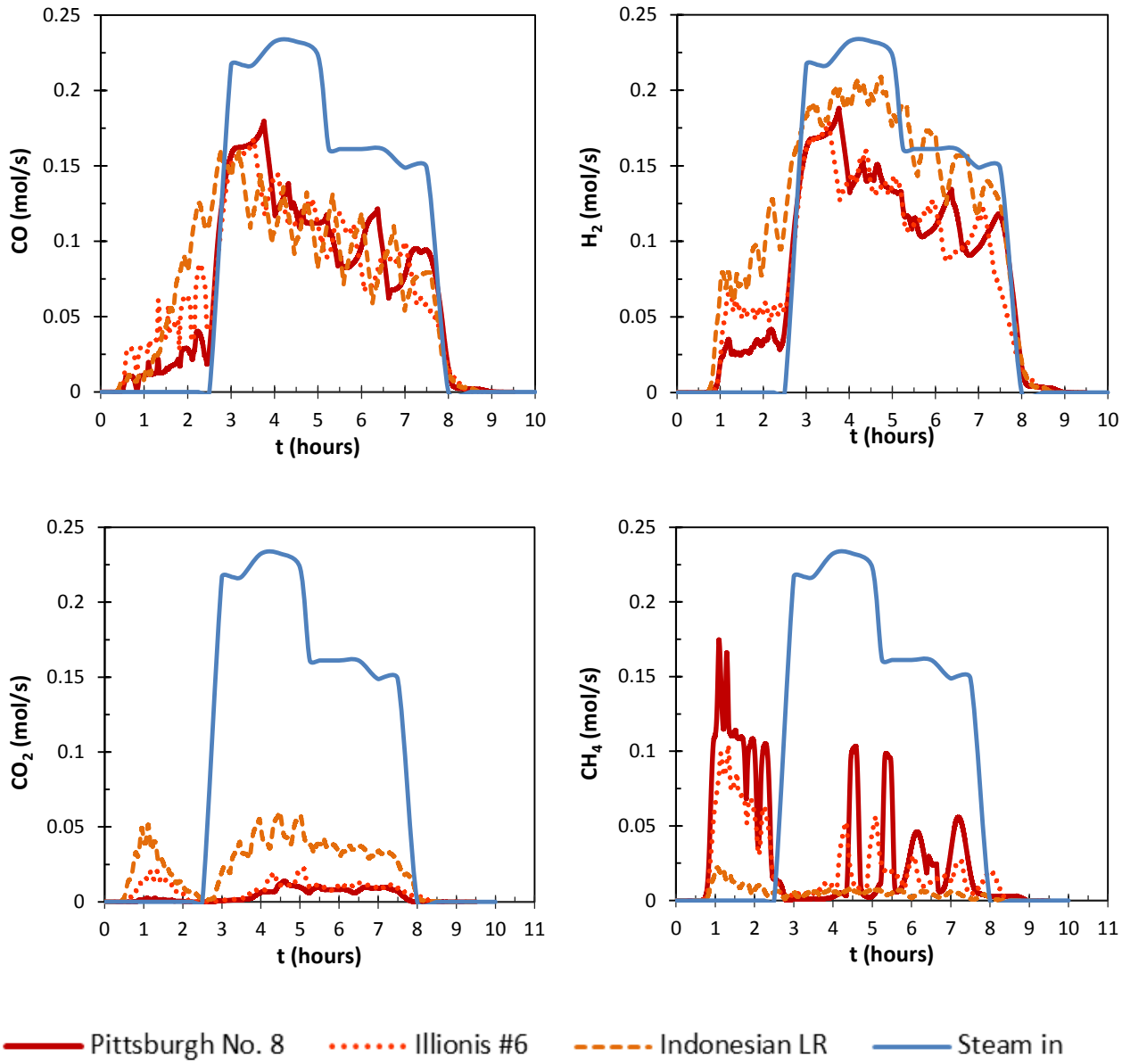

Figure 7: Evolution of 15 min rolling averaged syngas mole flow profiles for the gas species CO, H_2, CO_2 and CH_4 (clockwise from left) for the steam gasification of Pittsburgh No. 8, Illinois #6 and Indonesian low-rank coals, assuming an initial batch mass, m_0 = 180 kg and an initial fuel bed height, z_L = 20 cm [21, 22].

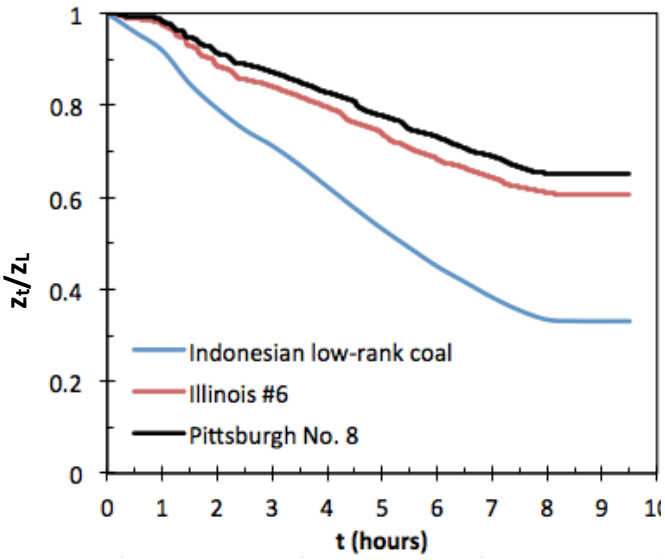

Figure 8: Evolution of normalised fuel bed depths with time, for the steam gasification of the three coals. In all cases, the initial batch mass and fuel bed height are constant at m_0 = 180 kg and z_L for the Pittsburgh No. 8, Illionis #6 and Indonesian low-rank coals being 19.8 cm, 20 cm and 18.5 cm respectively.

3.3 Sensitivity to initial mass

3.3.1 Carbon conversion

Figure 9 presents the dependence on $m_0/m_{0\ Nc,t\ (max)}$ – the initial batch mass (m_0) normalised to the batch mass that maximises the moles of carbon converted ($N_{c,t}$) to X_c the fraction of carbon converted relative to the initial number of moles of carbon in the fuel bed ($N_{c,0}$). The trends shown in Figure 9 are corroborated by experimental results published by Piatkowski [13] for the steam gasification of beech charcoal for varying bed depths. Figure 10 presents the predicted dependence of the number of moles of carbon converted to syngas with (average composition presented in Figure 11) ($N_{c,t}$) on $m_0/m_{0\ Nc,t\ (max)}$ for the gasification of the three coals.

Figure 10 shows that the total amount of carbon converted, $N_{c,t}$, is less sensitive to $m_0 < m_{0\ (Nc,t\ max)}$ than $m_0 > m_{0\ (Nc,t\ max)}$. For the Illinois #6 coal, decreasing $m_{0\ (Nc,t\ max)}$ by 40% reduces $N_{c,t}$ to 80% of the maximum yield over the range studied, but increasing $m_{0\ (Nc,t\ max)}$ by 40% reduces $N_{c,t}$ to only 88% of that yield. For the Indonesian low-rank coal increasing $m_{0\ (Nc,t\ max)}$ by 50% reduces $N_{c,t}$ by 8% relative to $N_{c,t\ (max)}$ but reducing it by the same fraction reduces total output by 34%, even though total carbon conversion (X_c) is 81% higher. While Figure 9 shows that X_c increases with decreasing m_0, Figure 10 shows that the value of $m_{0\ Nc,t\ (max)}$ is significantly greater. This constitutes trade-off, in that it is not possible to maximise both $N_{c,t}$ and X_c. Hence, to maximise the production rate in light of uncertainty in reliably predicting the exact solar insolation ahead of each day, it is better to over-fill the reactor than to under-fill it

The predicted greater sensitivity of the carbon conversion rate, $N_{c,t}$, to $m_0 < m_{0\ (Nc,t\ max)}$ than to $m_0 > m_{0\ (Nc,t\ max)}$ follows from the dependence of the gasification rate on the steady-state fuel bed surface temperature (T_{bs}) (see Figures 4-7). For $m_0 < m_{0\ (Nc,t\ max)}$, the rate of conduction through the bed is faster, thus lowering T_{bs}. This has a large impact on carbon conversion because of the exponential relationship between char gasification reaction rates and temperature. In contrast, $m_0 > m_{0\ (Nc,t\ max)}$ leads to a lower rate of conduction through the bed and a higher T_{bs} . A comparison of the three curves in Figure 10shows that the Illinois #6 and Pittsburgh No. 8 coals are more sensitive to $m_0 > m_{0\ (Nc,t\ max)}$ than the Indonesian low rank coal.

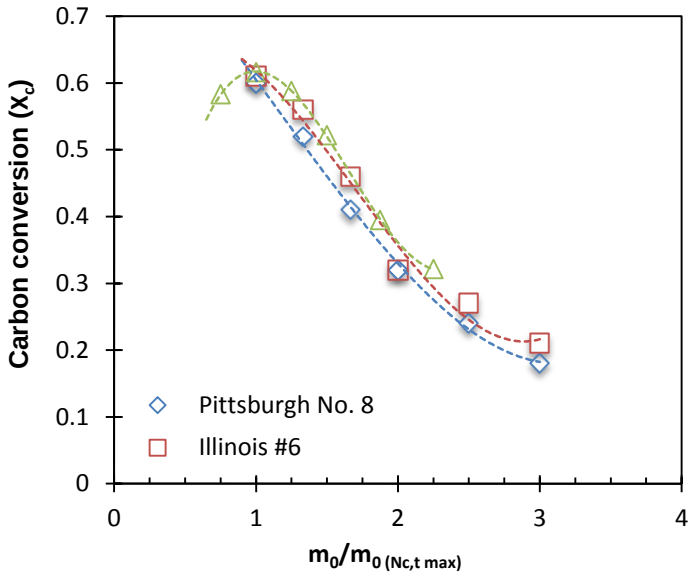

Figure 9: Modelled relationship between the carbon conversion percentage relative to the moles of carbon present at the start of the day (X_c) to $m_0/m_{0\ Nc,t\ (max)}$ – the initial batch mass normalised to the batch mass that maximises the moles of carbon converted, for the gasification of Indonesian low-rank, Pittsburgh No. 8 and Illinois #6 coals.

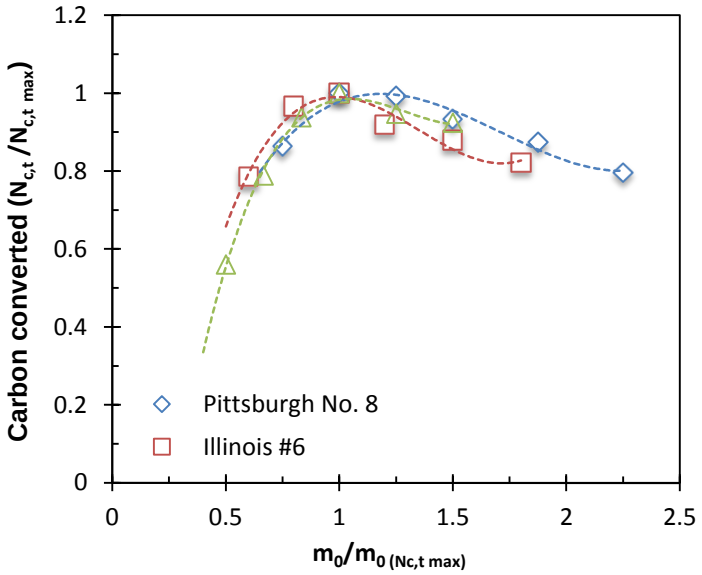

Figure 10: Modelled relationship between the moles of carbon ($N_{c,t}$) converted to, $m_0/m_{0\ Nc,t\ (max)}$ – the initial batch mass normalised to the batch mass that maximises the moles of carbon converted, for the gasification of Indonesian low-rank, Pittsburgh No. 8 and Illinois #6 coals.

The three panels of Figure 11 present the predicted relative mole fractions of CO, H_2, CH_4 and CO_2 in the final syngas product for a range of initial batch masses ($m_0/m_{0\ Nc,t\ (max)}$) for the three coals. It can be seen that decreasing initial batch mass is predicted to result in a slight increase in the molar fraction of CO_2 by 1 – 2 percentage points and the H_2/CO ratio in the syngas produced from all three coals. This is a result of the forward WGS reaction being favoured by a lower steady-state T_{bs}. It can further be seen from Figure 11b and c that 15% of the syngas produced by the gasification of Pittsburgh No. 8 coal, and 9% of the Illinois 6 syngas is represented by CH_4 volatiles. In comparison CH_4 volatiles comprise only 1% of the syngas produced from the Indonesian low-rank coal. Water vapour makes up the balance of the mole fractions shown in Figure 11. Given that it will be necessary to vary the initial mass of fuel in response to the diurnal and cloud-related variability in solar insolation, these data reveal that significant changes in day-to-day composition of the syngas are inevitable, which must be accommodated by downstream processing for FT fuels production.

Figure 12 compares the relative contribution of CO, H_2 and CH_4 to the calorific value of syngas from the solar gasification of the three coals for a range of $m_0/m_{0\ Nc,t\ (max)}$ scenarios. This reveals the large contribution of CH_4 to the calorific value for the Pittsburgh No. 8 and Illinois 6 coals, complementing the mole-fraction data (Figures 6, 7 and 11). It can be seen that, for the Pittsburgh No. 8 and Illinois #6 coals, the energy content in the volatile gases (mainly CH_4 but also CO and H_2 are products of devolatilisation) is comparable with that of the CO and H_2. Hence, for these fuels, it is unlikely to be either viable or acceptable to simply flare these gases, so that additional processing plant will be required to utilize them. Furthermore, this plant must be responsive to large swings in the composition of these gases (Figure 7).

Figure 13 presents the dependence of the predicted syngas calorific upgrade factor for the same three coals on $m_0/m_{0,ref}$. By comparing, Figure 13 and Figure 12 it can be seen that a larger CH_4 fraction in the syngas is predicted to lead to a larger calorific upgrade. The average calorific upgrade of the Pittsburgh No. 8 coal is 8% greater than the Illinois 6 coal, which in-turn is 11% larger than that predicted for the Indonesian low-rank coal. It is also apparent that the syngas upgrade factor is not particularly sensitive to m_0.

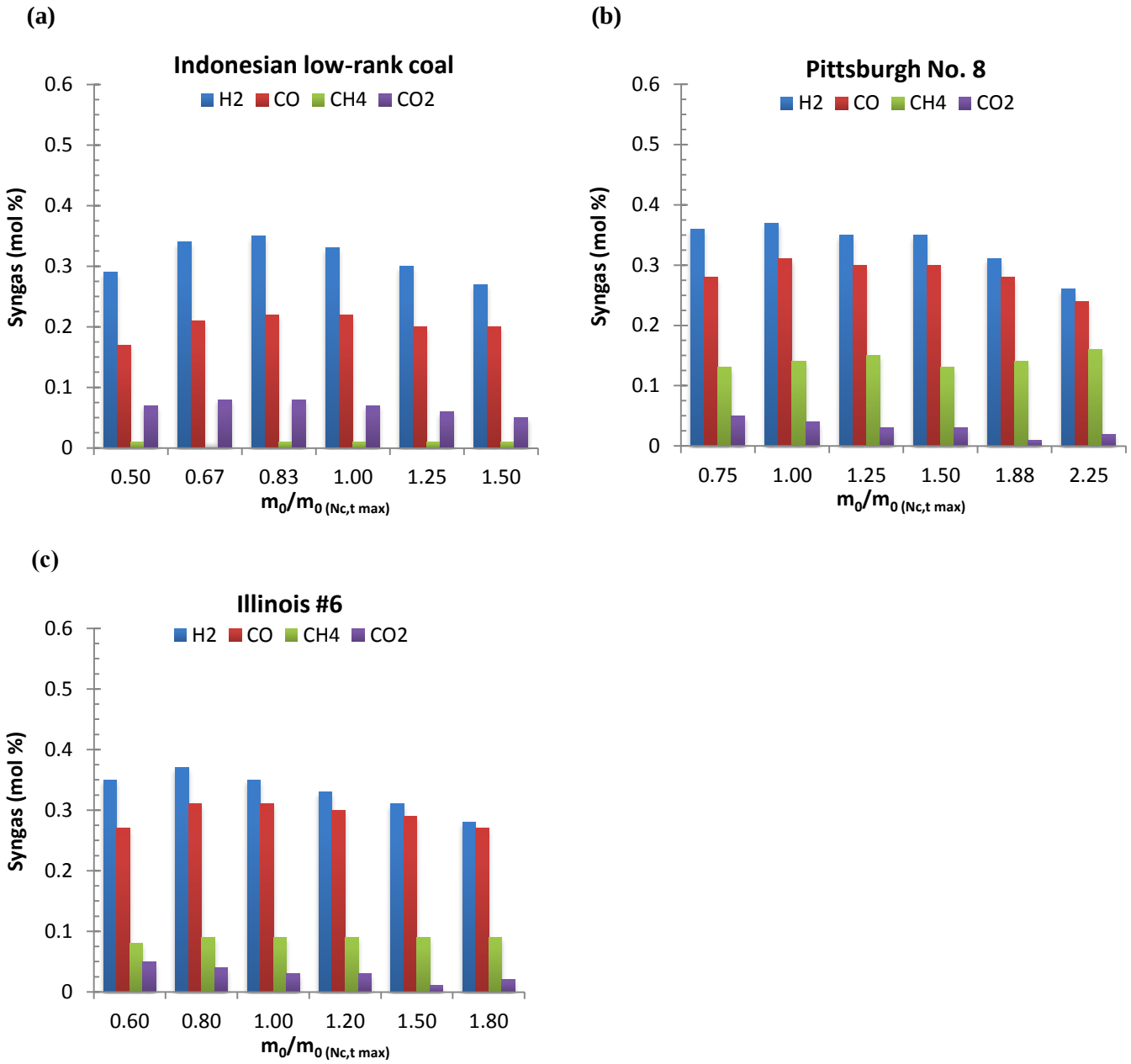

Figure 11: Modelled relationship between $m_0/m_{0\ (Nc,t\ max)}$ and syngas molar composition H_2, CO, CH_4 (and CO_2) for the gasification of (a) Indonesian low-rank coal, (b) Illinois #6 and (c) Pittsburgh No. 8 coals.

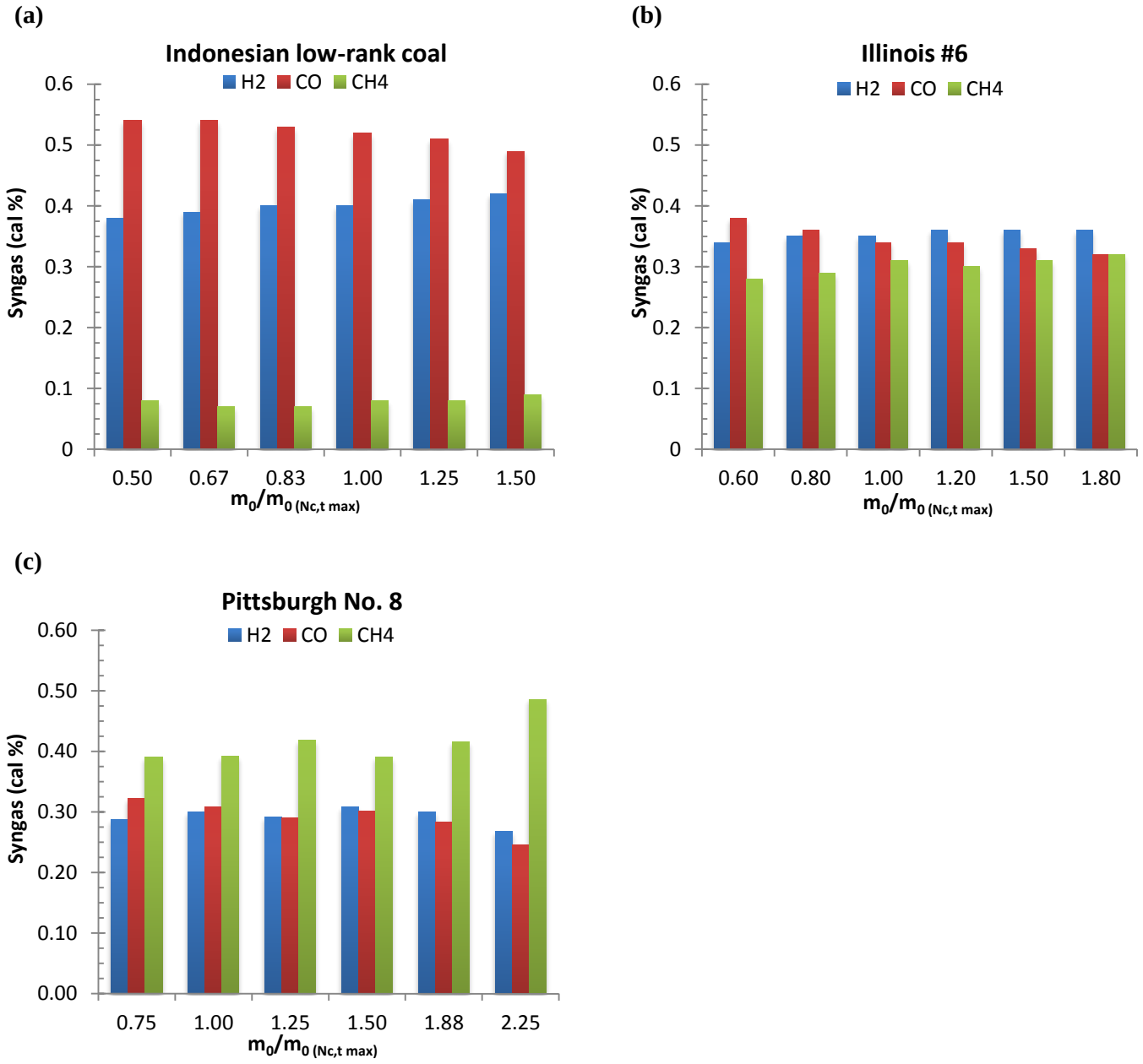

Figure 12: Modelled relationship between $m_0/m_{0\ (Nc,t\ max)}$ and the relative calorific (cal %) contributions of H_2, CO and CH_4 to the syngas heating value , for the gasification of (a) Indonesian low-rank, (b) Illinois #6, and (c) Pittsburgh No. 8 coals.

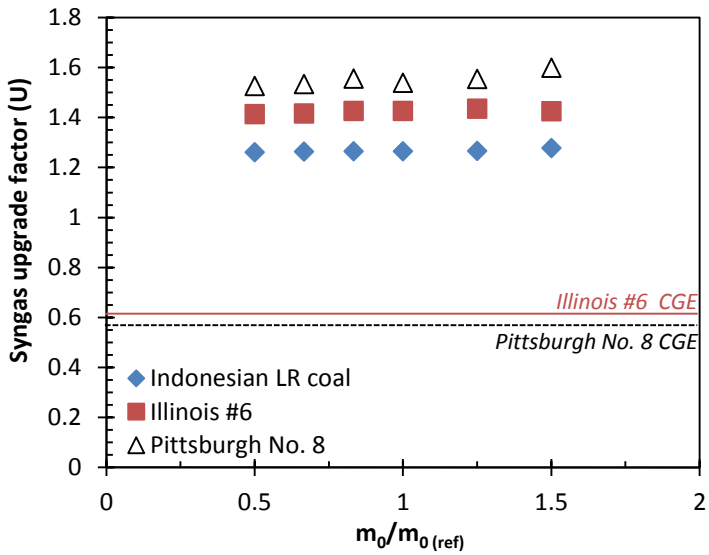

Figure 13: Modelled relationship between the reference-normalised initial fuel batch mass ($m_{0,ref}$ = 180 kg) and the syngas upgrade factor (see equation 17) for the gasification of Indonesian low-rank, Pittsburgh No. 8 and Illinois #6 coals. Also presented are the cold gas efficiencies predicted from measured effluent compositions for the autothermal gasification of Illinois #6 (0.61) and Pittsburgh No. 8 (0.57) coals in a Lurgi gasifier [22].

3.4 Residual fuel composition

Figure 14 presents the distribution of the coal, moisture and ash matter fractions of the fuel that remains in the bed at the end of the solar day as a function of distance from the floor of the reactor. The step-change in the distribution at z = 0.059 m, represents the top of the fuel bed. It can be seen that the final composition of fuel in the bed is highly non-uniform, with significant differences in the residual composition for z < 0.059 m by the end of the solar day. This is because of the highly non-uniform nature of the temperature-controlled reactions that take place through the fuel bed. Indeed, this figure shows that the fuel that is present at the end of the solar day has a vastly different composition to that charged into the reactor bed at the start of the solar day. This has implications on the re-use or disposal options for the

residual material, since it neither is pure char, nor pure ash. The lack of homogeneity would need to be considered in any plans for the process.

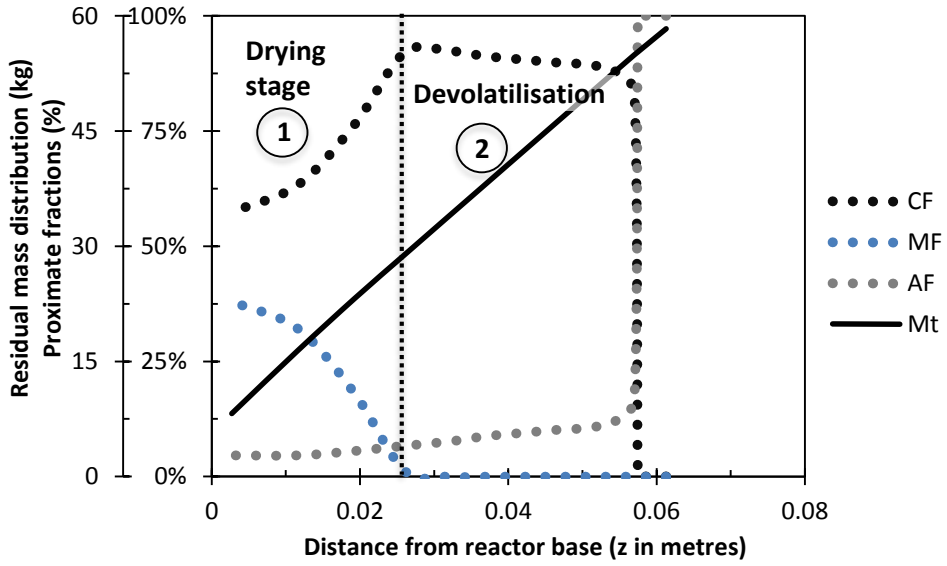

Figure 14: Modelled residual mass distribution (M_t) of Indonesian low-rank coal through the fuel bed and the proximate fractions of coal (CF), moisture (MF) and ash (AF) with distance from the reactor bottom that remain at the end of the solar day.

4.0 Discussion

The present model has shown that the composition and rate of syngas produced from this reactor are dependent upon both the composition and the mass of fuel charged into the bed at the start of each solar day. These two factors determine the rate of conduction through the fuel bed and the thermal gradient from the bed surface to the base, and thus also the temperature-dependent devolatilisation and gasification reactions within various layers of the fuel bed. As shown above in Figure 10, there is an optimum initial batch mass to maximise fuel conversion to syngas. Not only does this highlight the need to predict reliably the initial mass of the fuel bed to maximise productivity, it also generates the challenge as to how to utilise the unconverted residual fuel that remains in the bed at the end of the solar day, which has a markedly different composition of char, moisture and volatiles than the original fuel. That is, day-to-day variation in the extent of conversion of the residual fuel, will further augment the variability in the daily syngas production rate and composition. This, in turn, will add to the cost of the downstream syngas upgrading plant. Finally, the present results provide insight into the potential impact of cloud-based variability in solar insolation. As apparent from the rapid fall in the predicted (and measured) bed temperature at the end of the day, any cloud induced variability in solar insolation can be expected to have a significant adverse impact both on the rate of syngas evolution from this reactor and the extent of conversion.

5.0 Conclusions

A simplified one-dimensional heat transfer and detailed chemistry model of a solar packed bed gasifier has been developed by a methodology, that for the first time, integrates, semi-empirical functional group devolatilisation with gasification reaction kinetics adapted from models of autothermal gasifiers. The model was found to provide reasonable qualitative and quantitative agreement with the experimental results to an accuracy that is comparable with that of the overall uncertainty in the experimental data for the solar gasification of Indonesian low-rank coal. The average steady-state bed-surface temperature and the carbon conversion rate are within 8% and 10%, respectively of the measured values. Similarly, the overall gas evolution rates agree well. While, the agreement in the relative compositions of CO, H_2 and CO_2 are within 50% of the measured data, the differences are consistent with knowledge that the measured composition of syngas was recorded after the gases had been cooled, which was not accounted for because the extent of cooling was not reported. This cooling favours the forward WGS reaction, which provides a plausible explanation for the discrepancy. However, there is insufficient experimental data to conclusively corroborate these assertions. The wide variability in syngas composition through the solar day and its strong sensitivity to fuel type has significant implications on the design and control of the downstream processing plant, especially for a FT process. The present model was found to be sufficiently robust to provide tractable and accurate inputs to a process modeling analysis. The simplicity of this model has allowed the limitations and design constraints that a solar packed bed reactor would impose on a chemical process such as FT production, to be identified with reasonable computational expense whilst accommodating the variability of the solar resource over a full solar year [27].

The modelling results showed that the final syngas composition is strongly sensitive both to the rank of the fuel and to time through the solar day. In particular, the mole fraction of tars

(modelled as CH_4) in the product gas is found to be much larger for the high rank fuels, comprising 13-16% and 8-9% for the Pittsbsurgh No. 8 and the Illinois #6 coals, respectively, in contrast to the 1% for the Indonesian low-rank coal. Similarly, the sum of H_2 and CO comprises 55% of the syngas fraction for Indonesian low-rank coal, and ~65% of the mole fraction of the Pittsburgh No. 8 and Illinois #6 coals. The large CH_4 fractions produced from the high rank coals can be explained by the low temperatures at the top of the bed, which do not enable fast reforming of methane and given the absence of any air or O_2 fed to the reactor. The syngas upgrade factor is also sensitive to the fraction of CH_4 (and tars), being 1.55 for the Pittsburgh No. 8 coal, which is 8% larger than that for the Illinois #6 coal and 19% larger than that for the Indonesian low-rank coal.

Both the carbon conversion efficiency and the syngas production rate were found to be strongly dependent on both the initial fuel batch mass and on the fuel composition. However, the optimum initial mass required to maximise production rate is significantly different from that required to maximise conversion efficiency, making it impossible to maximize both simultaneously. This is a significant challenge, especially because the fraction of incomplete conversion is large, with around half of the initial fuel remaining in-situ. These sensitivities arise from carbon conversion being dependent on both the rate of coal devolatilisation and char gasification. The model predictions showed that, syngas production falls by a smaller fraction for a super-optimal initial batch mass relative to a sub-optimal initial batch mass. This is because syngas production is driven by char gasification rather than coal devolatilisation. Coal devolatilisation, because it occurs at lower temperatures, is generally a function of the average bed temperature, which is higher for reduced initial batch mass. In comparison, char gasification, which occurs at temperatures in excess of 1000°C occurs near the top of the bed and is a function of the maximum steady state temperature at the bed surface and is higher for larger initial batch mass. Hence, if there is uncertainty in the amount

of solar insolation over a given day, the model predictions show that the risk to reduced syngas production is lower for an over-filled reactor.

Finally, the slow rate of heat transfer through the fuel bed means that the composition of the bed changes at varying rates through its depth as the day progresses. The composition of the residual fuel at the end of the solar day was found to exhibit not only considerable variability through the bed but also to differ greatly from the proximate composition of the initial fuel. This has significant implications on the operation of the reactor. It is likely to be preferable to either direct the residual fuel to an alternative application or blend/homogenise the residual fuel to reduce day-to-day fluctuations in residual fuel composition. This, in-turn will further impact on the cost of the syngas upgrading facility downstream from the gasifier.

Acknowledgements

A.A.K. would like to thank Ricoh for providing the Clean Energy Scholarship. P.J.v.E. would like to acknowledge the support of the Australian Solar Institute (ASI) for providing a postdoctoral fellowship. The Australian Government, through the ASI, is supporting Australian research and development in solar photovoltaic and solar thermal technologies to help solar power become cost competitive with other energy sources. G.J.N. wishes to thank the Australian Research Council (ARC) for the Discovery Outstanding Researcher Award used to support this work. The authors would also like to thank the helpful comments of Prof. Aldo Steinfeld of ETH Zurich for his comments on this work which greatly improved it. The authors gratefully acknowledge the financial and other support received for this research from the Energy Pipelines Cooperative Research Centre (EPCRC) which was established under the Australian Government's Cooperative Research Centre's program.

References

1. Adams II T, Barton P. Combining coal gasification and natural gas reforming for efficient polygeneration. Fuel Processing Technology 2011;92:639-55.

2. Apt J, Newcomer A, Lave L, Douglas S, Dunn L. An engineering-economic analysis of syngas storage. NETL: 2008.

3. Bell D, Towler B. Coal gasification and its applications. Elsevier: Oxford, UK, 2011.

4. Kreutz T, Larson E, Liu G, Williams R. In Fischer-Tropsch fuels from coal and biomass. 25th Ann. Intl Pittsburgh Coal Conference, Pittsburgh, PA, USA 2008.

5. Meerman J, Ramirez A, Turkenburg W, Faaij A. Performance of simulated flexible integrated gasification polygeneration facilities. Part A: A technical-energetic assessment. Renewable and Sustainable Energy Reviews 2011;15:2563-87.

6. O. van Vliet, A. Faaij, W. Turkenburg, Fischer-Tropsch diesel production in a well-to-wheel perspective: A carbon, energy flow and cost analysis. Energy Conversion and Management 2009;50:855-76.

7. Woods M, Capicotto P, Haslbeck J, Kuehn N, Matuszewski M, Pinkerton L, Rutkowski M, Schoff R. Volume 1: Bituminous coal and natural gas to electricity final report. DoE/NETL -2007/1281; US DoE: 2007.

8. Chen Y, Adams II T, Barton P. Optimal design and operation of flexible energy polygeneration systems, Industrial Engineering and Chemistry Research 2011;50:4553-66.

9. Larson E, Fiorese G, Liu G, Williams R, Kreutz T, Consonni S. Co-production of decarbonized synfuels and electricity from coal + biomass with CO_2 capture and storage: an Illinois case study. Energy Environmental Science 2010;3:28-42.

10. Kaniyal AA, van Eyk PJ, Nathan GJ, Ashman PJ, Pincus JJ. Polygeneration of liquid fuels and electricity by the atmospheric pressure hybrid solar gasification of coal. Energy Fuels 2013;27:3538-55.

11. Liu G, Larson E, Williams R, Kreutz T, Guo X. Making Fischer-Tropsch fuels and electricity from coal and biomass: performance and cost analysis. Energy Fuels 2011;25:415-37.

12. Wieckert C, Obrist A, von Zedtwitz P, Maag G, Steinfeld A. Syngas production by thermochemical gasification of carbonaceous waste materials in a 150 kW_{th} packed-bed solar reactor. Energy Fuels 2013;27: 4770-6.

13. Piatkowski N. Solar driven steam gasification of carbonaceous feedstocks feedstock characterization to pilot facility testing. ETH Zurich 2011.

14. Piatkowski N, Steinfeld A. Solar-driven coal gasification in a thermally irradiated packed-bed reactor. Energy Fuels 2008;22:2043-52.

15. Piatkowski N, Steinfeld A. Solar gasification of carbonaceous waste feedstocks in a packed-bed reactor - dynamic modeling and experimental validation. AIChE Journal 2011;57:3522-33.

16. Piatkowski N, Wieckert C, Steinfeld A. Experimental investigation of a packed-bed solar reactor for the steam gasification of carbonaceous feedstocks. Fuel Processing Technology 2009;90:360-6.

17. Piatkowski N, Wieckert C, Weimer A, Steinfeld A. Solar-driven gasification of carbonaceous feedstock - a review. Energy Environmental Science 2011;4:73-82.

18. Biba V, Macak J, Klose E, Malecha J. Mathematical model for the gasification of coal under pressure. Industrial Engineering Chemical Process Design & Development 1978;17:92-8.

19. Govind R, Shah J. Modeling and simulation of an entrained flow coal gasifier, AIChE Journal 1984;30:79-92.

20. Sundaresan S, Amundson N. Studies in char gasification - I A lumped model. Chemical Engineering Science 1979;34:345-54.

21. Hobbs M, Radulovic P, Smoot L. Modeling fixed-bed coal gasifiers. AIChE Journal 1992;38:681-702.

22. Hobbs M, Radulovic P, Smoot L. Prediction of effluent compositions for fixed-bed coal gasifiers. Fuel 1992;71:1177-94.

23. Solomon P, Hamblen D, Carangelo R, Serio M, Deshpande G. General model of coal devolatilisation. Energy Fuels 1988;2:405-22.

24. Atkinson B, Merrick D. Heat transfer and temperature profiles in a coke-oven charge. Fuel 1983;62:553-61.

25. Merrick D. Specific heats and heats of reaction. Fuel 1983;62:540-6.

26. Eisermann W, Johnson P, Conger W. Estimating thermodynamic properties of coal, char, tar and ash. Fuel Processing Technology 1980;3:39-53.

27. Kaniyal AA, van Eyk PJ, Nathan GJ. Storage capacity assessment of liquid fuels production by solar gasification in a packed bed reactor with a dynamic process model. The University of Adelaide, School of Mechanical Engineering 2015.

28. Laurendeau NM. Heterogeneous kinetics of coal char gasification and combustion. Progress in Energy & Combustion Science 1978;4:221-70.

Page Intentionally Left Blank

Statement of Authorship

Title of Paper	A one-dimensional heat transfer, devolatilisation, gasification model of a solar packed bed coal gasifier
Publication Status	Unpublished and unsubmitted work written in a manuscript style
Publication Details	

Principal Author

Name of Principal Author (Candidate)	Ashok A Kaniyal		
Contribution to the Paper	Developed reactor model and the structure upon which paper was written and modelling scenarios were presented. Carried out all drafting and paper revisions following editorial advice from primary and co-supervisor who were the two co-authors.		
Overall percentage (%)	55%		
Certification:	This paper reports on original research I conducted during the period of my Higher Degree by Research candidature and is not subject to any obligations or contractual agreements with a third party that would constrain its inclusion in this thesis. I am the primary author of this paper.		
Signature		Date	

Co-Author Contributions

By signing the Statement of Authorship, each author certifies that:

i. the candidate's stated contribution to the publication is accurate (as detailed above);

ii. permission is granted for the candidate in include the publication in the thesis; and

iii. the sum of all co-author contributions is equal to 100% less the candidate's stated contribution.

Name of Co-Author	Mehdi Jafarian		
Contribution to the Paper	Provided early and ongoing guidance on conceptual design of modelling activities. Provided editorial assistance.		
Signature		Date	15/01/2016

Name of Co-Author	Philip J van Eyk		
Contribution to the Paper	Provided early and ongoing guidance on conceptual design of modelling activities. Provided editorial assistance.		
Signature		Date	15/2/2016

Name of Co-Author	Graham J Nathan		
Contribution to the Paper	Provided early and ongoing guidance on conceptual design of modelling activities. Provided editorial assistance.		
Signature		Date	04 February 2016

Please cut and paste additional co-author panels here as required.

5

STORAGE CAPACITY ASSESSMENT OF LIQUID FUELS PRODUCTION BY SOLAR GASIFICATION IN A PACKED BED REACTOR USING A DYNAMIC PROCESS MODEL

Ashok A Kaniyal [a,c], Philip J van Eyk [b,c], Graham J Nathan [a,c]

[a] School of Mechanical Engineering, The University of Adelaide South Australia 5005
[b] School of Chemical Engineering, The University of Adelaide South Australia 5005
[c] Centre for Energy Technology, The University of Adelaide South Australia 5005

Abstract

The first multi-day performance analysis of the feasibility of integrating a packed bed, indirectly irradiated solar gasification reactor with a downstream FT liquids production facility is reported. Two fuel-loading scenarios were assessed. In one, the residual unconverted fuel at the end of a day is reused, while in the second, the residual fuel is discarded. To estimate a full year time-series of operation, a simplified statistical model was developed from short-period simulations of the 1-D heat transfer, devolatilisation and gasification chemistry model of a 150 kW_{th} packed bed reactor (based on the authors' earlier work). The short time-series cover a variety of solar conditions to represent seasonal, diurnal and cloud-induced solar transience. Also assessed was the influence of increasing the solar flux incident at the emitter plate of the packed bed reactor on syngas production. The combination of the annual time-series and daily model of syngas production was found to represent reasonably the seasonal transience in syngas production. It was then used to estimate the minimum syngas storage volume required to maintain a stable flow-rate and composition of syngas to a FT reactor over a full year of operation. This found that, for an assumed heliostat field collection area of 1000 m^2, at least 64 days of storage is required, under both the residual fuel re-use and discard scenarios. This figure was not sensitive to the two solar sites assessed, Farmington, New Mexico or Tonopah Airport, Nevada. Increasing the heliostat field collection area from 1000 to 1500 m^2, led to an increase in the calculated daily rate of syngas throughput that could be maintained over a full year by 74%, to 5.9 kmol/day. Importantly, a larger heliostat field collection area was calculated to reduce the required storage capacity to approximately halve 35 days, which in absolute terms corresponds to 3.0 tons of syngas. Nevertheless, a requirement for this capacity of storage suggests that the use of the packed bed solar gasification reactor for FT liquids production is unlikely to be viable without substantial changes to the design and operation of the reactor and/or downstream processing plant.

1 Introduction

Energy storage is essential to the high capacity factor operation of electricity generation or fuel production systems integrated with concentrated solar thermal (CST) power systems. Numerous studies have investigated the key drivers of the amount of energy storage required to integrate CST collectors with power generation [1-7] and fuel production cycles [8, 9]. These analyses have largely been based on hybrid energy systems, where CST power is indirectly introduced through a secondary thermal loop [1-6] or the combustion of fossil fuels is either supplemented through the direct introduction of CST power into a thermochemical reactor [8], directly into a boiler volume to drive a power cycle [7]. These analyses further evaluate the sensitivity of the required storage volume to over capacity in the size of the heliostat field, the solar region and the capacity factor of the energy conversion (power) block [1-4]. It is well established that hybridizing conventional power systems to receive direct or indirect solar thermal input [1-7] requires a lower amount of energy storage but this is inevitably at the expense of reduced solar share. While there have been fewer assessments of standalone solar energy systems, Kueh et al recently presented the storage requirements for a stand-alone solar thermal power generation cycle to have no unscheduled shut downs [10]. However, there has been no study assessing the storage requirements of standalone CST systems designed to provide input to a chemical reactor. Indeed, no study has presented an evaluation of the minimum quantity of syngas storage required to enable the integration of a standalone solar thermochemical reactor with a downstream upgrading system such that it has no shut-downs over a full solar year. The present assessment aims to meet this gap.

A recent full-year process modelling analysis of a system integrating an atmospheric pressure hybrid solar gasifier with a FT liquids production system, using an hourly averaged solar dataset, showed that as little as eight hours of syngas storage was required to enable steady state operation of the downstream syngas upgrading reactor over a full solar year [8]. This analysis proposed a hybrid, continuously operational solar, entrained flow gasifier based on the experimentally proven solar vortex reactor [11, 12], assuming that CST power drives gasification in the reactor volume when it is available and autothermal reactions in pure O_2 drive gasification, within the same volume, when solar energy is not available [8]. Although this system required a modest quantum of syngas storage, it was estimated to contribute as much as 15% of the plant's total capital cost and between 10-15% of the levelised cost of fuel [13]. While the proposed hybrid solar vortex reactor enables a constant non-zero syngas output, there are several notable challenges to scaling this reactor to the same capacity as a

pressurised, autothermal entrained flow gasifier [8, 11, 12]. These challenges include maintaining a clean window through which CST energy is introduced to the reactor volume, and because the window prevents the reactor from being operated above 1 bar-a [11, 12]. In comparison, with this reactor concept, the indirectly irradiated packed bed reactor, has been proven to be operationally robust at a scale of 150 kW_{th}. However, solar heat is transferred to the fuel bed via a SiC emitter plate [14-19], which makes it less efficient than the solar vortex reactor where coal particles are directly irradiated [11, 12]. Furthermore, because the packed bed reactor relies on solar energy alone to drive thermochemical reactions, it is far more susceptible to solar intermittency. Thus, it may require a much larger amount of storage than that estimated for the hybrid solar gasification reactor [10]. The present study thus aims to assess the feasibility of integrating sufficient storage, so as to enable the steady state of operation of a downstream syngas upgrading process

The indirectly irradiated, packed bed solar gasifier has been proven, at a scale of 150 kW_{th}, to be operationally robust [14-19]. Concentrated solar thermal radiation is introduced into this reactor through a compound parabolic concentrator (CPC) at the top to irradiate a SiC-coated metal emitter plate (see Figure 1). This emitter plate then re-radiates the thermal energy to the fuel bed that is batched into the reactor before the start of each solar day. The emitter plate reaches temperatures of up to 1400 K after only one hour from the start of the solar day. However, the top of the fuel bed can take 2 – 3 hours to reach steady-state temperatures [14, 19]. As the temperature at the top of the bed rises, the fuel is dried, undergoes thermal decomposition (devolatilisation) to release volatile gases and is then slowly gasified at temperatures above 1000 K in the presence of steam. The reacting layer then descends through the bed, causing the bed to shrink at a rate that is approximately linear with time. Although, this leads to acceleration in the rate of heat conduction through the bed [14, 20], the accumulation of ash on top of the fuel bed insulates the more active char layers underneath. In practice, this has meant that the bed surface temperature has been more than 500 K hotter than the base by the end of a solar day, on a day with consistent solar irradiation [14, 19]. This temperature gradient through the fuel bed leads to a large variance in the rate at which devolatilisation and gasification reactions proceed through the bed. It has also meant that only 50-60% of the fuel that is batched into the reactor at the start of a solar day is converted to syngas and the average composition of the residual fuel at the end of the day is vastly different to that of the original feedstock [20]. Building on previous work [14-19], Kaniyal et al. [20] developed a simplified model of the packed bed gasification reactor using one-

dimensional heat transfer, functional group devolatilisation and gasification reaction kinetics to compare syngas production and composition for a range of fuels with varying volatile content [21, 22]. While the Kaniyal et al. model broadly represented the fuel conversion rate that the packed bed reactor was measured to achieve experimentally, no study has presented a multi-day analysis of the packed bed reactor's gasification performance. Hence, to assess the impact of the potential operational impacts of variations in solar energy over a full year, on syngas production and composition, the present assessment aims to estimate these performance parameters for two scenarios, one where residual fuel that is left ungasified from each day is reused and a scenario, and second where fuel at the end of each solar day is discarded.

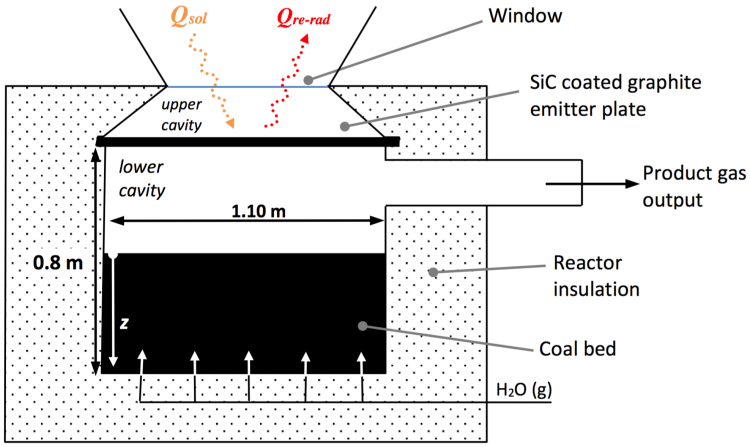

Figure 1: Schematic diagram of the solar packed bed gasifier, based on the experimental configuration reported by Wieckert et al [19].

Two options to upgrade the syngas produced with the packed bed solar gasifier are electricity generation (typically in a combined cycle gas turbine system) [23-25] and/or the production of synthetic crude oil by a FT process [23, 26-30] (see Figure 2). Typically the FT option is likely to be more desirable due to the higher value of liquid fuels over electricity [13, 31]. However, a prerequisite to FT liquids production with currently available FT reactors is the need to propose a method with which to achieve a steady-state output in both the flow-rate and composition of the upgraded syngas over a full solar year despite variable output from the packed bed gasifier. The preferred type of FT reactor for solar thermal operations is likely to be a micro-channel reactor, since these can reduce by an order of magnitude the throughput needed to achieve viability over a conventional fixed bed FT reactor [32, 33]. However, it is necessary to maintain a precise temperature of 210 ± 2°C within a microchannel FT reactor to achieve high syngas conversion rates of ~70-75% and enable >90% C5+ (i.e. C_nH_{2n+2} hydrocarbons where n≥5) for high value products [32, 33]. This tight control of reactor

temperatures in turn requires the steady throughput and composition of both CO and H_2. It also requires the continuous cooling of the reactor with a cold organic heat transfer fluid to meet the load from the highly exothermic nature of reaction 1 which has an enthalpy, ΔH = -165 kJ/mol of CO.

$$nCO + (2n+1)H_2 \rightarrow C_nH_{2n+2} + nH_2O \quad (1)$$

Given the sensitivity of the micro-channel FT reactor to even slight variations in temperature, it takes at least four days to reach steady-state operation after a complete shut-down [32]. Hence, to maintain high productivity these reactors require continuous and steady syngas flow [32]. Thus the present assessment aims to evaluate the relationship between syngas storage capacity and the rate of syngas flow that can be maintained to a downstream FT liquids plant over a full solar year.

In summary, the primary aim of this paper is to evaluate the minimum quantum of syngas storage required to integrate a packed bed solar gasifier with a FT liquids production system, such that it enables continuous operation over a full solar year, using a time-series of syngas production that accounts for diurnal, seasonal and cloud-induced transience in solar energy. A subsequent aim is to quantify the impact of increasing the heliostat field collection area and thus the solar flux at the inlet of the packed bed reactor emitter plate on the relationship between the amount of storage required and the capacity factor of the FT liquids production system. A further aim is to assess the operational impact of two fuel management strategies on the performance of the packed bed reactor, namely to re-use the residual, unconverted fuel from one day to the next or to discard the residual fuel that remains unconverted at the end of each solar day. An additional aim is to determine the minimum gas storage capacity required under the fuel-reuse or fuel dump operational strategies. The final aim is to evaluate the constraints that the required amount of storage may present to the feasibility of integrating a solar packed bed gasifier with a downstream FT liquids production system.

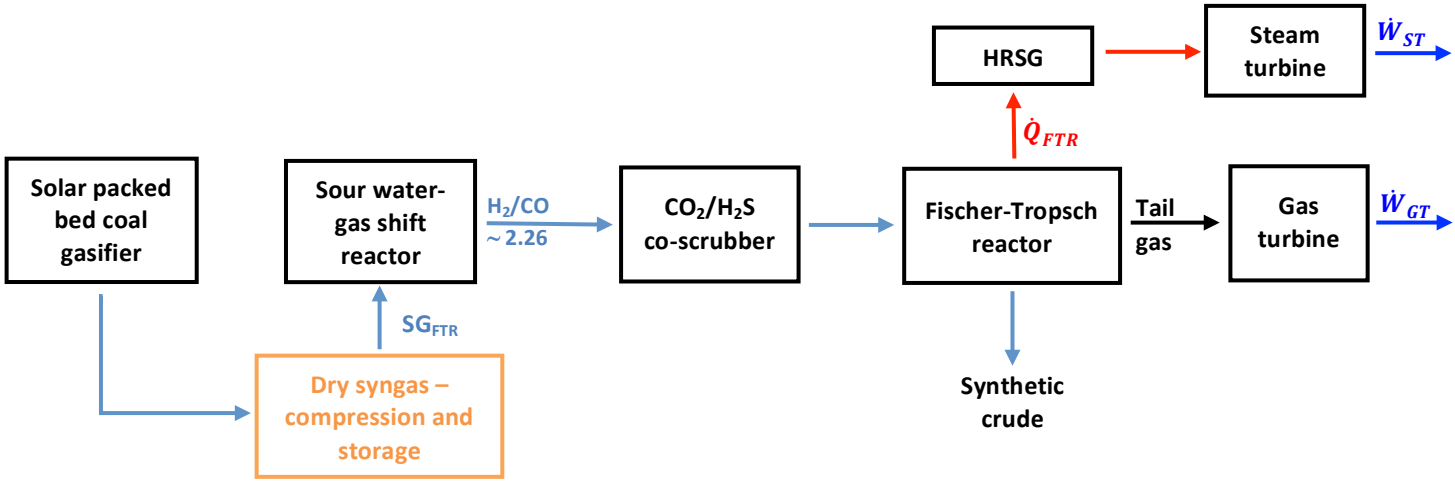

Figure 2: Schematic flow diagram of solar packed bed gasifier system integrated with pressurised gas storage and a Fischer-Tropsch reactor and power generation island.

2 Methodology

Figure 2 presents a schematic process flow diagram of a packed bed gasification reactor that is integrated with a pressurised syngas storage system and the downstream unit operations for upgrading and cleaning the raw syngas to achieve a H_2/CO ratio of 1.5 – 2, before directing it to the FT reactor [32]. The target for the modeling study is to identify storage capacity and SG_{FTR} that enable syngas flow with constant composition to the FT over a full year of operation.

2.1 Multi-day simulation of packed bed reactor operation

To estimate a semi-empirical relationship between cumulative daily solar thermal power and syngas production/composition, the one-dimensional, devolatilisation and gasification chemistry model developed by Kaniyal et al. was used [20]. This model was simulated on a 1-second time-step for two separate fuel loading operating strategies, Residual Fuel Re-Use and Residual Fuel Discard.

For the Residual Fuel Re-Use scenario, model simulations are used to predict the relationship between syngas production and cumulative daily solar insolation, assuming that the ash that accumulates at the top of the reactor is replaced by new as-received (AR) fuel at the end of each solar day. That is, new fuel is assumed to be loaded over the unconverted fuel remaining from the previous day. This scenario is likely to apply where the value of the residual fuel (whose quantity is ~50% that of the original fuel [19]) is sufficient high, to warrant its re-use.

For the Residual Fuel Discard scenario, model simulations predict the relationship between syngas production and cumulative daily solar insolation, assuming that any fuel that remains ungasified at the end of each solar day is discarded. This means that the batch of fuel loaded into the reactor from one day to the next is assumed to have the same composition. This scenario is likely to apply where the cost of using new fuel is lower than the alternative option of extracting all of the solids from the reactor at the end of the solar day, separating the ash from the unconverted fuel and then blending and/or layering the residual fuel over the new as-received (AR) fuel.

The relationship between syngas production/composition and solar input under the *Fuel Re-use* scenario was estimated following a simulation of the 1-D reactor model over twelve solar

days. These twelve solar days were designed to represent solar insolation conditions representative of summer, spring, autumn and winter. This scenario also assessed inter-day variance in syngas composition from the reuse of partly gasified fuel. The *Fuel Discard* scenario used five days of simulation data from the 1-D packed bed reactor model because no evaluation of the impacts of composition variability in residual fuel feedstock on syngas production and composition was assessed.

Both scenarios are based on the gasification of Indonesian low-rank coal, the same fuel as that assessed by Wieckert et al. in the 150 kW_{th} prototype of the solar packed bed reactor [19]. The modeling methodology applied herein was not optimised to yield the maximal syngas production rate over each day of the year but rather to accurately calculate a time series of daily syngas production and composition that is representative of seasonal, diurnal and stochastic variations in solar insolation.

Subsections 2.1.1 and 2.1.2 present the relationship between syngas production and the cumulative daily solar thermal power input to the reactor normalised to the annual maximum for the two reactor operational scenarios described.

2.1.1 Residual Fuel Re-use Model – Key Observations

For this assessment, the solar insolation time-series used to represent the seasonal influence of solar input to the reactor were artificially varied in a systematic way from the insolation profile corresponding to the experimental conditions reported by Wieckert et al. [19]. Assessments were performed for a representative:

i. summer period – with consistent solar radiation over five days varied with the peak solar flux varied by ±20%, m_0 = 180 kg;
ii. spring/autumn period: solar insolation profile consistently interrupted at the same periods over five-days by short-periods (< 0.5 h) of cloud induced transience, m_0 = 80 kg;
iii. winter period: with solar radiation absent over long periods over two days, m_0 = 80 kg.

On the basis that low cumulative daily solar insolation would lead to reduced total fuel conversion, different values of m_0 were used for the different simulation periods to approximate optimal reactor operation.

Figure 3 present the time-series of calculated production of syngas for each of the three short-term time-series of data across three seasons summer, spring/autumn and winter, using the 1-D model of Kaniyal et al. [20]. Over all 12 days simulated, the average H_2:CO ratio was ~1.46

± 0.22. Principally, Figure 3 shows the significant variance in syngas productivity that can be expected over different seasonal events through a solar year. These representative time-series, based on a time-step of 1 second, were used to estimate a relationship between normalised daily solar insolation, syngas production and composition from this reactor over a full year of operation.

Figure 3 also presents the corresponding performance impacts of cloud-induced transience when the solar input is approximately zero. The duration of these cloudy periods is sufficient for the calculated average rate of syngas production to fall steadily to zero. It can also be seen that the time-lag between when production was estimated to return to steady-state conditions was ~30 min from when the solar input to the reactor returns to its maximal level. Figure 3 presents the equivalent response during the selected short-term winter period, during which the cumulative daily solar flux input is 65% lower than that through the summer period and 30% lower than that through the spring period. This leads to an average syngas production rate of 65% of that through spring and 77% lower than that through summer. These results consistently show that the CH_4 fraction in the syngas tends to be high when solar availability is low, which is an expected trend given that devolatilisation occurs at much lower temperatures than char gasification.

Residual Fuel Re-use Scenario – Summer

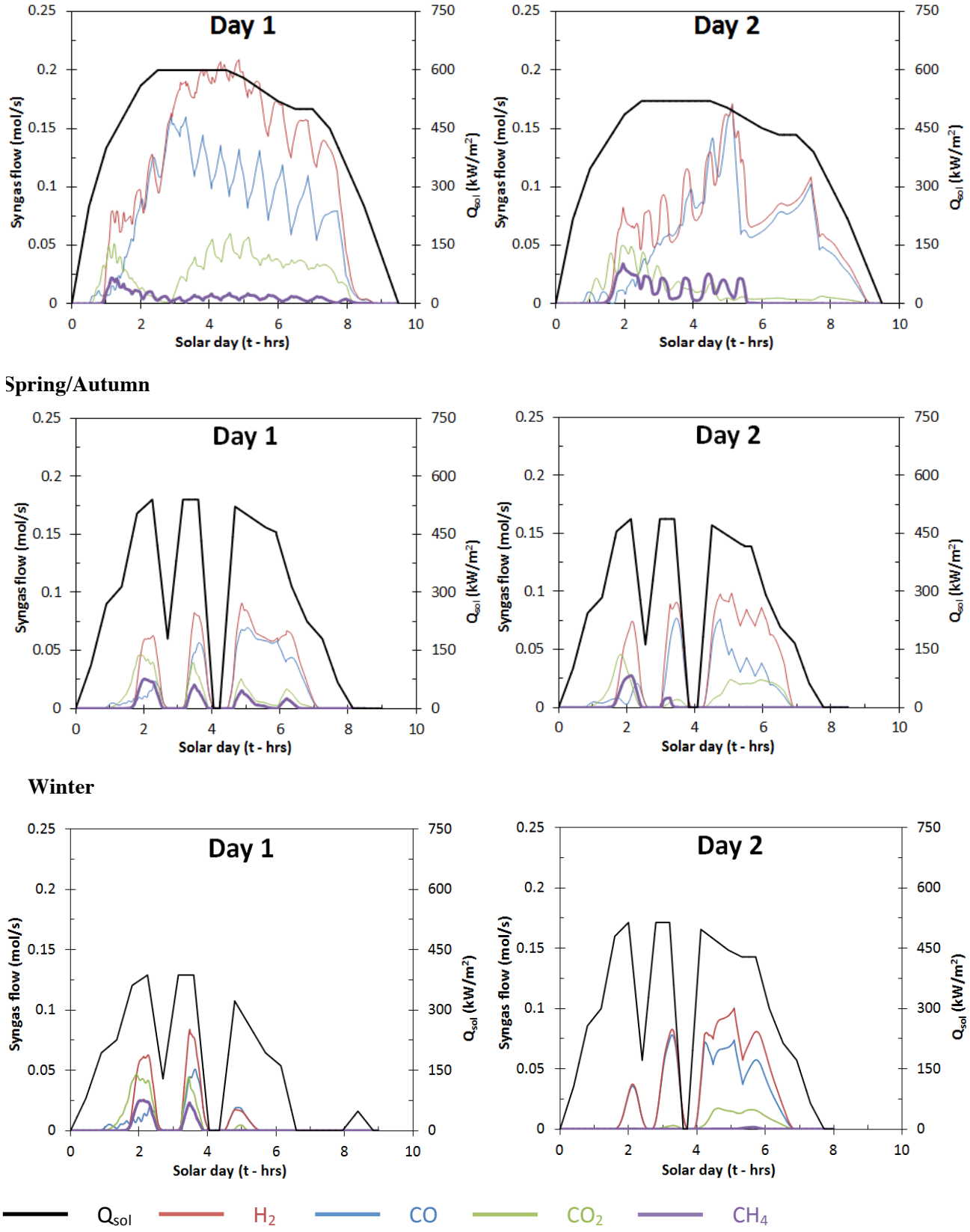

Figure 3: Residual fuel reuse scenario: dynamic one-second time-series of predicted syngas flow for syngas species, H_2, CO, CO_2 and CH_4 from the gasification of Indonesian LR coal assuming operation of 150 kW_{th} packed bed gasifier over representative summer, spring/autumn and winter periods. Full list of time series and corresponding discussion can be found in the Supplementary Material (online).

Figure 4 presents the relationship between the cumulative daily solar input to the reactor, normalised by the maximum cumulative daily solar insolation over a full solar year, and the outputs of CO and H_2 from the reactor for each day in the three time series calculated above, (see steps 1 and 2 in Section 2.1.2). It can be seen that despite some scatter, H_2 and CO production are well correlated with cumulative daily solar insolation when described by a fitted quadratic relationships of Equations 1 and 2, respectively. The error bars correspond to the RMS of the scatter in daily-calculated production relative to the mean values.

$$SG_{CO}(x) = 2690x^{2.27};\ R^2 = 0.97 \quad | x = Q'_{sol} \tag{2}.$$

$$SG_{H_2}(x) = 3597x^{2.05};\ R^2 = 0.98 \quad | x = Q'_{sol} \tag{3}.$$

$$SG_{CO_2}(x) = 384.8x^2 - 208.4x;\ R^2 = 0.77 \quad | x = Q'_{sol} \tag{4}.$$

$$SG_{CH_4}(x) = 160.9x^2 - 33.156x + 7.34;\ R^2 = 0.66 \quad | x = Q'_{sol} \tag{5}.$$

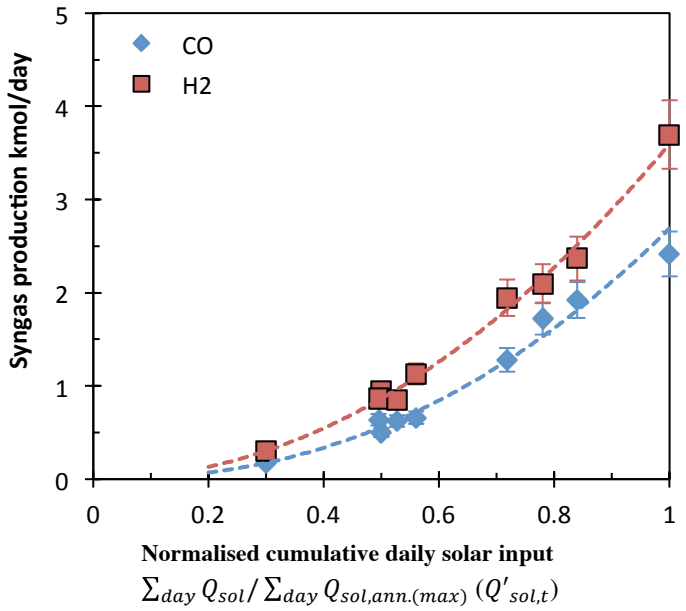

Figure 4: Residual fuel re-use scenario: predicted power-law trends between H_2 and CO production and the cumulative daily solar input to the packed bed gasifier normalised to the peak over all of the days modeled.

Figure 5 presents the relationship between $Q'_{sol,t}$ and the mass conversion ratio, where m_0 and m_T denote conditions at the start and end of the solar day. Although there is somewhat more scatter than in Figure 4, this relationship is nevertheless reasonably well described by a logarithmic function that is calculated to terminate to zero at $Q'_{sol,t} \sim 0.2$ (R^2>0.66).

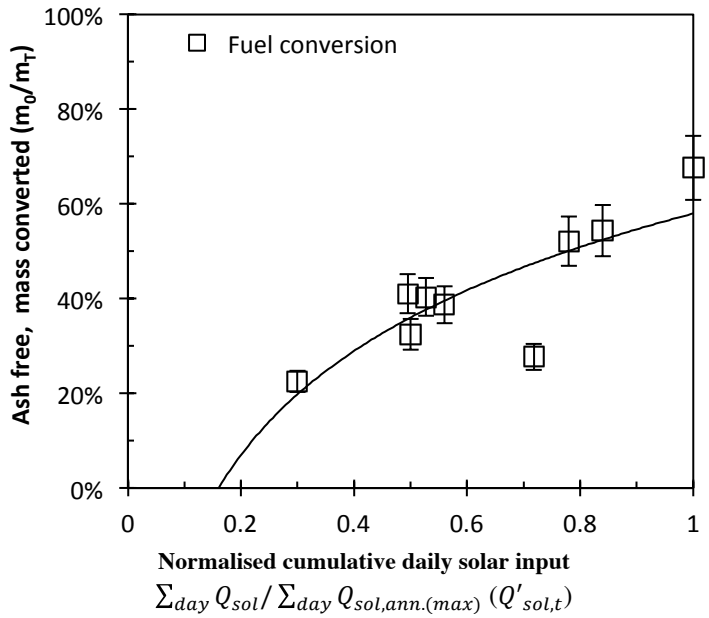

Figure 5: Residual fuel re-use scenario: calculated relationship between (ash, free) fuel mass conversion rate relative to initial batch mass (m_0) and the cumulative daily solar input to the packed bed gasifier normalised to the maximum over all of the days modeled.

Table 1 shows the deviation of the average and RMS of the (CO + H_2) production rate calculated for the annual time-series relative to that calculated using the 1-D model of Kaniyal et al. [20] for each of the scenarios presented in Figure 3. It shows that the average magnitude and variability of the annual time-series predicted using the quadratic statistical model is within 8% of that calculated using the 1-D model of Kaniyal et al [20], which is sufficiently accurate for the annual time-series calculations. This statistical model thus presents a robust reflection of the output of the syngas production time series predicted using the dynamic 1D packed bed reactor gasification model.

Table 1: Residual fuel re-use scenario: difference in the average and RMS of the daily syngas output ($CO+H_2$) predicted for the annual time-series relative to that predicted for each period simulated with the 1-D reactor model of Kaniyal et al. to represent summer, winter and spring/autumn conditions [20].

Solar site	**CO + H_2**	
	Average	**RMS**
Farmington, NM	8%	7.5%
Tonopah, NV	0.1%	2.2%

2.1.2 Residual Fuel Discard Scenario – Key Observations

The five non-contiguous days that were selected correspond to solar insolation conditions representative of summer, spring, autumn and winter. The same initial batch mass (m_0) assumptions were made under this scenario as that described in Section 2.1.1.

This scenario was also used to evaluate the impact of the heliostat field collection area ratio (A_{coll}) on the productivity of the packed bed solar reactor over a full solar year. Assuming $\eta_{optical}$ = 60% [8] and solar insolation profiles over five non-contiguous days, three values for A_{coll} = 1000, 1300 and 1500 m^2 were assessed. Here too, Q_{sol} (kW/m^2) to the reactor emitter plate was calculated as a multiple of solar insolation (I), $\eta_{optical}$ and A_{coll}.

Figure 6 presents the calculated relationship between H_2 and CO production (kmol/day) as a function of the cumulative daily solar input to the packed bed reactor normalised by the maximum cumulative daily solar input to the reactor over a full solar year. This figure shows that, while the H_2, and CO production rates for A_{coll} = 1000 m^2 are reasonably described by a linear relationship, those for A_{coll} = 1500 m^2 are better described by a logarithmic function. Figure 6 also shows that increasing the solar input to the reactor by 1.5 times leads to an increase in syngas (CO + H_2) production of between 30 and 100%. That is, increasing the heliostat field collection area has a greater impact on improving reactor productivity during periods of poor solar insolation than when solar insolation is diurnally consistent, e.g. in summer. Similar relationships are presented for CO_2 and CH_4 in the online Supplementary Material.

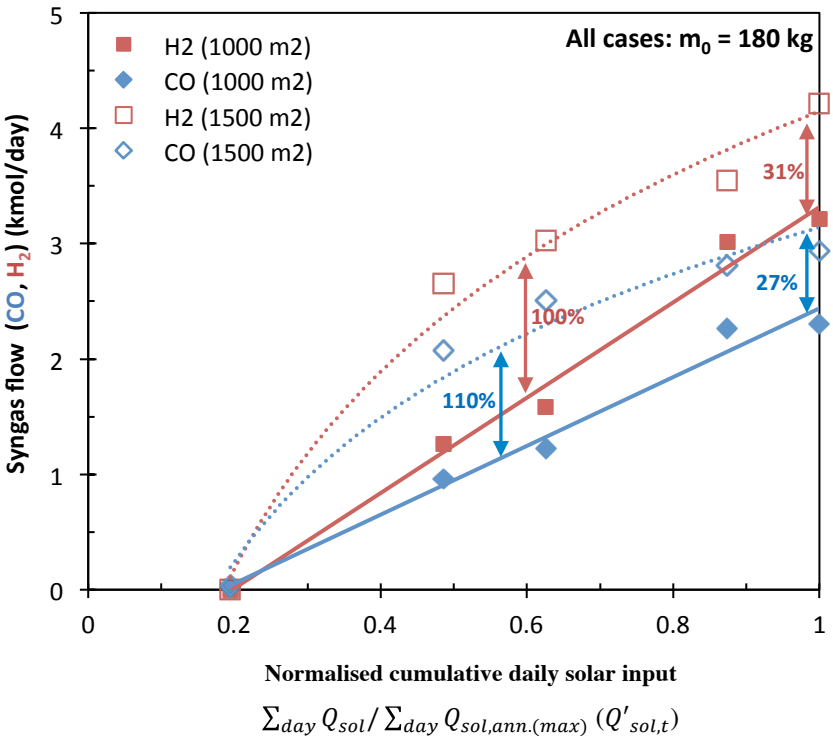

Figure 6: Residual fuel discard scenario: calculated relationship between the normalised cumulative daily solar input to the packed bed reactor and the production of CO, H_2, CO_2 and CH_4. Trend lines were calculated from the explicitly modelled time-series shown in the supplementary material.

2.2 Estimating a time series of syngas production and composition over a full solar year

A full-year time-series for syngas production and composition was estimated for the residual fuel reuse and fuel discard scenarios using the relationships presented in Figure 4 and Figure 6, respectively. A simplified model was assumed to provide sufficiently robust time-series of syngas production and composition over a full solar year because of the limited experimental data that was available with which to verify the predictions from the one-dimensional model over different solar insolation conditions.

It was also assumed to be appropriate because a syngas production time-series based on a one-second time-step would present a level of precision that would not add value to a process modelling analysis which would represent storage requirements on the order of hours or days. The pedagogy for estimating the annual time series of syngas production and composition for the fuel reuse and fuel discard scenarios is summarised below:

1) normalise a 365 day time-series of daily cumulative solar insolation ($Q'_{sol,t}$ see equation 6) by the maximum for that year;

$$Q'_{sol,t} = \left(\frac{Q_t}{Q_{T,max}}\right)_{sol,T=365days} \quad (6)$$

2) estimate a 365 day time-series of daily H_2, CO, CH_4 and CO_2 gas production rates (see Equations 1-4) using the normalised cumulative daily time-series, $Q'_{sol,t}$ evaluated in step 1, as the independent variable for the:
   a. Fuel Re-Use scenario: for two solar sites – Farmington, New Mexico and Tonopah Airport, Nevada [34] (using the relationship in Figure 4 see Figure 8 for estimated annual, daily syngas production time-series);
   b. Fuel Discard scenario: for A_{coll} = 1000 and 1500 m^2 for the Tonopah Airport site (using the relationship in Figure 6 and see Figure 11 for calculated annual daily production time-series).

This procedure enables the development of a 365 point time-series of daily syngas production and gas composition that accounts for diurnal variation in solar insolation through the year, the cloud-induced variation in solar insolation over any one particular day and the influence of seasonal variation in syngas production.

2.3 Storage system model

A storage system model was used to estimate the minimum syngas storage volume required to achieve a constant flow of syngas from the storage tank (SG_{FTR}) to downstream unit operations (see Figure 2 and Figure 7).

The system model is run for each of the following scenarios with the specified value of the independent variable, SG_{FTR} from the storage tank that is systematically varied over the range identified below in steps of 100 kmol/day for the Fuel Reuse and Fuel Discard scenarios:

Fuel Re-Use scenario: 1800 < SG_{FTR} < 3200 kmol/day

Fuel Discard scenario: 5400 < SG_{FTR} < 6400 kmol/day for A_{coll} = 1500 m^2

6100 < SG_{FTR} < 5300 kmol/day for A_{coll} = 1300 m^2

3700 < SG_{FTR} < 3000 kmol/day for A_{coll} = 1000 m^2

SG_{FTR} was varied over the range specified above under each scenario to determine, the flow rate that minimises the storage capacity required ($C_{t.max}$ mols) and maximises $SG_{FTR,des}$ – the maximum, constant flow rate that can be maintained over a full solar year – under the condition that downstream facilities are not shut down. It is assumed that downstream

facilities would be shut down if the storage volume on any day (C_t mols) over a full solar year falls below 15% of its capacity.

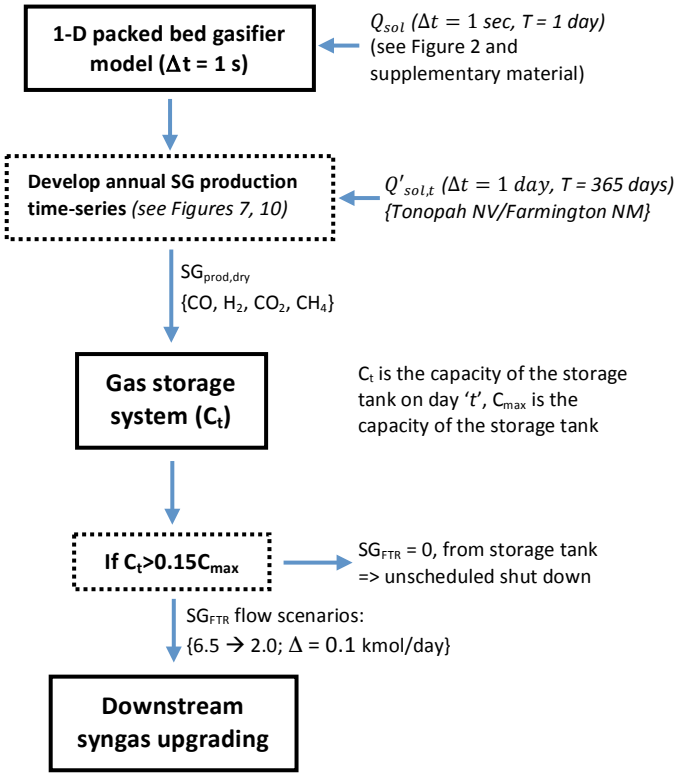

Figure 7: Logic diagram used to calculate the size of downstream processing components in the solar to liquids system from a time series of solar direct normal insolation data.

3 Process Modelling Results

3.1 Residual fuel re-use scenario

For the Fuel Reuse scenario, Figure 8 presents the modeled annual time-series of the three-day rolling average dry syngas flow from the packed bed gasifier to the gas storage tank for the Farmington, New Mexico solar site [34]. Also shown is the corresponding solar insolation time-series, normalised by the maximal cumulative daily solar insolation value for the year. Importantly, the periodicity in the time-series shown in Figure 8 is evident in both the normalised solar insolation dataset and the syngas production time-series. This is a result of the rolling time-series averaging procedure that was applied to smooth, the cumulative daily solar insolation time-series.

The correlation between the predicted annual time-series and the normalised insolation data is 0.98 for the Farmington NM solar site and 0.99 for the Tonopah Airport site. For the Farmington site, the average output through autumn is 52% of that through summer, 50% for winter and 77% for spring. For the Tonopah Airport site, the seasonal average syngas output (moles/day) calculated for the winter time-series is approximately 45% of that calculated for summer, while the corresponding values for autumn and spring, are 60% and 70%, respectively.

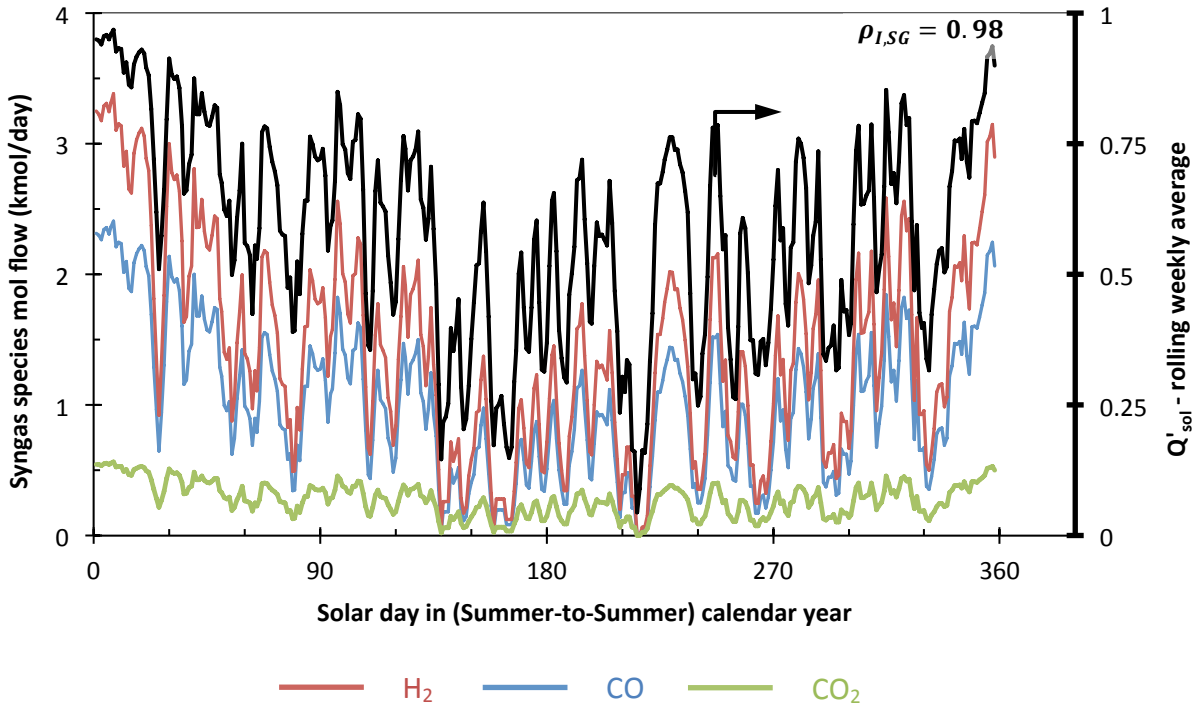

Figure 8: Residual fuel re-use scenario: predicted three-day rolling average time-series of CO, H_2, CO_2 (kmol/day) production (primary axis) and normalised solar insolation (secondary axis) over a full solar year for the Farmington, New Mexico site.

Figure 9 presents the relationship beween the independently varied rate of syngas flow to the downstream plant (SG_{FTR}), syngas storage tank capacity in days and the number of days in a year when $SG_{FTR} = 0$, i.e. where the stored level of syngas falls below 15% of tank capacity. The abscissa of Figure 9 presents the syngas flow scenarios, SG_{FTR} normalised by the design flow, $SG_{FTR,des}$ (required to yield continuous operation over a full solar year).

Figure 9 shows that the syngas storage tank capacity required to maintain continuous operation over a full year is not sensitive to the two solar sites presented. For the Tonopah Airport and Farmington sites respectively, $SG_{FTR,des}$ was estimated to be 2.9 and 2.6 kmol/day. Furthermore, the required level of syngas storage to achieve this design condition was estimated to be 66 days for the Tonopah Airport site and 63 days for the Farmington site. Figure 9 also shows that increasing SG_{FTR}, relative to $SG_{FTR,des}$ by 10% leads to about 26 days of zero flow to downstream unit operations for both sites.

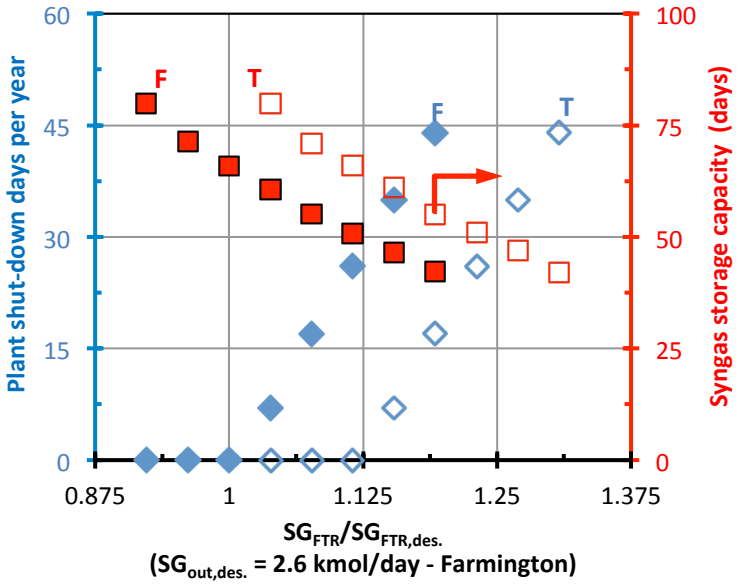

Figure 9: Residual fuel reuse scenario: dependence on the systematically varied syngas flow out of the storage system, (normalised by the (ideal) design flow rate ($SG_{FTR,des}$) for the Farmington (F) and Tonopah (T) site) of the number of days through the calendar year when the downstream plant is shut-down because $SG_{FTR} = 0$ (LH axis); and the gas storage capacity (RH axis) required to achieve the calculated number of plant shut-down days, assuming $A_{coll} = 1000$ m^2

Table 2: Residual fuel reuse scenario: predicted utilisation of the downstream plant and syngas storage facility for the scenario that yields continuous operation over a full solar year with the minimum gas storage capacity.

Solar site	Utilisation factor	
	Storage facility	Downstream plant
Farmington, NM	56%	97%
Tonopah, NV	51%	98%

Figure 10 presents the predicted molar composition of the stored, dry syngas components, H_2, CO, CO_2 and CH_4 as a function time over the full solar year on the primary axis and the quantity of stored dry syngas in tons on the secondary axis for both the Farmington and Tonopah Airport sites. This calculation was performed for a storage tank capacity of 165 kmol (2.64 tons) for the Farmington site and 193 kmol (3.06 tons) for the Tonopah site. The corresponding values of SG_{FTR} are 2.9 kmol/day and 2.6 kmol/day for the Tonopah Airport and Farmington sites respectively. Table 2 reports the key outputs from the model, at the same conditions as that for Figure 10. It can be seen from Figure 10 that the raw syngas

composition in the storage tank is fairly stable over the full solar year at both sites. This is a reasonable outcome, given the storage model assumes that the tank is well-mixed. Thus daily variations in syngas output from the gasifier have a low impact on overall composition as the stored gas volume increases.

The daily averaged H_2:CO ratio was estimated to vary marginally over the full year from 1.40 over the first 100 days of operation before increasing to 1.42 at day 270 and then falling back to 1.41 by the end of the year. Figure 10 also shows the fluctuation in the stored quantity of syngas over a full year of operation on the secondary axis in metric tons. A comparison of the two graphs reveals that the Tonopah airport site requires 16% more gas storage but also yields 11% greater syngas throughput from the storage system to downstream plant. Consistent with this finding, it can be seen in Table 2 that the utilisation factor of 54% for the syngas storage tank is approximately the same for both solar sites. Also presented in Table 2 are two syngas flow and composition stability parameters to downstream plant, which shows that the day-to-day variance is small.

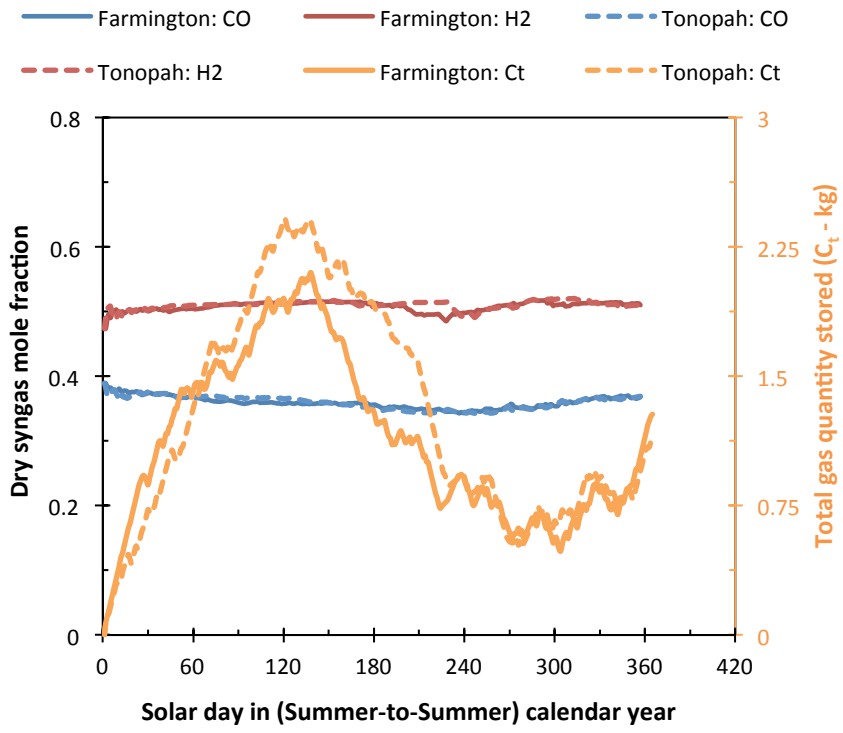

Figure 10: Residual Fuel Re-Use scenario: predicted variation in the dry mole fraction of syngas in the storage tank (that is assumed to be perfectly mixed), with a capacity of 63 days storage for the Farmington site and 66 days storage for Tonopah Airport. Predicted results correspond to the minimum syngas storage mass that yields continuous, constant flow of syngas to downstream unit operations over a full solar year assuming A_{coll} = 1000 m^2.

3.2 Residual fuel discard scenario – influence of heliostat field collection area (A_{coll})

Using the production functions for syngas species (Figure 6) and a normalised cumulative daily solar insolation time-series (see equation 5), the annual syngas production time-series for the Fuel Discard scenario was calculated. Figure 11 presents this time-series of daily syngas production for A_{coll} = 1000 and 1500 m^2.

Over a full year, increasing A_{coll} by 50%, led to an 85% increase in the annual average daily (CO + H_2) production rate. Figure 11 also shows that increasing A_{coll} to 1500 m^2 leads to a reduction in the seasonal dip in the annual syngas production time-series calculated for A_{coll} of 1000 m^2. On average, increasing A_{coll} by 50%, leads to an increase in syngas production of 100% over autumn/spring, 127% over winter and an increase of 58% over summer.

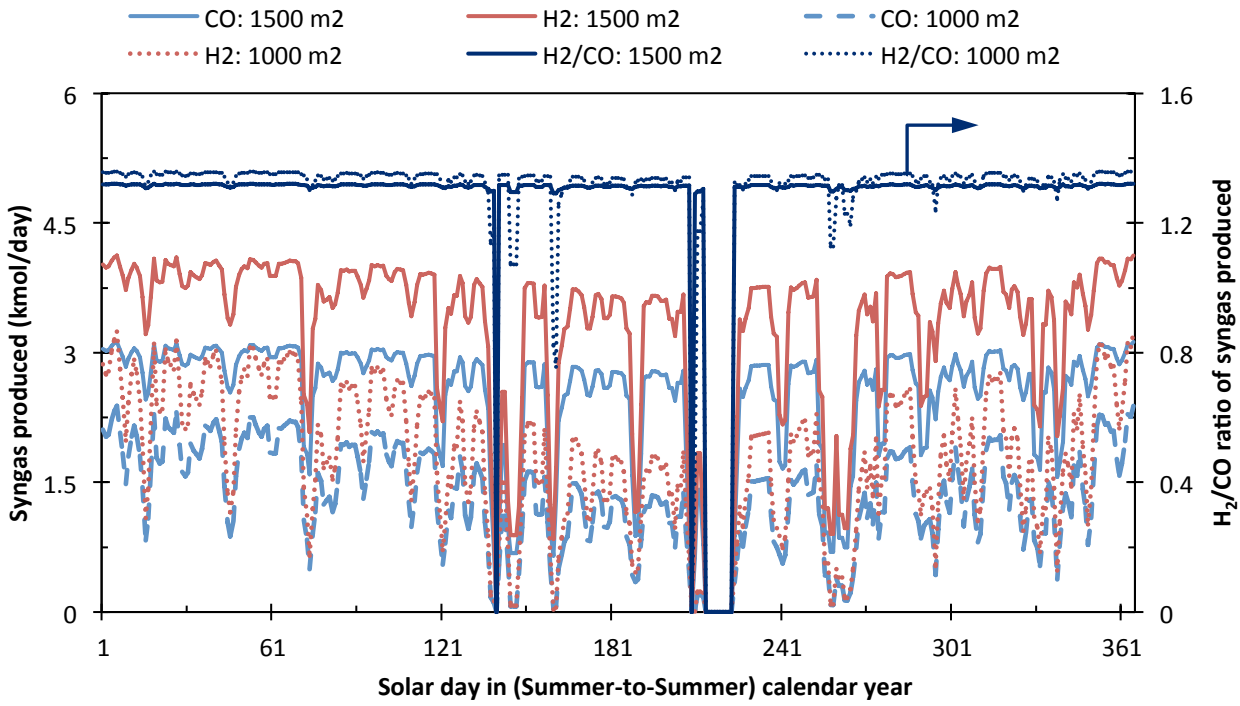

Figure 11: Scenario B: annual 3-day rolling average time-series of daily syngas production (kmol/day) predicted using the normalised Tonopah Airport time-series using the trend relationships presented in

Figure 12 presents the impact of increasing A_{coll} on the syngas storage capacity that is required to deliver continuous operation of systems downstream from the packed bed solar gasifier. It can be seen that increasing A_{coll} from 1000 to 1300 m^2 leads to a 67% improvement in the syngas design flow-rate ($SG_{FTR, des}$) that can be maintained to downstream plant without any unscheduled plant shut downs. Increasing A_{coll} from 1300 to 1500 m^2 yields only a 7% increase in $SG_{FTR,des}$.

For both A_{coll} = 1300 and 1500 m^2 the amount of storage required was calculated to be about 35 days (3.1 tons) while for A_{coll} = 1000 m^2, the quantum of storage required was estimated to be on the order of 65 days of daily averaged syngas flow or 3.7 tons. The potential impact of this large storage requirement on the economic viability of a FT liquids polygeneration system integrating a packed bed solar reactor is discussed in Section 4.

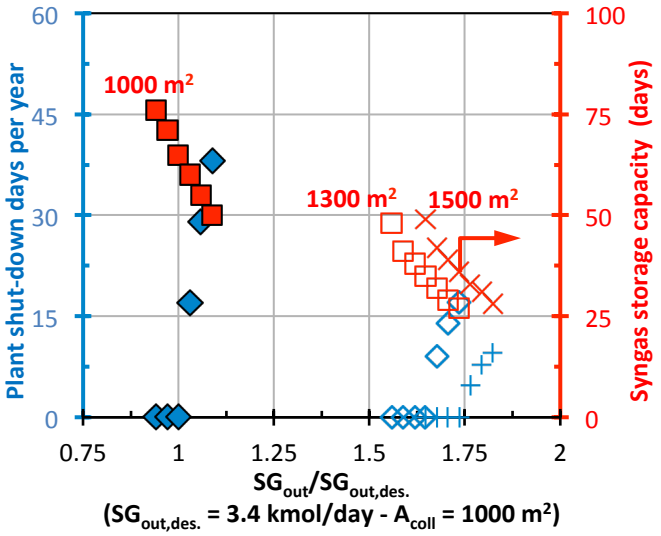

Figure 12: Scenario B: dependence on the systematically varied syngas flow out of the storage system (normalised by the ideal design flow rate $SG_{FTR,des}$ for A_{coll} = 1000 m^2) of the number of days through the calendar year when the downstream plant is shut-down because SG_{FTR} = 0 (LH axis); and the gas storage capacity (RH axis) required to achieve the calculated number of plant shut-down days. Calculations based on Tonopah Airport site.

4 Discussion

Although, increasing A_{coll} by 50% is estimated to have the required syngas storage capacity, the rate of capital utilisation of the storage facility is estimated to be only ~64%. Given both the low capital utilisation and the large capacity required for the storage system, relative to the throughput of the FT liquids process, together with the high cost of syngas storage the capital cost of such a system may be prohibitive for this process. For example, while the hybrid solar coal-to-liquids system described by Kaniyal et al. [8], requires <6 hours of syngas storage, it accounts for >30% of the total depreciated plant capital expenditure [13], assuming a capital cost for storage of $1000/kg [13]. Increasing the storage capacity to the order of one day would already cause this to dominate the capital cost of the entire facility and increasing it by a further 30 times may thus be prohibitive. Hence there is strong incentive to find alternative approaches.

While one of the potential alternative approaches is to increase the capacity of the heliostat array and thereby the solar input to the reactor during periods of low insolation, this scenario would result in spillage of solar radiation, as evidenced by the impact on syngas production in Figure 6 during periods of high solar insolation. This, in turn, would decrease the economic utilisation of the heliostat field and increase costs. Given the amount of storage required without solar spillage, over-sizing the array would not be sufficient to solve the problem of high cost. In addition, it would not address the limitation of the packed bed reactor, specifically that associated with the build-up of ash on the bed surface.

An alternative approach is to introduce autothermal reactions into the bed by the addition of pure O_2. This could be done either with the existing batch process or with a further extension to a continuous (or semi-continuous) reactor. The introduction of an autothermal process would allow the heat input to the bed to be maintained independent from the solar resource, but would have the trade-off of decreasing the solar share and introduce the associated disadvantages of requiring a supply of O_2 from an air separation unit [8, 9]. In addition, it would introduce new challenges to the control of the process, since the heat from an autothermal process generated throughout the bed, while that from the solar process is introduced through the top of the bed. Hence, the temperature profile with the bed would differ for the autothermal process relative to that from the purely solar thermal process.

A further extension of the process toward a continuously operating system could be achieved by drawing on the experience of the commercially proven gravity-fed Lurgi gasifier, which also facilitates continuous ash removal by way of a lock-hopper at the bottom of the reactor [21, 22]. Configuring the packed bed to achieve continuous operation with a moving bed would allow the bed height to be optimised throughout the day, such that average bed temperature that facilitates devolatilization throughout the bed and a high temperature at the top of the bed >1200°C will lead to fast char gasification. Such a configuration, incorporating continuous ash removal would also address the productivity impacts of ash accumulation on the bed surface in the current configuration [14, 19]. In summary, whilst options do exist to modify the packed bed reactor to reduce the size of storage, any of these approaches would require significant further research before their effectiveness can be adequately evaluated.

5 Conclusions

Presented for the first time is a novel approach to estimating an annual syngas production from a long-term time-series of DNI with a packed bed solar gasification reactor in a way that accounts for the diurnal, cloud-induced and seasonal variance in solar insolation over a full year. With this approach, it was found that the capacity of a syngas storage vessel required to achieve a sufficiently stable supply of syngas for continuous operation of a FT liquids polygeneration system is about 64 days assuming a A_{coll} = 1000 m^2 at the reactor emitter plate. While this figure was not found to be sensitive to the two solar sites assessed namely, Farmington NM and Tonopah Airport NV, it was found that the required storage capacity decreased from 65 to 35 days when the A_{coll} was increased by 50%. It was further found that:

1. the reuse of residual fuel that remains unconverted from one-day to the next does not appreciably influence the composition of syngas that is stored in the vessel or the required syngas storage capacity to ensure feasible operation over a full solar year;
2. the calculated difference in syngas throughput achieved over a full year of stable operation for the Farmington sites relative to the Tonopah Airport was a modest ~11%, with 87% of syngas being calculated to be composed of H_2 and CO;
3. increasing A_{coll} to 130% of the reference case leads to an increase in annual net syngas throughput to unit operations downstream from the gasifier of 67% and decreases the absolute syngas storage capacity required from 3.7 to 3.2 tons;
4. a further increase in A_{coll} to 150% of the reference case leads only to a modest further increase in the annual average syngas throughput to unit operations downstream by 74% and decreases the absolute syngas storage capacity required to 3.1 tons from 3.7 tons.

The large storage capacity required for the packed bed reactor is controlled primarily by the much lower output from the gasifier during the winter months relative to summer, rather than by the need to smooth out variations in syngas composition from one day to the next. That is, the storage capacity required to damp fluctuations in composition is significantly less than those to accommodate low outputs during winter. For the cases assessed here, the assumption that the composition of the tank is well-mixed is expected to be reasonable and steady state output in composition was achieved after only some three days of operation. As a point of comparison, the hybrid solar vortex reactor that integrates autothermal combustion was found to require only 3 to 5 hours of storage to maintain productive operation over a full solar year. The storage requirement of the packed bed solar reactor for the cases evaluated here is more

than 200 times larger. Finally, the finding that even the best case scenario requires storage capacities of about 36 days has significant implications for the viability of the present configuration of the solar packed bed reactor together with current generation FTL reactors and syngas storage technologies, since the current expectation is that such costs would be prohibitive.

Acknowledgements

A.A.K. would like to thank Ricoh for providing the Clean Energy Scholarship. P.J.v.E. would like to acknowledge the support of the Australian Solar Institute (ASI) for providing a postdoctoral fellowship. The Australian Government, through the ASI, is supporting Australian research and development in solar photovoltaic and solar thermal technologies to help solar power become cost competitive with other energy sources. G.J.N. wishes to thank the Australian Research Council (ARC) for the Discovery Outstanding Researcher Award used to support this work. The authors gratefully acknowledge the financial and other support received for this research from the Energy Pipelines Cooperative Research Centre (EPCRC) which was established under the Australian Government's Cooperative Research Centre's program.

References

1. Wu J, Hou H, Yang Y, Hu E. Annual performance of a solar aided coal-fired power generation system (SACPG) with various solar field areas and thermal energy storage capacity. Appl. Energy. 2015;157:123-33.
2. Nithyanandam K, Pitchumani R. Cost and performance analysis of concentrating solar power systems with integrated latent thermal energy storage. Energy. 2014;64:793-810.
3. Peterseim JH, White S, Tadros A, Hellwig U. Concentrating solar power hybrid plants – Enabling cost effective synergies. Renewable Energy. 2014;67:178-85.
4. Polonsky G, Kribus A. Performance of the solar hybrid STIG cycle with latent heat storage. Appl Energy. 2015;155:791-803.
5. Abdin Z, Webb CJ, Gray EMacA. Solar hydrogen hybrid energy systems for off-grid electricity supply: A critical review. Renew. Sustain. Energy Rev. 2015,52;1791-808.
6. Pierce W, Gauche P, von Backstrom T, Brent AC, Tadros A. A comparison solar aided power generation (SAPG) and stand-alone concentrating solar power (CSP): A South African case study. Appl. Therm. Eng. 2013;61:657-62.
7. Nathan G, Battye D, Ashman, P. Economic evaluation of a novel fuel-saver hybrid combining a solar receiver with a combustor for a solar power tower. Appl. Energy. 2014;113:1235-43.
8. Kaniyal AA, van Eyk PJ, Nathan GJ, Ashman PJ, Pincus JJ. Polygeneration of liquid fuels and electricity by the atmospheric pressure hybrid solar gasification of coal. Energy Fuels 2013;27:3538-55.
9. Kaniyal AA, van Eyk PJ, Nathan GJ. Dynamic modelling of the co-production of liquid fuels and electricity from various fuel blends via a hybrid solar gasifier. Energy Fuels 2013;27:3556-69.
10. Kueh KCY, Nathan GJ, Saw WL. Storage capacities required for a solar thermal plant to avoid unscheduled reductions in output. Solar Energy. 2015;118:209-21.
11. Z'Graggen A, Haueter P, Maag G, Vidal A, Romero M, Steinfeld A. Hydrogen production by steam-gasification of petroleum coke using concentrated solar power – III. Reactor experimentation with slurry feeding. Int. J. Hydrogen Energy. 2007;32:992-6.
12. Z'Graggen A, Steinfeld A. Hydrogen production by steam-gasification of carbonaceous materials using concentrated solar energy – V. Reactor modelling, optimization and scale-up. Int. J. Hydrogen Energy. 2008; 33:5484-92.11,
13. Saw WL, Kaniyal AA, van Eyk PJ, Nathan GJ, Ashman PJ. Solar hybridised coal-to-liquids via gasification in Australia: Techno-economic Assessment. Energy Procedia. 2015;69:1819-27.
14. Piatkowski N. Solar driven steam gasification of carbonaceous feedstocks, feedstock characterization to pilot facility testing. ETH Zurich 2011.
15. Piatkowski N, Steinfeld A. Solar-driven coal gasification in a thermally irradiated packed-bed reactor. Energy Fuels 2008;22:2043-2052.

16. Piatkowski N, Steinfeld A. Solar gasification of carbonaceous waste feedstocks in a packed-bed reactor - Dynamic modeling and experimental validation. AIChE Journal 2011;57:3522-33.
17. Piatkowski N, Wieckert C, Steinfeld A. Experimental investigation of a packed-bed solar reactor for the steam gasification of carbonaceous feedstocks. Fuel Process. Technol. 2009;90:360-6.
18. Piatkowski N, Wieckert C, Weimer A, Steinfeld A. Solar-driven gasification of carbonaceous feedstock - a review. Energy Environ. Sci. 2011;4:73-82.
19. Wieckert C, Obrist A, von Zedtwitz P, Maag G, Steinfeld A. Syngas production by thermochemical gasification of carbonaceous waste materials in a 150 kW_{th} packed-bed solar reactor. Energy Fuels 2013;27:4770-6.
20. Kaniyal AA, van Eyk PJ, Nathan GJ. A one-dimensional heat transfer, devolatilisation and gasification chemistry model of a solar packed bed coal gasifier. School of Mechanical Engineering, The University of Adelaide.
21. Hobbs M, Radulovic P, Smoot L. Modeling fixed-bed coal gasifiers. AIChE Journal 1992;38:681-702.
22. Hobbs M, Radulovic P, Smoot L. Combustion and gasification of coals in fixed-beds. Prog. Energy Comb. Sci. 1993;19:505-86.
23. Woods M, Capicotto P, Haslbeck J, Kuehn N, Matuszewski M, Pinkerton L, Rutkowski M, Schoff R. Volume 1: Bituminous coal and natural gas to electricity final report DoE/NETL -2007/1281. US DoE:Aug 2007.
24. Adams II T, Barton P. Combining coal gasification and natural gas reforming for efficient polygeneration. Fuel Process. Technol. 2011;92:639-55.
25. Apt J, Newcomer A, Lave L, Douglas S, Dunn L. An engineering-economic analysis of syngas storage. NETL: 2008.
26. Kreutz T, Larson E, Liu G, Williams R. Fischer-Tropsch fuels from coal and biomass. In 25th Ann. Intl Pittsburgh Coal Conference, Pittsburgh, PA, USA 2008.
27. Kreutz T, Williams R, Consonni S, Chiesa, P. Co-production of hydrogen, electricity and CO_2 from coal with commercially ready technology – Part B: Economic analysis. Int. J. Hyd. Energy 2005;30:769-84.
28. Larson E, Fiorese G, Liu G, Williams R, Kreutz T, Consonni S. Co-production of decarbonized synfuels and electricity from coal + biomass with CO_2 capture and storage: an Illinois case study. Energy Environ. Sci. 2010;3:28-42.
29. Liu G, Larson E, Williams R, Kreutz T, Guo X. Making Fischer-Tropsch fuels and electricity from coal and biomass: performance and cost analysis. Energy Fuels 2011;25:415-37.
30. Meerman J, Ramirez A, Turkenburg W, Faaij A. Performance of simulated flexible integrated gasification polygeneration facilities – Part A: A technical-energetic assessment. Renew. Sustain. Energy Rev. 2011;15:2563-87.
31. Meerman J, Ramirez A, Turkenburg W, Faaij A. Performance of simulated flexible integrated gasification polygeneration facilities – Part B: Economic evaluation. Renew. Sustain. Energy Rev. 2012;16:6083-102.

32. Deshmukh S, Tonkovich A, Jarosch K, Schrader L, Fitzgerald S, Kilanowski D, Lerou J, Mazanec T. Scale-up of microchannel reactors for Fischer-Tropsch synthesis. Ind. Eng. Chem. Res. 2010;49:10883-8.
33. Hargreaves N. The Microchannel Advantage: Enabling the Pioneering Projects Pemex – World Bank GGFR Gas Utilization and Flare Reduction Workshop, Veracruz, Mexico, 2012.
34. NREL National solar radiation database 1991-2005 update: User manual. US DoE: Golden, CO 2007

Supplementary Material

Residual Fuel Re-Use Scenario

Figures 13-15 show the significant variance in syngas productivity that can be expected over different seasonal events through a solar year. These representative time-series, based on a time-step of 1 second, also provide a solid basis for evaluating the annual performance of syngas production from this reactor over a full year of operation.

In Figure 13 the peak and cumulative solar input through Day 2 are 17% and 13% lower, respectively, than that through Day 1, while those for Day 3 are 7% and 8% lower, respectively than for Day 1. These changes were predicted to reduce syngas productivity over Day 2 and Day 3, by 36% and 28% respectively relative to the output predicted for Day 1, showing that relatively small changes in the magnitude of flux result in a larger change in output. It also suggests that the productivity depends more strongly on the magnitude of the peak solar flux for the day than on the cumulative value, although it should be noted that the output from each day also depends on the mass and composition of the residual fuel from the previous day. Over Days 4 and 5 the composition of the syngas produced is calculated to correspond more closely to that predicted for Day 1 than for Days 2 and 3. However, the syngas molar flow rate is ~75% of that predicted for Day 1 over Days 4 and 5 even though the peak flux is almost the same over both days. This is a result of the higher char fraction in the combined AR/residual fuel that makes up the fuel bed. The influence of the residual fuel is further evident in the concentration of CH_4 in the syngas, which increases over days 1 to 3 from 2.5 to 5% (mol) and then decreases over days 4 and 5 to 2.5%. During the same period, the predicted H_2:CO molar ratio produced during day 1 is 1.53, closely matches that for day 4 of 1.52, but is different from the ratio produced during days 2 and 3, of ~1.22 and on day 5 of 1.37. This corresponds to a standard deviation of ~10% over the mean value of 1.37. Over all twelve days that were explicitly modeled the average H_2:CO ratio was ~1.46 ± 0.22.

Figure 14 presents the corresponding performance during the spring/autumn season when the solar days are on average 1.8 hours shorter than that through the assessed summer period. The time-series also includes two periods of cloud-induced transience when the solar input is approximately zero. The duration of these cloudy periods is sufficient for the calculated average rate of syngas production to fall steadily to zero. It can also be seen that the time-lag between when production was estimated to return to steady-state conditions was ~30 min

from when the solar input to the reactor returns to its maximal level. In the spring/autumn period, the calculated CH_4 fraction decreases from 6.5%(mol) on Day 1, to 3.2% on Days 2 and 3 and then increases again to 4.5% on Days 4 and 5. On average, the calculated CH_4 fraction through this period is 30% greater than through the summer period presented in Figure 13. The absolute syngas output is ~35% of that the summer period in Figure 13. These results consistently show that the CH_4 fraction in the syngas is high when solar availability is low, which is an expected trend given that devolatilisation occurs at much lower temperatures than char gasification.

Figure 15 presents the equivalent response during the selected short-term winter period, during which the cumulative daily solar flux was 65% lower than that through the representative summer period and 30% lower than that through the representative spring period. This leads to an average syngas production rate equal to 65% of that estimated for spring and 77% lower than that through summer.

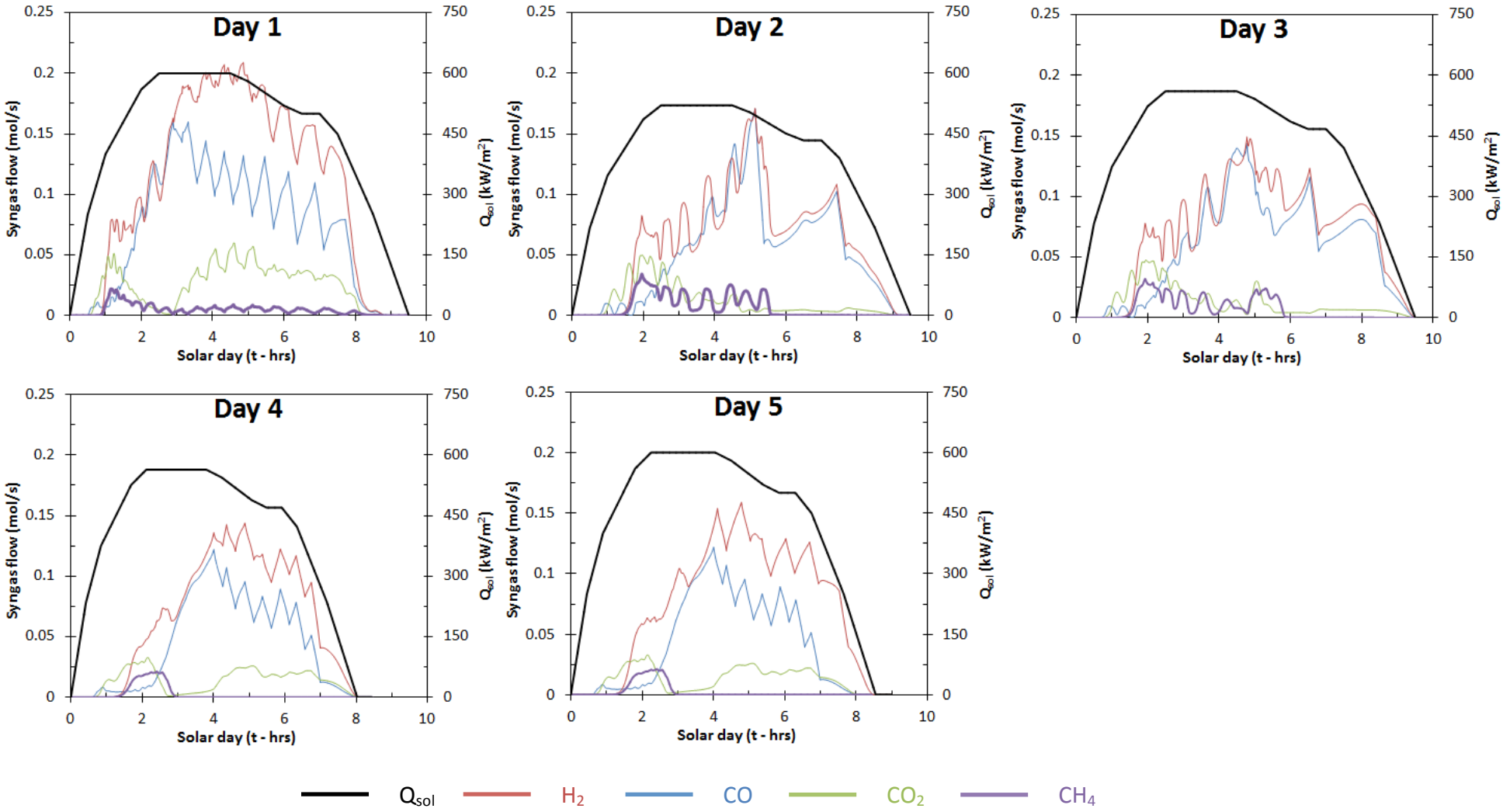

Figure 13: Fuel Re-use scenario: dynamic one-second time-series of predicted syngas flow for syngas species, H_2, CO, CO_2 and CH_4 from the gasification of Indonesian LR coal. The 150 kW_{th} packed bed gasifier was simulated for five consecutive days to represent a period in summer – when solar insolation is diurnally consistent through each day, but whose magnitude is variable (assumed to be decreased by 16% from days 1 to 2 and by a further 6% each day from days 2 to 4 and then increased by 8% from Day 4 to 5).

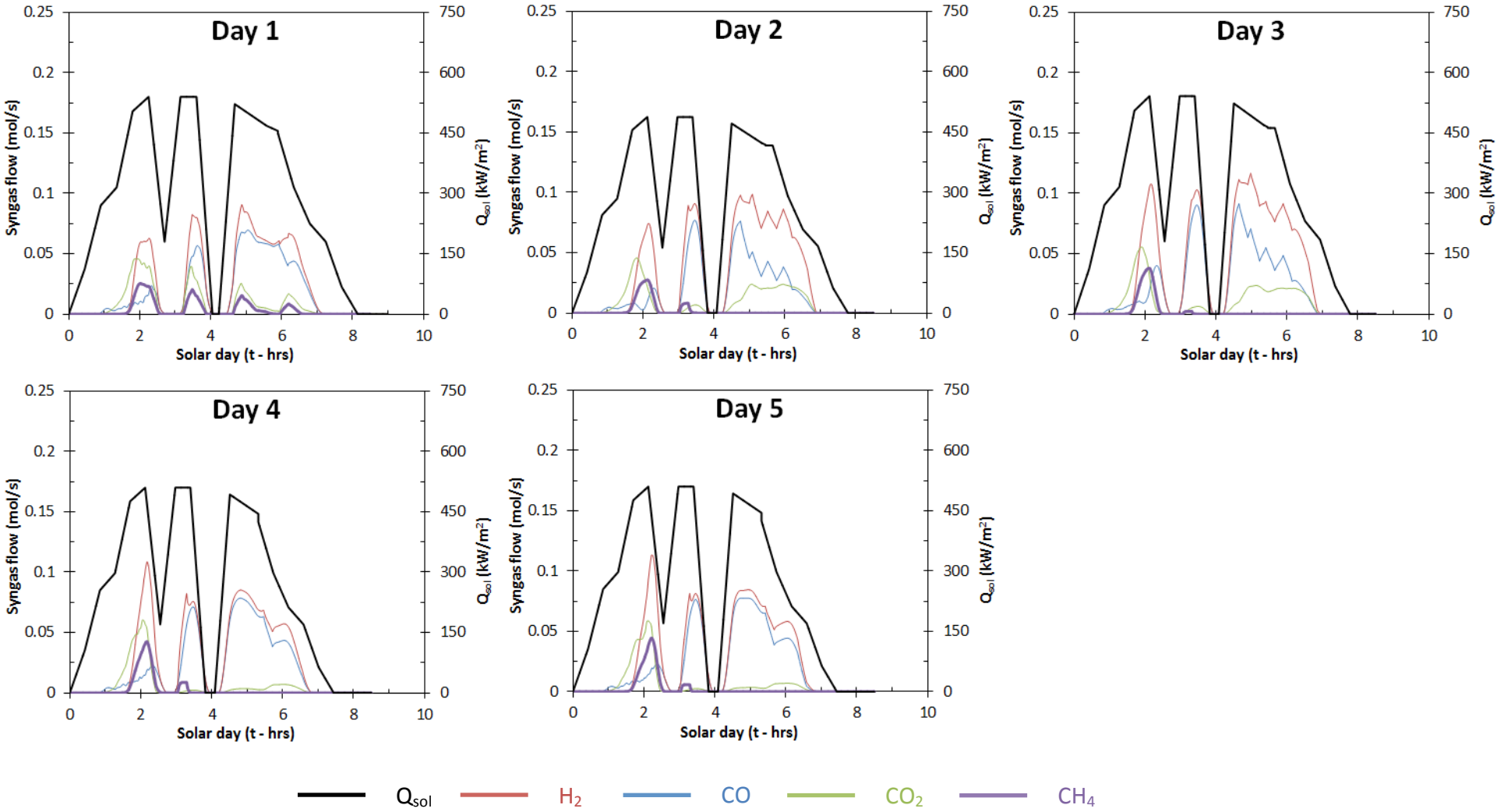

Figure 14: Fuel Re-use scenario: dynamic one-second time-series of predicted syngas flow for syngas species, H_2, CO, CO_2 and CH_4 from the gasification of Indonesian LR coal. The 150 kW_{th} packed bed gasifier was simulated for five consecutive days in a period representative of Spring/Autumn – when solar insolation is interrupted each day by clouds. The magnitude of the flux profile is increased by 12% from day 2 to 3, and then decreased by 5% from day 4 to 5.

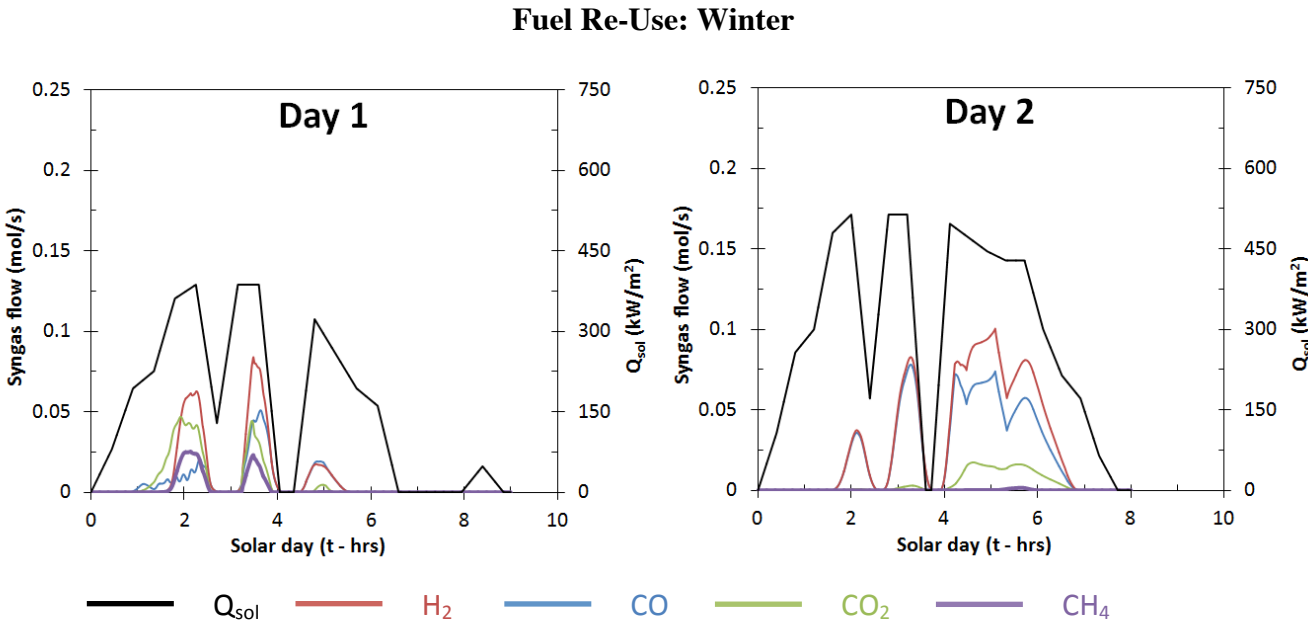

Figure 15: Fuel Re-use scenario: dynamic one-second time-series of predicted syngas flow for syngas species, H_2, CO, CO_2 and CH_4 from the gasification of Indonesian LR coal with the 150 kW_{th} packed bed gasifier over two consecutive days through a period representative of Winter – when solar insolation is assumed to be absent for three days in a week and is intermittent on the two days when it is available.

Residual Fuel Discard scenario

Figures 16 and 17 present a comparison of the syngas production time-series for heliostat collection areas (A_{coll}) of 1000 and 1500 m^2 respectively for the same five non-contiguous solar days through the 2004/05 calendar year from the Tonopah Airport site, also calculated using the 1-D model of Kaniyal et al (based on a 1-second time-step). The time-series for Days 1 and 2 in Figure 16 shows that the rate of syngas production falls sharply at t = 8 hours. This is caused by ash accumulation on the top of the fuel bed, which inhibits heat transfer through the bed and hence decreases the rate of char gasification in the layers below.

The increase in A_{coll} (Figure 17) by 1.5 times is calculated to cause this reduction to occur earlier in the day, when t ~ 6.5 hours. This reduction in output has the potential to cause a serious loss in capital productivity from the plant. On the other hand, the higher flux is also calculated to increase H_2 production rates by ~1.5 times relative to that calculated for a similar stage in the time-series in Figure 16 for days 1 and 2. For Days 3 and 4, with the lower heat flux (Figures 6 and 7) the increase in A_{coll} yields a commensurate increase in syngas production, with little loss in productivity from ash accumulation at the top of the bed. Furthermore, it is also evident that the calculated syngas CH_4 mol fraction decreases with the increase in A_{coll} from 5% and 6%, respectively for days 3 and 4 in Figure 16 to 2.5% and 3%, respectively, as shown in Figure 17.

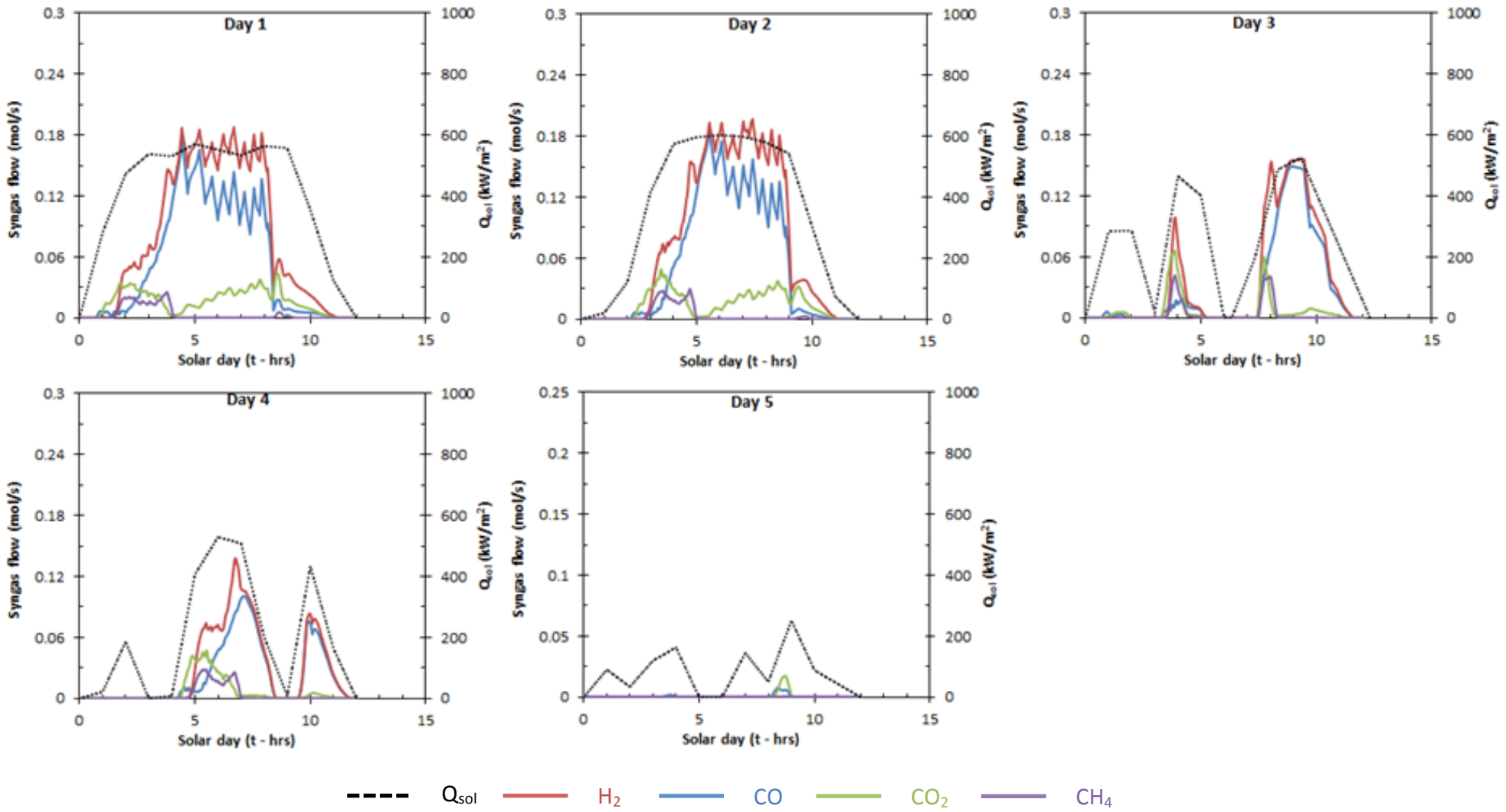

Figure 16: Residual Fuel Discard scenario: calculated daily syngas production and composition time series estimated by simulation of the 1-D packed bed gasifier model for five non-contiguous solar days representing periods in summer, winter, spring/autumn. All scenarios based on Indonesian low-rank coal as the fuel and A_{coll} = 1000 m².

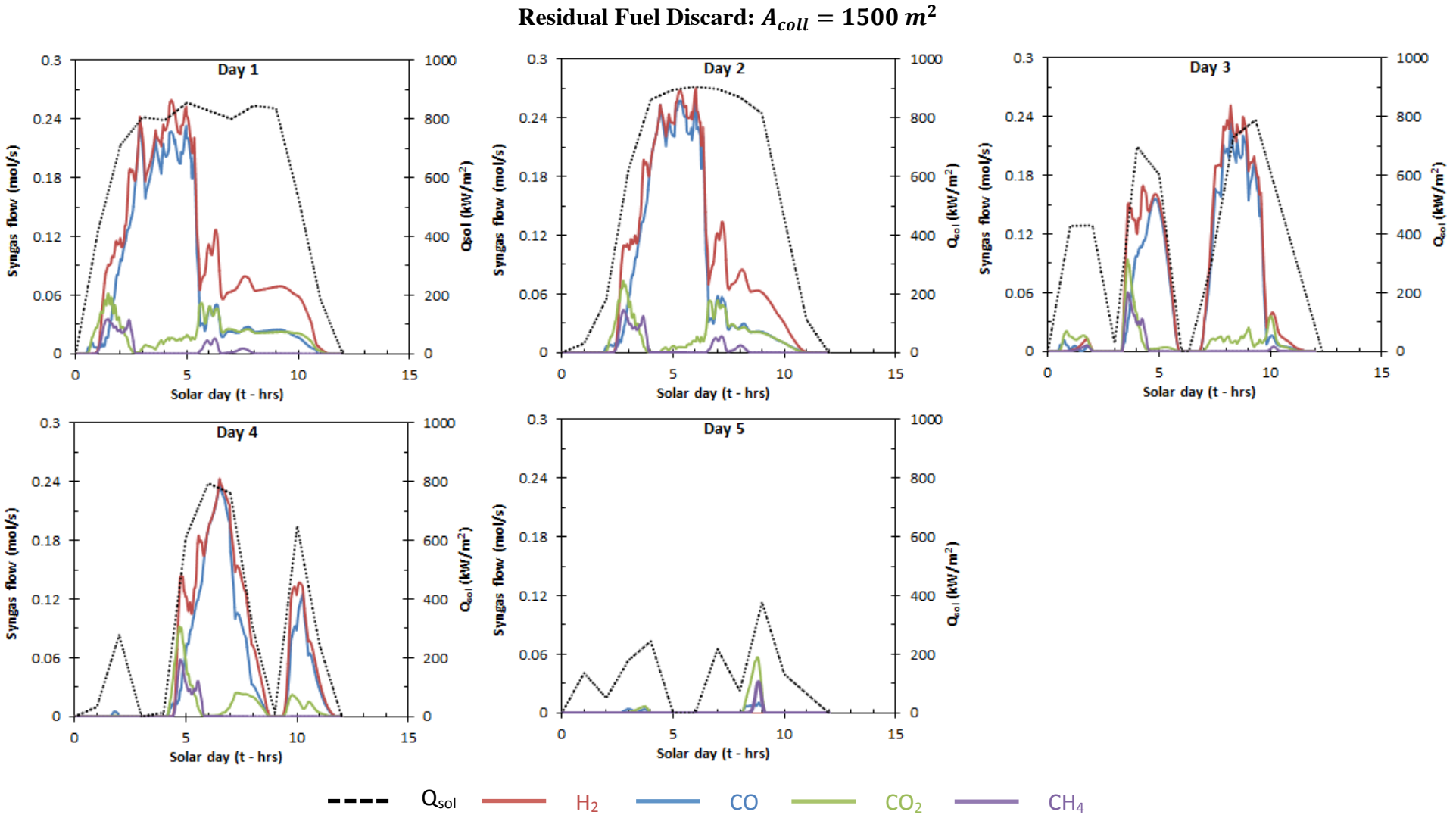

Figure 17: Residual Fuel Discard scenario: calculated daily syngas production and composition time series estimated by simulation of the 1-D packed bed gasifier model for five non-contiguous solar days representing periods in summer, winter, spring/autumn. All scenarios based on Indonesian low-rank coal as the fuel and A_{coll} = 1500 m^2.

Figure 18 presents the calculated variation of H_2, CO, CO_2 and CH_4 production (kmol/day) as a function of the cumulative daily solar input to the packed bed reactor normalised by the maximum cumulative daily solar input to the reactor over the days shown in Figures 6 and 7. This shows that, while the H_2, CO and CO_2 production rates for A_{coll} = 1000 m^2 are reasonably described by a linear relationship, those for A_{coll} = 1500 m^2 are better described by a logarithmic function. Consistently, Figures 13 and 14 also show that increasing the solar input to the reactor by 1.5 times leads to an increase in syngas (CO + H_2) production of between 30 and 100%. In terms of moles of carbon converted the effect of increasing the solar input to the reactor is predicted to be between 24 and 89%.

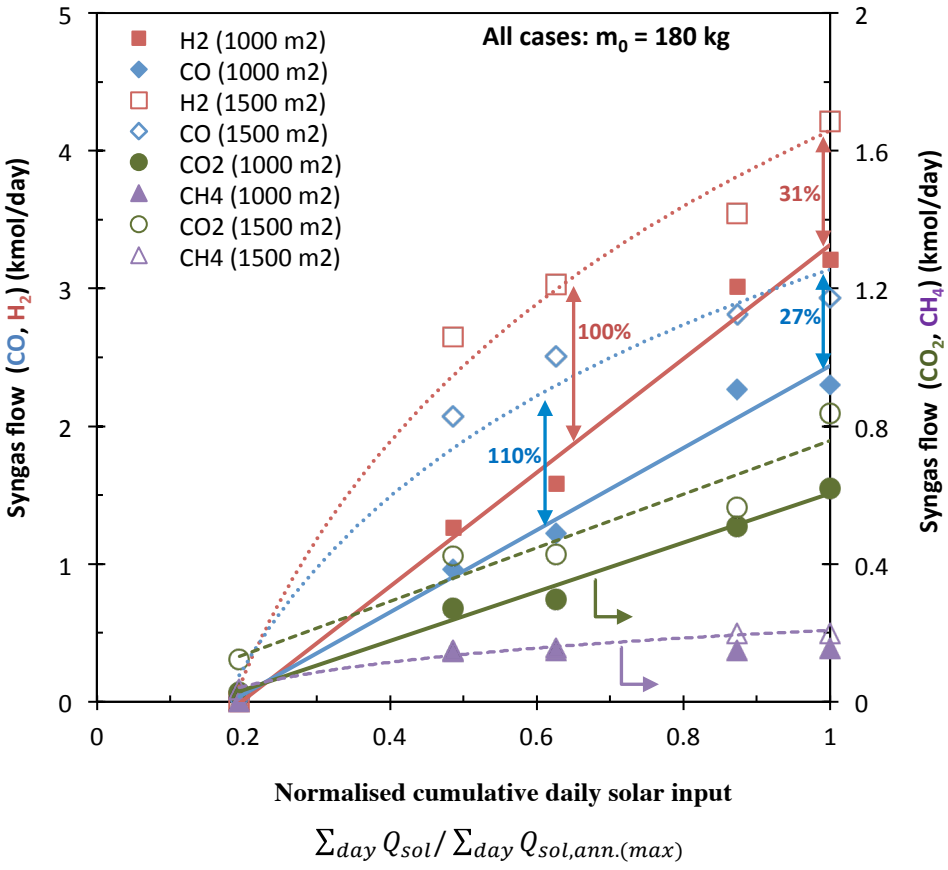

Figure 18: Calculated relationship between the normalised cumulative (cum.) daily solar input to the packed bed reactor and the production of CO, H_2, CO_2 and CH_4. Trend lines were calculated from the explicitly modelled time-series shown in Figures 4 and 5.

Page Intentionally left Blank

Statement of Authorship

Title of Paper	Storage Capacity Assessment of Liquid Fuels Production by Solar Gasification in a Packed Bed Reactor using a Dynamic Process Model
Publication Status	Submitted for Publication
Publication Details	Kaniyal AA, van Eyk PJ, Nathan GJ. 2015. Storage Capacity Assessment of Liquid Fuels Production by Solar Gasification in a Packed Bed Reactor using a Dynamic Process Model. Submitted to Applied Energy 26 Dec 2015.

Principal Author

Name of Principal Author (Candidate)	Ashok A Kaniyal		
Contribution to the Paper	Integrated one-dimensional heat-transfer and chemistry model of packed bed solar gasification reactor reported in an earlier unpublished piece of work with a process modelling analysis that evaluated the minimum syngas storage volume required to facilitate continuous full year operation. Carried out all drafting and paper revisions following editorial advice from primary and co-supervisor who were the two co-authors.		
Overall percentage (%)	60%		
Certification:	This paper reports on original research I conducted during the period of my Higher Degree by Research candidature and is not subject to any obligations or contractual agreements with a third party that would constrain its inclusion in this thesis. I am the primary author of this paper.		
Signature		Date	

Co-Author Contributions

By signing the Statement of Authorship, each author certifies that:

i. the candidate's stated contribution to the publication is accurate (as detailed above);

ii. permission is granted for the candidate in include the publication in the thesis; and

iii. the sum of all co-author contributions is equal to 100% less the candidate's stated contribution.

Name of Co-Author	Philip J van Eyk		
Contribution to the Paper	Provided ongoing guidance on development of model and verification relative to experimentally published results for a prototype reactor. Provided editorial assistance.		
Signature		Date	15/2/2016

Name of Co-Author	Graham J Nathan		
Contribution to the Paper	Provided early and ongoing guidance on conceptual design of modelling activities. Provided editorial assistance.		
Signature		Date	04 February 2016

6

THE POTENTIAL ROLE OF DATA-CENTRES IN ENABLING INVESTMENT IN GEOTHERMAL ENERGY

Ashok A Kaniyal [a,b], Graham J Nathan [a,b], Jonathan J Pincus [a,c]

a Centre for Energy Technology, The University of Adelaide South Australia 5005
b School of Mechanical Engineering, The University of Adelaide South Australia 5005
c School of Economics, The University of Adelaide South Australia 5005

Applied Energy 2012 (98) 458-66

Applied Energy 98 (2012) 458–466

Contents lists available at SciVerse ScienceDirect

Applied Energy

journal homepage: www.elsevier.com/locate/apenergy

The potential role of data-centres in enabling investment in geothermal energy

Ashok A. Kaniyal [a,c,*], Graham J. Nathan [a,c], Jonathan J. Pincus [a,b]

[a] University of Adelaide, Centre for Energy Technology, North Tce, South Australia 5005, Australia
[b] University of Adelaide, School of Economics, North Tce, South Australia 5005, Australia
[c] School of Mechanical Engineering, University of Adelaide, North Tce, South Australia 5005, Australia

ARTICLE INFO

Article history:
Received 10 October 2011
Received in revised form 3 April 2012
Accepted 10 April 2012
Available online 15 May 2012

Keywords:
Techno-economic assessments
Stranded geothermal energy
Incremental investment
Fibre optic networks
Data centres
Direct use

ABSTRACT

A techno-economic analysis is presented, of the potential for data-centres and fibre optic networks to drive investment in geothermal resources. The concept is attractive because of data-centres' stable demand for electricity and refrigeration at a scale of <5 MW_e, corresponding to the output of a single well doublet; because the cost of establishing a fibre optic link is an order of magnitude less than augmenting an electricity transmission network; and because it offers an opportunity for geothermal systems to compete with the retail price of electricity. A comparison of energy delivery outcomes was performed for both engineered geothermal systems (EGS) and hot sedimentary aquifer (HSA) reservoirs to identify the minimum conditions that could make the concept economically attractive. For the high temperature EGS, a single and dual pressure binary organic Rankine cycle (EGS-ORC, EGS-2×ORC), a single stage flash (EGS-flash) and a hybrid flash-binary system (EGS-hybrid) were studied. The HSA system investigated the direct use (HSA-DU) of the geo-fluid in an absorption chiller for refrigeration and the use of coincidental natural gas resources to deliver electricity via an internal combustion engine. The technical performance of these systems was assessed for a range of well-head pressure (EGS only) and geo-fluid flow rate scenarios. The economic performance of the combined set of investments in optical fibre and energy infrastructure was examined by estimating the expected internal rate of return (E[IRR]). The HSA-DU option yielded an E[IRR] of 14%, following the installation of energy capacity equivalent to the output of one well-doublet assuming the displacement of the Australian retail price of electricity; and 12% for the US retail price. In comparison, the EGS-hybrid was found to have an E[IRR] of 8%, if the Australian retail price were displaced and 4% if the US retail price were displaced. The EGS-flash, ORC and 2×ORC scenarios were found to be progressively less attractive than the EGS-hybrid. To identify the conditions under which the concept could satisfy commercial hurdle rates, the sensitivity of the E[IRR] was investigated for the cost of an optical fibre link; the EGS resource depth; the retail price of electricity displaced; and a data-centres' energy consumption profile. Credits for CO_2 emissions abatement at $23/ton were found to have only a marginal influence on the economic performance of the EGS and HSA scenarios examined.

1. Introduction

Energy from hot rock (HR) geothermal resources could contribute significantly to the supply of large-scale renewable electricity worldwide. For example, both the US and Australia have an estimated resource base of 200 ZJ ($\times 10^{21}$ J) [1,2] with a temperature range of 200–350 °C. However, investment in these resources has been limited by uncertainty about reservoir permeability, above ground systems [3–6] and induced seismicity from hydraulic fracturing for engineered geothermal systems (EGS) [7]. Concern over induced seismicity suggests that large scale generating facilities are likely to be sited far from urban markets. Further, the profitable delivery of electricity to a grid is expected to require plants of 500–1000 MW_e, while EGS is yet to be reliably demonstrated even at scales of a few MW [7,8].

One alternative to the long-distance transmission of electricity is to use existing pipelines to transport methane produced by the methanation of hydrogen from electrolysis [9]. However, the technical challenges of a project of this magnitude—involving 50 MW_e of geothermal EGS capacity—were not fully addressed [9]; and a considerable public subsidy would be required.

Where induced seismicity is not an issue, a profitable use of (non-EGS) geothermal energy is to meet the combined heat and power requirements of established district communities (e.g. small towns or stranded industries) [10–16]. Although this approach can provide an attractive revenue stream by returning the retail price of electricity, the viability of a CHP system is sensitive to weather conditions [10–16]. More importantly, the number of suitable sites is limited.

* Corresponding author at: School of Mechanical Engineering, University of Adelaide, North Tce, South Australia 5005, Australia. Tel.: +61 403691321.
E-mail address: ashok.kaniyal@adelaide.edu.au (A.A. Kaniyal).

0306-2619/$ - see front matter © 2012 Elsevier Ltd. All rights reserved.
http://dx.doi.org/10.1016/j.apenergy.2012.04.009

Nomenclature

ΔT_p	pinch point temperature difference
0	thermodynamic dead state condition (subscript)
$	refers to US dollars (2011), assuming parity with Australian dollar
AGEA	scenario based on the delivery of electricity to the grid from Australian Geothermal Energy Association report
bar-g	gauge pressure in bars
CO_2-e	CO_2 equivalent emissions
CSIRO	Commonwealth Scientific and Industrial Research Organisation
CHP	combined heat and power
d	depth in feet (subscript)
e	electricity (subscript)
$\dot{E}_R$	exergy of the geo-fluid with respect to the dead state temperature of 303 K
$\dot{E}_{CHP}$	useful heating effect of the geo-fluid after it passes through the electricity generation cycle in exergy terms
EGS	engineered geothermal system
E[IRR]	expected internal rate of return - averaged across all geo-fluid production conditions (and uncertain sensitivity parameters where indicated)
E[NPV]	expected net present value – averaged across all geo-fluid production conditions and (uncertain) sensitivity parameters
EPCM	engineering, procurement, construction and management
Flash	single stage flash cycle
GHG	greenhouse gas
gf	geo-fluid (subscript)
HSA	hot sedimentary aquifer
HSA-DU	direct use of geo-fluid from HSA to deliver refrigeration via an absorption chiller
Hybrid	hybrid single pressure flash-binary cycle
ICE	internal combustion engine
IT	information technology (refers to data-centre server infrastructure)
ORC	single pressure binary organic Rankine cycle
2×ORC	dual pressure ORC
LCOE	levelised cost of electricity (US$/kWh$_e$)
P_{wf}	thermodynamic cycle working fluid pressure
P_{wh}	geo-fluid pressure at the well-head
PH	ORC pre-heater (subscript)
PUE	power usage effectiveness is the ratio of the total electrical load of a data-centre to the electricity delivered to the facility's IT infrastructure
E	ORC evaporator (subscript)
η_{th}	first law thermodynamic efficiency of cycle
η_u	utilisation (second law) efficiency of thermodynamic cycle
NG	natural gas
r	refrigeration (subscript)
t	turbine (subscript)
th	thermal (subscript)

The final possibility for connecting a remote geothermal site to market is to bring customers, like data-centres and telephone exchanges, to the geothermal site. Owing to their stable demand for electricity and refrigeration [17,18], these types of facility offer the potential to mitigate some of the disadvantages of the options described above. Like, district communities, data-centres offer geothermal resources the potential to displace the retail price of electricity. Data-centres also offer greater flexibility in geothermal site selection given their modularity, the ubiquity of optical fibre networks and their low cost of extension (see Fig. 1) [3,9,19]. However, to induce them to co-locate with a geothermal facility, it is necessary to offer energy prices to data-centres that are no higher than in an urban area.

The energy demands of co-located data centres could be met by EGS, using a single well doublet. Alternatively, the technical risks associated with EGS could be avoided altogether [5], by the direct use of the geo-fluid from shallower lower temperature (<150 °C [11]) hot sedimentary aquifers (HSA-DU) in an absorption chiller [13]. However, this latter option requires a supplementary source of power for data-centre's electrical load. Here, it is assumed that supplementary power is provided by natural gas, given the strong correlation between high grade geothermal resources and natural gas production and/or distribution infrastructure. This confluence has arisen in part from the use of historical data from exploratory gas (also oil and water) wells to predict subterranean temperatures [2,5,9,20]. Further, urban data-centres often use natural gas internal combustion engines to generate electricity [21,22], demonstrating both the technical and economic feasibility of this approach.

Although the complementarities between geothermal resources and data-centre's load have been noted previously by commercial operators, there has been no systematic assessment in the open literature [23,24] of the potential synergies between natural gas infrastructure and geothermal resources, to satisfy data-centres' electrical and refrigeration load.

Given this background, the objectives of the present assessment are:

- to design energy delivery systems that can meet a data-centre's demand for electricity and refrigeration using:
  - a high temperature EGS CHP or electricity only plant by employing:
    - a single (EGS-ORC) or dual pressure (EGS-2×ORC) binary organic Rankine cycle,
    - a single pressure flash system (EGS-flash),
    - a hybrid flash-binary system (EGS-hybrid),
  - or a lower temperature HSA direct use (HSA-DU) system incorporating a natural gas internal combustion engine for electricity generation;
- to evaluate the economic prospects of a combined set of investments in energy and optical fibre infrastructure, and their sensitivity to data-centre load profile, geological characteristics of EGS/HSA reservoir and proximity to the fibre network.

2. Methodology

The technical and economic performance of each geothermal energy delivery system, data-centre combination was calculated for the cumulative energy output from a series of up to four well doublets that are assumed to yield the same geo-fluid temperature and flow-rate. All energy delivery scenarios assume the geo-fluid to be pure water. For the economic assessment, a real options approach was taken, so that no further aboveground plant is installed unless warranted by the production conditions of the first well doublet.

2.1. Data-centre energy consumption profile

A data-centre's power usage effectiveness ratio was used to determine its refrigeration and electrical load. The PUE is defined

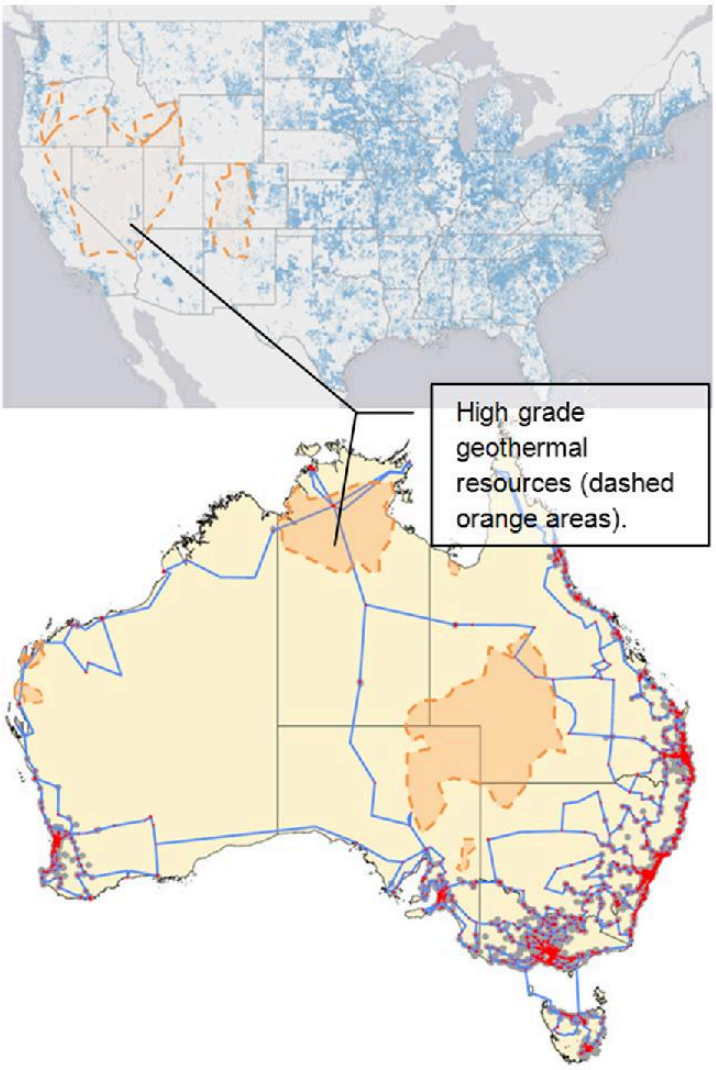

Fig. 1. Coincidence of high-grade geothermal resources $T_{reservoir}$ > 200 °C at ~6.5 km in US [25], ~5 km in Australia [26] with the respective broadband/optical fibre networks [27,28].

as the ratio (>1) of the total electrical (equivalent) load to the electrical load of the facility's IT infrastructure [29]. Here, the total load was assumed to be dominated by refrigeration and IT infrastructure [21]. Assuming an annual average data-centre load equal to 75% of the peak [17], the economic sensitivity of the set of investments in energy and communications infrastructure was assessed for PUE = 1.2, 1.4 and 1.6 [30].

2.2. Geothermal energy delivery scenarios

The performance of the EGS scenarios was investigated with respect to:

- twelve geo-fluid production scenarios comprising:
  - Well-head pressures (P_{wh}): P_1 = 13 bar, P_2 = 15 bar, P_3 = 16 bar and P_4 = 19 bar.
  - Geo-fluid flow rates: high: 70 kg/s, moderate: 50 kg/s and low: 30 kg/s.
- four above-ground plant configurations:
  - Single stage binary organic Rankine CHP (ORC).
  - Dual pressure ORC – electricity only (2xORC).
  - Single stage flash CHP (flash).
  - Hybrid flash-binary CHP (hybrid) and
- resource depth: 5 km or 6.5 km.

For the CHP systems, a proportion of the geo-fluid was assumed to be directed to a single-effect absorption refrigeration cycle [31], whose output was estimated using manufacturer's data: see Section 2.3.3.

Performance sensitivity for the HSA-DU system was limited to the three aforementioned geo-fluid flow rates [5,32], while assuming the availability of the geo-fluid at 125 °C to drive a single-effect

absorption cycle. Data-centres' electrical load was assumed to be met via a natural gas internal combustion engine (NG ICE).

For all scenarios, the parasitic, electrical load of pumping the geo-fluid from the reservoir was assumed to be 10% of the calculated net electrical output [33].

2.3. Energy delivery system

2.3.1. Enhanced geothermal system (EGS)

For the four above-ground plant configurations introduced above, the steady state analytical methodology outlined by DiPippo [11] was adopted. The parasitic loads of the above-ground plant components can be found in Supplementary material (see Table S.1).

Analyses of the single and hybrid flash systems ignore the potential parasitic effects of non-condensable gases (NCGs) on output (and GHG emissions). Given high variability in the concentrations of NCGs in the geo-fluid, a comprehensive assessment is outside of the scope of the present investigation [6].

The utilisation efficiency (η_u) of each EGS plant configuration was estimated using Eq. (1), where $\dot{W}_t$ is the turbine work output, $\dot{E}_{CHP}$ (given in Eq. (2)) is the geo-fluid's residual useful heating effect (in exergy terms) and $\dot{E}_R$ (see Eq. (3)) is the geo-fluid exergy at dead-state conditions [11].

$$\eta_u = \frac{\dot{W}_t + \dot{E}_{CHP}}{\dot{E}_R}, \tag{1}$$

$$\dot{E}_{CHP} = (1 - x_2)\dot{m}_{gf} c_p \left[T_{in} - T_{out} - T_0 ln \frac{T_{in}}{T_{out}} \right]. \tag{2}$$

Here x_2 is the geo-fluid vapour fraction at the well-head (for ORC and 2×ORC systems $x_2 = 0$), $\dot{m}_{gf}$ is the geo-fluid flow rate, c_p is the specific heat capacity of water, T_{in} = 398 K/378 K and T_{out} = 378 K/368 K are the absorption chiller hot water inlet/outlet conditions, and T_0 = 303 K is the dead state temperature [31].

$$\dot{E}_R = \dot{m}_{gf}(h_{gf} - T_0 s_{gf} - e_0). \tag{3}$$

where h_{gf} and s_{gf} are the enthalpy and entropy of the geo-fluid at the production well and $e_0 = h_0 - T_0 s_0$ is the geo-fluid's specific exergy at dead state [11].

2.3.1.1. Single stage flash (EGS-flash). The EGS-flash system's electrical output was maximised with respect to separator temperature in the range 125–160 °C, assuming condensation at 50 °C. System thermal efficiency was estimated using Eqs. (4) and (5), where $(\dot{Q}_{in} - \dot{Q}_o)$ is the net heat added to the cycle and $\dot{W}_e$ is the net work delivered.

$$\eta_{th} = \frac{\dot{W}_e}{\dot{Q}_{in}}; \tag{4}$$

$$\dot{Q}_{in} - \dot{Q}_o = \dot{W}_e. \tag{5}$$

Liquid geo-fluid separated at the well-head was assumed to be used in an absorption refrigerator, but an auxiliary vapour compression chiller was also assumed to be employed to meet a data-centre's peak refrigeration demand. Before re-injection, the two geo-fluid streams directed to the absorption chiller and steam turbine were assumed to be re-combined.

2.3.1.2. Single pressure binary-organic Rankine cycle (EGS-ORC). The single stage EGS-ORC cycle was assumed to be sub-critical with pentane as the organic working fluid. Given pentane's high critical properties (T_c = 197 °C), it does not need to be superheated for geo-fluid temperatures up to 210 °C (P_{wh} = 19 bar-g) [34,35]. For well-head pressures (P_{wh}) from 13–19 bar-g, performance was calculated for the working fluid pressure (P_{wf}) range: 19–27 bar-g.

The pinch point method was used to model the evaporation and vapourisation of pentane by the geo-fluid assuming ΔT_p = 5 K. To enable its use in a single-effect absorption chiller a pre-reinjection geo-fluid temperature of 125 °C was assumed. Eq. (6) was used to estimate the ORC's first law thermal efficiency [11].

$$\eta_{th} = \frac{\dot{W}_{net}}{\dot{Q}_{PH/E}}. \tag{6}$$

2.3.1.3. Dual pressure ORC (EGS-2×ORC). The electricity only, EGS-2×ORC plant was modelled with the same working fluid as the single stage ORC and P_{wf} for the high pressure stage, with 2–3 bar-g assumed for the low pressure stage. The configuration of the set of pre-heaters (PH) and evaporators (E) in series enabled the maintenance of a geo-fluid temperature of 50–60 °C at re-injection.

2.3.1.4. Hybrid flash-binary cycle (EGS-hybrid). The combined work output of the flash-ORC hybrid was maximised with respect to separator temperature in the range 125–160 °C, with pentane assumed to be the ORC working fluid. Eq. (7), which accounts for the work contribution of the ORC and flash cycles as a proportion of the total, was used to estimate the system's thermal efficiency. For its use in a single-effect absorption chiller, a pre-reinjection (after passing through the flash separator, ORC preheater and evaporator) geo-fluid temperature of 105 °C was assumed [31].

$$\eta_{th} = \frac{\dot{W}_{ORC}}{\dot{W}_{ORC+flash}} \eta_{th\_ORC} + \frac{\dot{W}_{flash}}{\dot{W}_{ORC+flash}} \eta_{th\_flash}. \tag{7}$$

2.3.2. Hot sedimentary aquifer direct use (HSA-DU)

The geo-fluid extracted from a hot sedimentary aquifer at 125 °C was assumed to have a fouling factor within the range required by the absorption chiller's generator, eliminating the need for a secondary heat exchanger [31,36].

The data-centre's electricity demand was assumed to be met using a reciprocating natural gas (NG) internal combustion engine (ICE) with a work rate of 9 MJ/kWh$_e$ [21]. At the proposed scale an ICE is approximately 20% more efficient than a Brayton cycle [37] and costs half as much. Additionally, its selection over a gas turbine is affirmed by its dominance within industrial scale data-centres [22] and the CSIRO assessment of energy options for data-centres [21]. (The cost of using natural gas for both electricity and absorption refrigeration was assumed to be equal to the urban retail price of electricity [21].)

2.3.3. Absorption refrigeration system

The refrigeration output of a single-effect absorption cycle was calculated based on its linear relationship with hot water flow at a given temperature, 125 °C (for EGS-ORC, flash and HSA-DU) or 105 °C (EGS-hybrid) (see Ref [31]).

2.4. Costs

This subsection discusses the significant project-specific costs. Full lists of equipment and costs are provided in Supplementary material. All money amounts are given in US dollars.

2.4.1. Estimates

2.4.1.1. Geothermal above-ground plant. Standard techniques in chemical engineering cost handbooks were used to calculate the costs of the ORC and flash plant components [38–41]. Costs for all plant configurations include engineering, procurement, construction, management and auxiliary infrastructure.

The specific (per kW_e) costs for all CHP systems included the absorption system's refrigeration output, which was represented in equivalent electrical units by dividing by 3.2 – an electric chiller's coefficient of performance [21].

2.4.1.2. Drilling expenditure. The geo-fluid was assumed to be available at 5 km [26] or 6.5 km [2] for the EGS scenarios, and 3.5 km for the HSA scenario [2,5]. Eq. (8) presents the empirical relationship used to calculate the cost of establishing a geothermal well [42,43], with the EGS well stimulation cost assumed to be \$525 k per production well [42].

$$C_{d(ft)} = 580000 \cdot e^{0.000149d}. \quad (8)$$

2.4.1.3. Fibre optic link. The cost of establishing the trenches for the fibre optic cable was assumed to be \$40 k/km [19], with an additional \$5 M for ancillary network infrastructure. This assessment examines two distances of network augmentation: 1500 km and 100 km, but the cost of trenching is ignored for the latter scenario.

A network subscription cost of \$56 per server per month was assumed [44], with the number of servers being estimated by assuming a power density of 2.3 servers per kW_e IT load [45]. In a typical data-centre only 60% of servers are pinged at any one moment in time [29], so this analysis conservatively assumes that only 40% of a data-centre's servers are financial subscribers to the network.

2.5. Economic analysis

While it is conventional to assume that projects which feed into the electricity grid can sell their output at a price that is invariant to the quantity, our study is dependent upon the amount of power that can be sold at the exogenous price, namely, the power generated by up to four, annual well doublet increments. Here, the geothermal energy delivered was assumed to exactly displace the retail prices of \$0.20/kWh_e in Australia [46] and \$0.11/kWh_e in the US [47]. The economic life of each well-doublet increment and the accompanying energy generating plant was assumed to be 25 years.

The comparison of the economic performances of the set of investments in energy and optical fibre infrastructure for all sensitivity scenarios (see Figs. 6 and 7 and Supplementary material) uses the expected internal rates of return (E[IRR]). This parameter was calculated by assuming equal probabilities for all uncertain sensitivity scenarios, P_{wh} (EGS only) and geo-fluid flow rates.

2.6. GHG emissions

The rate at which a data-centre could abate their CO_2-e (equivalent) emissions was calculated relative to secondary emissions associated with the purchase of electricity from the grid. An average emission factor of 0.9 kg CO_2-e/kWh was assumed, which accounts for the mix of electricity generating technologies across Australia's six mainland networks [48]. Sensitivity of the E[IRR] was also assessed for a CO_2 emissions penalty of \$23/ton [49].

3. Technical and economic performance of geothermal scenarios

3.1. Above-ground plant performance

3.1.1. Engineered geothermal system scenarios

Fig. 2 shows that the EGS-hybrid system yields the largest specific work output for each of the well head pressure (P_{wh}) scenarios assessed. For all P_{wh}, the work output from the EGS-hybrid cycle and EGS-flash were maximised at a flash separator temperature of 140 °C and 125 °C respectively.

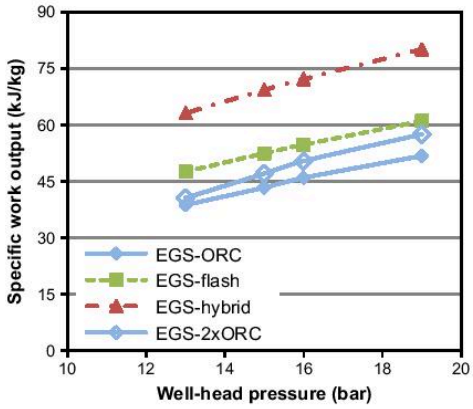

Fig. 2. Specific work output for all EGS scenarios as a function of P_{wh}.

Fig. 3 illustrates the sensitivity of work output to geo-fluid flow rate for the four above-ground technologies. The EGS-hybrid provides the largest useful turbine work, followed by the flash cycle, the 2×ORC and finally the ORC. Importantly, the turbine output is strongly dependent on geo-fluid flow rate, which is difficult to predict and so causes high risk in an electrical generating plant. Table 1 shows the EGS-hybrid thermal efficiency to be 20% higher than the EGS-ORC and flash and 80% higher than the EGS-2×ORC. These results are as expected from DiPippo [11].

For the high geo-fluid flow rate scenario, Table 2 presents the refrigeration output for the EGS-hybrid, flash and ORC CHP configurations. As with power output, the refrigeration output is strongly sensitive to flow rate. Also the cycle with the largest refrigeration output, the ORC, corresponds to the lowest electrical output. Fig. 4 shows that the CHP EGS configurations have utilisation efficiencies that are about 25% higher than the electricity-only EGS-2xORC scenario. The EGS-flash system's utilisation efficiency is independent of P_{wh}, as the positive relationship between electrical output and P_{wh} is balanced by its negative relationship to refrigeration output (see Fig. 5).

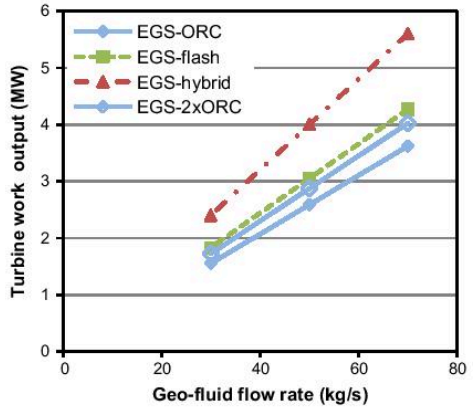

Fig. 3. Turbine work output for all EGS scenarios as a function of the geo-fluid flow rate.

Table 1
Estimated thermal efficiency for all EGS above-ground plant systems for P_{wh} = 19 bar.

Thermal efficiency (%)	
EGS-ORC	15
EGS-2×ORC	10
EGS-flash	15
EGS-hybrid	18

Table 2
Estimated absorption refrigeration output for the EGS-ORC, flash and hybrid systems for geo-fluid flow = 70 kg/s.

Refrigeration output (kW_r)	
EGS-ORC	4214
EGS-flash	971
EGS-hybrid	2094

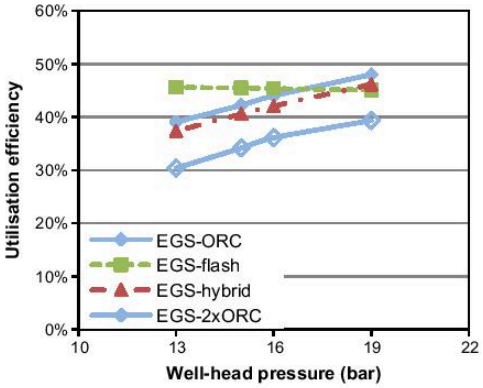

Fig. 4. Utilisation efficiency for all EGS scenarios as a function of P_{wh}.

3.1.2. Hot sedimentary aquifer direct use (HSA-DU) system

Table 3 shows that the HSA-DU scenario's refrigeration output exhibits a similar performance to the more expensive EGS-ORC system. For each data-centre PUE scenario, the fixed refrigeration output from the geothermal system was used to calculate the net electrical output required from the NG ICE.

3.2. Cost of combined system

3.2.1. Above ground geothermal plant

Table 4 presents the total and specific costs of each resource and above ground plant combination, for P_{wh} = 19 bar (EGS only) and geo-fluid flow = 70 kg/s. (The costs of various plant components are given in Supplementary material.) Although a direct comparison of the calculated and historically realised costs [50] may not be appropriate, the calculated costs are in the expected range, given the higher specific cost of the ORC relative to the EGS-flash and EGS-hybrid: see Fig. 5 [51–54].

3.2.2. Drilling

Drilling costs for the EGS scenarios are roughly two (5 km – \$9.3 M) to four (\$19.5 M – 6.5 km) times larger than that required to drill a 3.5 km (\$4.5 M) well to recover geo-fluid from a HSA reservoir. The EGS scenarios (unlike the HSA) also assume a well stimulation cost of US\$525 k per production well.

3.2.3. Fibre optic network augmentation

The cost of the fibre cable for the 1500 km distance was calculated to be \$65 M, with the passive infrastructure forming the largest component of the cost. For the connection over 100 km the total cost of establishment was assumed to be \$5 M.

3.3. Economic performance

Table 5 shows that the HSA-DU scenario enables the highest E[IRR] from a combined set of investments in a fibre optic network and energy generating capacity that corresponds to the output of a single well-doublet. In comparison, the EGS-hybrid and ORC systems are expected to yield considerably smaller returns. (The EGS-hybrid and ORC scenarios represent the best of the flash and non-flash above-ground plant systems.) As is shown later, all sensitivity scenarios yield positive E[IRR]s, but a hurdle rate of 24% is exceeded for HSA-DU alone. Assuming a commercial hurdle rate of 24%, the E[NPV] of the HSA-DU system was calculated to be −\$4 M assuming the Australian retail price and −\$7 M assuming the US retail price.

Although some EGS scenarios seem to be economically attractive, their development entails a considerably higher risk relative to shallower HSA resources. In particular, the performance of the flashed steam cycles depends on the concentration of NCGs (typically CH_4 and CO_2) in the geo-fluid, with higher concentrations reducing turbine output by decreasing condenser heat transfer efficiency [6]. Although this study has not considered the technical or economic impact of employing systems to mitigate the impact of NCGs [6], the economic performance of the next-best alternative to the flash system being the ORC reflects the uncertain impact of NCGs on plant performance.

3.3.1. Sensitivity analysis

Using increments to energy generating capacity that correspond to the output of a well-doublet ('capacity increments') as the basis of comparison, Fig. 6 shows the HSA-DU scenario to yield the best rates of return, with E[IRR] of about 21% (1500 km cable) or 38% (100 km cable) assuming the displacement of the Australian retail price of electricity. Next most attractive was the EGS-hybrid scenario, with a calculated E[IRR] of 10% (1500 km cable) or up to 19% (100 km cable). The EGS-ORC and flash systems are progressively less attractive than the EGS-hybrid. Figures in Supplementary material present the E[IRR] as a function of: 'capacity increments' for the US and Australian retail electricity prices; the cost of drilling; the type of resource (EGS or HSA); and a carbon emissions penalty for all above-ground plant systems.

For the HSA-DU scenario the data-centre's IT electrical load was calculated as a function of the geothermal system's fixed refrigeration output. So, in Fig. 7 the HSA-DU scenario's E[IRR] is negatively correlated with data-centre PUE. With increasing PUE, comes a decrease in the electrical load that can be satisfied by the geothermal system's fixed refrigeration output. For the EGS scenarios, the data-centre refrigeration demand is determined by the system's fixed electrical output. The E[IRR] is positively correlated with PUE for the EGS-ORC system, since the ratio of a data-centre's refrigeration demand to the system's maximum output is ~40% for a PUE = 1.2, but >90% for a PUE = 1.6. For the EGS-hybrid scenario, the larger refrigeration demand at higher PUEs has a parasitic impact on the geothermal system's electrical output. Although this leads to a net increase in total electrical demand, this revenue effect is offset by a decrease in the electricity delivered to the facility's IT infrastructure, and thus the rate of subscription to the fibre network.

Table 3
Estimated output from absorption refrigeration cycle for geo-fluid flow rate = 70 kg/s and corresponding PUE dependant electrical output of NG ICE.

Refrigeration (kW_r)	NG IC engine: net electrical output (kW_e)		
	PUE = 1.2	PUE = 1.4	PUE = 1.6
4214	5853	3292	2194

Table 4
Estimated total and specific costs for above ground geothermal plant for 70 kg/s geo-fluid flow and P_{wh} = 19 bar-g (EGS only).

Configuration	Total ($M)	Specific cost ($/kWe)
EGS-ORC	$9.8	$2502
EGS-2×ORC	$11	$3665
EGS-flash	$4.4	$1281
EGS-hybrid	$7.7	$1757
HSA-DU	$11	$2332

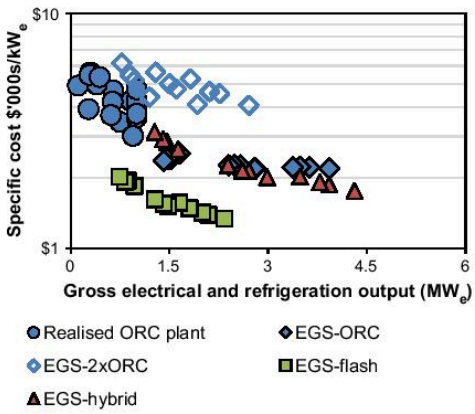

Fig. 5. Comparison of specific costs for realised ORC plant with capacity <1 MW_e to those calculated for EGS-ORC, 2×ORC, flash, and hybrid configurations; CHP systems include output from absorption chiller [50].

Table 5
Expected internal rates of return (E[IRR]) for investment in fibre optic network and generating capacity equivalent to the output of a single well-doublet for the HSA-DU, EGS-hybrid and ORC systems.

Configuration	E[IRR]	
	Australia (%)	US (%)
HSA-DU	14	12
EGS-hybrid	8	4
EGS-ORC	6	3

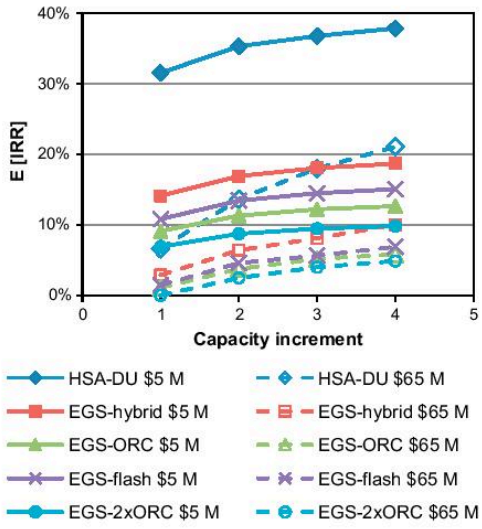

Fig. 6. Dependence of E[IRR] on the cost of establishing the fibre network for all energy delivery systems. Results are for EGS resource depth = 5 km, data centre PUE = 1.2, Australian retail price of electricity ($0.20/$kWh_e$).

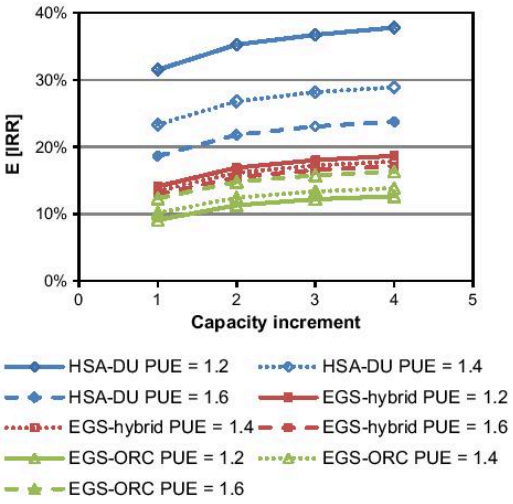

Fig. 7. Dependence of E[IRR] for the HSA-DU, EGS-hybrid and ORC systems on data centre PUE. Results are for fibre optic network cost = $5 M and the Australian retail price of electricity.

Table 6
Comparison of annualised discounted capital (at 12%) required to establish 22 MW_e (unless noted otherwise) of geothermal capacity for delivery to the electrical grid or data-centres.

Scenario	Annualised capital outlay	Over period (yrs)	Installed capacity (MW_e)	Estimated LCOE ($/$kWh_e$)	Price ($/$kWh_e$ wholesale/retail)	Geothermal LCOE/price of electricity
AGEA#2 [55]	~$420 M	6	200	0.08–0.120	0.06 (W)	1.67
AGEA [55]	~$127 M	1	22	0.09–0.135	0.06 (W)	1.88
HSA-DU	$13 M	4	22	0.08	0.20 (R)	0.40
EGS-ORC	$10–17 M	14	22	0.16–0.30	0.20 (R)	1.15
EGS-2xORC	$7–13 M	15	22	0.27–0.49	0.20 (R)	1.90
EGS-flash	$9–17 M	10	22	0.14–0.31	0.20 (R)	1.13
EGS-hybrid	$12–21 M	11	22	0.10–0.22	0.20 (R)	0.8

3.3.2. Comparison of annualised capital outlays

Table 6 presents a comparison of the annualised discounted capital outlay and investment period necessary to establish 22 MW_e (equiv.) of geothermal energy generating capacity under the scenarios investigated here. Also presented are the 'AGEA' scenarios that propose the delivery of electricity to the grid. These data show that the data-centre concept has the potential to reduce the annualised discounted capital requirement by at least an order of magnitude relative to the AGEA scenarios. The proposed concept thus enables investors' to significantly reduce their financial exposure to the extant technical risks even though the investment periods are considerably longer. The last column of Table 6 also shows that all scenarios presented here, except the EGS-2xORC, are up to five times more competitive than the AGEA strategies (albeit at an optimistic discount rate of 12%). This increase in competitiveness is, in part because data-centres enable geothermal energy to displace the retail price of electricity.

3.4. Carbon price impact

The EGS scenarios could enable a PUE variant annual abatement potential of 7–10 t CO_2 per kW_e data centre IT load, in comparison the HSA-DU was estimated to have an abatement potential that is up to four times smaller. However, a CO_2 emissions penalty of $23/ton, was estimated to yield only a one percentage point improvement in expected returns for all scenarios assessed (see figures in Supplementary material).

4. Conclusions

In summary, data-centres have been found to offer the geothermal industry a valuable opportunity to incrementally develop energy generating capacity and progressively reduce the uncertainty associated with resource productivity. The opportunity arises from data-centres' modularity, together with the ubiquity of fibre optic and natural gas networks. The proposed concept was estimated to have an annual capital requirement one-thirtieth of that required for the establishment of 200 MW_e of capacity to deliver electricity to the grid, or one-tenth of that required for 22 MW_e of capacity. Although all scenarios were found to yield positive expected rates of return, only the direct use of the geo-fluid from a hot sedimentary aquifer (HSA-DU) was estimated to exceed a 24% hurdle rate, offering 38% in the most favourable circumstances: four well doublets; a fibre optic link costing $5 M; the Australian retail electricity price; a data-centre power usage effectiveness ratio of 1.2; and with natural gas being available with no additional cost of infrastructure. The EGS-hybrid system was estimated to yield up to 19% (under the same conditions); however this is well below the returns required for commercial viability. The EGS-flash, ORC and 2×ORC scenarios were estimated to be progressively less attractive. Crediting the HSA-DU, EGS-hybrid and ORC systems for their carbon abatement potential at a rate $23/ton CO_2-e, improves their E[IRR] by only one percentage point.

No other modular source of load offering either as great a flexibility in geographical site selection or with so high a ratio of thermal to electrical energy consumption characteristics has been identified for geothermal resources by a publicly reported study. Although a firm conclusion about the concept's viability requires an assessment of site-specific conditions, the proposed concept offers the geothermal industry a distinctive opportunity to establish a 'green niche' around the growing market for data-centres, to reduce financiers' perceived risks about the technology, and thereby the size of any public subsidy.

Acknowledgements

The authors would like to recognise the generous financial support of the Ricoh Clean Energy Scholarship. The authors would also like to thank the anonymous referees for their helpful comments. A. Kaniyal would like to thank D. Tempesti from the University of Florence for his helpful comments on an earlier draft of this paper.

Appendix A. Supplementary material

Supplementary data associated with this article can be found, in the online version, at http://dx.doi.org/10.1016/j.apenergy.2012.04.009.

References

[1] Goldstein B, Hill A, Budd A, Holgate F, Malavazos M. Hot rocks in Australia – National Outlook. In: 33rd Workshop on Geoth Reserv Eng. Stanford, CA: Stanford Univ.; 2008. p. 14.
[2] MIT. The future of geothermal energy – impact of enhanced geothermal systems (EGSs) on the United States in the 21st century. In: Tester J, editor. Idaho: US Dept. of Energy; 2007.
[3] Gurgenci H. Challenges for electrical power generation from EGS. In: World Geoth. Congress. Bali, Indonesia: Int. Geotherm. Assoc.; 2010. p. 5.
[4] Kaltschmitt M, Streicher W, Wiese A. Utilisation of Geothermal Energy. Renewable energy: technology, economics, and environment. Springer; 2007 [Chapter 10].
[5] Beardsmore G, Cooper G. Geothermal systems assessment – identification and mitigation of EGS exploration risk. In: 34th Workshop on Geotherm Reserv Eng. Stanford, CA: Stanford Univ.; 2009.
[6] Vorum M, Fritzler E. Comparative analysis of alternative means for removing noncondensable gases from flashed-steam geothermal power plants. Golden, Colorado US: NREL; 2000.
[7] Giardini D. Geothermal quake risks must be faced. Nature 2009;462:848–9.
[8] Huang S, Liu J. Geothermal energy stuck between a rock and a hot place. Nature 2010;463:293.
[9] Dickinson R, Battye D, Linton V, Nathan G. Alternative carriers for remote renewable energy sources using existing CNG infrastructure. Int J Hydrogen Energy 2010;35:1321–9.
[10] Barbier E. Geothermal energy technology and current status: an overview. Renew Sustain Energy Rev 2002;6:3–65.
[11] DiPippo R. Geothermal power plants: principles, applications and case studies. Elsevier Science; 2005.
[12] Kanoğlu M, Cengel Y. Economic evaluation of geothermal power generation, heating and cooling. Energy 1999;24:501–9.
[13] Kececiler A, Ibrahim Acar H, Dogan A. Thermodynamic analysis of the absorption refrigeration system with geothermal energy: an experimental study. Energy Conv Mange 2000;41:37–48.
[14] Oktay Z, Aslan A. Geothermal district heating in Turkey: The Gohen case study. Geothermics 2007;36:167–82.
[15] Ozneger L, Hepbasli A, Dincer I. Energy and exergy analysis of geothermal district heating systems: an application. Build Environ 2005;40:1309–22.
[16] Østergaard P, Lund H. A renewable energy system in Frederikshavn using low-temperature geothermal energy for district heating. Appl Energy 2011;88:479–87.
[17] Muenstermann S. Industrialising data centers to reach PUE benchmark 1.2. Honeywell Process Solutions white paper Phoenix, AZ: Honeywell; 2011.
[18] Grayson I. Green computing wins admirers as operators invest in energy efficiency. The Australian: News Ltd.; 2011.
[19] Lehpamer H. Microwave transmission networks: planning, design and deployment. New York: The McGraw-Hill Companies; 2004.
[20] EIA. Top 100 oil and gas fields of 2009. US crude oil, natural gas, and natural gas liquids reserves, 2009: US DOE; 2009.
[21] James G, Horn M, Lilley W. Alternative energy solutions for data centre consolidation. Energy Transformed Flagship CSIRO; 2009.
[22] Aurecon. Engineering response to Director General's requirements Sydney2: Global Switch. Environmental assessment report. Sydney: NSW Govt. Dept. of Plan. and Infrastruct.; 2010.
[23] Grove-White G. ASX announcement 20 May 2009 – Innamincka Data Centre – feasibility study. Sydney: Geodynamics Ltd., ASX; 2009.
[24] Bacon K. Google.org invests more than $10 million in breakthrough geothermal energy technology. Google; 2008.
[25] Blackwell D, Negraru P, Richards M. Assessment of the enhanced geothermal system resource base of the US. Nat Resour Res 2006;15:283–308.
[26] Gerner E. OZTemp – interpreted temperature at 5 km depth image. Canberra: Geoscience Australia; 2010 [p. 1].
[27] NTIA. National broadband map – how connected is my community? Washington, D.C.: US Govt.; 2010.
[28] NBNCo. National coverage maps. Melbourne, Australia: NBN Co Ltd.; 2010.
[29] Barroso L, Holzle U. The case for energy-proportional computing. Computer 2007;40:33–7.

[30] Mares K. Data centers workshop. Boston, MA: CEE, LBL; 2010.
[31] Carrier Asia Co. Ltd. 16JL (single effect steam type), 16JLR (single effect hot water type) Lithium Bromide Absorption chiller.: Carrier Asia Co. Ltd.; 2010.
[32] Polster W, Barnes H. Comparative hydrodynamic and thermal characteristics of sedimentary basins and geothermal systems in sediment-filled rift valleys. In: PO, editor. Basin compartments and seals. Tulsa, Oklahoma USA: Am. Assoc. Pet Geologists; 1994.
[33] Wendt D, Mines G. The effect of ambient design temperature on air-cooled binary plant output. Idaho: DoE Idaho National Laboratory; 2011.
[34] Liu B-T, Chien K-H, Wang C-C. Effect of working fluids on organic Rankine cycle for waste heat recovery. Energy 2004;29.
[35] Chen H, Goswami Y, Stefanakos E. A review of thermodynamic cycles and working fluids for the conversion of low-grade heat. Renew Sustain Energy Rev 2010;14:3059–67.
[36] Hernandez-Galan J, Alberto P. Determination of fouling factors for shell-and-tube type heat exchangers exposed to Los Azufres geothermal fluids. Geothermics 1989;18:121–8.
[37] Siemens. Industrial gas turbines. Houston TX: Siemens AG; 2010.
[38] Ulrich G. A guide to chemical engineering process design and economics. 1st ed. New York: John Wiley & Sons; 1984.
[39] Peters MT, Timmerhaus KD, West R. Plant design and economics for chemical engineers. 5th ed. New York: McGraw-Hill; 2003.
[40] Perry R, Green D, Maloney J. Perry's chemical engineers' handbook. 7th ed. New York: McGraw-Hill; 1997.
[41] Vasudevan P, Ulrich G. EconExpert – an expert system for capital cost estimation Process Publishing; 2000.
[42] Entingh D, Mines G, Nix G, Mansure A, Bauer S, Petty S. Volume I – technical reference manual. In: Etingh D, editor. Geothermal electricity technology evaluation model (GETEM). Washington DC: US DoE and NREL; 2006.
[43] Entingh D, Mines G. A framework for evaluating research to improve US geothermal power systems. Geoth. Resour. Counc. Ann. Meet. San Diego, CA: GRC; 2006.
[44] NBNCo. Corporate plan 2011–2013. NBN Co Pty Ltd.; 2010. p. 105.
[45] SGI. SGI ICE Cube modular data center. Fremont California: Silicon Graphics Intl. Corp.; 2009.
[46] EnergyAustralia. Network price list 2010/11. Sydney, Australia: TRUenergy Pty Ltd.; 2010.
[47] DOE. Colorado. Salt Lake City, UT US DoE Intermountain Clean Energy Application Center; 2010.
[48] National greenhouse accounts (NGA) factors. Canberra, Australia: Dept. of Climate Change and Energy Efficiency; 2010.
[49] GoA. Clean energy future Canberra: Australian Government; 2012.
[50] Gawlik K, Kutscher C. Investigation of the opportunity for small-scale geothermal power plants in the western United States. Golden, CO: NREL; 2000.
[51] Kagel A, Bates D, Gawell K. A guide to geothermal energy and the environment. Washington DC: Geoth. Energy Assoc; 2007.
[52] Shibaki M, Beck F. Geothermal energy for electric power. In: Beck F, editor. Washington DC: Renewable Energy Policy Project; 2003. p. 26.
[53] Kutscher C. Small-scale geothermal power plant field verification projects. In: GRC 2001 Annual Meeting. San Diego, CA: NREL; 2001.
[54] Franco A, Villani M. Optimal design of binary cycle power plants for water-dominated, medium-temperature geothermal fields. Pisa, Italy: Università di Pisa; 2009.

Page Intentionally Left Blank

Statement of Authorship

Title of Paper	The potential role of data-centres in enabling investment in geothermal energy
Publication Status	Published
Publication Details	Kaniyal AA, Nathan GJ, Pincus JJ. 2012. The potential role of data-centres in enabling investment in geothermal energy. Applied Energy 98:458-66.

Principal Author

Name of Principal Author (Candidate)	Ashok A Kaniyal		
Contribution to the Paper	Developed all energy system and financial models for techno-economic analyses. Carried out all drafting and paper revisions following editorial advice from primary and co-supervisors.		
Overall percentage (%)	50%		
Certification:	This paper reports on original research I conducted during the period of my Higher Degree by Research candidature and is not subject to any obligations or contractual agreements with a third party that would constrain its inclusion in this thesis. I am the primary author of this paper.		
Signature		Date	

Co-Author Contributions

By signing the Statement of Authorship, each author certifies that:

i. the candidate's stated contribution to the publication is accurate (as detailed above);

ii. permission is granted for the candidate in include the publication in the thesis; and

iii. the sum of all co-author contributions is equal to 100% less the candidate's stated contribution.

Name of Co-Author	Graham J Nathan		
Contribution to the Paper	Provided early guidance on conceptual design of modelling activities. Provided editorial assistance.		
Signature		Date	Thursday, 04 February 2016

Name of Co-Author	Jonathan J Pincus		
Contribution to the Paper	Provided early guidance on conceptual design of modelling activities. Provided editorial assistance.		
Signature		Date	

7

CONCLUSIONS

This thesis presents conceptual designs, feasible operating regimes and comprehensive performance assessments of two hybrid energy systems. These analyses showed that:

1. the targeted integration of concentrated solar energy to the autothermal coal gasification process for the production of FT liquid fuels, can improve energy productivity by 21%, yield continuous operation over a full solar year and reduce the minimum required production scale to 1500 barrels per day – a tenth of that previously proposed in the literature;
2. the targeted development of geothermal resources to meet the stable refrigeration load of modular data-centres, using natural gas to generate electricity, offers the potential to reduce the minimum capital requirement of a geothermal resource development by at least 30 times, displace the retail instead of the wholesale price of electricity and thus generate returns >24%.

1 System analysis of converting solar gasified/reformed syngas to Fischer-Tropsch liquids

It was shown for the first time that, the conventional coal-to-liquids process can be adapted to integrate concentrated solar thermal input, achieve continuous production over a full year of operation and enable a significant improvement in energy productivity together with a reduction in greenhouse gas emissions. For the particular case chosen here, using Illinois #6 coal due to the widely studied nature of this fuel and the site of Farmington (New Mexico) because of its good solar availability, a predicted increase in net energy productivity of 21% and reduction in greenhouse gas emissions of 28% was reported. Significantly, it was also shown that the solar coal-to-liquids system could be developed with commercially available plant components such that no unit operation with the exception of the solar hybrid vortex flow gasifier requires further development. Of the two solar reactor concepts that were assessed, the hybrid solar vortex reactor, which enables a continuous non-zero flow of syngas to downstream unit operations was shown to require only eight hours of syngas storage, whereas the stand-alone solar packed bed gasifier requires between 59 - 62 days of gas storage to enable continuous operation over a full solar year. If the heliostat field area were increased by 50%, it was shown that the quantity of storage required decreased from 62 days to 34 days. However, a significant limitation of the hybrid solar vortex flow gasifier is associated with the need to oversize the heliostat field to achieve a peak output that is between 1.44 and 2.39 times the hybrid gasifier's total endothermic demand. This oversizing of the heliostat collection capacity results in a modest improvement to energetic productivity of between 20 and 22%, respectively, relative to the baseline, but also reduces the utilization of the heliostat field from 100% to between 92% and 67% respectively. Given the required syngas storage capacity for the solar coal-to-liquids process integrating the packed bed reactor

is at least three orders of magnitude larger than that calculated for the hybrid vortex reactor, integrating autothermal reactions within a solar gasification reactor has clear benefits.

The integration of a natural gas co-reformer with the coal gasification was calculated to improve the utilisation of the heliostat field from 67% to 76% and to reduce emissions by a further 15 kg CO_2-e/GJ. However, for the case of a coal-natural gas calorific blend of 70-30, the predicted emissions were still 42 kg CO_2-e/GJ greater than the lowest-emission form of mineral crude oil. To reduce mine-to-tank CO_2 emissions of the solar coal-to-liquids process below all forms of conventional mineral crude oil, a biomass-coal blend fraction of 55-45% was calculated to be required in the solar hybrid co-gasifier. This biomass blend fraction was shown to be 16% smaller, by weight than that required by the autothermal co-gasification process. Indeed, a solar (100%) biomass-to-liquids system was found to improve overall energetic productivity relative to the autothermal coal-to-liquids system by 4%. This is significant because the autothermal biomass-to-liquids system yields 72% of the energetic output of the conventional coal-to-liquids process and because biomass is typically three to four times more expensive than coal. Importantly, the present process modeling assessment of a solar coal-to-liquids system provides the first unambiguous benchmark relative to which system performance can be evaluated for alternative processes and fuels.

A significant limitation of the packed bed solar reactor was identified to be that almost half of the initial fuel mass batch at the start of a solar day remains largely unconverted at the end of the solar day. For the experimentally calibrated reactor modeling scenario, which assumed Indonesian low-rank coal as the feedstock, it was found that reducing the optimal batch mass by 50%, led to an absolute reduction in the amount of carbon converted by 45%, whereas increasing the optimal batch mass by 50% only reduced the absolute carbon conversion rate by 10%. While a sub-optimal initial batch mass favours faster coal devolatilisation, a super-

optimal batch mass favours faster char gasification. As the fixed carbon fraction in the dry, ash free coal is increased from 46% to 75% the optimal initial batch mass was estimated to decrease by 17%. Thus given the sensitivity of the optimal batch mass to fuel composition, and uncertainty in both fuel composition and solar insolation from one day to the next, maximising reactor productivity over a full solar year will be a significant optimisation challenge. While the present analysis has not sought to address this challenge, it was shown that at least 34 days of gas storage would be required to maintain continuous system operation over a full solar year. The requirement for this amount of gas storage places a significant barrier to the development of the packed bed reactor technology with a FT liquids polygeneration facility. Nevertheless, the analysis presented provides the first comprehensive benchmark of the designs constraints that have to be satisfied to enable productive operation of the downstream FT liquids polygeneration system.

2 Addressing impediments to investment in geothermal energy

It was found that the stable energy load of data-centres, the ubiquitous availability of fibre optic network infrastructure and established oil and gas pipelines, offer an opportunity to generate returns >24%, from an investment in geothermal energy resources. All of the scenarios that generated these returns were based on the use of low-temperature geothermal heat from hot sedimentary aquifers (HSA) to meet the refrigeration load of data-centres and the use of co-located natural gas resources to meet their electrical load. Relative to electricity transmission infrastructure, fibre optic networks also offer greater geographical flexibility with respect to where resources are developed and the scale of development. Importantly, capitalising on synergies with established natural gas resources offers the potential to reduce the minimum well depth required to establish a viable geothermal resource development from at least 3.5 km to less than 1.5 km. Reducing the minimum well-depth thus reduces the minimum capital outlay required to develop a given geothermal resource and also the uncertainty in the energy recovery potential of a geothermal reservoir, assuming a negative log-linear relationship between reservoir permeability and depth. Thus, presented was the first comprehensive analysis of a business case for investment in geothermal resources that is not reliant on proximate access to residential or industrial energy consumer, but the generally ubiquitous access to fibre optic network infrastructure and the modularity of data-centres.

3 Conceptual parallels

Both the proposed solar coal-to-liquids and the geothermal-data centre proposal offer the potential to reduce the minimum viable scale of development, capitalise on access to common-use network infrastructure and offer an opportunity to displace a high value energy commodity. For the solar coal-to-liquids concept these characteristics are evident in the recent emergence of micro-channel FT reactor technology, which enable a reduction in the minimum viable production scale of a FT liquids plant to 1500 bbl/day from an output >>15,000 bbl/day for conventional fixed-bed FT reactors. This corresponds to a predicted reduction in the minimum capital outlay from >US$1.6 b to ~US$200 M. Reducing the minimum viable scale of a plant also reduces the project construction lead time from five to two years, the revenue foregone through this phase and the large portfolio risks associated with significant debt positions. Furthermore, just as the retail price of electricity offers a geothermal resource an opportunity to displace a high value energy commodity that is five times larger than the wholesale price of electricity, the use of solar energy to produce synthetic crude oil offers the potential to generate ~1.5 times more revenue per GJ of output than wholesale electricity. The solar coal-to-liquids process also offers the potential to capitalise on established mineral resource value chains and oil and gas pipeline infrastructure as an energy storage medium, just as the geothermal concept capitalises on established natural gas infrastructure. These broad parallels

4 Future work

The system analyses of the solar coal-to-liquids processes presented offer a benchmark relative to which optimisation studies that reduce energy storage requirements, improve overall capital productivity, and energetic and GHG emissions performance could be carried out. The present assessments provide this benchmark for two solar thermochemical process gasification reactors integrated with a FT liquids production facility. Future work could be directed towards improving the productivity of the solar packed bed reactor and identifying opportunities to optimise performance by incorporating autothermal reactions within the packed bed reactor to enable a continuous non-zero flow of syngas irrespective of solar resource availability. The development of this reactor concept could capitalise on the successful commercialization of the Lurgi solid fuel gasification system over many decades.

The commercial relevance of the hybrid geothermal energy system proposed here, is evident in the CSIRO's recent development of a conceptually identical process that proposes the use of natural gas fired electricity and geothermal driven absorption cooling to meet the energy load of the Pawsey Centre Supercomputer. Indeed the present assessment of the economic performance of this concept over a wide-range of technical, commercial and financial scenarios, offers a benchmark relative to which future developments of geothermal energy systems can be compared.